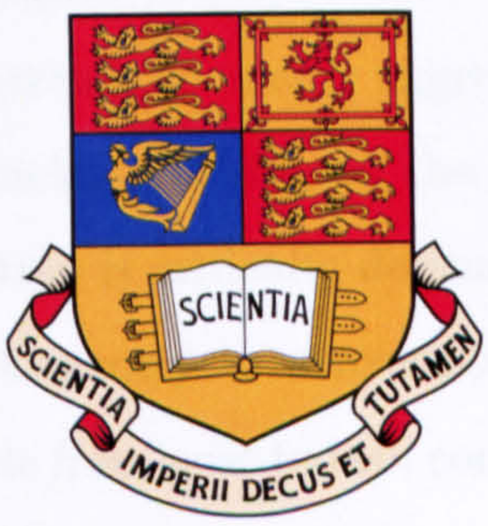
Development Of Conceptual And Preliminary Design Methodologies For Hypersonic Military Aircraft

By

Kashif H. Javaid



Department of Aeronautics

Imperial College London

South-Kensington Campus

London. SW7 2AZ

U.K.

A thesis submitted to the University of London for the degree of Doctor of Philosophy and for the Diploma of Imperial College.

July 2005

RIBL

Abstract

A hypersonic cruise vehicle designed for high-speed, high altitude flight, with global-range capability and airplane-like features, presents desirable attributes for military operations. Emerging mission scenarios have resulted in a growing resurgence in hypersonic vehicles with applications in long-range military payload delivery. These vehicles could offer *global-strike* potential to *time-critical* targets within a matter of hours, increased survivability and would act as an effective deterrence to enemy aggression.

Without existing baseline vehicles and due to the generally complex nature of the problem, a technically viable solution is critically dependent on the successful integration of key component technologies. Contrary to conventional aircraft design, the complete lower surface of a hypersonic vehicle from nose to tail, contributes to the propulsion system. Therefore, the design is highly-dependent on tight airframe-propulsion integration.

The main objective of the current research programme was to develop an automated initial design methodology that facilitates the design and captures the salient features of airbreathing hypersonic vehicles. These vehicles should be capable of sustained hypersonic cruise, horizontal takeoff / landing and have a global-reach potential. The vehicles will be uninhabited and use slush hydrogen as the fuel.

The methodology is an automated tool to expedite the design, evaluation and multi-variable optimisation of vehicle configurations using a small initial parameter set, within a relatively short execution time. The software presents a visual environment for ease of use and flexibility.

A vehicle that has theoretically demonstrated its suitability for hypersonic cruise operations is the waverider. It generates high lift-to-drag ratios at its design-point and it can readily accommodate airbreathing propulsion systems, which is widely considered to be

the key enabling technology in hypersonic vehicles. In this regard, turbine-based turbo-ramjets are used for low-speed operation, that is, takeoff / landing and for accelerating the vehicle from standstill until transition to a scramjet, which will push the vehicle to the desired hypersonic speed. Both engines are integrated with the lower surface of the waverider.

Various aspects relating to airframe / propulsion integration have been investigated, including the smooth performance matching between the two engines considered. In addition, multi-variable optimisation was performed on the design to achieve rapid results for a maximised $Isp \times L/D$ objective function. The code is based on well-established methods and physics-based models, which helped to reduce uncertainty. The methodology was applied successfully to a Mach 10 optimised vehicle. The design cycle time has been significantly reduced compared to detailed CFD analyses, which are too slow and expensive for the preliminary design level.

Acknowledgements

The arduous, interesting and compelling Ph.D. journey draws to an end upon writing this acknowledgement. However, without the help and support of friends, colleagues and family, this research would not have been possible.

Firstly, I would like to thank my supervisor and friend; Dr. Varnavas Serghides for his technical insight and enthusiasm in this work. He has provided continuous support and encouragement during the most trying of times especially with omnipresent paper deadlines. Our discussions at his office door before, during or after meetings were always fascinating. Also, the technical support and encouragement from Prof. Richard Hillier is gratefully acknowledged. I am thankful to The Department of Aeronautics for offering me a research bursary and to the Royal Academy of Engineering, Royal Aeronautical Society, Old Centralians' Trust and the Imperial College Trust for their conference grants.

My time in London was enriched through the support of several friends and colleagues. Most noteworthy of whom include Riz and Manny who have stood by me and offered the much needed distraction. Also to my colleagues in the aero department, including Nikos, Vince and Pino for our light-hearted discussions. The programming wisdom of Asim and Saami was always appreciated. I further wish to thank Fuad, both Imran's, Damian, Andy, Ishthiaq, Suhaib & Zeshan plus to the residents of Goldsmith House and dear friends at The Victoria League for two unique, exciting and fun-packed years.

Finally, I am indebted in gratitude to my parents initially: for supporting me throughout my education, their endless words of encouragement and for believing in me. An equal sentiment is deserved by my loving sisters: Rabyia, Amna and Mariam. Shahzad and my nephew Yaqoob also deserve a mention as do Auntie Qamar and Uncle Farooq for their unconditional kindness.

Dedicated to

Mum and Dad

Contents

Abstract 1

Acknowledgements 3

List of Figures 15

List of Tables 17

Nomenclature 18

1 Introduction 22

1.1 Motivation 22

1.2 Design Challenge 28

1.2.1 Airframe Design 29

1.2.2 Propulsion System 31

1.3 Aims and Objectives 32

2 Review of Relevant Literature 35

2.1 Historical Perspective 35

2.2 Aircraft Geometry 38

2.2.1 Background 38

2.2.2 Waverider Configuration 38

2.3 Airbreathing Propulsion 43

2.3.1 Scramjet 46

2.3.2 Combined Cycle Propulsion Systems 50

2.4 Airframe-Propulsion Integration 52
2.4.1 Design Methodologies 53

3 Design Synthesis Process **56**
3.1 Introduction 56
3.2 Baseline Configuration 56
3.2.1 Assumptions 56
3.2.2 Airframe Design 58
3.2.3 Aircraft Systems Selection 59
3.2.3.1 Fuels 60
3.2.3.2 Propulsion 61
3.3 Mission Profile 63
3.4 Program structure 65
3.4.1 Design tool 65
3.4.2 Flow Chart 66
3.5 Weights Estimation 69
3.5.1 Aerothermodynamics 70

4 Airframe Design **73**
4.1 Introduction 73
4.2 Waverider Theory 75
4.2.1 Flowfield solution 75
4.2.2 Waverider Lower Surface 77
4.2.3 Outboard Waverider definition 79
4.3 Inlet 80
4.4 Force Estimation 86
4.4.1 Viscous Forces 86
4.4.2 Vehicle Force 88
4.5 Optimisation 90
4.5.1 Design Variables and Constraints 90
4.5.2 Method 92

5 High-Speed Propulsion 96

5.1 Scramjet 96

5.1.1 Isolator 97

5.1.2 Quasi-One-Dimensional Combustor Model 100

5.1.3 Model Validation 102

5.1.4 Test cases 104

5.2 Fuel-Air Reaction 108

5.3 Supersonic Nozzle 110

5.3.1 Theory 110

5.3.2 Method 112

5.4 Stream-Thrust Analysis 114

5.5 Summary 116

6 Low-Speed Propulsion 117

6.1 Turboramjet 117

6.1.1 Cycle Analysis 118

6.2 Low-Speed Inlet Design 122

6.2.1 Calculation Procedure 124

6.3 Summary 130

7 Airframe-Propulsion Integration Results 131

7.1 Introduction 131

7.2 Propulsion System Performance 132

7.2.1 Nozzle 132

7.2.2 Scramjet 135

7.2.3 Turboramjet 135

7.2.3.1 Variation of ptp/p_0 138

7.2.3.2 Variation of $Ttp/T0$ 141

7.2.3.3 Variation of Dynamic Pressure, Q_0 144

7.3 Performance-Matching 147

7.3.1 Cycle Analysis 147

7.3.2 Integration of IMOC 149

7.4 Low-Speed Inlet sizing 151
7.5 Airframe-Propulsion Integration 155
7.6 Optimisation 161
7.6.1 Model Validation 161
7.6.2 Mach 10 Waverider 164
7.7 Summary 170

8 Program Architecture **177**
8.1 Introduction 177
8.2 Interface 177
8.3 Point-Design 178
8.4 Multiple Design 182
8.5 Turboramjet 185
8.6 Optimisation 187

9 Discussion **192**
9.1 Waverider 192
9.2 Scramjet 195
9.3 Turboramjet 197
9.4 Integration and Optimisation 198
9.5 Applications 201

10 Conclusions **203**
10.1 Achievements 203
10.2 List of Publications Produced 204
10.3 Recommendations For Further Study 204

Appendices **208**

A Compressible Flow Relations **208**

B Waverider Calculations **210**
B.1 Breguet Range Equation 210
B.2 Integration 210

B.2.1 Runge-Kutta 210
B.2.2 Simpson Method 211
B.3 Nozzle 212
B.4 Simplex Method 213
B.4.1 Rosenbrock's Parabolic Valley: A test problem 215

Bibliography **216**

List of Figures

1.1 The black X-43A attached to the Pegasus booster rocket under the wing of a B-52B. 23

1.2 Air Launch of NASA's X-43A experimental test vehicle over the Pacific Ocean. 23

1.3 Three-view of DARPA's Hypersonic Combat Vehicle (HCV) concept (formely Hypersoar) designed to reach targets 9000nmi away in 2 hours. 27

1.4 Airframe-integrated scramjet from Cockrell *et al.* (2002). 29

1.5 Waverider constructed from a conical body with leading edge shock attachment from Cockrell *et al.* (1996). 30

2.1 SpaceShipOne and its carrier White Knight, first privately manned space vehicle. 36

2.2 Timeline of major achievements from Lewis (2003). 37

2.3 Maximum L/D ratios for hypersonic vehicles and the "L/D barrier" (from Corda and Anderson (1988)). 39

2.4 Nonweiler's caret wing also known as waverider (taken from Corda and Anderson (1988)). 40

2.5 Mach 6 viscous optimised waveriders shown for different generating shock angles (Bowcutt *et al.* (1987)). 41

2.6 Waveriders generated using (a) osculating cones and (b) conical-derived method in the base plane. Diagram adapted from Center *et al.* (1991). . . . 43

2.7 Air Breathing Hypersonic Propulsion Cycles Provide Enhanced Propulsion Efficiency from Moses (2003). 44

2.8 Schematic of a ramjet showing inlet, burner and nozzle. Note the lack of a turbine. Image taken from wings.avkids.com. 45
2.9 Airbreathing Engine Flight Envelope from NASA Langley Research Center. 46
2.10 The NASP programme intended to use scramjets to achieve Low-Earth-Orbit. 47
2.11 Dimensions of the X-43 vehicle 48
2.12 Mach 4-8 operation of a single modular airframe-integrated scramjet, which shows important physical processes occurring before, during and after combustion. Taken from Rogers *et al.* (1998). 52
2.13 Optimised scramjet integrated airframes for two classes of waveriders. . . . 55

3.1 Design mission profile for cruise-type vehicles 64
3.2 Flowchart illustrating the processes with the automated initial design methodology. 67
3.3 NASA's heat-pipe-cooled wing leading edge (HPCLE) concept for active cooling of leading edges. 71

4.1 Key geometric parameters in Waverider design 74
4.2 Determination of the hypersonic flowfield and hence semi-apex cone angle. . 76
4.3 Waverider initial design parameters at the inlet plane. 77
4.4 Forebody Length variation with different bow Shock Angles. 79
4.5 Forebody generation using an inverse design approach starting at the inlet plane. 80
4.6 Mach 9 example of waverider shape, Plan View. 81
4.7 Mach 9 example of waverider shape, Front View. 81
4.8 Single two-dimensional planar ramp for additional compression. Shocks are shown with dashed lines. 83
4.9 Force estimation procedure by integrating forces on cells adapted from Starkey (2000). 88
4.10 Areas involved in lower-surface force accounting. Not to scale. 89
4.11 The series of steps in the downhill simplex method for converging to a minimum. Figure adapted from Press (2002). 94

5.1 Simple schematic of a dual mode ramjet / scramjet with station numbers representing separate parts of the design. Heiser and Pratt (1994). 98
5.2 Region of core flow in the isolator. Heiser and Pratt (1994). 99
5.3 The experimental hydrogen-fuelled combustor geometry specifications of Billig and Grenleski (1970) with a 0.28m constant area section. 102
5.4 Comparison of HICAD's combustor model with the axial pressure distribution from wall pressure measurements of Billig in a cylindrical hydrogen-fuelled scramjet combustor model. 103
5.5 Various thermodynamic flow properties through a scramjet combustor. . . . 104
5.6 On-Design variation of thermodynamic variables and Mach number at a constant altitude at the scramjet combustor face (station 2). 105
5.7 a) The variation of combustor entrance pressure, P_2 with a range of Mach numbers and altitudes, b) a contour plot for improved visualisation. 106
5.8 a) The variation of combustor entrance temperature, T_2 with a range of Mach numbers and altitudes, b) a contour plot for improved visualisation. . 107
5.9 Internal unit process of a streamline that has left and right running characteristics lines. 112
5.10 Expansion net comprising nodes and characteristic lines. 113
5.11 Control Volume for uninstalled performance estimation where $A_{10} > A_0$. . . 115

6.1 Schematic of an axisymmetric turboramjet. 118
6.2 Performance of an idealised turboramjet at sea level: α tends to zero around Mach 2. 120
6.3 Performance of an idealised turboramjet at sea level: α remains positive for longer thereby permitting airbreathing operation to higher Mach numbers. . 121
6.4 The limit of the air-breathing segment indicated by the bypass ratio tending to zero at Mach 5 and a higher altitude. 122
6.5 On-Design operation of a turboramjet inlet system (not to scale) illustrating a four-ramp arrangement that generates four-oblique shocks and a terminating normal shock at station 5. 124
6.6 Program flow chart for thrust-matching and low-speed inlet design. 125
6.7 Required inlet airflow at various altitudes. 127

6.8 Intake loss associated with a four-ramp inlet system. 129

7.1 An example expansion net of a Mach 9 waverider using IMOC for the visualisation. This nozzle has an entry Mach number of 2.8, cowl chamfer of 6° and thrust wall angle is 20°. 133

7.2 A close-up version of Figure 7.1 showing the cowl expansion. 133

7.3 Nozzle thrust output as a function of the upper wall angle for a Mach 9 waverider 134

7.4 Nozzle Specific Impulse output as a function of the upper wall angle for a Mach 9 waverider 134

7.5 Thrust variation as a function of Mach number and altitude for a Mach 9 waverider. 136

7.6 Specific Impulse variation as a function of Mach number and altitude for a Mach 9 waverider. 137

7.7 Variation of bypass ratio as a function of ptp/p_0 for a range of Mach numbers. 139

7.8 Variation of specific thrust as a function of ptp/p_0 for a range of Mach numbers. 139

7.9 Variation of specific impulse as a function of ptp/p_0 for a range of Mach numbers. 140

7.10 Variation of specific fuel consumption as a function of ptp/p_0 for a range of Mach numbers. 140

7.11 Variation of bypass ratio as a function of Ttp/T_0 for a range of Mach numbers. 142

7.12 Variation of specific thrust as a function of Ttp/T_0 for a range of Mach numbers. 142

7.13 Variation of specific impulse as a function of Ttp/T_0 for a range of Mach numbers. 143

7.14 Variation of specific fuel consumption as a function of Ttp/T_0 for a range of Mach numbers. 143

7.15 Variation of bypass ratio as a function of Q_0 for a range of Mach numbers. 145

7.16 Variation of specific thrust as a function of Q_0 for a range of Mach numbers. 145

7.17 Variation of specific impulse as a function of Q_0 for a range of Mach numbers. 146

7.18 Variation of specific fuel consumption as a function of Q_0 for a range of Mach numbers. 146
7.19 Specific Thrust at different altitudes. 148
7.20 Thrust-Matching of low-speed and high-speed engine. 148
7.21 Thrust Matching of low-speed and high-speed engine. 149
7.22 Thrust Matching of low-speed and high-speed engine for a Mach 10 waverider. 150
7.23 Specific Impulse Matching of low-speed and high-speed engine for a Mach 10 waverider. 151
7.24 Inlet area variation with Mach number for an $A_{0_{ref}} = 2.42m^2$ and minimum occurring at the design point Mach 2, 12.2km. 153
7.25 Total pressure recovery for a 4-ramp variable geometry external compression inlet. The recovery exceeds the MIL spec up to Mach 2.5 then trails off. . . 153
7.26 Required inlet area ratio variation with Mach number. 154
7.27 Turboramjet and scramjet - over / under integration (front-view). 157
7.28 Turboramjet and scramjet integration (side-view) for fully low-speed operation. 158
7.29 Turboramjet and scramjet integration (side-view) for transition stage. . . . 159
7.30 Turboramjet and scramjet integration (side-view) for high-speed cruise operation. 160
7.31 Multiple views of a Mach 10 waverider. 162
7.32 Optimisation histories of the (a) objective function and (b) L/D factor for a Mach 9 baseline vehicle. 165
7.33 Optimisation history of the Isp for a Mach 9 baseline vehicle. 166
7.34 Optimisation history of the seven geometric wing curve variables that exist at the tail station. 167
7.35 The (a) Shock and (b) Engine width parameters used in the optimisation. . 168
7.36 Lift and Drag of the Mach 9 optimised waverider. 168
7.37 Front and plan views of Mach 9 optimised waverider. 169
7.38 Optimisation histories of the objective function and L/D factor for a Mach 10 baseline vehicle. 171
7.39 Optimisation history of the Isp for a Mach 10 example waverider. 172

7.40 Mach 10 Optimisation history of geometric wing curve variables. 173
7.41 Mach 10 (a) shock and (b) engine width optimisation histories. 174
7.42 A cubic polynomial fit through the wing-curve points that forms the base curve from which to generate the remaining lower surface. 174
7.43 Mach 10 waverider, $Alt = 33km$, $a_e = 20.5m$, $\epsilon_{min} = 11°$. 175
7.44 Lift and Drag of the Mach 10 waverider. 176

8.1 Organisational structure of GUI made up of an MDI interface. 180
8.2 Point-design calculation flowchart. 182
8.3 HICAD pages for forebody length and scramjet performance estimation. . . 183
8.4 Output data file from HICAD representing the 18° nozzle wall angle. for 18 degree ramp angle. 184
8.5 HICAD Vehicle analysis, lift and drag plus optimisation. 185
8.6 Multiple-design calculation flowchart. 186
8.7 HICAD - Iterate on Mach number. 187
8.8 HICAD Turboramjet design and analysis. 188
8.9 OFFX called from Turboramjet Page in HICAD. Inputs are provided by a batch file (.bat). 188
8.10 Off-Design Mach range data from OFFX that produces mass flow data . . . 189
8.11 Reference file 189
8.12 The optimisation solution flowchart structure. 191

9.1 Completed models of HICAD shown in colour. Refer also to Figure 3.2 for the complete methodology. 193

B.1 Nozzle thrust surface defined by a cubic polynomial. 212

List of Tables

1.1 Possible hypersonic technology transfer from Blankson (1994). 25

3.1 The makeup of a hypersonic vehicle encompasses prominent scramjet flow-path parameters that affect airframe integration. 58

3.2 Fuel properties from Bertin and Cummings (2003) in SI units 60

3.3 Definition of mission profile segments in Fig. 3.1 64

4.1 Inlet / combustor junction flow properties. 86

4.2 Optimisation design variables and side constraints. 91

4.3 Characteristic length scale, λ possibilities in the simplex method. The final column labelled *value* represents suggested values by Nelder and Mead. . . 95

5.1 Billig's experimental pressure measurements, initial conditions. 103

6.1 Inputs for the on-design calculation addressing a Turbojet engine from Mattingly *et al.* (1987). 126

6.2 Outputs for the on-design calculation addressing a Turbojet engine from Mattingly *et al.* (1987). 126

7.1 Comparison of initial data and performance of different waverider examples. 138

7.2 Selection of variables for a Mach 10 waverider undergoing a Mach 5 transition from turboramjet to scramjet propulsion. 150

7.3 Inlet ramp angle selections. 154

7.4 Difference in L/D values compared to HICAD. 163

7.5 Inputs and outputs for Mach 10 case. 166

8.1 Class information from MFC ClassWizard in alphabetical order. (N) stands for numerical code and (G) for GUI. A number of numerical subroutines exist within each class. 179

Nomenclature

ae	semi-minor axis of inlet curve
be	semi-major axis of inlet curve
A	Capture Area
$Alt.$	Altitude
A/A^*	Isentropic Area ratio
A_x	Area Distribution
$ASTP$	Advanced Space Transportation Program
C	Constant specific heat
$CONUS$	Continental United States
$CIAM$	Central Institute of Aviation motors
D	Drag
$DARPA$	The Defense Advanced Research Projects Agency
e_i	Simplex unit vector in ith dimension
f	fuel / air ratio
$FALCON$	Force Application and Launch from CONtinental United States.
$F/\dot{m}_0$	Specific Thrust
g_0	Gravitational acceleration
h_{PR}	Heating value of fuel
H	Height
$ICBM$	Intercontinental Ballistic Missiles
I_{sp}	Specific Impulse
L	Lift

$LaRC$	NASA Langley Research Center
L_{fore}	Length of Forebody
$\dot{m}$	Mass Flow rate
M	Mach number
NAI	National Aerospace Initiative
$NASA$	National Aeronautics Space Administration
$NASP$	The National Aero-Space Plane
P	Absolute Pressure
PAI	Propulsion-Airframe Integration
P_0	Simplex starting value
P_i	Simplex result
p_{tp}	Total pressure of primary flow in turboramjet
$P\&W$	Pratt and Whitney
Q	Dynamic Pressure
R	Radius
Rs	Radius of shock
R_{gas}	Universal Gas Constant
RLV	Re-useable Launch Vehicles
RTA	Revolutionary Turbine Accelerator
SFC	Specific Fuel Consumption
S_a	Stream thrust function
$SEAD$	Strike/suppression of Enemy Air Defenses
SJ	Scramjet
$SSTO$	Single-Stage-to-Orbit
T	Absolute Temperature
$TBCC$	Turbine-based Combined Cycle
TJ	Turbojet
TRJ	Turboramjet
$TSTO$	Two-Stage-to-Orbit
T_{tp}	Total temperature of primary flow in turboramjet
T_{tx}	Total Temperature Distribution

$USAF$	United States Air Force
V	Velocity
W	Width
Ye	Inlet curve half span

Greek

α	Bypass ratio
β	Bleed air fraction
δ	Streamline deflection angle
ϵ	Bow Shock Angle; Cooling air mass flow rate
γ	Ratio of specific heats of pressure and volume
η	Efficiency
η_R	Inlet Total Pressure Recovery
λ	Simplex characteristic length scale
π_F	Turboramjet total pressure ratio
π_r	Isentropic freestream pressure recovery ratio
π	Total Pressure Ratio
τ	total temperature ratio
τ_r	Adiabatic freestream recovery temperature ratio
θ	semi-span angle
$\upsilon(M)$	Prandtl-Meyer Function

Subscripts

AB	Afterburner
b	Burner
c	Compressor; upstream of main burner
c'	Fan
cH	High-pressure compressor
d	Diffuser
eng	Engine at inlet plane
i	Inlet station
λ	Enthalpy
mH	High-pressure spool

mL	Low-pressure spool
mP	Power takeoff shaft
M	Mixer
n	Nozzle
p	Turboramjet Primary Flow
P	Propulsive
pAB	Pressure leaving afterburner
pc	Pressure upstream of main burner
pt	Pressure downstream of main burner
r	radial
R	Gas constant
ref	Reference or design point
req	Required engine airflow
$shock$	Shock position at given station
t	total or stagnation conditions; turbine
$tail$	waverider trailing edge
tH	High-pressure turbine
TH	Thermal
tL	Low-pressure turbine
TO	Power Takeoff
$turb$	turbulent
$wing$	Wing curve
x	axial station

Superscripts

$*$	Reference temperature condition

Numbers

0	Freestream
1	Inlet capture
$1--7$	Inlet curve geometric parameters
$2-10$	Scramjet station numbers

1

Introduction

1.1 Motivation

On 27 March 2004, NASA's X-43A hypersonic research aircraft flew at the world-record speed of Mach 7 (4,780 mph) for air-breathing flight. The vehicle was attached to a modified Pegasus booster rocket as shown in Figure 1.1 and was air launched from the wing of a B-52B aircraft carrier at 40,000 feet, shown in the photograph of Figure 1.2. Moments later, the rocket climbed, accelerated to 95,000 feet and released the vehicle over the Pacific Ocean at booster burnout. The scramjet (Supersonic Combustion Ramjet) then ignited and the X-43A reached its test speed of Mach 7. The flight lasted for the duration of its hydrogen fuel supply; about 10 seconds and achieved positive thrust. Following the test, the X-43A performed a series of aerodynamic maneuvers for six minutes before deliberately terminating in the Ocean. The vehicle, developed largely by NASA Langley Research Center (LaRC), marked the first time a non-rocket, air-breathing scramjet engine successfully powered an autonomous vehicle in flight at hypersonic speeds.



Figure 1.1: The black X-43A attached to the Pegasus booster rocket under the wing of a B-52B.



Figure 1.2: Air Launch of NASA's X-43A experimental test vehicle over the Pacific Ocean.

A vision for hypersonic vehicles has resided within the aerospace community ever since the sound barrier was breached by the Bell X1 in 1947. The obvious advantage for such vehicles is that they offer high-speed travel over long distances with a significant reduction in time. However, the technical challenges that face the development of these concepts remain the same as they did during the quest for supersonic flight over 50 years ago. In general, the hypersonic regime begins when flow exceeds Mach 5 or five times the speed of sound.

Owing to the unconventional nature of hypersonic vehicle design, there are large number of unknowns that must be overcome before this vision becomes a reality. These challenges have compounded the development of operational vehicles yet research into hypersonics is not a new initiative. Military programs during the 1950's cold war saw the design of rocket-based Intercontinental Ballistic Missiles (ICBM) but these were expensive to operate and offered little mission flexibility. Later, a milestone in high-speed research was attained in 1961 when Yuri Gagarin became the first man in orbit. The impetus behind this program was to provide reusable launch capability with a large payload size to make access-to-space a flexible, efficient and inexpensive activity. This embodied the 'space race' and led to the design of NASA's Space Shuttle in 1963 with its inaugural flight by Columbia, in 1981.

A resurgence of interest in hypersonics evolves from the potential to link manned and unmanned vehicle concepts for military operations strike/reconnaissance operations, advanced weapon concepts and the speed/survivability of hypersonic bombers. Recent world conflicts have illustrated how military operations can benefit from space systems assisted operations. The USAF and Army are particularly interested in long-range hypersonic cruise missile capabilities. These systems could strike "time-critical, deeply-buried targets" anywhere on Earth in a matter of hours shortly after being detected from space and before counter-strike by enemy defences. Furthermore, launching short-term communication satellites, remote sensing or navigation capabilities in a target region have obvious strategic implications.

Hypersonic military vehicles require a high probability of mission success for them to be effective in a war situation. There is a need for rapid response, all weather, highly survivable strike potential. The advantages offered by these vehicles are numerous. Even

	Endoatmospheric	Transatmospheric
Military	Global or in-theatre strike	Ballistic missile launch
	Strategic bombers	Satellite launch
	Reconnaissance	Communications maintenance
Civilian	long-haul journeys	Space tourism
	Freight transportation	Space exploration
	technology demonstration	Access to ISS

Table 1.1: Possible hypersonic technology transfer from Blankson (1994).

today's best stealth fighters are vulnerable to interception by enemy defences and are not as effective during the day. Furthermore, weapon systems depend on foreign bases from which to conduct military operations. Hypersonic vehicles will be able to travel long distances and operate from their home base, which will minimise ground support. Their survivability is enhanced as they will operate at high altitudes and high Mach numbers such that counterattack by enemy attacks becomes minimal. Even if a missile interception was launched, it would need to have both a high-speed and high-altitude capability, which is a technology that is hard to acquire and develop. Standoff weapons could be deployed from a far distance; away from hostile airspace. The use of near-term technology in this study will minimise funding expenditure from the current highly constrained aerospace budgets. Adopting an uninhabited concept alleviates any pilot induced limitations. The cost is further minimised since such a vehicle is designed for high-reusability.

Many potential military and civilian applications are listed in Table 1.1 for endo-atmospheric and trans-atmospheric missions.

Civilian hypersonic programs will primarily focus on reusable launch vehicles (RLV) for routine and flexible access-to-space. The aging and costly-to-operate Space Shuttle orbiter is designed for vertical launch and a large fraction of its takeoff weight is made up by rocket-engine propellant. This restricts the useful payload capacity and a replacement for "faster, better, cheaper" RLV's is therefore long overdue. This has been accentuated by the recent Columbia Shuttle disaster* and impending completion of the International

*Mission STS-107, 16 January 2003.

Space Station (ISS), which will require frequent ferrying of crew and equipment.

Imagine also the prospect of high-speed long-haul commercial flights between London and Sydney in just two hours or RLV's using hypersonic cruise trajectories that would make space tourism as easy as commercial air travel.

Fully reusable, recoverable vehicles with rapid turnaround times, would need to have a horizontal takeoff and landing capability (HTOL) to improve their overall efficiency. This would provide aircraft-like operations and minimise ground support. Launch schedules would become more flexible as they would no longer be restricted to specific sites around world.

To maximise propulsive efficiency, RLV's will depend heavily on airbreathing propulsion systems in a similar fashion to the National Aerospace Plane, NASP (or X-30) to avoid carrying large quantities of propellant. NASP was designed to integrate an airbreathing dual-mode scramjet system with its airframe and the complexity of this task was blamed for the project's demise in 1994. Since the cancellation of NASP, NASA decided to focus its attention on more manageable targets for rapid prototyping and short-term technology demonstration. Hypersonic experimental X-vehicles (Hyper-X) emphasised subscale, unmanned, autonomous testing and as a consequence, reduced cost and risk. Flight validation of the scramjet's in-flight performance and airframe-propulsion integration methodology are some of the primary objectives.

The economic and strategic advantages that a hypersonic vehicle could provide to civilian or military applications are far-reaching and has been recognised by industry at large. As with many aerospace research programs, military requirements tend to drive the state-of-art. Bertin and Cummings (2003) highlighted three areas for future US air superiority that have remained unchanged during the last 50 years of hypersonic research. These are to deliver munitions anywhere on Earth (global strike), do it quickly and at high-speed (rapid response) and have flexible, affordable, routine access-to-space (space operations).

According to DARPA: "The intent is to hold adversary vital interests at risk at all times, counter anti-access threats, serve as a halt-phase shock force and conduct suppression of enemy air-defence and lethal strike missions as part of integrated strategic campaigns in the 21st Century."

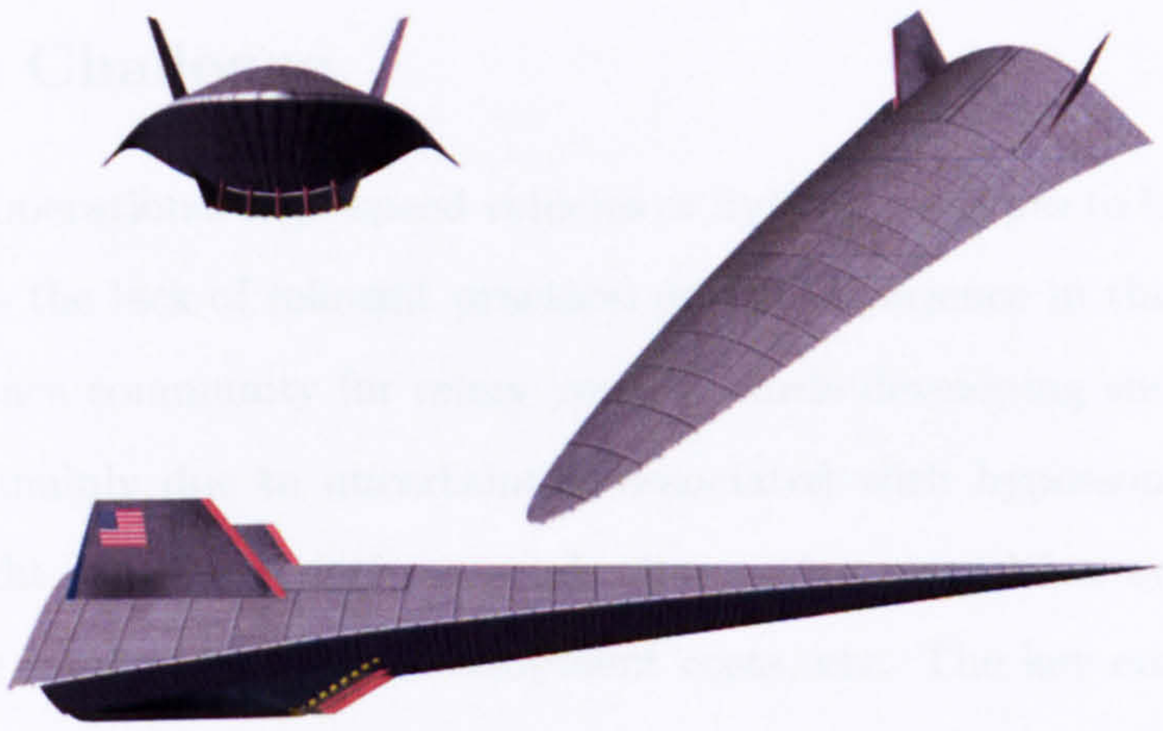


Figure 1.3: Three-view of DARPA's Hypersonic Combat Vehicle (HCV) concept (formely Hypersoar) designed to reach targets $9000nmi$ away in 2 hours.

Global strike ($9000nmi$) is the project goal of a current DARPA/USAF program called FALCON[†] leading to a Hypersonic Cruise Vehicle (HCV) expected by 2025 for HTOL and global-range. The concept is illustrated in Figure 1.3. This strategic philosophy allows the ability to deploy vehicles for the purpose of surveillance, reconnaissance and power projection globally without reliance on overseas bases.

The motivation behind the presented study evolves from a consideration of emerging operational scenarios and developments in hypersonic research. The focus is on uninhabited endo-atmospheric long-range hypersonic cruise vehicles for military payload delivery with HTOL capability. The vehicle will have a highly-integrated airbreathing dual-mode scramjet in a similar manner to the X-43A baseline vehicle, to maximise propulsive efficiency and be able to cruise at Mach 10. Airbreathing propulsion systems will be used since they provide lower specific fuel consumption compared to rockets. These hypersonic concepts are advantageous over ICBM as the latter are not reusable but one-shot devices.

The X-43A now holds the speed record for airbreathing engine aircraft and the test demonstrated that scramjet airframe-propulsion integration is possible and is a large step forward in realising high-speed vehicles. As a comparison, NASA's X-15 achieved Mach 6.7 using rocket engines and the SR-71 "Blackbird" reached Mach 3.2 using airbreathing engines. A hypersonic cruise concept has not yet matured into a practical application mainly due to slowly developing enabling technologies.

[†]`http://www.darpa.mil/tto/programs/falcon.html`

1.2 Design Challenge

The lack of other operational high-speed vehicles or flying prototypes to be used as baseline vehicles as well as the lack of relevant practical design experience in this case, have challenged the aerospace community for many years towards developing such aircraft. These complexities are mainly due to uncertainties associated with hypersonic aerothermodynamics, lightweight structures and materials, innovative propulsion systems, optimised airframe / engine integration, high development costs, etc. The key enabling technology is widely considered to be advanced airbreathing propulsion systems that offer high efficiencies and easy integration with a suitable airframe. (Gustafson and Livingston (2002)).

A technically viable solution for the design of hypersonic vehicles, demands an accurate integration of the propulsion system with the forebody lower part of the vehicles airframe. The freestream capture area must be large for the engine to generate sufficient thrust and the nozzle exit area should be large for sufficient expansion. As demonstrated by the X-43A, the forebody served as the compression surface for efficient combustor operation at hypersonic speeds and the aftbody functioned as an extension to the nozzle expansion surface. The entire undersurface of hypersonic vehicles, therefore, constitutes the propulsion system and contributes to the propulsive force. This high level of interaction between the design of these vehicle components is illustrated in Figure 1.4 where engine characteristics affects the aerothermodynamics.

A rich parameter set and design options for hypersonic cruise vehicles exists ranging from high specific impulse propulsion selection (airbreathing or rocket engine), reusability, takeoff / landing options, high temperature materials, fuel selection, safety and control technology. It is the task of the designer to find the optimum combination of these variables eventually leading to affordable and flexible design solutions for a given set of requirements (Bowcutt (2003)).

The study of hypersonic flow around a vehicle differs to supersonic/subsonic flow due to the high stagnation temperatures and enthalpies experienced. The vehicle will travel along a high dynamic pressure trajectory, with high heat transfer implications and a change in the near-field characteristics of air. This can directly affect combustion of a supersonic stream. Advances in topics such as aerothermodynamics, combined cycle

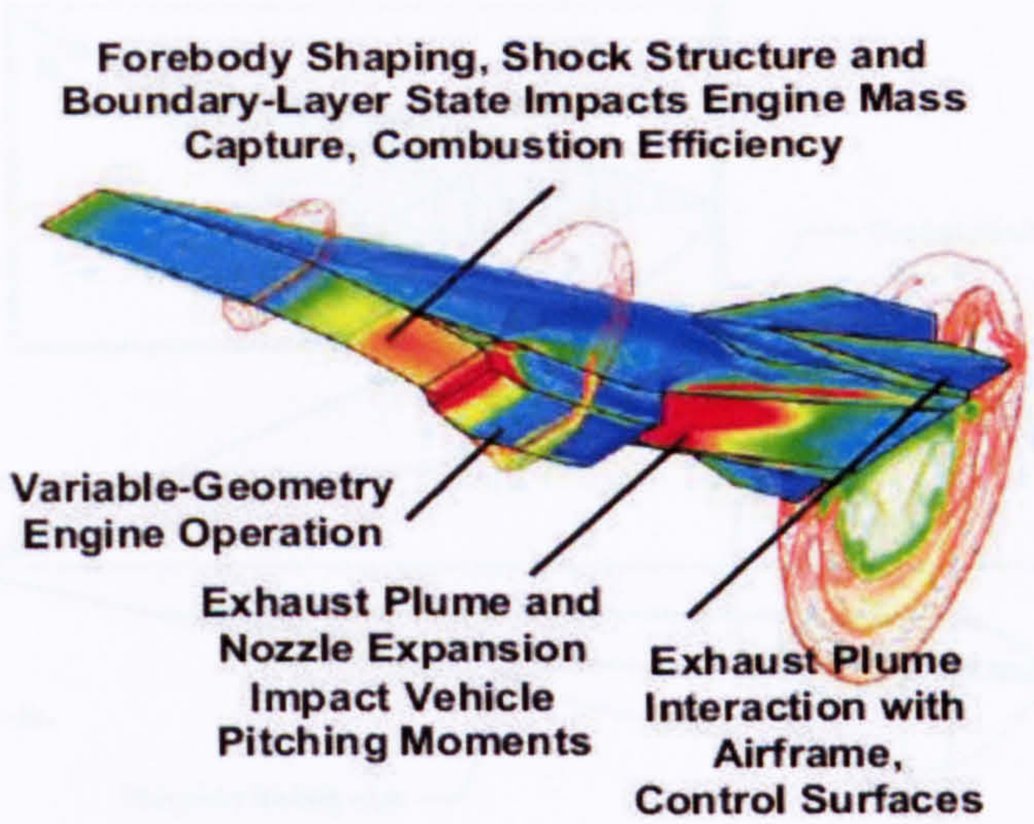


Figure 1.4: Airframe-integrated scramjet from Cockrell *et al.* (2002).

propulsion systems, high-temperature materials, cost etc have, however, expedited the design challenge as discussed by Bertin and Cummings (2003). Before the advent of the Space Shuttle in the 1960's, the difficulties of hypersonic flight were well understood.

Ablative materials and active cooling mechanisms were implemented to alleviate reentry conditions. Steady advancements in materials technology have facilitated the design of high-speed vehicles that can dissipate heat effectively and survive the high-temperatures generated during flight.

Substantial achievements have been made since the late 1950's in the areas of Computational Fluid Dynamics (CFD) and multidisciplinary optimisation; both necessary in reducing the overall development cost.

1.2.1 Airframe Design

A good measure of the aerodynamic efficiency of an aerospace vehicle is its L/D ratio and specific impulse. The L/D ratio becomes particularly important in selecting a suitable airframe in order to achieve a global range. High aerodynamic and propulsion efficiency are required at cruise Mach numbers leading to slender aerodynamic shapes with the potential of integrating the highly specialised propulsion system.

A number of vehicle concepts are available to the designer. A possible candidate to address this challenge, which is also the one selected for this study, is a hypersonic

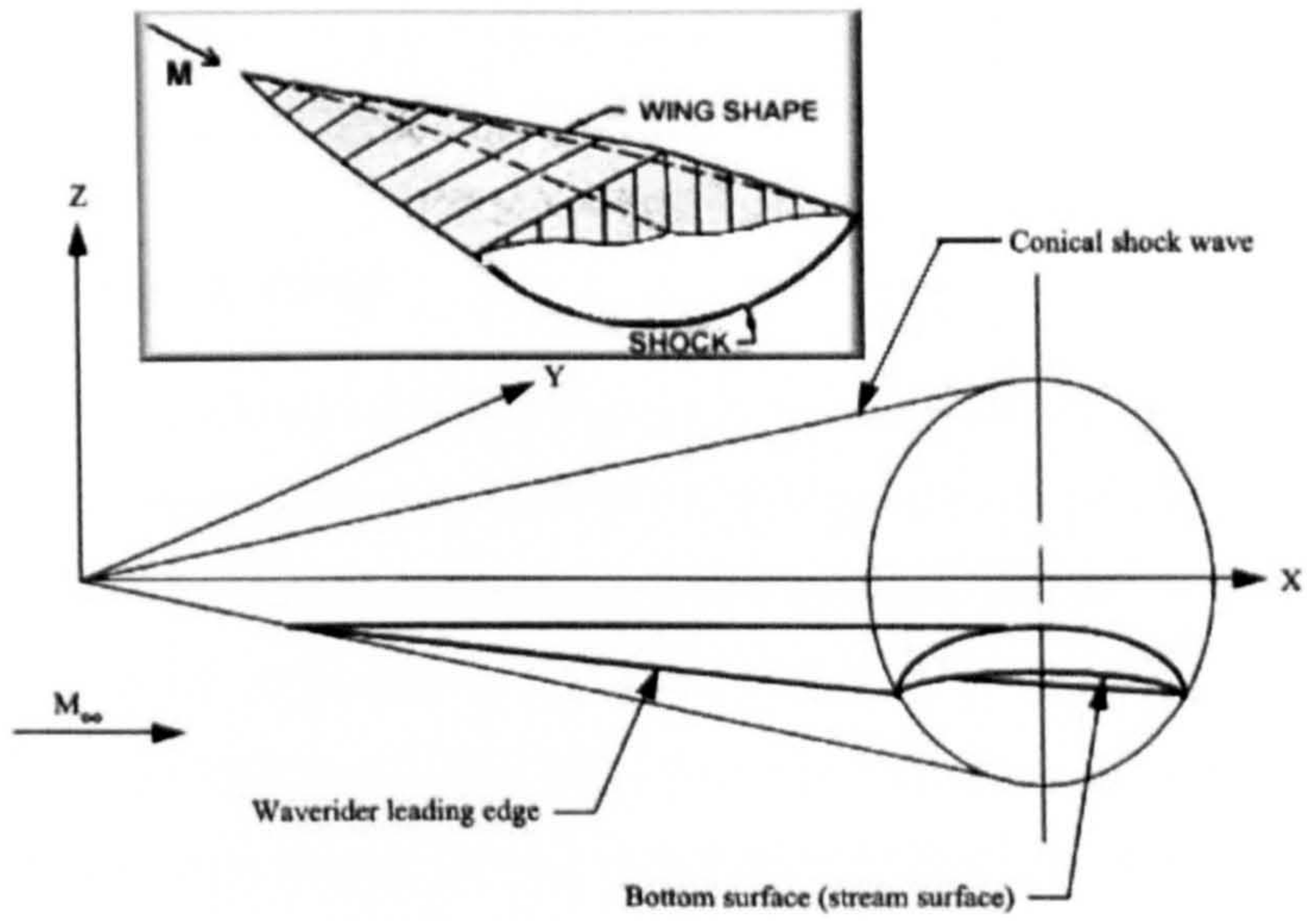


Figure 1.5: Waverider constructed from a conical body with leading edge shock attachment from Cockrell *et al.* (1996).

waverider; first proposed by Nonweiler (1959). A waverider is a shape that generates a bow shock wave that is attached all along its leading edge thereby containing a high pressure region at its lower surface. The vehicle appears to ride its own shock wave, hence the deserved name.

Several advantages exist for selecting waveriders. The perfectly-attached leading edge shock prevents high-pressure flow spillage to the top surface thereby producing high L/D compared to conventional concepts as demonstrated by Küchemann (1978). This also permits the independent design of the lower and upper surfaces. Apart from aerodynamic performance benefits, waveriders have good airframe / propulsion integration characteristics. The lower surface flowfield provides good flow uniformity, which is important for combustion and integration of engine modules.

Other advantages include good volumetric efficiency, favourable off-design performance and practical issues such as leading edge blunting can be accommodated with only a small drop in L/D (Blankson (1994)). Suitability for scramjet integration is another reason for the interest in waveriders. For a space shuttle, its low L/D value (1.5) means it has limited down and cross-range capability. A waverider with possible L/D value of 4, can significantly increase operational flexibility.

Figure 1.5 illustrates how the leading edge of the waverider is inversely constructed

from the shape of a right-circular conical shock. The length of the cone and semi-apex angle of the shock are specified by the designer.

1.2.2 Propulsion System

Airbreathing powerplants were selected over rocket engines based on performance benefits (I_{sp} and SFC) and reusability criteria offered during endo-atmospheric cruise missions. In particular, the takeoff weight and volume are reduced as storage of an on-board oxidiser is not required. Instead, airbreathers will use atmospheric oxygen (like jet engines) along the vehicle's mission trajectory, which will also extend the operational envelope.

Potential airbreathing engines for hypersonic flight include the scramjet, Rocket-Based-Combined-Cycle (RBCC) engine and the Turbine-Based-Combined-Cycle (TBCC) engine. The airflow through a scramjet remains supersonic, contrary to ramjets and this type of engine is expected to be used for future aerospace planes. There are considerable technical challenges that must be overcome before a scramjet of superior performance, becomes practical. A number of research organisations around the world are continuing to develop this technology. One such challenge is the efficient mixing and combustion in a supersonic flow within a combustor of reasonable size.

The RBCC concept blends the performance of the rocket, ramjet, and scramjet into one system for seamless ground-to-orbit operation offering high Isp compared to rockets (Bradford and Olds (1999)).

The TBCC combines jet and ramjet/rocket propulsion. Initially, inlet ducts provide air to turbojets that have common exhaust ducting with a ramjet/rocket propulsion system. At low to moderate Mach numbers the turbojets provide thrust. At higher speeds, the system closes off the inlet flow from the atmosphere, shuts down the turbojets and converts to ramjet/rocket propulsion.

As scramjets require a supersonic stream, takeoff, landing and acceleration to high supersonic speeds are only possible if alternative engines are used in combination with them. A turboramjet is an example of a TBCC-type engine and avoids installation of separate turbojet and ramjet systems, which saves on dead weight considering the turbojet becomes inefficient above Mach 3. The turboramjet will also be more fuel and volume efficient and also avoids the extra complexity associated with the added transition from

turbojet to ramjet.

The turboramjet is rendered inoperable at large Mach numbers (around Mach 5) due to high temperature effects and dissociation losses, which necessitates transition to a scramjet. For turboramjet systems, questions concerning the arrangement of the propulsion system with the high-speed part is resolved with consideration of fuel issues, aerodynamic design of inlets, nozzles together with thermal analysis of these components, which is a major consideration.

As expected, notable challenges are associated with efficient operation of multiple engines with regards to flowpath integration and maximising performance as the capture area required for efficient combustion is large.

1.3 Aims and Objectives

Hypersonic vehicles offer exciting future prospects, but the lack of historical data, practical design experience and baseline vehicles, are some of the formidable challenges that must be overcome. Further challenges are associated with the unconventional nature of the design process, high-temperature effects, highly non-linear aerodynamics and airframe-propulsion system integration. The low-speed flight characteristics and off-design conditions need to be adequately addressed for practical configurations.

In an attempt to reduce the complexity of hypersonic vehicle design and analysis, the investigation must begin at the conceptual / preliminary level to gain an understanding of the underlying physics and sensitivities between the large number of vehicle parameters. Preliminary design tools offer low development costs, are simple and flexible and they have a comparatively short design cycle time. When compared to CFD tools, which although provide detail and accuracy, they require longer times to arrive at a solution and their search of a design space is limited in scope.

The overall aim of this research programme is to develop a part of a conceptual and preliminary design methodology for hypersonic military aircraft with a particular emphasis on propulsion / airframe integration and optimisation; addressing the on-design issues.

The main objective therefore, is to develop a practical, initial methodology that will facilitate the design of hypersonic military vehicles. It will enable the investigation of the synergy between the main airframe and propulsion system components on performance

and design.

In particular, the conceptual methodology will provide an aid for the expedited development and analysis of hydrogen-fuelled hypersonic cruise airbreathing vehicles with global reach and HTOL capabilities. The application will focus on uninhabited operational vehicles through a consideration of the benefits resulting from the elimination of constraints associated with crew / passenger accommodation. This is also a likely development strategy with the recent emphasis towards development of UCAV's, thereby reducing associated risk.

The success of such a vehicle is critically dependent on the correct modelling and tight integration of its propulsion units, inlets and nozzles with the waverider airframe. This is the subject of airframe-propulsion integration, which must be considered early in the design process if mission requirements are to be met. Notable challenges are associated with efficient operation of multiple engines with regards to flowpath integration and performance requirements.

Multidisciplinary optimisation has been incorporated into the methodology to concurrently analyse multiple variables to determine the optimum combination from a given set of user requirements and constraints. This is particularly important for searching the design space and has been shown to produce significantly better performing configurations. Trade-off studies can be performed for producing conceptual level results in minimum time.

The focus on the initial development will be towards the on-design hypersonic flight case and salient features with regards to propulsion and airframe.

The models that will be developed in this study are intended for further optimisation analysis of range, low-speed performance and trajectory during follow-on research programmes.

The external surfaces of the waverider affect both the lifting capability and volumetric capacity, the forebody influences the inlet and the aftbody influences the nozzle and thrust. The thrust requirements are related to engine size, which in turn is dependent on the vehicle airframe size, design and integration of multiple flowpaths and their individual and combined performance. The thrust transition between a low-speed and high-speed engine should be smooth and will be analysed using simple physics models for propulsion

and geometry. In this way, aerodynamic and propulsive efficiency will be maximised when used in conjunction with properly matched inlet and nozzles.

For cruise-type vehicle optimisation as considered in this study, the objective function will be to maximise the range for a given payload so that to yield a high value of the product of I_{sp} and L/D. Furthermore, the high-speed propulsion system must provide low specific fuel consumption and high propulsive lift at cruise, thereby reducing the aerodynamic lift requirement. The low-speed propulsion system design will begin after high-speed engine analysis and integration so that the engines and their inlets can be adequately sized for high-speed transition.

An interactive software program will be developed as part of this research programme that will facilitate the rapid generation of practical hypersonic configurations from a small set of parameters. That will provide an environment for the user to search the design space through the use of parametric engineering models and to perform engineering trade studies, optimisations and visualisation of results. The program will also assist in quickly identifying any trends in vehicle shape and their effects on performance. A vehicle may then be rapidly designed aided by real-time visualisation in a short time cycle.

Off-design issues will not be dealt with in this study due to time restrictions. It is intended that recommendations will be made to deal with mass capture and combustion. Other issues including weight, balance, stability and low-speed performance are outside the scope of the study.

2 Review of Relevant Literature

2.1 Historical Perspective

Research and development of high-speed jet or rocket-powered aircraft have been pursued both during and after World War II. Since the Wright brothers first successful flight of a heavier-than-air vehicle in 1903, many significant achievements have contributed to the impetus for hypersonic flight. Supersonic flight was first achieved by the Bell X1 in 1947 and towards the end of WWII, the German V2 rocket flew hypersonically in 1949 using a more pointed and slender body shape to reduce wave drag.

In 1961, Russian Cosmonaut, Yuri Gagarin became the first human to travel at hypersonic speed when his Vostok I capsule attained Mach 25 during atmospheric reentry. Mission flexility for manned mission was addressed during the development of the winged-glider Dyna-Soar (X-20) concept in 1957 but was later cancelled in 1963 due to huge technical challenges. Many astronauts have been following suit ever since as they leave and return the Earth's atmosphere with an orbital speed of 18,000 mph (5 mi/s) or Mach 24 in the Space Shuttle.

In the the United States, generic studies for aero-maneuvering and aeroassisted orbital transfer vehicles included the Space Shuttle Orbiter and National AeroSpace Plane (NASP). In Europe, noted programs during this same period included HERMES, Sänger (Kuczera (1993)) and the British spaceplane concept HOTOL.



Figure 2.1: SpaceShipOne and its carrier White Knight, first privately manned space vehicle.

RLV's include single-stage-to-orbit (SSTO) or two-stage-to-orbit (TSTO) systems. SSTO are generally accelerator-type vehicles and require a greater technology leap than TSTO, which offer near-term development. This is primarily due to its propulsion system, which will cover a wide range of Mach numbers using either multiple engines or cycles or both.

This strategy (TSTO) of small low-cost advances in technology and near-term development was successfully implemented by the non-government Scaled Composites team, contenders for the X-prize. They flew to the edge of space and back in their privately-funded manned vehicle in June 2004. The design concept consists of a launcher, called SpaceShipOne, underslung beneath its carrier vehicle, the White Knight, in Figure 2.1. Their design demonstrated the potential of access-to-space at a fraction of the cost of normal launch programs.*

The rocket-powered X-15 experimental research vehicle broke the speed record as it achieved Mach 6.7 in 1967 and now recently the X-43A achieved sustained Mach 7 flight using an airbreathing scramjet integrated with its airframe. The Australian HyShot program had a recent success as shown in Figure 2.2 along with other prominent achievements.

Current research focuses on sustained hypersonic cruising flight within the atmosphere. Airbreathing engines are therefore necessary to maintain high efficiency as they use atmospheric oxygen for combustion instead of onboard tanks. Engine - airframe integration is very critical in the design of such vehicles.

The hypersonic region of flight is generally accepted to begin at Mach 5 because that is

*At the time of writing, SpaceShipOne successfully completed the first of the two required flights.

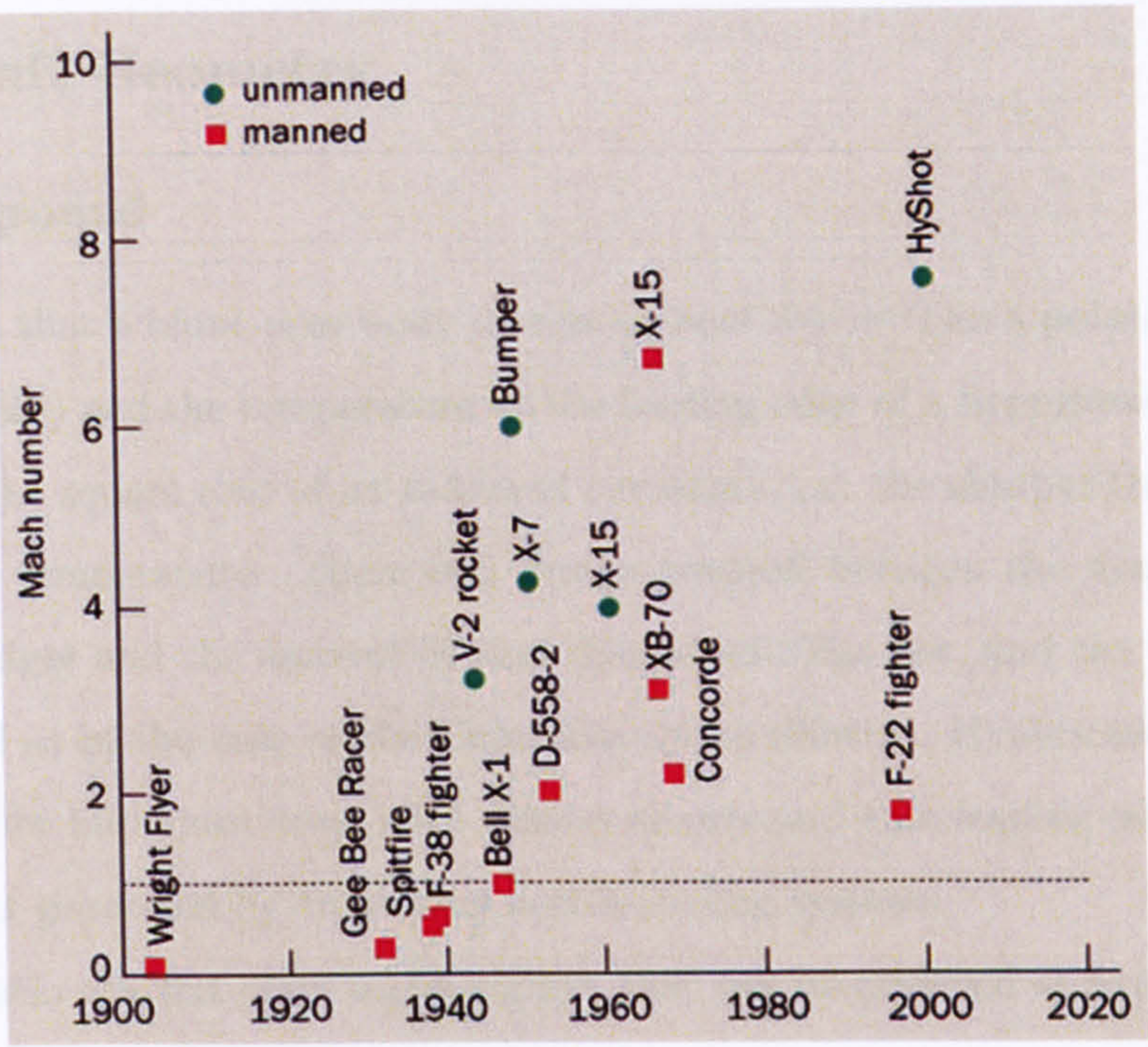


Figure 2.2: Timeline of major achievements from Lewis (2003).

when aerodynamic heating becomes important, with temperatures in the boundary layer and on the surface of an object that is travelling at Mach 5 reaching 1,000°C (Bertin (1994)). For hypersonic flight to be feasible, many challenges are faced that range from designing high-speed air-breathing engines to developing advanced materials, thermal protection and cooling systems.

The lift force is reduced due to the presence of the shock waves and the shock pattern dictates that hypersonic vehicles have highly swept, wedge-shaped wings merged into the fuselage to form an integrated unit. During transition from supersonic to hypersonic flight, merging of the shock layer and the boundary layer affects drag and thermal reactions in the flow increase aerodynamic heating and cause dissociation of nitrogen and oxygen molecules. Aerodynamic heating is related to work done against skin friction while work done against pressure drag produces heat only in the wake. It is desirable to keep the ratio of skin friction to pressure drag small thus reducing convective heat transfer. This chemically reacting flow changes the flow physics and at extreme hypersonic speeds, air molecules can even become ionised leading to the "blackout" phase that hinders radio communication with returning spacecraft. Anderson (1989) provides an in-depth discussion on predicting hypersonic flowfield characteristics.

2.2 Aircraft Geometry

2.2.1 Background

It is well known that a blunt-nose body dissipates heat better than a pointed body (Allen and Eggers (1958)) and the temperature at the leading edge of a hypersonic vehicle scales inversely with the square root of its radius of curvature, i.e. the sharper the leading edge, the greater the temperature. There is a design tradeoff between the drag produced by blunt leading edges and the amount of heat dissipated. Too hot, and the vehicle's safety is compromised as in the case of the Columbia Space Shuttle. Hypersonic vehicles need to be designed for minimum drag, with slender shapes and thin leading edges, alleviating the intense heat generated by employing active-cooling systems.

The L/D ratio of a flat plate is the highest that can be achieved at hypersonic speeds. This, however, is not practical for operational vehicles due to the volume required for systems, fuel etc. It is clear from previous studies that L/D values for hypersonic vehicles are far below that achievable by subsonic or supersonic aircraft.

Küchemann (1978) developed an empirical formulation given by Equation 2.1 defining the upper limit of aircraft performance against speed, in terms of L/D, using data from existing aircraft.

$$L/D_{max} = \frac{4(M_\infty + 3)}{M_\infty}, \; M_\infty > 1 \tag{2.1}$$

This equation is represented by the solid curve in Figure 2.3, which shows L/D_{max} as a function of freestream Mach number, M_∞. Several other points are plotted on this figure with data obtained from wind tunnel experiments and data from flight vehicles. The general trend noted is the L/D_{max} value decreases with increasing Mach number due to the increased drag from the strong shock waves and viscous effects at high speed. The dashed curve and solid symbols on the figure represent research efforts to exceed this apparent "L/D barrier".

2.2.2 Waverider Configuration

A class of hypersonic vehicle, which supersedes the L/D barrier mentioned above, is the waverider and was first conceived by Terence Nonweiler in 1959. The impetus behind his

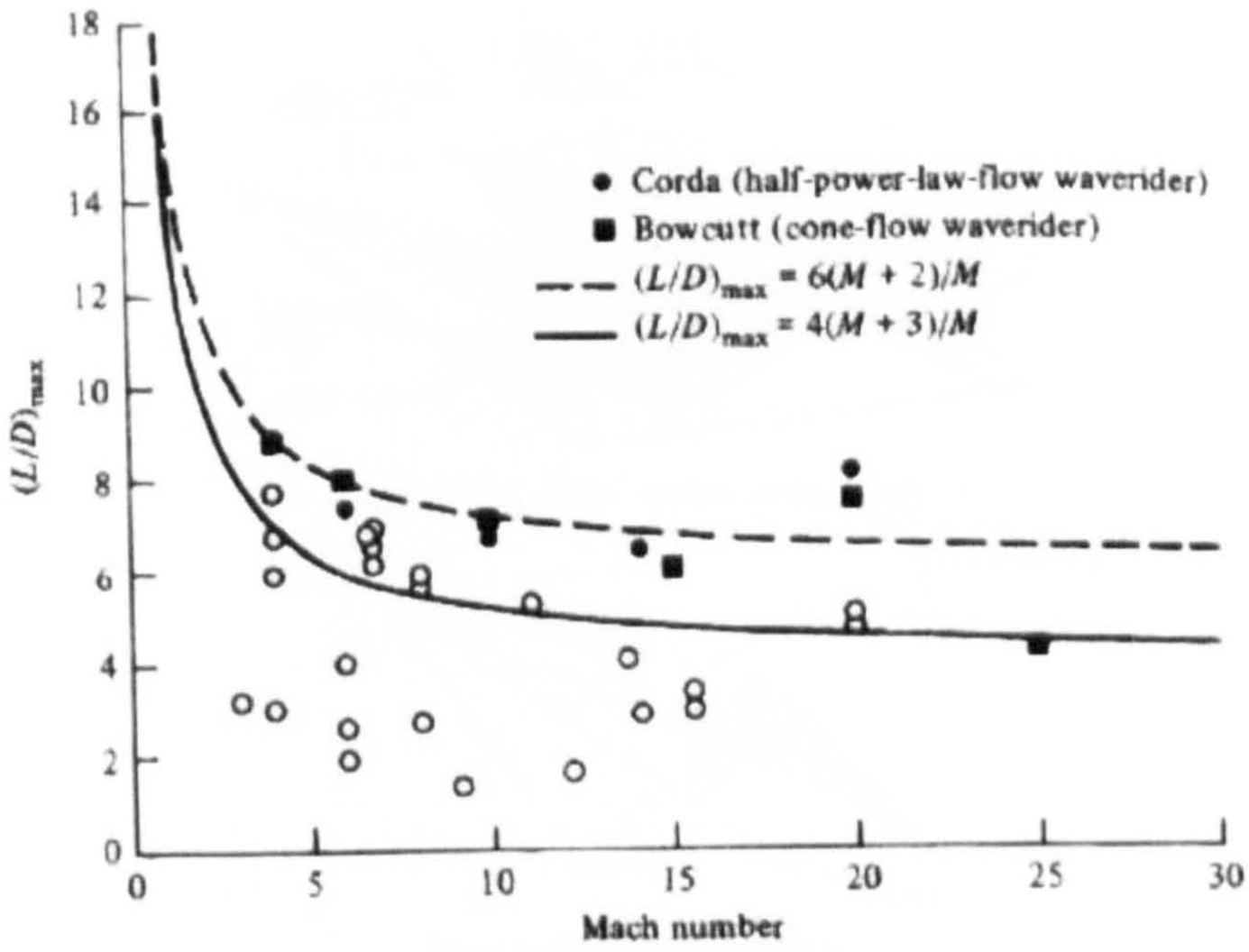


Figure 2.3: Maximum L/D ratios for hypersonic vehicles and the "L/D barrier" (from Corda and Anderson (1988)).

work was to lower peak heating rates on a manned reentry vehicle based on lifting bodies. He proposed a three-dimensional hypersonic vehicle that could be constructed from a known flowfield, which had convex or flat-bottomed lower surfaces (Nonweiler (1959)). Instead, Nonweiler (1963) proposed a *caret*-shaped (^) concave lower surface with a delta planform that generated a stronger planar shock. The stream surfaces behind the shock were used to generate the pyramid-shaped (caret) wing (later known as the waverider), and is illustrated in Figure 2.4. The XB-70 may have been the first practical waverider vehicle.

This design resulted in smaller losses in lifting pressure due to reduced cross flows as compared to lifting bodies. Furthermore, the perfectly attached shock to the sharp leading edges resulted in greater flow containment and hence less flow spillage. This in turn reduced rates of heat transfer at stagnation points for a given wing loading. An authoritative discussion and comparison of hypersonic vehicle research is given by Townend (1979), Eggers *et al.* (1990) and Anderson and Lewis (1993).

The concept of matching the wing leading edge to the shock formed off the vehicle forebody is the underlying principle behind the waverider concept. By virtue of its definition, a hypersonic waverider is designed from a known flowfield and appears to ride on

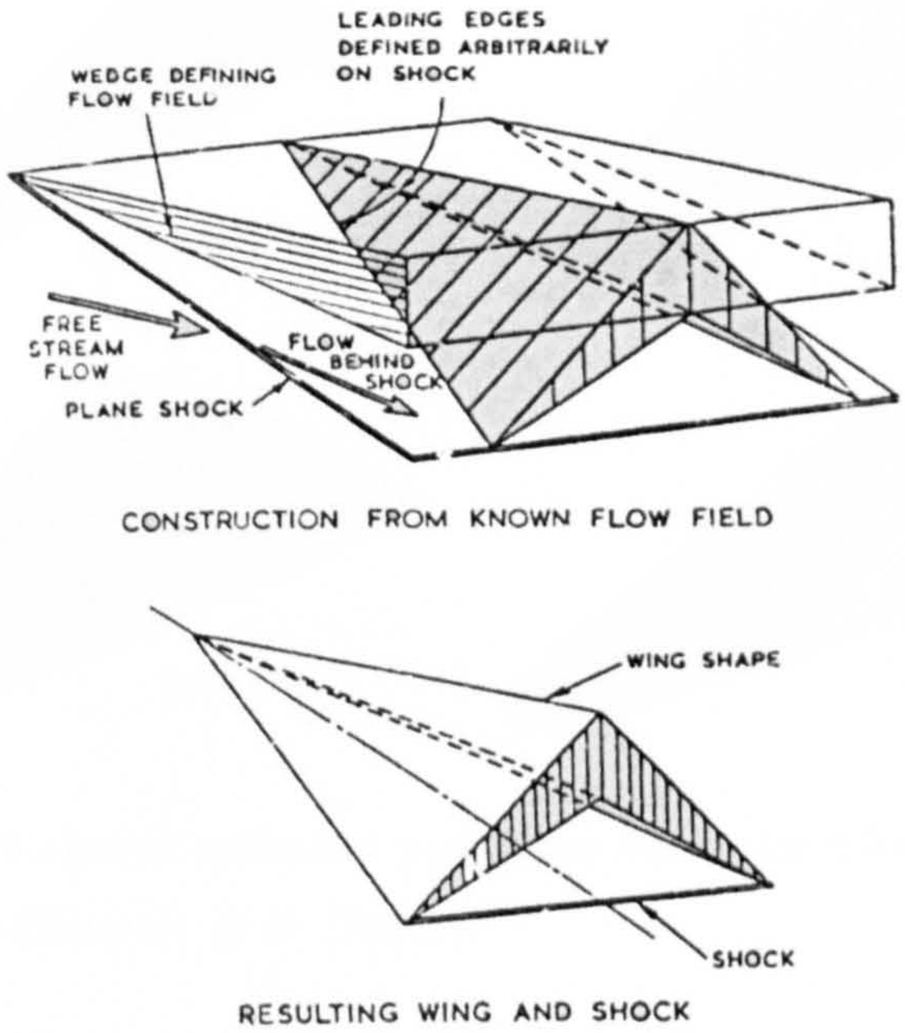


Figure 2.4: Nonweiler's caret wing also known as waverider (taken from Corda and Anderson (1988)).

top of its shock wave that is attached to its leading edge; hence the term waverider. The high post-shock pressure on the lower surface provides compression lift due to the close proximity of the thin shock layer and is isolated from the low pressure freestream at the design condition. These shapes provide high values L/D at the design Mach number and offer a good degree of volumetric efficiency (Blankson (1994)). Flower (1963) extended Nonweiler's work to include the design of upper surfaces and complete configurations. In a paper by Venn and Flower (1970), the shock patterns of simple caret wings were investigated for varying incidence, Mach number and wing geometry.

In contrast to conventional aircraft design, waveriders are generated by first specifying the shock wave, then calculating the vehicle that forms this shock and it is known as the inverse design process. The early caret wings were criticised for having poor engine/airframe integration, takeoff and landing concerns and low volume for payloads, fuel etc. However notable achievements by various research organisations have dispelled these thoughts, whose developments are addressed below.

The waverider concept was improved by Jones *et al.* (1968) to include a known axisymmetric flowfield, such as conical flow for the compression surface, to design slender

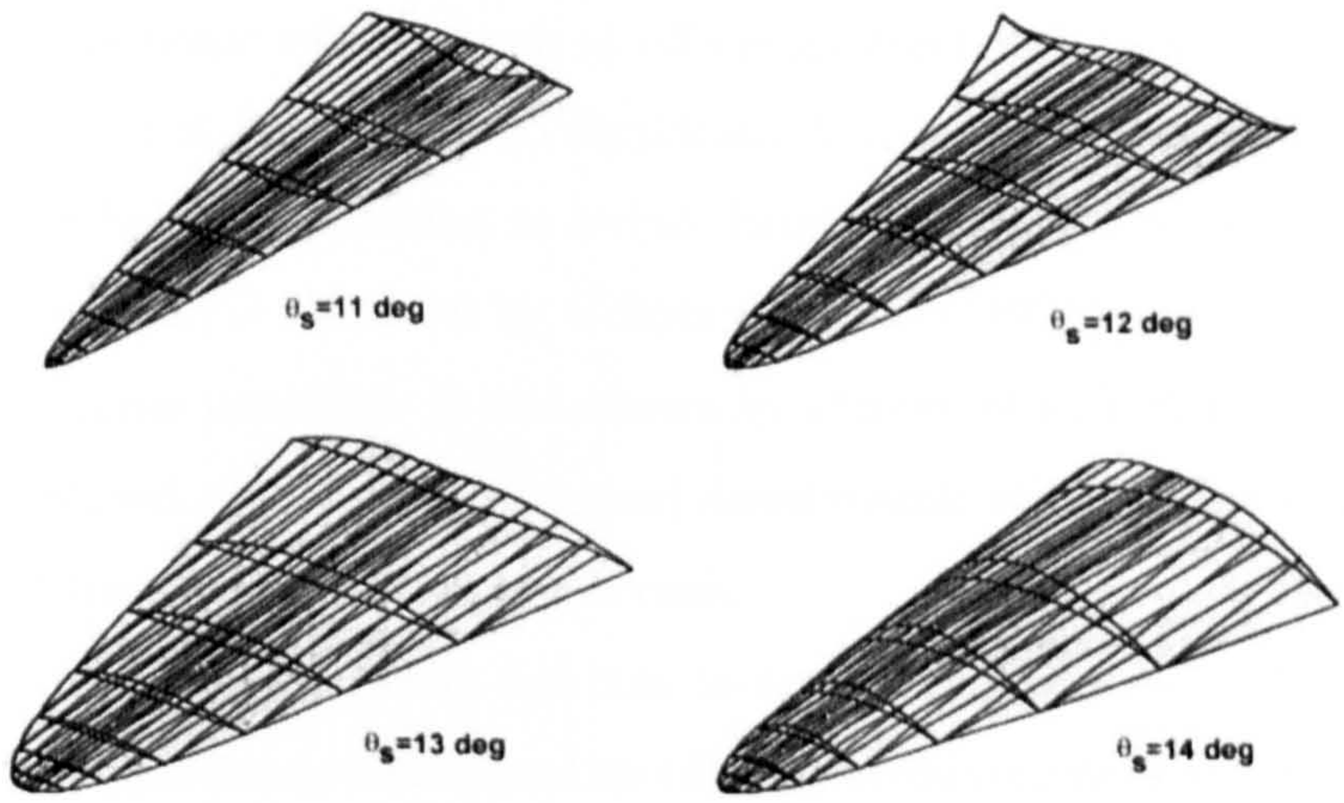


Figure 2.5: Mach 6 viscous optimised waveriders shown for different generating shock angles (Bowcutt *et al.* (1987)).

practical configurations in terms of better volume distribution for payload accommodation. Jones' method introduced a new class of non-planar waveriders that used a right-circular supersonic cone requiring a more rigorous calculation to determine the postshock flowfield. A Mach 4 aircraft was presented that incorporated airbreathing propulsion; the ultimate objective of this type of design.

Perturbations from the axisymmetric conical flowfield was investigated by Rasmussen (1980) who looked at curved waverider surfaces using inclined circular and elliptic cones. Hypersonic small disturbance theory was used to design waveriders analytically from right-circular conical and elliptical flowfields. The fact that all shocks and resulting flowfields were analytically well defined provided a platform for a calculus of variations for performance optimisation producing high L/D values.

To demonstrate both the practical applicability and to rejuvenate interest in waveriders, inviscid analysis was extended to viscous optimised waveriders by Bowcutt *et al.* (1987) that included both wave and skin friction drag. Waveriders maximised for L/D ratio were produced using optimisation techniques for conical flowfields. The shape of the vehicle changes when the shock angles change during L/D optimisation and is illustrated in Figure 2.5. This work was extended by Corda and Anderson (1988) for power-law minimum drag bodies as the generating flowfield also using viscous analysis. These waveriders delivered promising values of L/D and they are illustrated in the previous Figure 2.3.

Experimental observations on waveriders have shown that conical-waveriders are viable

candidates for hypersonic vehicles even at off-design Mach numbers and angles-of-attack shown by Cockrell *et al.* (1994) with no significant theoretical L/D degradation. Practical issues such as leading edge blunting to reduce heat transfer, can be accommodated with only a small drop in L/D as shown by Gillum and Lewis (1997) and hence did not incur excessive performance penalties. It was shown by Blosser *et al.* (1995) that wing leading edges can be designed sharp enough for good aerodynamic efficiency yet blunt enough for acceptable heat transfer for Mach 5 waveriders.

Boundary layer transition from laminar to turbulent flow was analysed by Vanmol (1992) for viscous-optimised vehicles and its effect on aerodynamic heating. Passive cooling of waveriders below Mach 10, is sufficient and aerodynamic performance was shown not to degrade significantly with blunting of leading edges. The application of waveriders in foreign environments was addressed by Lewis and Kothari (1990) who showed that $L/D = 10$ is achievable.

Osculating Cone Concept

Conical flow techniques for waverider design are relatively simple and these methods make them good candidates for developing complete design methodologies, offering practical configurations coupled with optimisers. These are the reasons behind their selection for this preliminary design study. For completeness, however, it is worth mentioning a modification of this technique - the *osculating cones* method. Disadvantages to conical methods are the volumetric efficiency, especially near the centre region and length of vehicles produced, although L/D values are comparable. (Takashima and Lewis (1994)).

This method was originally developed by Sobieczky *et al.* (1990) using non-axisymmetric flowfields and these waveriders are similarly designed inversely, that is, vehicle surfaces are carved out of known flowfields to take advantage of high post-shock pressures. Multiple cones are used to define a shock structure where points along a span are treated as a region of locally conical flow. This permits greater flexibility in vehicle design when considering engine and control surface integration.

Figure 2.6a shows the osculating plane at the base of the waverider whose flowfield is defined by spanwise points with *local* conical flow solutions. Hence, previous work on conical flow concepts can be adapted to this method down to the body surface. The steps

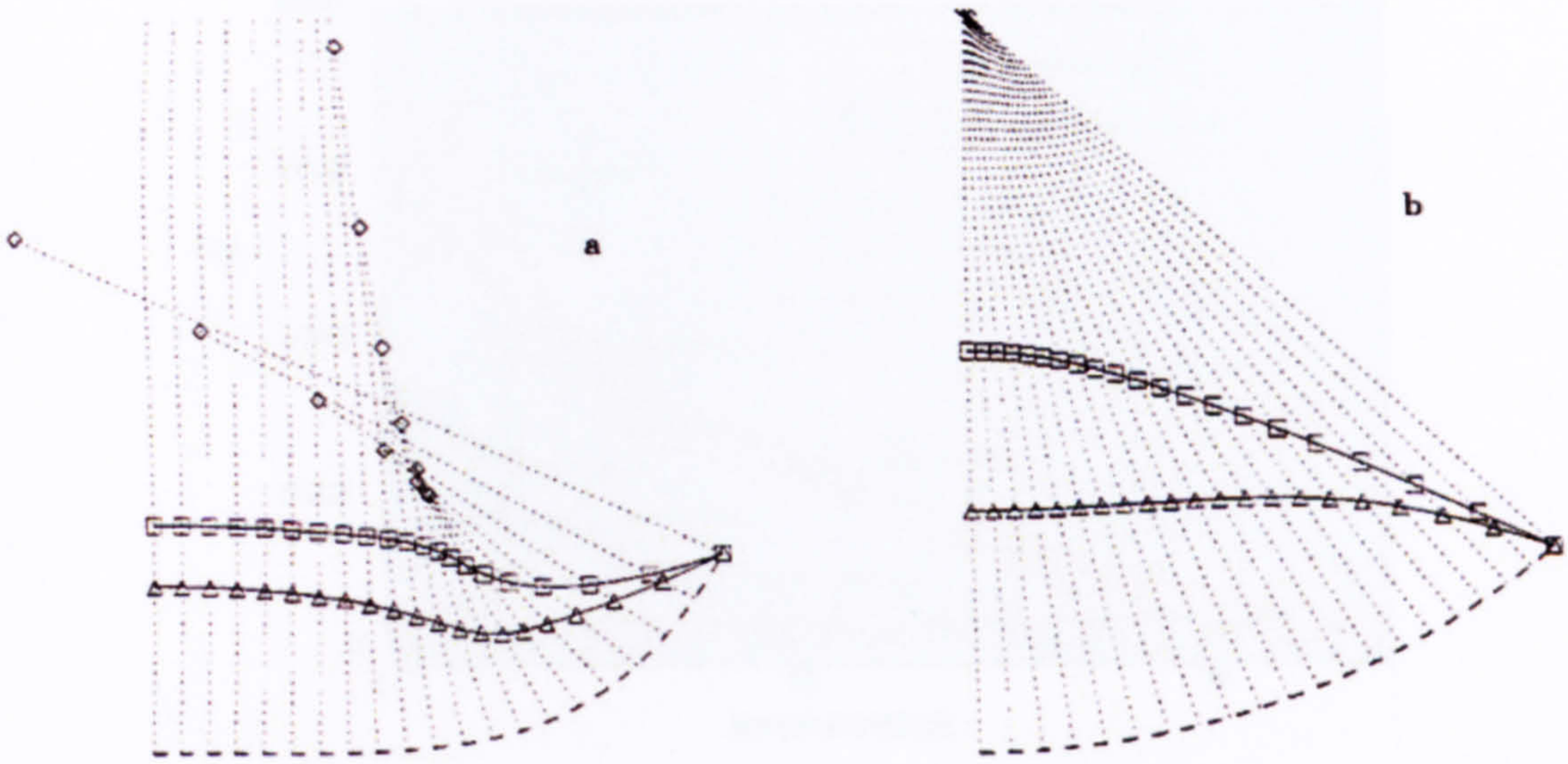


Figure 2.6: Waveriders generated using (a) osculating cones and (b) conical-derived method in the base plane. Diagram adapted from Center *et al.* (1991).

are outlined as follows: a shock profile is defined at the exit plane, with the figure showing a flat shock near the centreline (wedge flow). Then the vertex of each point spanwise normal to the shock profile is found using the slope and curvature at that point in the local conical flow region. Note, for conical flow, there is only one vertex (Figure 2.6b). An arbitrary line is defined a normal distance to each point on the shock (squares) and the lower surface is found by tracing the streamlines to the base plane (triangles). Experimental work by Miller *et al.* (1998) for a Mach 4 and 6 viscous optimised osculating-cone waverider indicates that numerical predictions from the interactive inverse-design code, WIPAR, by Center *et al.* (1991) agree well.

Optimisation for a given merit function can produce significantly different shapes and will be discussed later.

2.3 Airbreathing Propulsion

Airbreathing engines offer significant performance advantages over rocket propulsion and is illustrated in Figure 2.7 in terms of the specific impulse (Isp). Isp indicates the thrust produced per unit weight of propellant mass (fuel + oxidiser) injected into the engine per second. These engines are essential for sustained endoatmospheric hypersonic cruise vehicles and they have the potential to increase launcher efficiency due to a significant

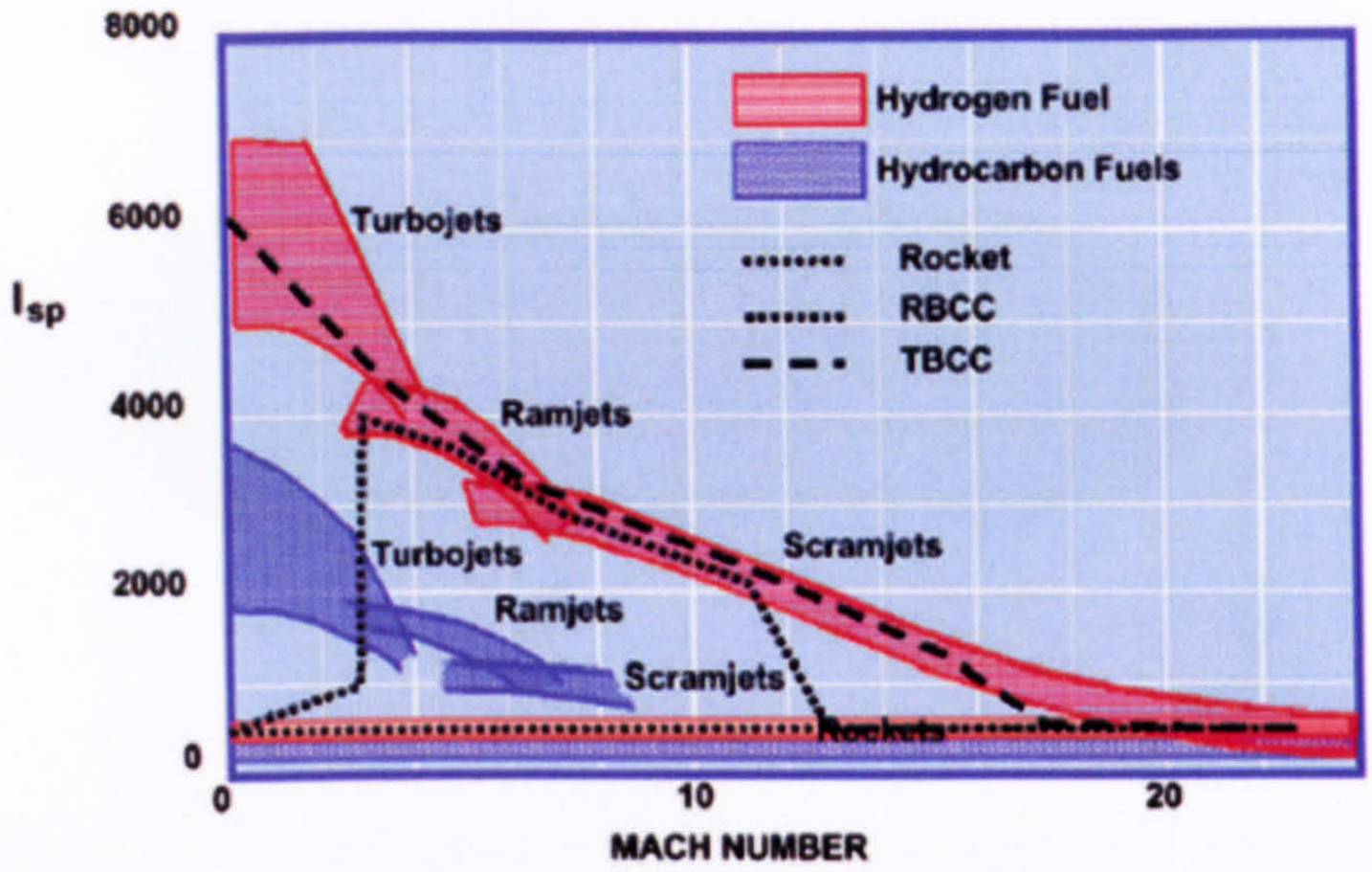


Figure 2.7: Air Breathing Hypersonic Propulsion Cycles Provide Enhanced Propulsion Efficiency from Moses (2003).

reduction in on-board propellant. The concept of Isp has been introduced to describe propulsive efficiency of all engines that generate thrust by expelling mass. A rocket's Isp has the same value as its exhaust gas velocity. The Isp of an airbreathing engine is one order of magnitude greater.

This permits horizontal takeoff, which reduces thrust loading, takeoff weight and increases structural mass fraction for improved design/operating margin. Development of high-temperature and efficient performance over a broad Mach number and altitude range are paramount in the successful development of vehicles.

Turbojets can be used on aircraft up to Mach 3; consider the J58 engine on the SR-71 Blackbird that achieved Mach 3.2.

Ramjets, on the other hand, are able to operate at higher supersonic speeds. They contain no moving parts but require the vehicle's forward velocity to maintain sufficient momentum of air through its ducts to operate as illustrated in Figure 2.8. Generally, Mach 3 is when a ramjet will begin to generate thrust as compression is achieved using a combination of oblique shocks generated from the diverging geometry of the engine intake. This is known as ram pressure. Supersonic flow is decelerated to subsonic flow through a normal shock at the throat where fuel is injected and ignited, generating expansion through a diverging duct.

Zero velocity means no thrust, therefore, combination with a low-speed engine is re-

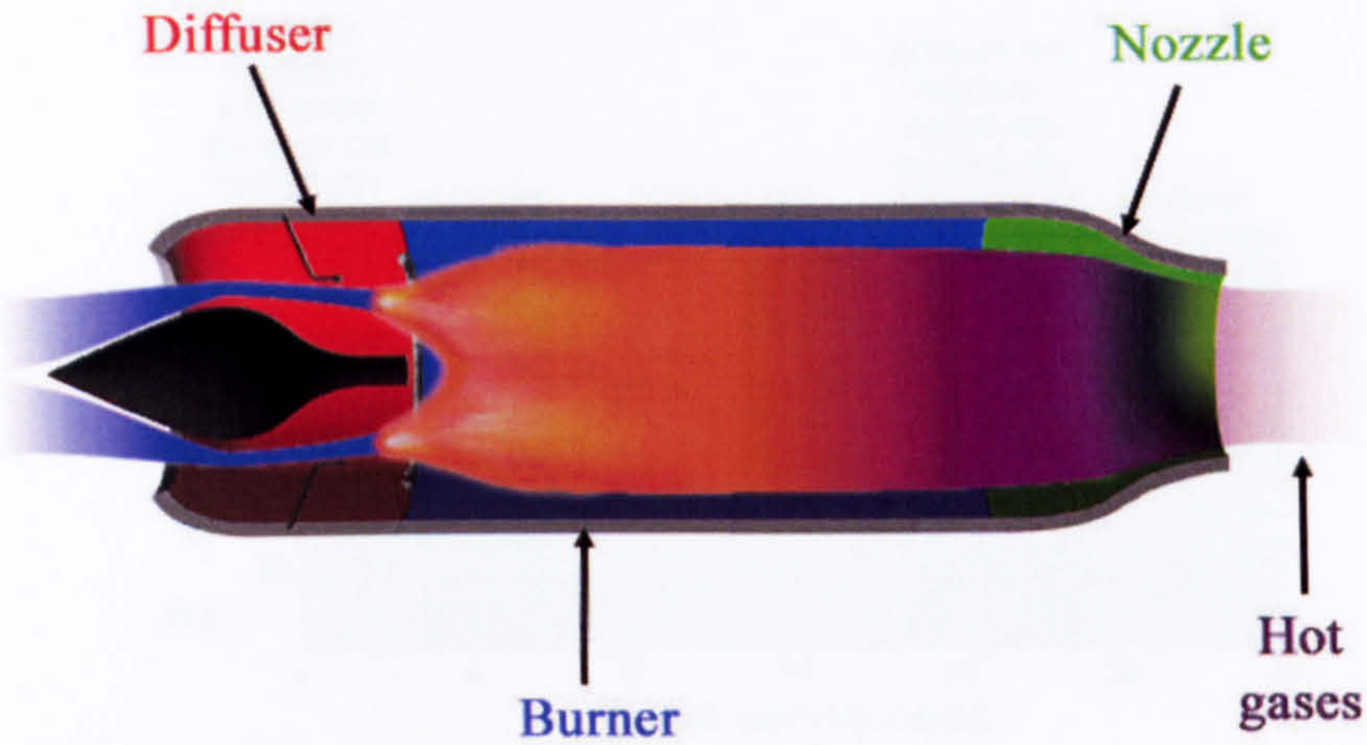


Figure 2.8: Schematic of a ramjet showing inlet, burner and nozzle. Note the lack of a turbine. Image taken from wings.avkids.com.

quired. The upper Mach limit is again dictated by the extreme temperatures reached during compression (about Mach 6) where the injected fuel will tend to absorb energy rather than release it thereby generating more drag than thrust.

When the external flow cannot be decelerated to subsonic speeds inside the combustion chamber, shocks begin to develop and supersonic flow occurs. This invalidates the principle of ramjets and a new device is required called a supersonic-combustion ramjet (scramjet). The main difference between a scramjet and a ramjet, is that the combustion process operates at supersonic speeds. The geometry is relatively simple but the aerodynamics involved are far more complex than ramjets. The static temperature remains low over the hydrogen combustion flame such that the material and decomposition problems are avoided.

An airbreathing flight envelope is shown in Figure 2.9 for various powerplants as a function of Mach number. The potential of the scramjet engine is widely recognised for hypersonic applications and it would enable sustained flight at around Mach 10, as considered in this study.

The altitude ceiling and floor are characterised by limits imposed by a combination of internal duct pressure, skin temperature and dynamic pressure loading within the combustor. The altitude floor should satisfy a minimum temperature and maximum pressure whereas the ceiling is set by maximum temperature and minimum allowable pressure both at the combustor entrance. An upper Mach number limit is imposed by dissociation and

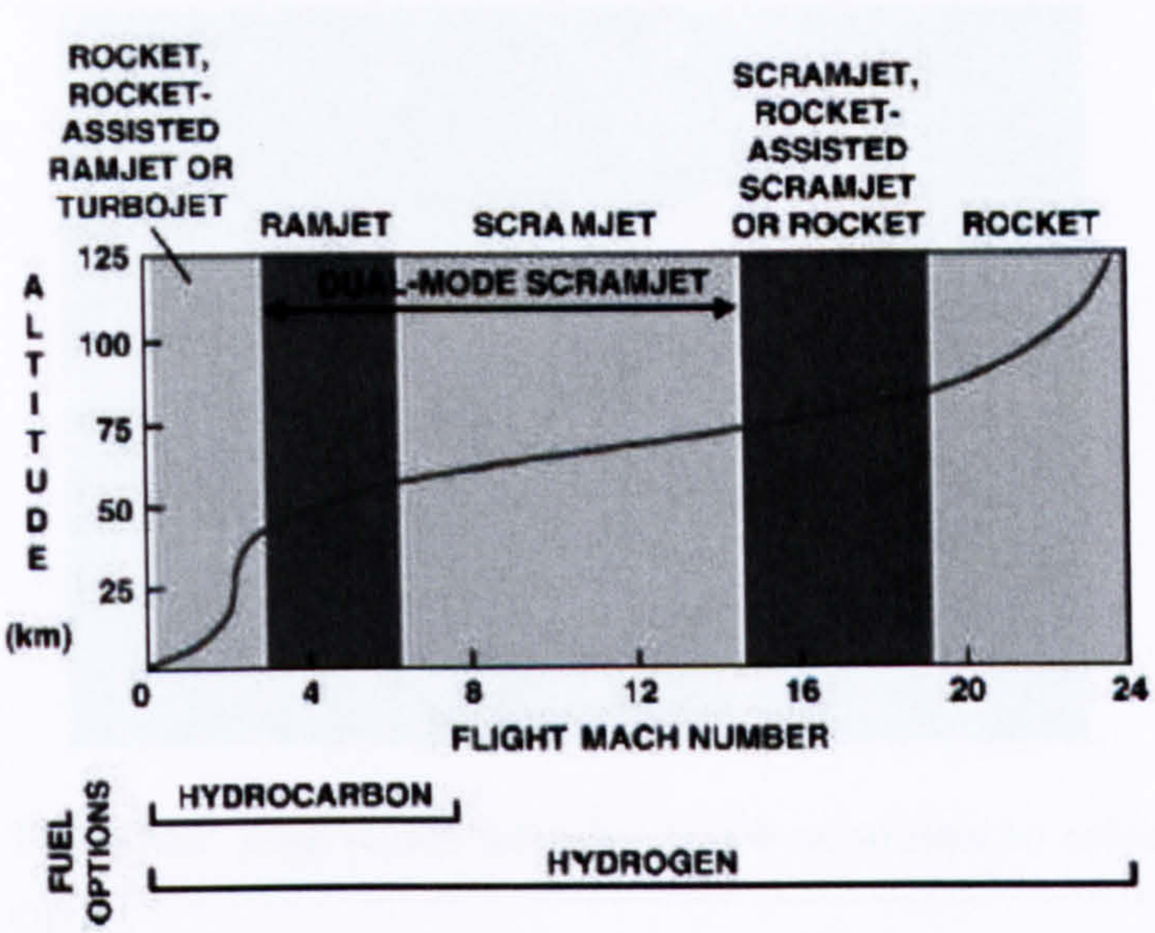


Figure 2.9: Airbreathing Engine Flight Envelope from NASA Langley Research Center.

high stagnation temperature and flow distortions that can negatively influence fuel injection and mixing, combustion, nozzle exhaust flow and therefore performance (Fry (2004)).

The propulsion technology sector of NASAs Hypersonic Investment Area (HIA) is prioritising scramjets, and combined-cycle engines such as the Turbine-Based-Combined-Cycle (TBCC) and Rocket-Based-Combined-Cycle (RBCC) systems (Hueter and McClinton (2002)). The TBCC and RBCC integrate more than one propulsion cycle into a single engine assembly and differs to multi-cycle propulsion, which is exactly the opposite (Bertin and Cummings (2003)). A brief review of possible propulsion systems for hypersonic cruise vehicles will now be presented.

2.3.1 Scramjet

In a scramjet, fuel is injected from the walls or in-stream protuberances, where it mixes with air decelerated from the freestream by a system of shocks, to burn in a diverging area combustor. A shock train exists upstream of the combustor entrance due to the combined effects of heat addition and the diverging combustor area, whose strength depends on flight conditions, fuel/air ratio and geometric combustor properties. Variable geometry scramjets will be necessary for vehicle applications due to the wide range of flight conditions to be encountered. To favour airframe integration, scramjets that are two-dimensional are being developed in countries such as USA, Japan, Australia, Russia, France and UK.

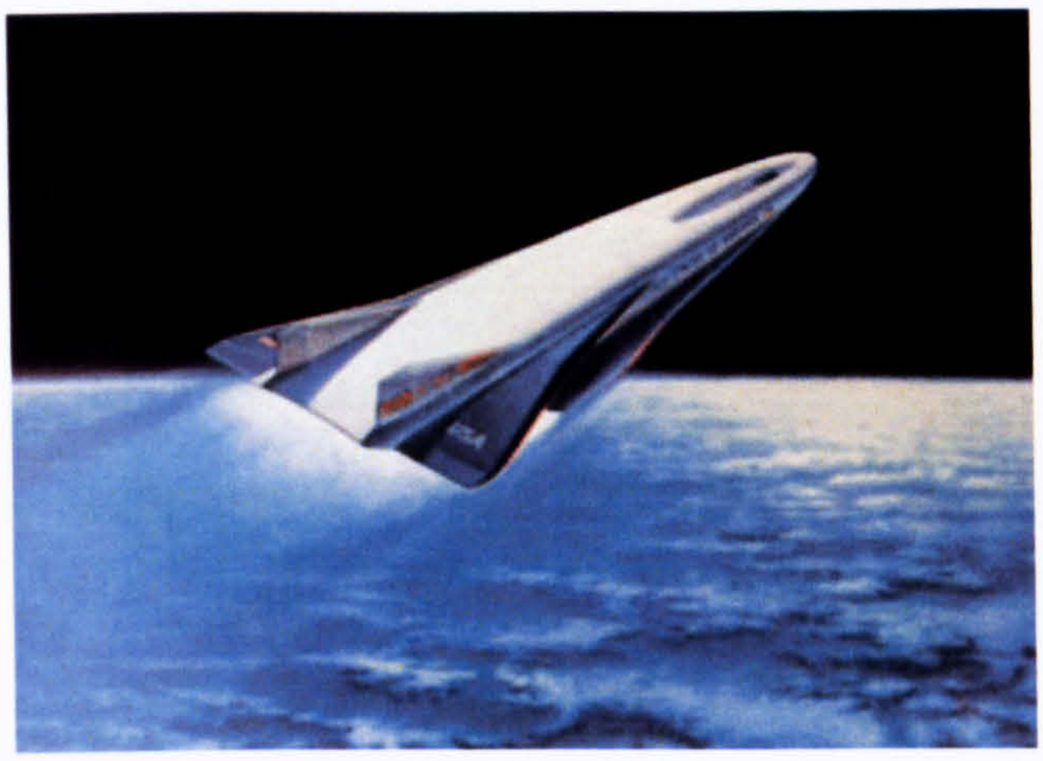


Figure 2.10: The NASP programme intended to use scramjets to achieve Low-Earth-Orbit.

Scramjet development reviews have been documented by Fry (2004), Billig (1993) and Bertin and Cummings (2003). The practical use of scramjets is discussed by Townend (2001), including a discussion on the potential of hydrocarbon fuels such as kerosene for a TSTO vehicle.

The NASA Langley Research Center (LaRC) has been conducting computational and experimental research on ramjet, scramjet and combined-cycle engines since the 1960's. Rogers *et al.* (1998) reviews the types of tests conducted at their facility.

The Hypersonic Research Engine (HRE) was one of the first projects to investigate various geometries for inlets, combustion chambers, and exhausts. The HRE program was a strut-mounted scramjet and was initiated in 1964 to demonstrate practical hydrogen -fuelled and -cooled technology.

The National Aero-Space Plane (NASP) or X-30 was developed as a successor to the Space Shuttle in 1984 to minimise the cost of launchers and it utilised research from HRE. The heart of the X-30 was its airframe-integrated hydrogen-fuelled ramjet/scramjet propulsion system, and posed the main technical challenge. NASP was designed to takeoff and land on conventional runways with significant cross-range capabilities and potential to reach orbit during a SSTO but was cancelled in 1995 due to spiralling costs. See McClinton *et al.* (1999) and Figure 2.10.

LaRC then initiated the Hyper-X program in 1996 to test and validate scramjet technology using numerical and experimental techniques for the design and performance predictions. The program focused attention on the smaller scale X-43A vehicle; scaled from

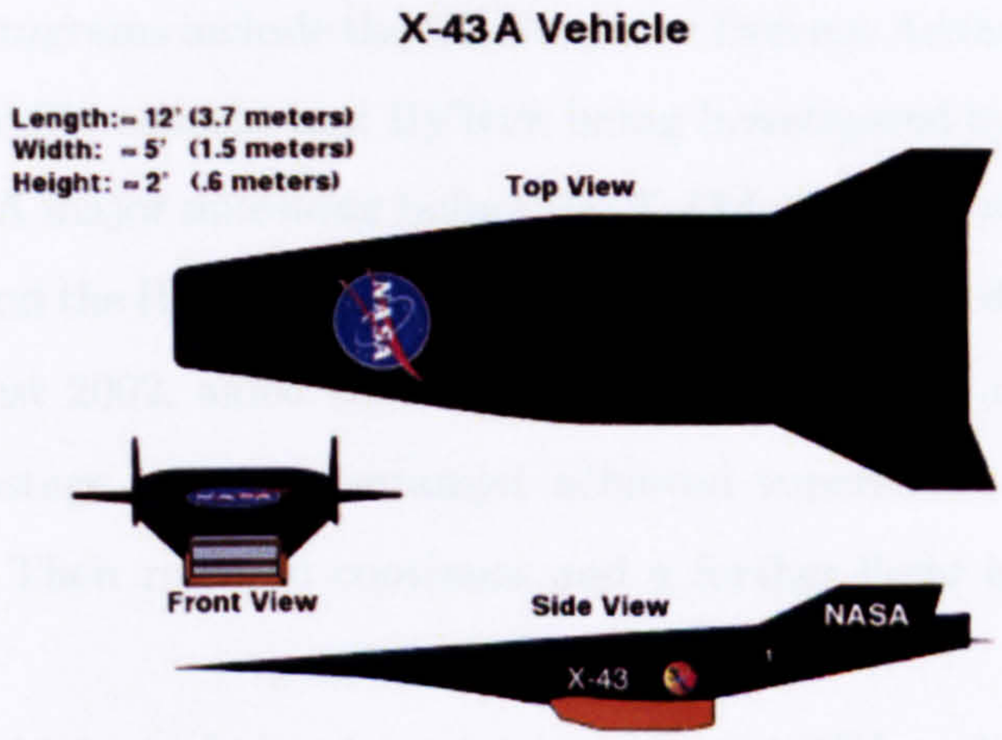


Figure 2.11: Dimensions of the X-43 vehicle

NASP but with a different propulsion flowpath. To date, this is the only official airframe-integrated scramjet-powered vehicle to fly autonomously under its own power, achieving positive hypersonic acceleration and a major milestone[†]. See Figure 2.11 for the relative scale of the vehicle. The Hyper-X program aimed to provide data to advance the hypersonic technology from the laboratory to flight experiment and demonstrate the propulsion/airframe integration (Voland *et al.* (1998)). The X-43C was designed to demonstrate TBCC powerplants but this was cancelled due to budget cuts. The first test flight of the X-43A in June 2001 failed due to a stabilisation problem with the booster rocket's directional fins.

International activities that have contributed to scramjet development include some of the following. The German Sänger II programme in the late 1980s, combined-cycle development in Japan for TSTO application, ORYOL program established in Russia for hypersonic research and development for advanced reusable space transportation. The French PREPHA, PROMETHEE and JAPHAR programmes developed a knowledge base for hydrogen-fuelled dual-mode ramjet technology for SSTO applications. The US air-breathing technology initiatives such as the National Aerospace Initiative (NAI) and Next Generation Launch Technology (NGLT) are focusing development in three key propulsion areas; scramjets, RBCC and TBCC systems.

[†]At the time of writing, NASA was planning to flight test the X-43A to Mach 10, scheduled at the end of 2004

Other scramjet programs include the US Navy and Defense Advanced Research Projects Agency (DARPA) HyFly concept and HyTech being investigated by the USAF and P&W for real flight tests. A major milestone before the X-43A test, was reached by The University of Queensland and the HyShot program. They were the first to demonstrate supersonic combustion in August 2002, aided by a number of governmental organisations. Using a vertical-launch two-stage rocket, a scramjet achieved supersonic combustion during its descent at Mach 7. Their research continues and a further flight is being planned in the near future.

An unmanned vehicle study has been initiated by DARPA and the USAF for development of a program called Force Application and Launch from CONtinental United States (FALCON), see Croft (2004) and Figure 1.3. The program aims for a Mach 8, prompt global reach and to build a Hypersonic Cruise Vehicle (HCV) by 2025. The HCV will have HTOL capability, a range of 9000nmi in less than 2 hours and able to carry a 12,000lb payload consisting of Common Aero Vehicles (CAVs) such as unpowered glide cruise missiles, small diameter bombs and other munitions. A near-term program called Small Launch Vehicle (SLV) is expected by 2010 and it will be a low-cost launch system capable of carrying CAVs (e.g. small satellites) to a Sun Synchronous Orbit with a payload ranging from 200-1000 lbs at a 450 mile orbit.

DARPA funded the Affordable Rapid Response Missile Demonstrator (ARRMD) program for Mach 6-8 100-600nmi capability. Although now cancelled, the potential for a low-cost airbreathing hypersonic missile design based on the HyTech hydrocarbon fuelled scramjet developed by P&W still remains. See Gustafson and Livingston (2002).

At the design level, performance analysis has relied on either experimental testing or parametric analysis using efficient quasi-one-dimensional codes that can include finite-rate chemistry like O'Brien and Lewis (2001*a*) and high-temperature gas models. These design studies can provide useful insight into the complex flow mechanisms but lack in *real* effects of viscosity and turbulence in multi-dimensions.

A performance prediction method by Ikawa (1991) used a first order approximation for the supersonic combustor analysis; similar to the approach of afterburning in a ramjet. Ikawa introduced a multiplying factor that eliminates the need for numerical integration solving for divergent channel flow. A simplified model using fundamental physics is devel-

BIBL. LON[illegible]IN. [illegible]IV.

oped by Schindel (1990) for predicting performance of missile configurations. Combustion is assumed to be a continuous process with constant area heat addition. Research continues in complex flow solvers coupled with optimisation and experimental testing to improve designs.

2.3.2 Combined Cycle Propulsion Systems

For takeoff and landing capability, various propulsion concepts have been proposed to address the Mach regime from brakes release to Mach 4/6 for ramjet/scramjet takeover speed (Moses *et al.* (1999)). Two main types of combined cycle engines were studied that either have single flowpath/multimodes (Type 1) or multiple flowpaths/multimodes (Type 2). See Fry (2004).

An example of Type 1 engine is the RBCC (also known as Ducted Rocket), which combines the characteristics of both airbreathing and rocket engines. It produces high specific impulse compared to a rocket engine and high thrust-to-weight ratio compared to an airbreathing engine (Bradford and Olds (1999); Czysz and Little (1993)). Liquid rocket motors are located in the dual-mode scramjet flowpath. Before the scramjet enjoys sufficient freestream compression (around Mach 3), rockets operate and behave as an ejector in which the air combines the total mix. During transition, the rocket shuts down, a thermal throat exists and the ramjet operates between Mach 3 and 6 after which scramjets begin to operate in a supersonic stream at Mach 6/7.

The rocket engine consumes atmospheric oxygen when flying in the atmosphere. When it leaves the atmosphere, the inlet ducts close and the rocket engine consumes stored liquid oxygen. The concept offers safety, reliability as well as cost advantages by making vehicles smaller and more efficient.

A Type 2 engine is the TBCC system, which employs a turbojet engine for providing thrust from takeoff up to Mach 3/4 and then transition to dual-mode scramjet operation. The TBCC allows more aircraft-like operation as discussed by Hueter and McClinton (2002). The French built the Griffon II airplane using TBCC turboramjet engines to reach speeds of Mach 2 in the 1950's. With more than one flowpath in TBCC engines, integration becomes more critical over the entire speed range and variable geometry inlets and nozzles are required.

A brief review of combined-cycle engines that have undergone development, will be provided here.

The US is investigating TBCC systems for access-to-space under the revolutionary turbine accelerator RTA/TBCC project as part of the NGLT (Bradley *et al.* (2002)). Near-term development goals RTA will concentrate on achieving at least Mach 4 and with dramatic increases in maintainability and operability. Moses *et al.* (1999) used a P&W Turboramjet (Ace-TR) in their multi-mode study. See also Johnson (1996) for developments at General Electric.

NASA initiated the ISTAR programme in 2002 aiming to power a flight test vehicle to Mach 5 using an RBCC-type engine. Although cancelled in 2003, ground testing will continue and the programme is based on the strutjet RBCC engine design. A web-based tool called SCCREAM has been developed by Bradford and Olds (1999), which enables performance estimation of an RBCC engine. A good description of RBCC engines is provided therein and SCCREAM showed excellent agreement with the industry-standard code SRGULL.

Japan has actively been pursuing the Air Turborocket Expander Program (ATREX) engine since the late 1980s for application in a TSTO flyback booster to provide thrust between takeoff and Mach 6 (Tanatsugu (1996)). It is a fan-boosted ramjet working on the expander cycle with heat exchangers, a precooler, a regeneratively-cooled combustor and employs a compact tip-turbine driven fan. It has a variable geometry inlet and a plug nozzle for operation under a wide range of flight conditions. Static ground tests have been performed on the ATREX-500; a smaller scale axisymmetric engine with future flight tests in the pipeline. Central Institute of Aviation motors (CIAM) in Russia have made experimental evaluations on incorporation of turbofan and variable cycle elements into a basic turboramjet configuration.

Some of the concepts mentioned above are well documented by Heiser and Pratt (1994) and Hewitt and Johnson (1991). Other concepts include the pulse detonation engine (PDE) and Air Turbo Rocket (ATR).

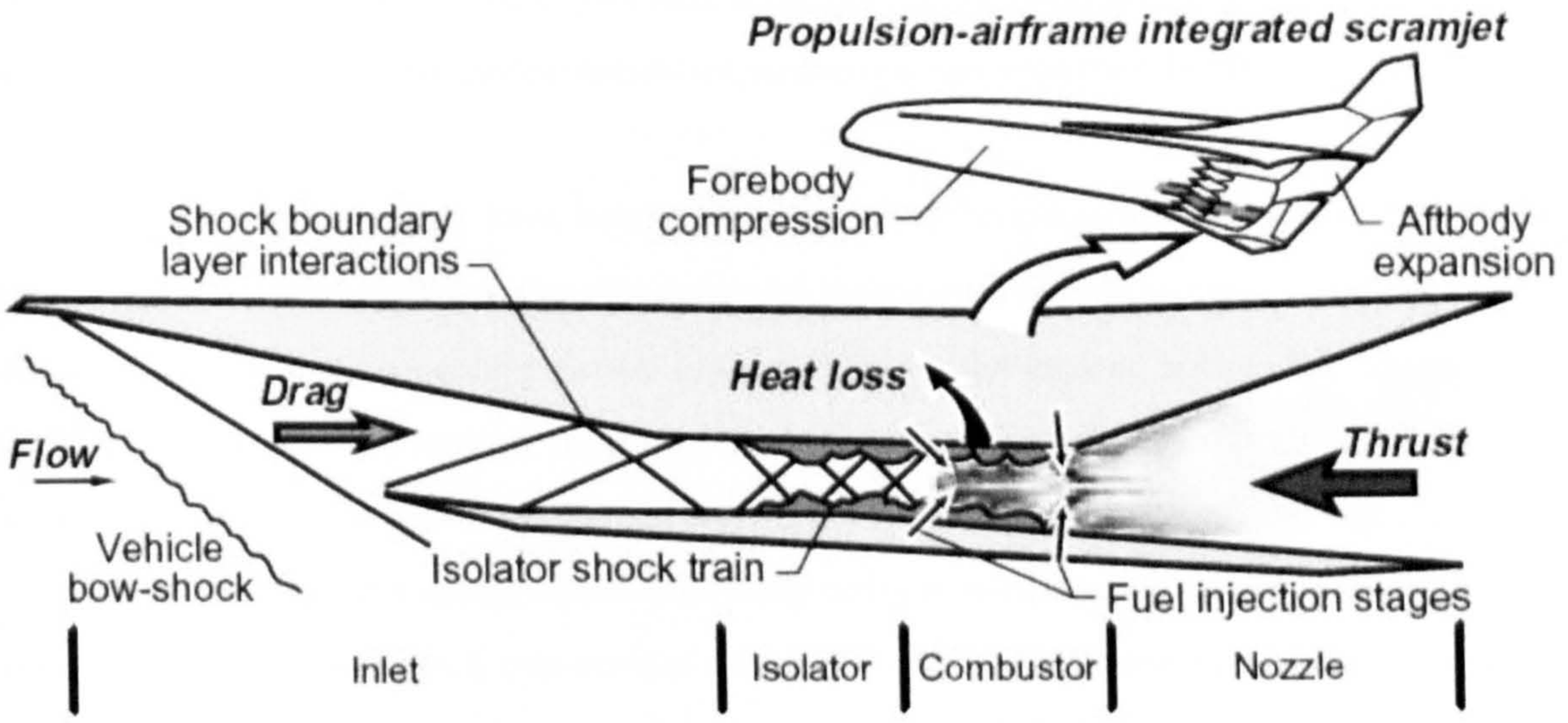


Figure 2.12: Mach 4-8 operation of a single modular airframe-integrated scramjet, which shows important physical processes occurring before, during and after combustion. Taken from Rogers *et al.* (1998).

2.4 Airframe-Propulsion Integration

Scramjet engines rely heavily on the shape of forebody of the vehicle for compression. The airframe-integrated scramjet (Henry and Anderson (1972)) became the basic flowpath for most vehicles and wind tunnel tests. A hypersonic cruise vehicle will spend most of its time in the cruise segment so emphasis is usually placed on the high-speed engine and integration for high propulsive efficiency.

At the on-design point, the forebody of a waverider is designed to produce a bow shock behind which the air is compressed and channelled into the combustor. The shock should meet the cowl lip for both maximum mass capture and pressure recovery to maximise thrust.

Figure 2.12, depicts off-design operation of an airframe-integrated scramjet at Mach 4-8, where transition from subsonic to supersonic combustion occurs. The insert in the top right of the figure shows the engine placement between the forebody and nozzle section. An example of an airframe-integrated scramjet is the X-43A shown previously, in Figure 2.11.

The conceptual design of a Mach 10 cruise vehicle was investigated by Espinosa and

Bonds (1993) that used turboramjets and scramjets in an over/under integration scheme. Flowpath integration and performance requirements are reported by Witte *et al.* (2003) in the ground tests.

The waverider forebody thus behaves as the inlet/compression system to provide the inlet area and necessary mass flow for scramjet combustor requirements. The other major feature of the integrated configuration and external to the engine, is the aftbody and this region is used as an extension to the nozzle. It allows higher engine exhaust velocities with modest area expansion in the nozzle thereby producing low drag.

The forebody / inlet compression effectively reduces the required engine size and weight requirements compared to a free-stream inlet. The inlet compression increases the overall engine efficiency. The Propulsion-Airframe Integration (PAI) issues on the vehicle include forebody/inlet interactions, exhaust nozzle flow of the aftbody and effect of the propulsion system on the vehicle control system as shown in Figure 1.4. The combined propulsion system is likely to be arranged in an over/under arrangement with the scramjet sitting below the turboramjet in a parallel configuration.

2.4.1 Design Methodologies

As mentioned earlier, the relationship between a vehicle's airframe and propulsion system are closely linked such that modelling their interaction will define the success of a proposed concept. These modelling methods are developed from experimental data and fundamental principles. The advantages of rapid performance estimation were the drive behind early methodologies that addressed the full Mach range. These, however, had considered either simple geometric shapes not accounting for the complex flowfield or focused on singular design cases (Molvik *et al.* (1993)).

Existing sizing methodologies include HASA by Harloff and Berkowitz (1988) that also included a weights analysis, PDWAP by Carreiro (1990) and a routine by Chaput (1992) that used conventional wing-body designs. A Design program called PrADO-Hy by Kossira *et al.* (1993) was developed for TSTO applications.

Waveriders for TSTO missions were investigated by Heinze and Bardenhagen (1998). In that research programme, a waverider was considered for the lower stage of the system, and a multidisciplinary analysis (including investigations into structural and heating con-

siderations) was performed. The results highlighted the high L/D available to waverider configurations (versus a blended body design), and indicated that a waverider planform could provide reduced wing loading for the lower stage, while at the same time allowing a large decrease in the required fuel and maximum take-off weight of the TSTO system.

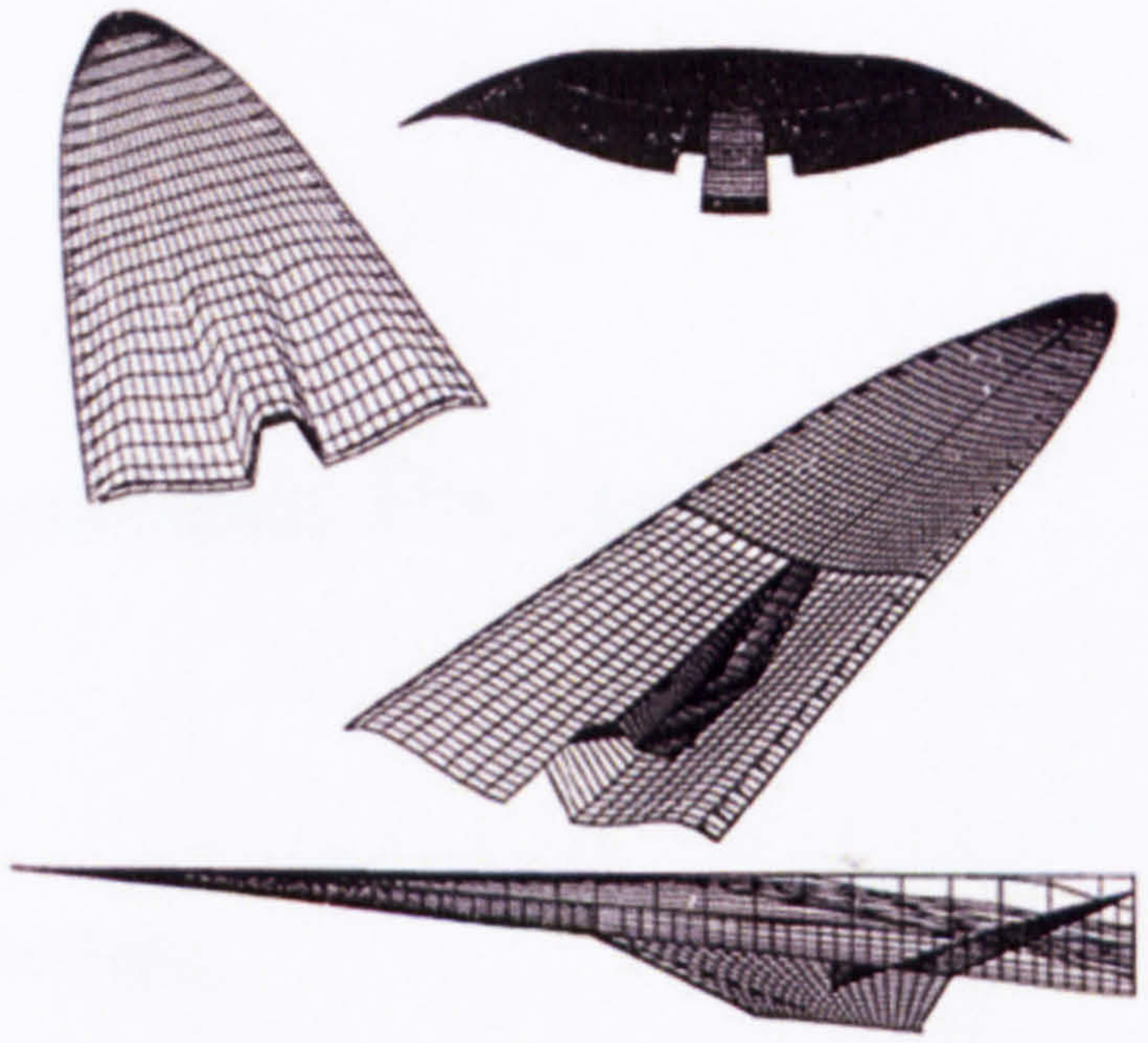
Improved studies have shown that airbreathing engines can be efficiently integrated and optimised with waverider airframes. Scramjet integration on a conical waverider was first investigated by O'Neill (1992) for design-point hypersonic Mach numbers. Figure 2.13(a) represents an optimised Mach 8 vehicle. Performance was estimated on both accelerators and cruisers and it was shown that L/D decreased when integrating the engine. The thrust margin was optimised and it was shown that the combustor can be supplied with required properties. Kothari *et al.* (1996) has furthered this work to include an investigation into inward-turning inlets.

Takashima (1997) used an osculating-cone waverider to investigate scramjet integration on this airframe as shown by the Mach 10, L/D optimised waverider in Figure 2.13(b). Both on and off-design point calculations were addressed using a Mach 10 vehicle design for a cruise mission. The design was optimised for maximum L/D, range coefficient and cruise range. Greater volumetric efficiency is obtained with this class of waverider, although L/D is comparable.

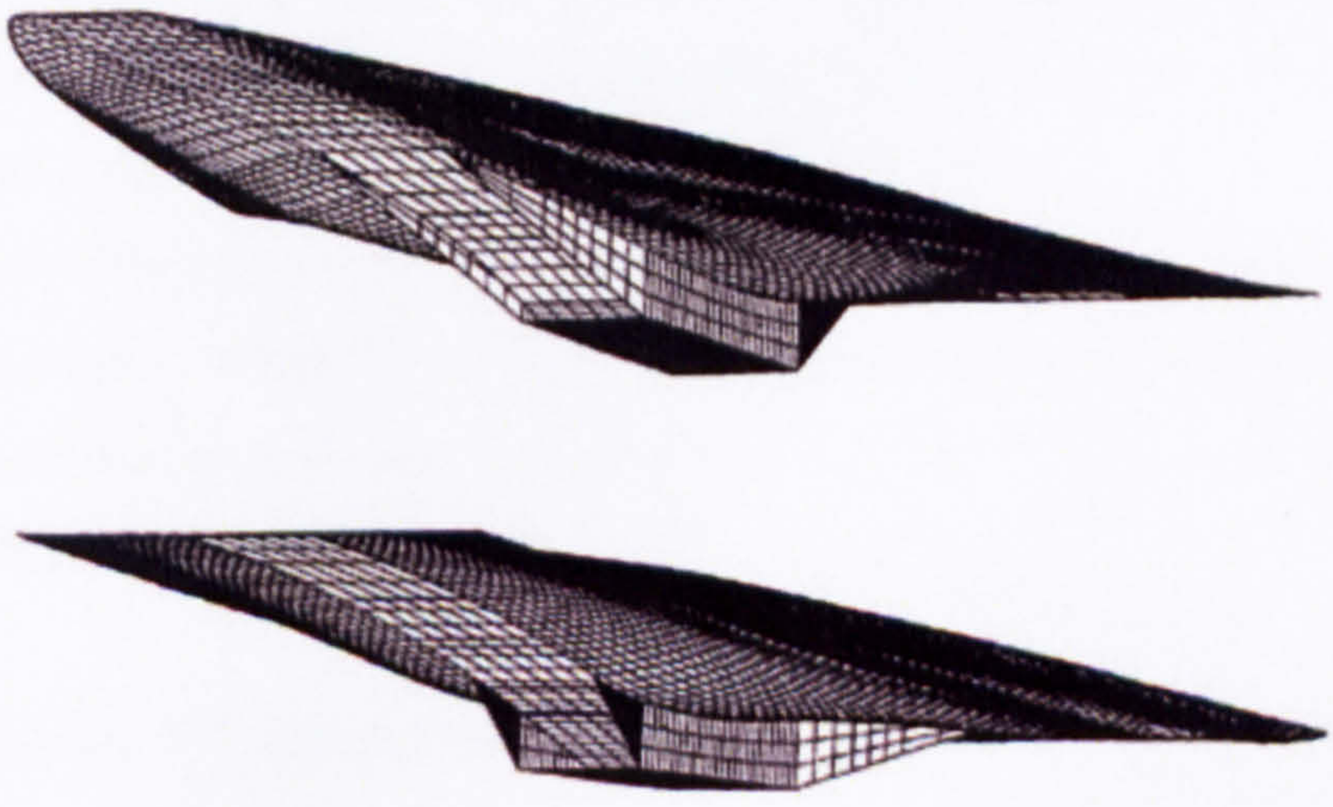
The integration of a RBCC-type engine with an osculating cone waverider was discussed by O'Brien (2001) and was shown to produce rapid results for the aerodynamic performance. The application was for an RLV and both on and off-design Mach numbers and angle-of-attack were investigated for their effect on performance through a trajectory. As with all initial design procedures, the emphasis was placed on rapid prediction of performance.

Finally, the WIPAR code by Center *et al.* (1991), used a graphics workstation to analyse osculating-cone configurations in real-time, which has proved to be a powerful design and optimisation tool. Furthermore, significant insight is gained by visually verifying a geometry for volumetric efficiency and planform shape. Adjustments can then be made accordingly.

In the following chapters, aspects of this review will be used to justify assumptions and decisions made in the development of a new design methodology in this research.



(a) Optimised scramet integration on a Mach 8 conical waverider from O'Neill (1992).



(b) L/D optimised scramjet integration on a Mach 10 osculating-cone waverider from Takashima (1997) showing front and rear views.

Figure 2.13: Optimised scramjet integrated airframes for two classes of waveriders.

3

Design Synthesis Process

3.1 Introduction

The design of a hypersonic cruise vehicle is compounded by a myriad of technical challenges. They are driven by major design targets such as L/D, specific impulse, volumetric efficiency and parameter optimisation (Blankson (1994)). The process is facilitated by accurately defining and modelling the associated parameters so that the feasibility of designing and operating such a vehicle can be established.

The purpose of the present chapter is to justify the decisions taken to define the design space. It is necessary to identify a viable vehicle design and suitable powerplants, discover the key technical issues and value their importance. Then finally, organise the analysis process to form a design procedure.

3.2 Baseline Configuration

3.2.1 Assumptions

For a hypersonic vehicle with a global-range mission, the decision to pursue an uninhabited concept reflects not only on the overall design, but it also has economic implications. Long-endurance Uninhabited Air Vehicles (UAV) such as the Global Hawk and Uninhabited Combat Air Vehicle (UCAV) such as Predator (originally built for reconnaissance) have

demonstrated their effectiveness during conflicts in Afghanistan, Yemen and Iraq.

Uninhabited combat aircraft do not risk a pilots life and long-endurance flights become much more practical without the human inhabitant considerations and associated life support system requirements. The latter is the primary reason for selecting an uninhabited concept for this study. For example, reduced vehicle weight, size, drag and increased operational capability. This also represents current military trends. However, a downside occurs if for example, the data-link is lost, which will undoubtedly have unsavoury consequences on the vehicle's mission especially if it carries munitions. On the other hand, the complexity of the avionics, guidance and control systems becomes increasingly complex. Future versions of this methodology, however, will be capable of dealing with manned missions if deemed necessary.

The propulsion system's longitudinal location on the vehicle requires a tradeoff study between the length of the forebody and nozzle expansion region. For a given vehicle length, the forebody length must not be too long otherwise a short nozzle section will produce an underexpanded exhaust flowfield and therefore reduced thrust. The nozzle contributes a significant amount to the lift so the centre of gravity of the vehicle must be balanced in accordance with fore and aft lift vectors. Since the shock layer becomes thicker downstream of the vehicle's nose, engine location is an important consideration in terms of incorporating boundary layer diverters.

The engine span in the inlet plane must not exceed the limits imposed by the generating cone. Plus a large span will result in excessive drag particularly from the forebody compression system.

The cowl is positioned so that a shock-on-lip condition is achieved for the design point. This maximises mass capture. Extension of the cowl into the nozzle flowfield will affect the lift in this region. The cowl will not exceed the geometry of the bow shock in order to avoid excessive heating.

With respect to orbital vehicles, airbreathing engines need to operate at low enough altitudes for high dynamic pressures. In other words, the engine should be able to capture sufficient air for combustion and hence thrust. As mentioned previously, the altitude ceiling and floor in Mach 10 flight corresponds to between 40km and 30km respectively (O'Neill (1992)).

Component	*Function*	*Attributes*
Forebody	Initial external compression	Contains fuel and payload.
Inlet	Secondary compression for combustor	Actively cooled
Isolator	Isolates compression and combustion to prevent undesirable inlet-combustor interactions	May require boundary layer bleed at low-speed to minimise length
Combustor	Burn fuel and air	Highest pressure, drag & heat transfer rates. Provides mixing & flame holding
Nozzle	Provides initial and final expansion for the combustor exit flow	Cowl length and position significantly affects lift. Radiation cooled.

Table 3.1: The makeup of a hypersonic vehicle encompasses prominent scramjet flowpath parameters that affect airframe integration.

Propulsion system integration on a conventional aircraft entails the amalgamation of individual component studies on propulsion (combustor, nozzle) and airframe (inlet). In hypersonic vehicle design, and in particular waveriders, key propulsion areas such as inlet (compression), engine selection (combustion) and nozzle integration (expansion) become part of the airframe and define the entire flowpath. Therefore, vehicle development is a multidisciplinary effort, which requires detailed tradeoff studies such as volumetric efficiency and vehicle lift/drag to establish the sensitivities between them. This is achieved through a nose-to-tail force accounting method. The attributes of these components have been summarised in Table 3.1 and are described in more detail by Ortwerth (2000).

3.2.2 Airframe Design

The L/D is a good figure of merit for cruise-type vehicles as considered in this study and waveriders have been shown to generate high L/D values.

The conically-derived waverider was selected for this study over the osculating-cones concept as the former is readily computed and appropriate for producing rapid configu-

rations. This avoids excessive computational cost especially when considering optimised configurations that undergo many iterations.

Waveriders are highly suited to long-range cruise missions and they have demonstrated their lifting effectiveness over lifting bodies. A key issue in the practical design of high-speed vehicles is their ability to reduce rates of heat transfer. This has been discussed by Townend (1979).

The theoretical design of waveriders assumes infinitely-sharp wing leading edges although this is not a practical solution due to manufacturing and aerodynamic heating issues. Instead, a certain degree of blunting will be required but too much can result in thick boundary layers being ingested into the engines, which can reduce propulsive efficiency. There is a tradeoff between blunting the leading edge for heat dissipation and maintaining minimum flow spillage due to the detached shock wave. Previous studies have shown, however, that leading edge blunting does not have a significantly detrimental effect on performance (Takashima and Lewis (1999)).

3.2.3 Aircraft Systems Selection

The high-speed engine is responsible for maintaining a desired hypersonic cruise Mach number. Several research investigations by Moses *et al.* (1999); Cockrell *et al.* (2002); Billig (1993) have indicated and demonstrated the scramjet as a viable airbreathing propulsion system. Reasons behind its selection in this study include its suitability for integration with a waverider airframe, the near-term development potential (successes with X-43A and HyShot) and the performance advantages over ramjet propulsion due to the lower hypersonic losses and lower heat loads. The scramjet integration will determine the overall length of the vehicle.

When integrating the scramjet with the inlet system, identical scramjet modules will be assumed. This simplifies the combustion calculation spanwise and the thrust can be calculated with knowledge of the mass capture area alone. The flow entering the combustor will be assumed as uniform spanwise and for the height of the inlet and mass flux is conserved for the on-design case.

Additional assumptions are based on a discussion by Henry and Anderson (1972), where forward sweep sidewall leading edges are incoporated upstream of the cowl lip to

	Hydrocarbon	Hydrogen
Heat of combustion (J/kg)	44×10^6	119×10^6
Specific heat (J/kg/K))	1926	11307-15495
Liquid density (kg/m^3	817	72
Boiling temperature (1 atm) (K)	456-508	20

Table 3.2: Fuel properties from Bertin and Cummings (2003) in SI units

allow for flow spillage. The fuel-injection struts will have the same sweep angle as the sidewalls throughout the geometry of the engine.

3.2.3.1 Fuels

Both hydrogen or hydrocarbon fuels may be used in a scramjet, although hydrogen is preferred for high Mach number flight due to its higher performance yield resulting from its lower molecular weight and also for its greater heat sink capacity. Hydrogen also has faster ignition, reaction and combustion especially at Mach 10. It is kinder to the environment as it produces low environmental pollutants since the major product of combustion is water. A study by Hunt and Eiswirth (1995) on dual fuel vehicles reveals the potential of using hydrocarbon fuels to enable in-flight refuelling for return-to-base missions. The benefits of the higher density hydrocarbon fuels was assessed over the high-energy content of hydrogen fuel by Lewis (2001). The gravimetric heating value $h_v = 119 \times 10^6$ J/kg (51570 Btu/lbm), which is 2-3 times greater than other fuels. See fuel comparison in Table 3.2. Due to the short residence times of hydrogen/air in the combustor ($\backsim$1 ms), it is important to establish proper mixing of fuel and air before the mixture exits the combustor. Fuel combustion in a supersonic stream becomes analogous to lighting a match inside a hurricane (Lewis (2003)). An injector concept must efficiently ignite and maintain complete reaction to minimise total pressure losses (Hunt *et al.* (1999)).

Hydrogen's high energy potential is well suited for hypersonic applications and has sufficient heat sink capability to cool a vehicle above Mach 6.

Storage of Hydrogen on-board is a limitation due its lower density than hydrocarbons. It requires a large volume in order to store an adequate amount of chemical energy for practical use. This typically increases vehicle size. Hydrogen gas will need to be stored

cryogenically under pressure to increase its density, but even after that, its density is about one tenth of other propellants. This will require special cryogenic tanks due to its low boiling point.

Another benefit of hydrogen is that it can be used for cooling the leading edges of the vehicle. It also has high values of heat of combustion. All the surface heat accruing on the walls of the combustor must be transferred to the fuel as in regeneratively-cooled rocket engines. Most of the initial design studies use quasi-one-dimensional combustor models for their ease in computation and the same procedure is adopted here.

Turbine-based engines (e.g. turbojets) have a limited Mach number of 2-3 due to heat loads on the turbomachinery. Ramjets can provide a compressible flow compression instead of mechanical for thrust at greater speeds but ramjets do not operate at low-speeds due to the ram-effect requirement. In light of that, the low-speed propulsion system will consist of turboramjets, which is a single flowpath TBCC-type powerplant. This combines the turbine engine and ramjet into a single system. This was adopted as a possible candidate to accelerate the waverider from brakes release until transition to a high-speed powerplant that can accelerate the vehicle to the desired hypersonic cruise Mach number. Hydrogen will be used for the turboramjets for compatibility with the scramjet.

In this study, the term *low-speed* will be used to represent turboramjets operating between brakes release to Mach 5 or subsonic to high supersonic flight. Whereas *high-speed* will imply the hydrogen-fuelled scramjet at speeds between Mach 5 to Mach 9/10 or for the desired hypersonic cruise Mach numbers.

3.2.3.2 Propulsion

Existing research studies by Hunt and McClinton (1997); Pegg *et al.* (1993); Espinosa and Bonds (1993) examine the potential of a turboramjet to meet this requirement and to avoid installing separate Turbojet and Ramjet systems. Similarly to the scramjet, turboramjets offer near-term development potential and good performance credentials over competing concepts. Furthermore, a turboramjet saves on dead weight considering the Turbojet becomes unusable above Mach 3. Dolvin (2002) also recognises the choice of a turboramjet / scramjet combination as a means to minimise operational cost, using near-term technology. Turboramjets are also more fuel and volume efficient and they

help to avoid the extra complexity associated with the added transition from Turbojet to Ramjet.

Further discussion on the inlet and nozzle for both the high-speed and low-speed propulsion system respectively will be given in Chapters 5 and 6.

The engine flowpath dictates the vehicle geometry in hypersonic waveriders. Since the low-speed and high-speed engine must operate over a broad Mach range of speeds, the geometry is selected to obtain maximum performance from this cycle.

The low-speed TBCC turboramjet and dual-mode scramjet have been selected to represent the propulsion system on the hypersonic vehicle. It provides the acceleration at takeoff and thrust up to the scramjet transition Mach number. The position of the engines must take advantage of the forebody precompression, which will reduce the physical dimensions of the inlet. The forebody must also provide the necessary mass-flow to the inlet whose shape will also affect aerodynamic performance.

Engine thrust depends on ingested mass flow, engine placement and forebody dimensions. As the forebody acts as the engine inlet, the flow properties entering the engine must be acceptable for combustion. This means that they must satisfy the narrow requirements for pressure and temperature for efficient combustion at a sufficiently high rate in supersonic flow. It is desirable for the flow to be nearly two dimensional, so that the boundary layer will remain laminar for as long as possible before entering the engine to reduce skin friction. This is accomplished using the two-dimensional scramjet ramp discussed in Chapter 4, which provides greater flowfield uniformity for the combustor and alleviates the complexity of the inlet design during off-design operation.

It is expected that the turboramjet will function during low-speed operation between Mach numbers $0 < M_0 \leq 5$ and the scramjet will operate between $5 < M_0 < 10$. The transition phase is therefore at Mach 5, where a parallel operation of the turboramjet and scramjet is anticipated. Rectangular inlet designs are generally easier for airframe integration.

The two engines are integrated in a dual (over/under) arrangement, which is a widely accepted method for integrating multiple engine flowpaths as explained by Espinosa and Bonds (1993); Moses *et al.* (1999); Cockrell *et al.* (2002). Hence, the turboramjet sits in parallel with and mounted above a scramjet with a variable geometry inlet and nozzle

door operating in a fashion to divert flow to and from either engine to a) protect the turbomachinery from the high-speed flow and b) avoid excess drag within the scramjet during low-speed operation.

This technique was chosen to demonstrate one possible configuration within the methodology although, several alternative combinations may eventually be possible. An alternative arrangement could be the use of a single-duct engine such as the RBCC or an ejector ramjet.

3.3 Mission Profile

Referring to the objective, the vehicle will be required to cruise at hypersonic speeds and deliver a payload above a specified target area. Typical mission radii will be of the order of 7000-9000 *nmi*; sufficient for global coverage. Range will determine required fuel and cruising speed. A target design study relevant to the present analysis is described by the mission profile of Figure 3.1 with the segments defined in Table 3.3.

The vehicle will be designed for horizontal takeoff followed by an accelerated climb using an array of turboramjets until the desired cruise altitude specified by the user is achieved at Mach 5. Prior to this, the turboramjet's propulsion system will continue operating in parallel with the scramjet and when thrust matching is achieved (near Mach 5) the airflow to the turboramjet will be shut off. The scramjet will then throttle-up and the aircraft will begin a constant-altitude acceleration to the desired cruise Mach number. At the end of the cruise segment (point 4), the vehicle will slow down and revert to turboramjet power at constant altitude. It will then begin a descent and loiter for a while before initiating a further descent and for delivering its payload over the target area. Following delivery, the vehicle will accelerate and climb to a return cruise altitude where a constant altitude hypersonic cruise will be sustained by transitioning back to scramjet engines. Then finally, the vehicle will decelerate, descend, loiter and land at the original starting point.

Takeoff speeds of 150 m/s have been documented by Billig (1991) for runway lengths between 2,000 and 3,000 m. These high values are due to the small wing area that needs to be minimised in order to minimise drag at hypersonic speeds.

Mach 10 was selected as a potential cruise design speed as this is in agreement with

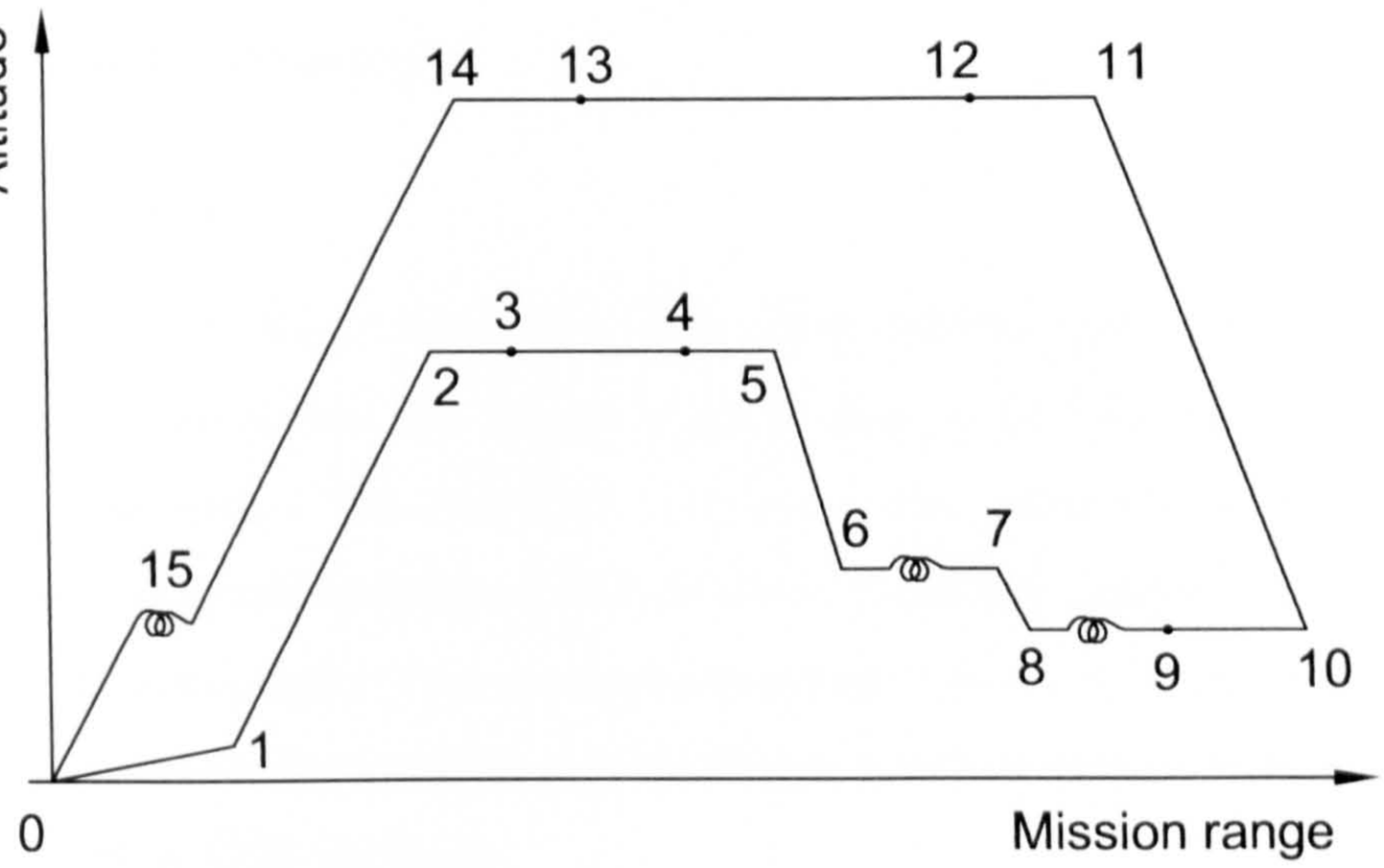


Figure 3.1: Design mission profile for cruise-type vehicles

Segment	Description
0 – 1	Takeoff
1 – 2	Climb & acceleration.
2 – 3	Constant altitude acceleration
3 – 4	Constant altitude hypersonic cruise
4 – 5	Constant altitude deceleration
5 – 6 – 7	Descent & loiter
7 – 8 – 9	Descent & payload release
9 – 10 – 11	Acceleration & climb
11 – 12 – 13	Acceleration & hypersonic cruise
13 – 14	Deceleration
14 – 15 – 0	Descent, loiter & landing

Table 3.3: Definition of mission profile segments in Fig. 3.1

current and previous research (Chapter 2) for this type of aircraft. If a lower Mach number was selected, e.g. Mach 7, then the full potential of the scramjet would not be exploited. Similarly, a length of $60m$ was adopted as that would accomodate the large volume of fuel required to achieve global range. Hydrogen was selected based on consideration presented in §3.2.3.1.

3.4 Program structure

3.4.1 Design tool

During the conceptual design stage of a hypersonic vehicle, many parameters need to be analysed concurrently and the vehicle systems need to be fully integrated in design, functions and operation. The maturity of a hypersonic waverider is contingent upon advances in computational techniques that can account for the complex three-dimensional viscous flowfields and complex wave systems around the vehicle. It is important, therefore, to avoid the expensive computational cost attributed to computationally-based interactive design algorithms or CFD methods.

The approach adopted for this study focuses on the use of direct methods, first principles and estimates that produce an acceptable level of accuracy without intensive computation. This is in order to overcome certain uncertainties associated with current limitations of the aerospace design methodologies.

Analytical techniques are a necessary alternative to define the design space and establish feasibility criteria to constrain the operating domain. This is especially important given that hypersonic vehicle design is dependent on the amalgamation of several aircraft components and tradeoffs between them. For example, tradeoffs in forebody and nozzle length determine the position of the engine along the vehicle. A shorter nozzle length results in reduced thrust due to an under-expanded nozzle flowfield. There is also an inherent tradeoff between producing thrust and lift due to the strong coupling between the engine and airframe (Starkey and Lewis (2001)).

The freestream dynamic pressure is often used to constrain the design space as the vehicle flies along a trajectory. If this value is too high, then heat transfer becomes excessive and if too low, the pressure entering the combustor is not sufficiently high to enable effective combustion leading to a low thrust output. Owing to the strong coupling of the external vehicle aerodynamics/propulsion and performance of the vehicle, modelling their interaction will define the success of a proposed concept.

To address the need of a methodology from a designers perspective, HICAD (*Hypersonic Interactive Combat Aircraft Design*) has been developed as an interactive visual environment application. The code is structured using an object oriented programming

approach, written in Visual C++ / MFC (Horton (1998)). This is an efficient way of developing algorithms and subroutines, combining the flexibility of a Graphical User Interface (GUI) and the power of a numerical language.

This methodology allows the user to explore the impact of initial design parameters such as the Mach number, cruise altitude and waverider forebody shock angle. There is capacity for mutli-variable optimisation; a necessary component of the design cycle to account for the non-linearity.

3.4.2 Flow Chart

HICAD consolidates various preliminary design tools and mathematical models to facilitate the design of practical operational aircraft. This allows for fast analysis and the study of a wide range of hypersonic vehicle concepts significantly reducing the initial design cycle time as compared to detailed component CFD analysis, which are too slow and expensive for the preliminary design level. Key elements of the present study are: a) design of a baseline waverider vehicle and b) analysis and integration of propulsion systems.

Having specified a mission objective, available models and a knowledge base is used to evolve a conceptual design consisting of aerodynamics, propulsion and systems integration. This process is iterative and HICAD's methodology follows the general pattern outlined in the flowchart of Figure 3.2. It shows the highly integrated nature of the design process and provides further information of the computational steps required for a complete design.

The design begins by performing an initial sizing routine that is dependent on the user-selected basic requirements as explained above. The mission profile determines the aircraft constraints, number of engines, range and therefore fuel required etc.

The waverider design is addressed first with a calculation of L_{fore} using a streamline tracing method. The cruise Mach number, altitude and geometric inputs such as the generating curve in the inlet plane, are required for this computation. Given an acceptable L_{fore}, the scramjet inlet size is determined for the on-design case from a predefined combustor pressure ratio. An iteration is performed that outputs optimum values for: inlet ramp angle, inlet height, flow properties at the inlet / combustor junction and the capture area. The scramjet computation then proceeds with an ideal combustor analysis to estimate the flow entry properties to the nozzle.

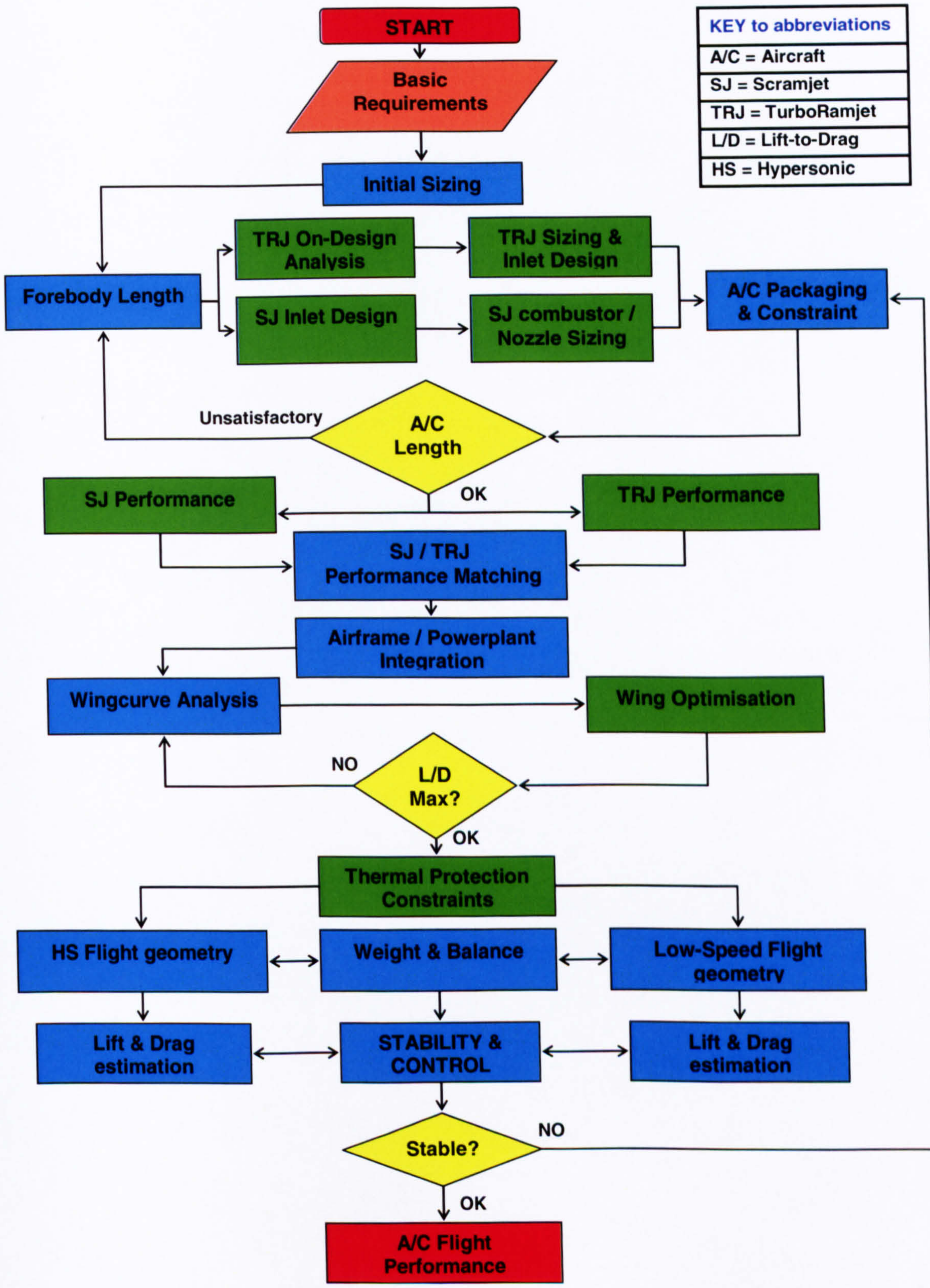


Figure 3.2: Flowchart illustrating the processes with the automated initial design methodology.

The two-dimensional Method of Characteristics is used to calculate the expansion flowfield from the combustor exit to the exit plane at the trailing edge of the vehicle. This fixes the total waverider length. The performance of the propulsion system can be determined in terms of thrust and specific impulse.

The wing section is then calculated that extends to the trailing edge of the vehicle and is subject to geometric constraints imposed on the design to maximise L/D. This is described by O'Neill and Lewis (1993) and completes the on-design case. Next is the low-speed propulsion analysis and is performed by selecting a turboramjet design condition and using idealised cycle analysis from Heiser and Pratt (1994). Performance parameters are determined for $0 \leq M_0 \leq 5$. The turboramjet inlet size is determined by using an off-design cycle analysis code, OFFX, written by Mattingly *et al.* (1987), which computes the required mass flow, $\dot{m}_0$ for a range of Mach numbers.

The required area ratio with respect to the design A_0 is plotted for different altitudes, and the most demanding $\dot{m}_0$ and altitude values are used to size the inlet. For the majority of cases studied that point was at Mach 5 / cruise altitude transition to scramjet mode. Once the inlet size and ramp angles are determined for the off-design conditions, fuel and other systems are accommodated into the vehicle's volume. Iteration is required to find an inlet size that will deliver the desired thrust during the turboramjet / scramjet transition stage. This is discussed in further detail in Chapter 7.

One of the most important aspects of a vehicle design of this nature is to incorporate optimisation into the procedure to search the large design space. This can account for the non-linear interaction between aircraft components. This type of multidisciplinary optimisation (MDO) has been shown by Bowcutt (1992) to produce significant performance benefits over non optimum concepts. For the purpose of this study, optimisation has been performed on the external vehicle geometry to establish a maximum L/D shape for given geometric constraints. The turboramjet and scramjet analyses are are also iterative. The design $\dot{m}_0$ for the turboramjet and the engine width, W_{eng}, for scramjet (amongst other parameters, discussed in the ensuing sections) are adjusted until I_{sp} and thrust matching is achieved with a smooth transition between the two powerplant modes.

HICAD will, however, be extended during follow-on research programmes to analyse the synergy between aerodynamics, propulsion, control and packaging and to reduce the

uncertainty with economics, trajectory and non-linear relationships. The preliminary level of design will be linked with a parametric CAD system as demonstrated by Bowcutt (2003) for two-way information sharing that is, a change in user requirements will send data to the CAD system and vice versa.

Relevant design parameters are iterated until convergence to a specified condition, for example, until the required and available propellants are matched.

The description above does not result in a fully-integrated concept that generally involves aerodynamics, performance, structures, subsystems, thermal protection system and design of entire vehicle structure. It does, however, provide the basic building blocks for the planned full automated system on which to improve. To account for missions specification, a trajectory will need to be accurately calculated to enable a fuel consumption calculation. See Billig (1990) for work on trajectory optimisation.

3.5 Weights Estimation

A weights and sizing methodology by Harloff and Berkowitz (1988) was used as a reference method as part of this study. This method has not yet been incorporated into HICAD yet, although the present author has programmed the equations by means of a spreadsheet and tested its potential as a promising weights prediction method. A brief summary of the program structure will be provided here for completeness.

The goal of the HASA (Hypersonic Aerospace Sizing Analysis) program was to develop a preliminary design methodology that deals with various hypersonic vehicle configurations. It is based on concepts originally proposed in the WAATS method (*Weight Analysis of Advanced Transportation System*) documented by Glatt (1974). WAATS is a weights prediction technique that is based on statistical correlations for specific vehicles. It uses existing software that was developed for the Space Shuttle to predict vehicle weight but did not account for subsonic and supersonic vehicles. HASA has been used extensively in vehicle sizing studies for example in Maita (1993).

HASA is able to predict vehicle size and system component weights of propellant, body, wing, horizontal and vertical stabiliser, thrust structure, propellant tank, landing gear, propulsion, thermal protections system, avionics, hydraulics, electronics, equipment and payload. The method was applied to SSTO, TSTO, hypersonic transports and a

hypersonic strike fighter for various propulsion systems, payload and mass fractions.

It is hoped that the spreadsheet analysis will be translated into HICAD so that the optimiser can make use of its correlations and enable sizing according the mission profile.

For the purpose of future investigations, an average value of $124kg/m^3$ has been widely used (e.g. Takashima and Lewis (1999)) for the density of hydrogen-fuelled hypersonic waverider.

3.5.1 Aerothermodynamics

A hypersonic cruise vehicle experiences large freestream Mach numbers, M_∞, and dynamic pressures. This results in high-temperature flow and high rates of convective heating over the vehicle. Changes in the gas chemistry could result, such as dissociation and ionisation due to the presence of a strong shock layer. The shock/shock interaction was responsible for the damage caused to the X-15-2 during the HRE test.

The rate at which heat is transferred to the surface of the vehicle depends on the material, temperature and freestream conditions of the flow, which may necessitate active cooling as part of the thermal protection system (TPS). The designer of such a vehicle needs to analyse both the thermodynamics and aerodynamics of the flow. This is collectively known as aerothermodynamics and determines the survivability of the vehicle during flight. The fatal Columbia incident highlights the importance of protecting a vehicle from extreme temperatures.

The high-temperature flow affects pressure, skin friction, convective/radiative heating and ablation on the vehicle. Their analysis is important to design the thermal protection system (TPS) to safeguard the structure from extreme temperatures and that will undoubtedly affect overall vehicle weight.

During the flight trajectory, boundary layer transition is likely to occur and predicting turbulent flow onset is necessary for designing TPS and surface geometries.

A proper treatment of the aerothermodynamic environment requires detailed heat transfer and boundary layer analysis that is beyond the scope of the present work.

For aerodynamic efficiency, leading edges need to be sharp to maintain shock attachment. Therefore, advanced materials that reduce surface conductivity and heat transfer are required to enable thin aerostructures to be manufactured. This will reduce overall

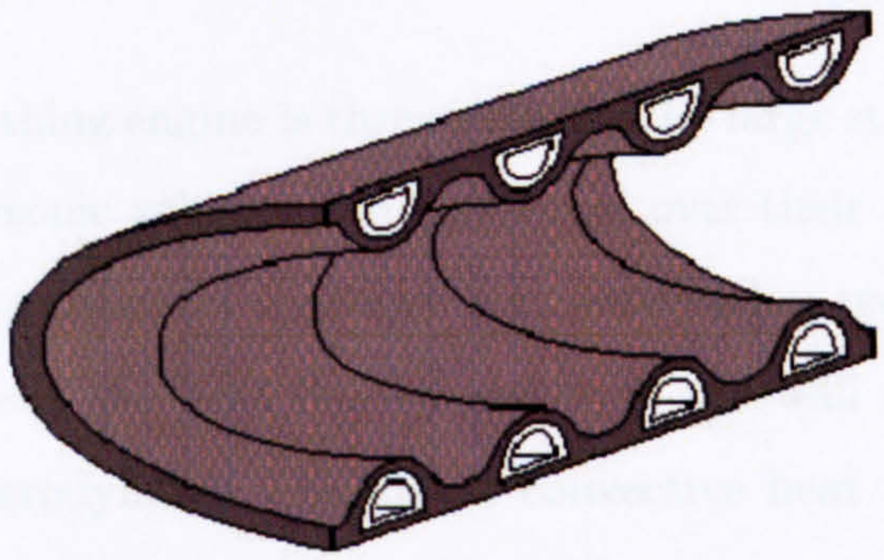


Figure 3.3: NASA's heat-pipe-cooled wing leading edge (HPCLE) concept for active cooling of leading edges.

weight and minimise drag. However, heat transfer issues require blunted shapes to spread heat flux over a larger area and to provide volume for the application of heat absorbing or ablative materials. This tradeoff is important when considering Mach 10 cruise aircraft. The expected temperature extreme on the leading edges is approximately 3,400 R for a leading edge radius of 1.0 in.

TPS can be divided into passive and active cooling systems. The type of TPS employed on a cruise vehicle depends on range and cruise Mach number. Passive cooling is when the material property itself either radiates heat away from the surface or acts as a heat sink. Advanced materials such as ultra high temperature ceramics and reinforced carbon-carbon composites, can alleviate aerodynamic heating.

For temperatures that exceed $2500°K$, passive cooling is not sufficient to keep the temperature low and active cooling becomes necessary. Cryogenic cooling systems pump low temperature fluids through the vehicle structure, especially along leading edges. The vehicle need not carry a special, additional fluid for this system if it is hydrogen-fuelled. A Mach 10 vehicle should employ active cooling on the engine cowl, sidewall and leading edges as recommended by Hunt and McClinton (1997).

NASA's Advanced Space Transportation Program (ASTP) has been looking into heat-pipe-cooled leading edges (HPCLE) as shown in Figure 3.3 and Glass *et al.* (2002).

Transition to a heat-pipe design should only be made when passive cooling can not be sustained. This is due to increased cost, complexity and weight of the leading edge and this type of cooling will probably only be required for reentry vehicles.

Other areas that will require heat protection include tails and fins, upper surface, and

lower surface.

The life of an airbreathing engine is threatened by the large stagnation enthalpies. The materials used on hypersonic vehicles can be heated over their allowable range reducing the strength and causing chemical reactions e.g. oxidisation requiring the need for wall cooling. The magnitude of the heat flux to and from the wall needs to be investigated. This is referred to as aerodynamic heating or convective heat transfer. The convective heat transfer from the hot side is absorbed by the coolant that flows on the cold side. Since this coolant is usually fuel that is later injected, the energy involved is available for the thermodynamic cycle. (See p480, Heiser and Pratt (1994).)

A positive value of heat flux, $\dot{q}_w$, indicates heat being transferred *to* the wall and a negative value means heat transferred *from* the wall.

4

Airframe Design

4.1 Introduction

In this chapter, the methodology for generating the airframe configuration of the vehicle will be presented. This starts with the inverse-design of the conically-derived waverider with its aerodynamic force estimation procedure. Presented here is the airframe-propulsion integration methodology for the on-design case.

Figure 4.1 illustrates a scaled two-dimensional diagram of the main components of an airframe-propulsion integrated waverider designed for Mach 9 flight. This figure will be referred to often, in subsequent sections.

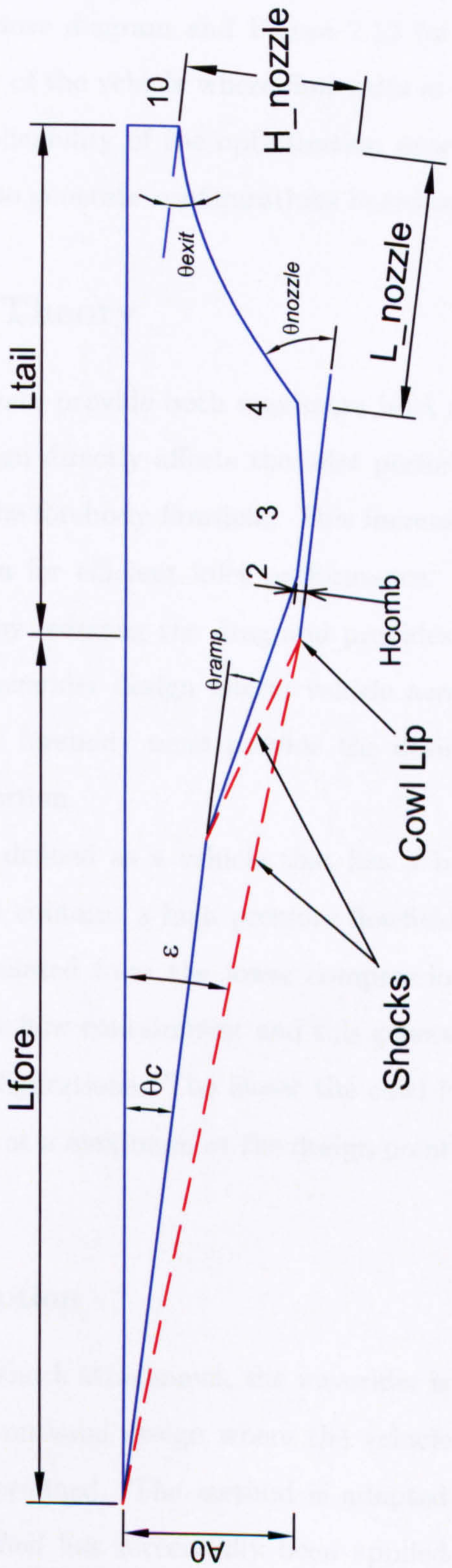


Figure 4.1: Key geometric parameters in Waverider design

The forebody is the section forward of the cowl lip in the inlet plane. A single planar inlet ramp further compresses the flow before entering the combustor. Refer also to station numbers both in the above diagram and Figure 2.12 for combustor sections. A nozzle section fits into the rear of the vehicle where flow exits at Mach 10.

The theory and applicability of the optimisation procedure will be outlined towards the end of this chapter to generate configurations based on a desired merit function.

4.2 Waverider Theory

Highly integrated airframes provide both maximum inlet capture area and nozzle expansion. The forebody design directly affects the inlet performance and is maximised if the inlet is located within the forebody flowfield. This increases the pressure ratio and maximises inlet capture area for efficient inlet performance. The overall dimensions of the inlet are reduced, thereby reducing the drag and provides greater flow uniformity at the combustor face. The waverider design affects vehicle aerodynamics and propulsive performance, therefore, the forebody must provide the desired mass flow to the inlet and minimise inlet flow distortion.

A waverider can be defined as a vehicle that has a bow shock wave attached to its sharp leading edges that contains a high pressure flowfield underneath the vehicle. Flow on the top surface is isolated from the lower compression surface. Pressure losses are minimised due to greater flow containment and this generates high L/D values compared to other hypersonic configurations. The closer the cowl is to the shock, the greater the mass capture and this is at a maximum at the design point where the bow shock impinges on the cowl lip.

4.2.1 Flowfield solution

To achieve leading-edge shock attachment, the waverider is carved from a known flowfield. This is contrary to conventional design where the vehicle is designed then the flowfield around the body is determined. The method is adapted from work by O'Neill (1992). This *inverse-design method* has successfully been applied to both conically-derived and osculating cone waveriders.

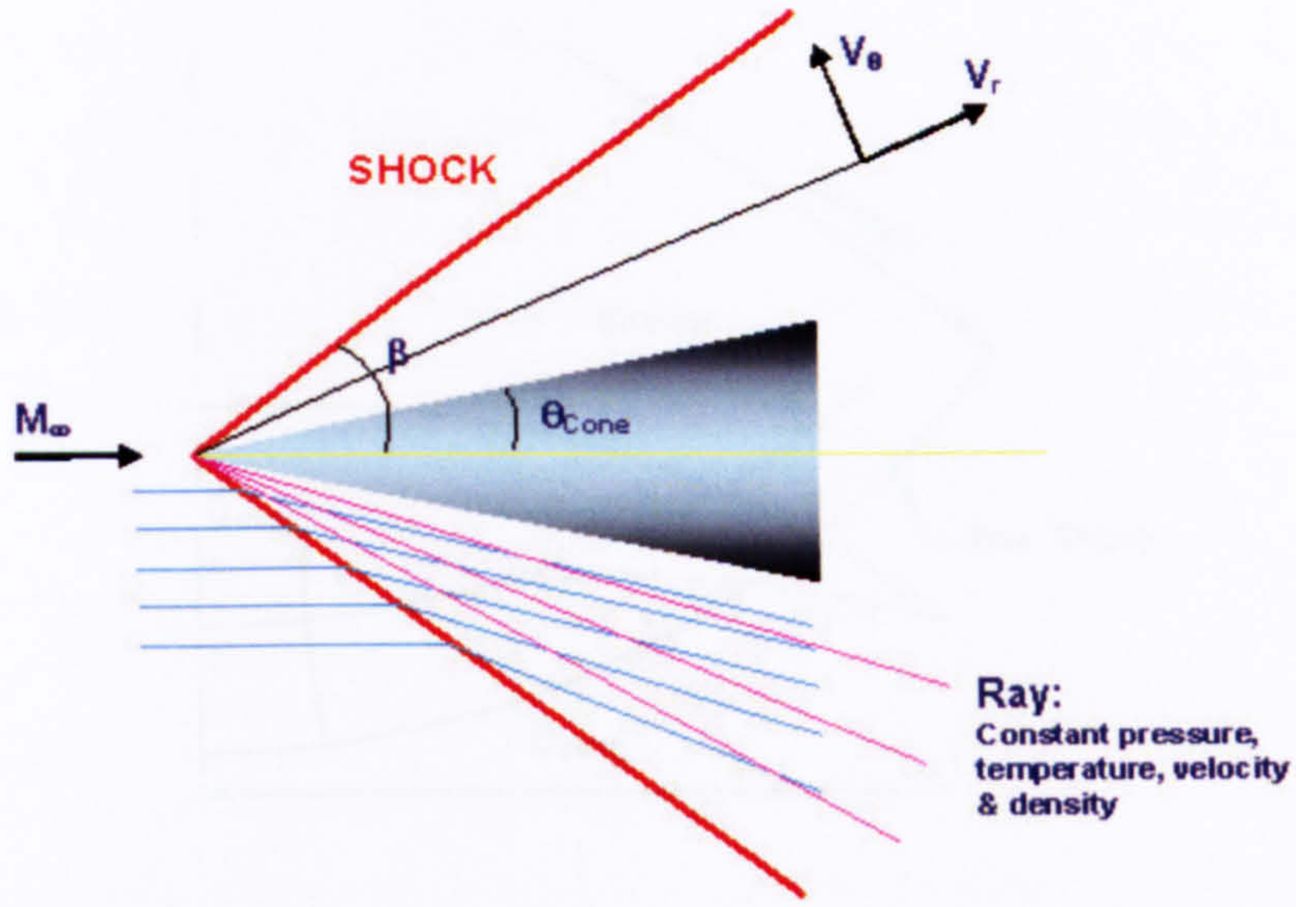


Figure 4.2: Determination of the hypersonic flowfield and hence semi-apex cone angle.

Typically, wedge or cone shapes are used to define a supersonic or hypersonic flowfield as these are easily computed.

By specifying both the semi-apex angle of a conical shock wave and the freestream Mach number, the semi-apex angle of the generating right-circular sharp cone can be calculated by solving the Taylor-Maccoll equation given by Equation 4.1 in spherical co-ordinates. The axis is aligned with the freestream direction at zero angle-of-attack

$$\frac{\gamma-1}{2}\left[1-V_r^{'2}-\left(\frac{dV_r^{'}}{d\theta}\right)^2\right]\left[2V_r^{'}+\frac{dV_r^{'}}{d\theta}\cot\theta+\frac{d^2V_r^{'}}{d\theta^2}\right]-\frac{dV_r^{'}}{d\theta}\left[V_r^{'}\frac{dV_r^{'}}{d\theta}+\frac{dV_r^{'}}{d\theta}\frac{d^2V_r^{'}}{d\theta^2}\right]=0 \qquad (4.1)$$

where V_r and θ are two independent variables. $V^{'}$ is the non-dimensional velocity, $V_r^{'}$ is the radial component and V_θ is the normal component of the velocity given by Equation 4.2 and shown in Figure 4.2. The properties immediately behind the shock can be found using oblique shock relations given in Appendix A.

$$V_\theta = \frac{dVr^{'}}{d\theta} \qquad (4.2)$$

An inverse approach is adopted to solve this equation numerically, using a fourth order Runge-Kutta technique. By inverse we mean that for a given shock wave, the cone angle, θ_{cone}, supporting the shock is computed. This is an iterative procedure, as outlined in Anderson (1990).

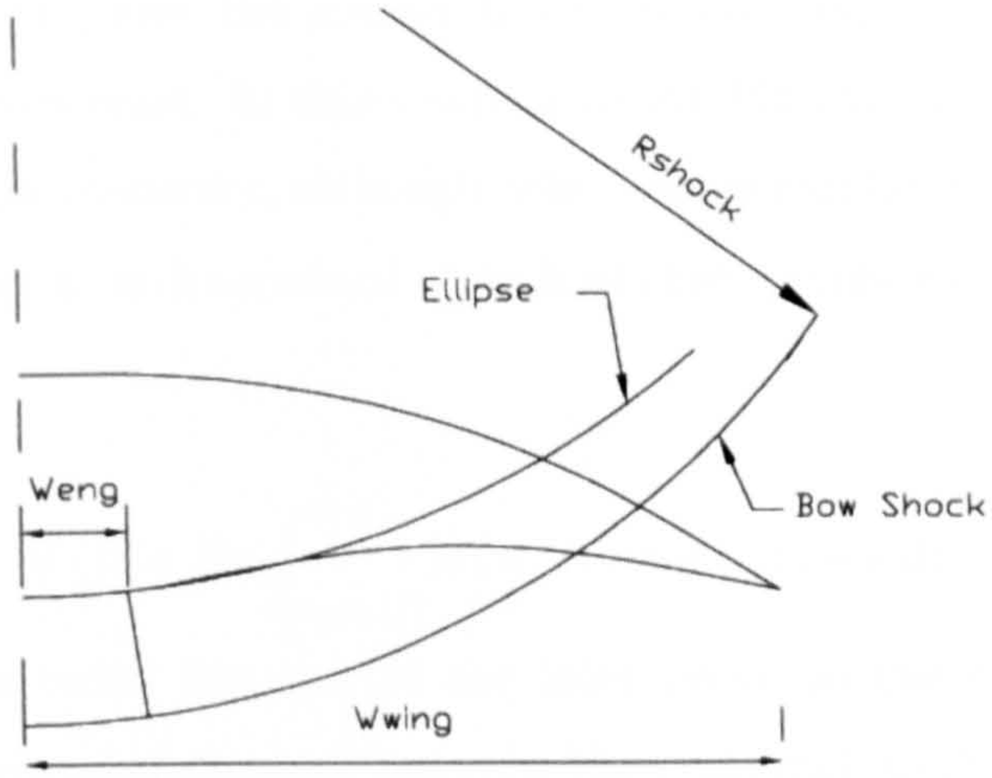


Figure 4.3: Waverider initial design parameters at the inlet plane.

Starting with the Mach number and shock angle, ϵ, the flow deflection angle, δ, V_r and V_θ, immediately behind the shock are calculated using oblique shock relations given by Equation B.3 in the Appendix. Using these initial boundary values behind the shock, Equation 4.1 was solved for $V_r^{'}$ in steps of a fixed d_θ, marching away from the shock. θ_{cone} is found when the value of $V_\theta \rightarrow 0$. Along a ray, flow properties are constant from a given vertex.

4.2.2 Waverider Lower Surface

The forebody shape and length, L_{fore}, is determined from an inlet curve corresponding to a segment of an ellipse with a lateral spacial limit equal to half-span of the engine, W_{eng}, as shown in Figure 4.3. The inlet curve has a semi-minor axis, ae, and semi-major axis, be, and is generated from seven points. Three of which are the last three points on the inlet curve and the remaining four are design variables selected by the optimiser. The end point is required to sit on the shock wave.

Aerodynamic heating and poor volumetric efficiency are the reasons behind relaxing the uniform inlet height. Therefore, a greater ellipticity of the inlet curve results in an increased forebody length.

By specifying ϵ and R_{shock} in the inlet plane, the axial location of the inlet plane and cowl lip is determined. The cowl lip is positioned such that it is in contact with R_{shock} at the inlet plane and to constrain the minimum and maximum length of the waverider.

The farther aft the inlet plane, the greater the forebody length, lower the pressure and smaller angle to the freestream. In this study, a length 60m is used for the length of the waverider from available literature, although other values can be input into HICAD.

The streamfunction, ψ, is determined at each of these points using the following equation

$$\psi(j) = 2\pi \int_{x_{cone}(j)}^{x_i(j)} \rho(z_i, x) * w(z_i, x) * x \, dx \tag{4.3}$$

where $x_i(j)$ is the radial distance of the inlet point on the curve from the cone's centerline and x is the radial distance between the cone and $x_i(j)$ point in one ϕ plane, z_i is the axial location of the engine inlet station, ρ is the local density and w is the local axial velocity taken from the Taylor-Maccoll solution.

As the flow is axisymmetric, ψ values between the cone and shock surface are independent of the ϕ plane chosen. Therefore $\psi(j)$ is determined throughout the flowfield by calculating values in one ϕ plane only.

A streamline is a line of constant streamfunction. So for a given $\psi(j)$ at each j point on the inlet curve, the streamline position, x, of the next upstream z point is found by integrating Equation 4.3 until the specified value of $\psi(j)$ is attained. This streamline tracing method is incremented with equal step size until the bow shock is intersected, whereby x is greater than x_{shock}. The calculation is repeated for each j inlet point up to W_{eng} (HICAD input) resulting in a streamsurface or compression surface, carved from the generating flowfield. A leading-edge shock attachment results, which reduces pressure leakage and maximises the mass flow capture for combustion.

The forebody length, L_{fore}, is dependent on the shape of this inlet curve, which is defined by *ae*, *be* and the shock radius, R_s, at the inlet plane. L_{fore} variation with Mach number is shown in Figure 4.4 for varying ϵ. In general, the length appears to increase linearly with M_0 for given values of *ae*, *be* and R_s.

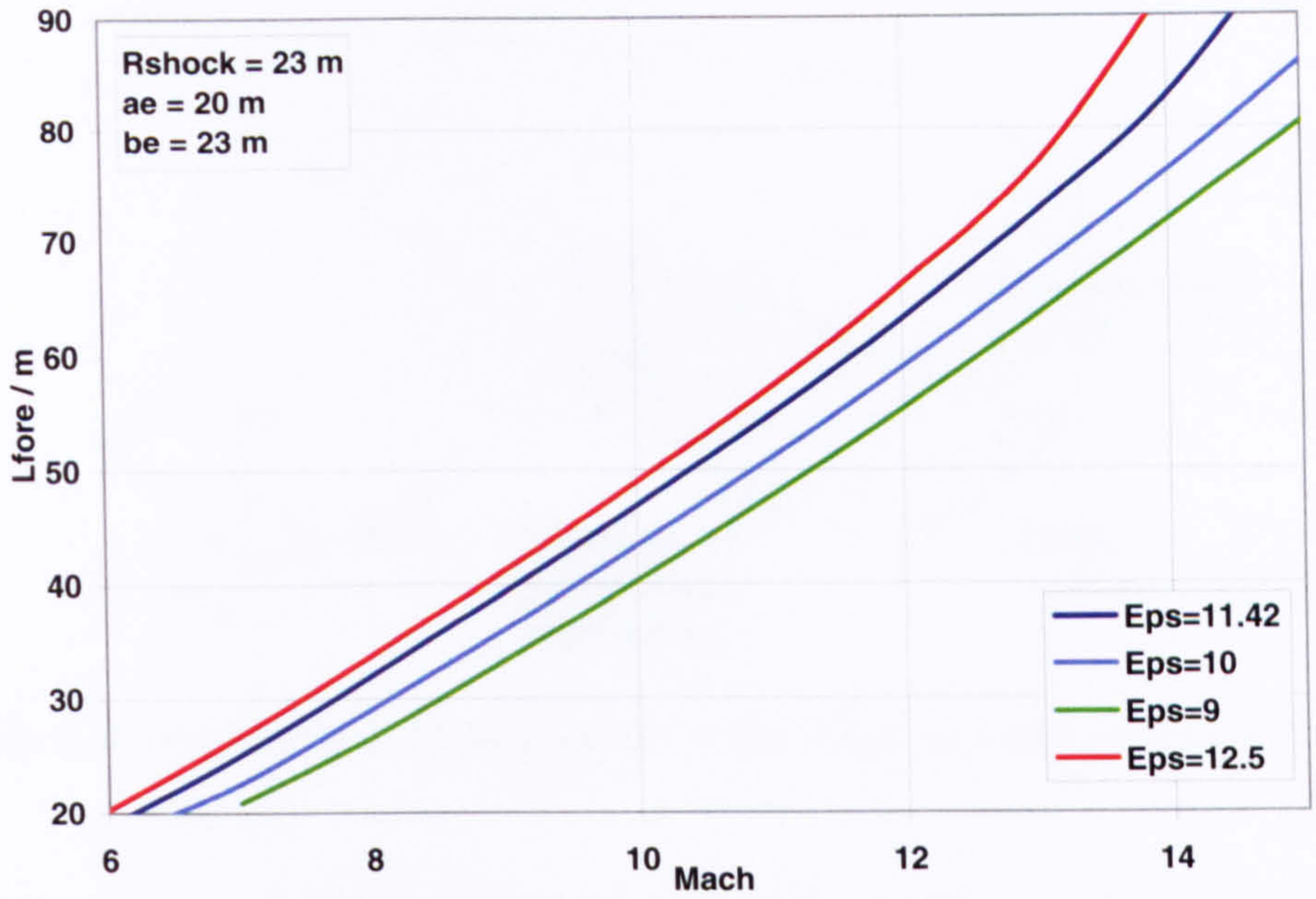


Figure 4.4: Forebody Length variation with different bow Shock Angles.

4.2.3 Outboard Waverider definition

The wing curve is a section that connects the edge of the elliptic section (W_{eng}) to R_s at the tail station. It is defined by fitting a third-order polynomial (Equation B.6) to the outer three points defined by streamlines at the vehicle tail station traced from three outer-most points of the ellipse at the inlet station, three trailing edge design variables (Points. 4,5,6) and one point that is required to sit on the shock. The closer the semi minor axis is to the shock, the smaller the forebody for a given vehicle length.

Streamlines are again traced until intersection with the shock, which completes the design of the lower surface, with a schematic shown in Figure 4.5, adapted from O'Neill (1992), and it appears that the vehicle is *riding* its shock wave attached to the waverider leading edge.

Certain constraints on the tail station points are necessary such that the design space does not extend beyond R_{shock} nor lie within the generating cone. In addition, the wing curve points should not produce a concave leading edge when traced forward of the tail plane and the point on the shock at the tail plane is constrained to be less than the cowl radius to avoid an excessive landing gear height.

Figures 4.6 and 4.7 illustrate the wing-curve and the main engine span section, of a Mach 9 pure waverider for a non-optimised configuration.

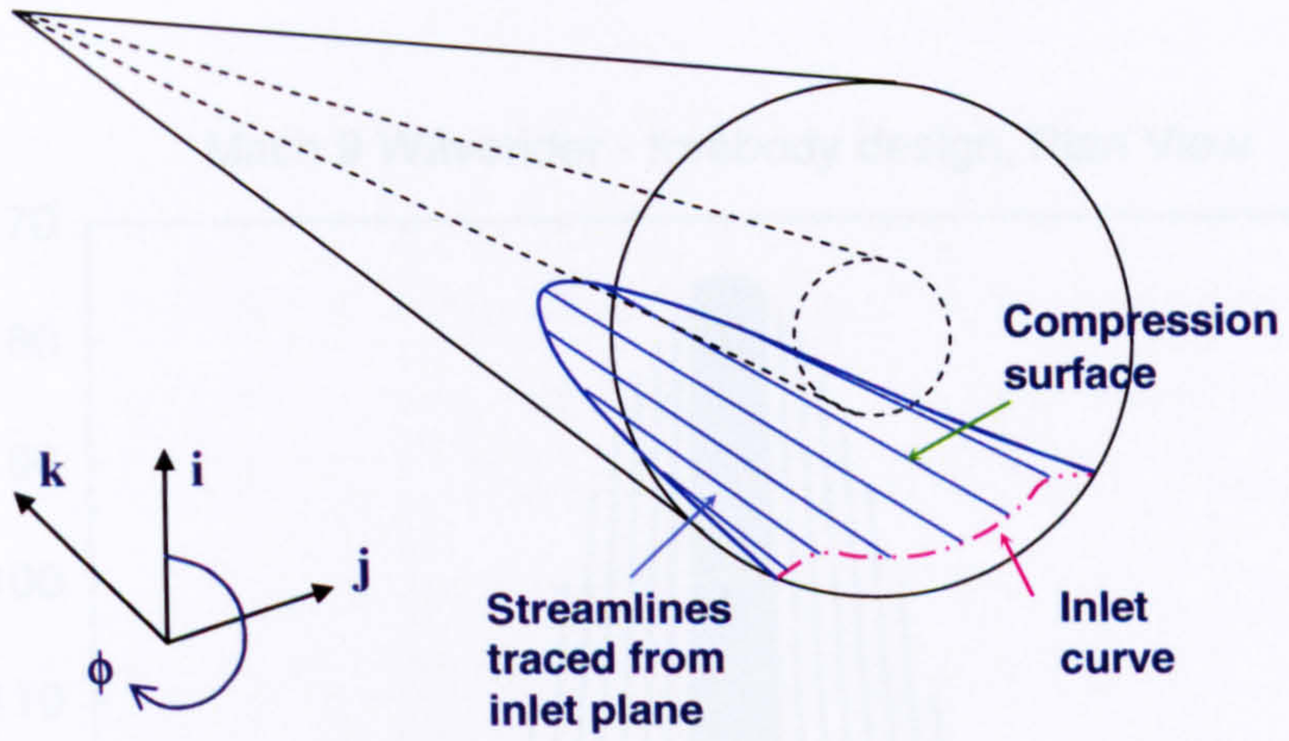


Figure 4.5: Forebody generation using an inverse design approach starting at the inlet plane.

For this study, the upper surface is simply aligned with the freestream direction by tracing back from the leading edge curve to the base of the vehicle. The flow is unperturbed and the pressure is therefore equal to the freestream pressure, p_∞.

Details of the maximum L/D optimisation of these shapes will be discussed at the end of this chapter. The waveriders were validated against already-validated studies by both Takashima (1997) and O'Neill (1992) with excellent agreement. L/D was estimated to be 7.51.

4.3 Inlet

The intake is one of the most critical components of an airbreathing engine and it should be properly shaped to accommodate the unstable nature of supersonic combustion. In addition to the compression provided by the bow shock of the waverider forebody, an inlet ramp and the reflected shock off the cowl lip are used to further compress the flow according to the inlet requirements. Inlet shock instabilities due to high back pressures from combustion are a current area of research. A thorough account of the inlet flow requires detailed CFD or experimental analysis, which is beyond the scope of this study.

Scramjet inlets may be subject to boundary layer separation that can result from the short length scale of the inlet and hence high-adverse pressure gradients. Separation is not desired as this causes shocks in the inlet, additional losses and high thermal loads. Possible mechanisms of separation are compression corners and shock/boundary layer

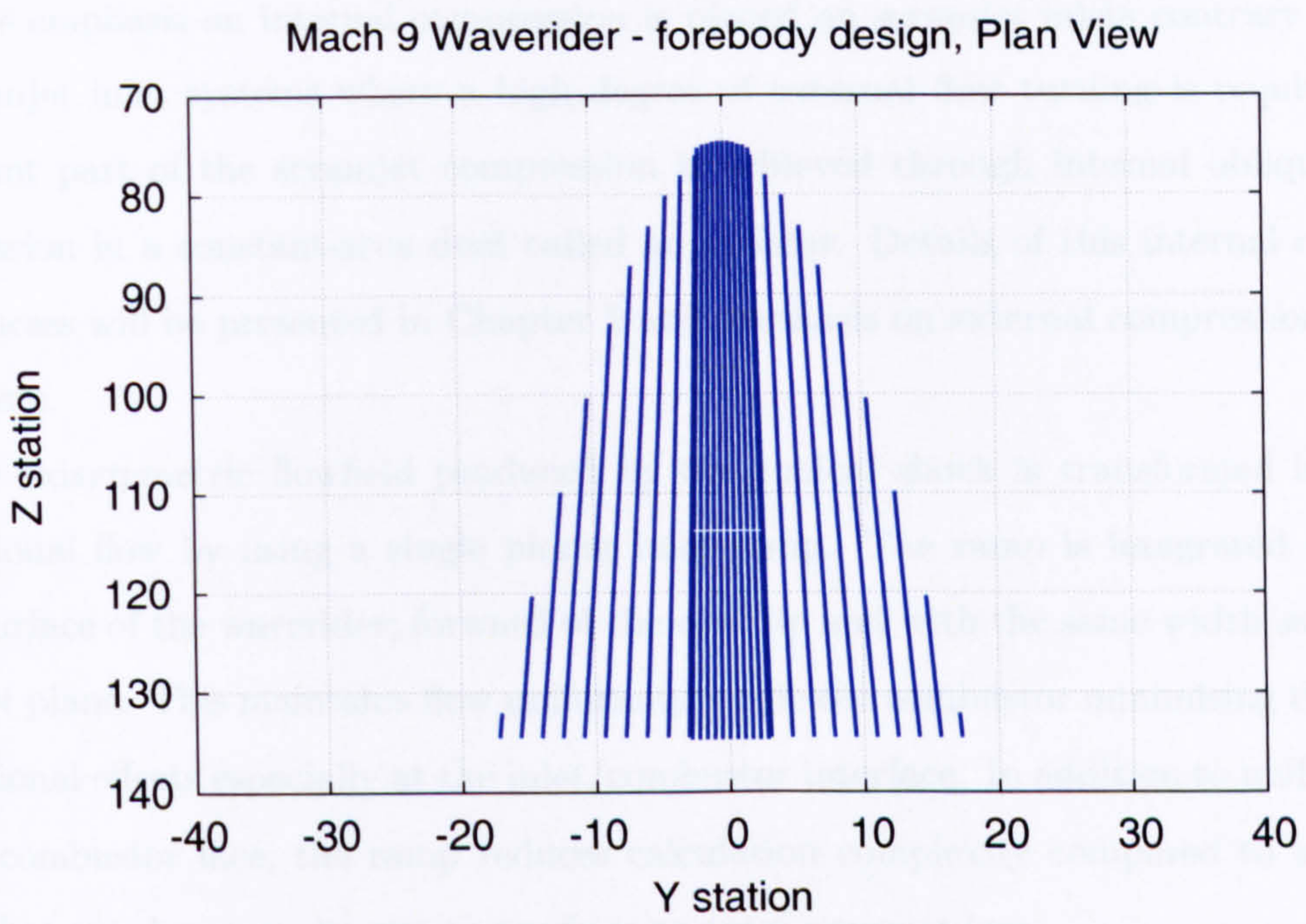


Figure 4.6: Mach 9 example of waverider shape, Plan View.

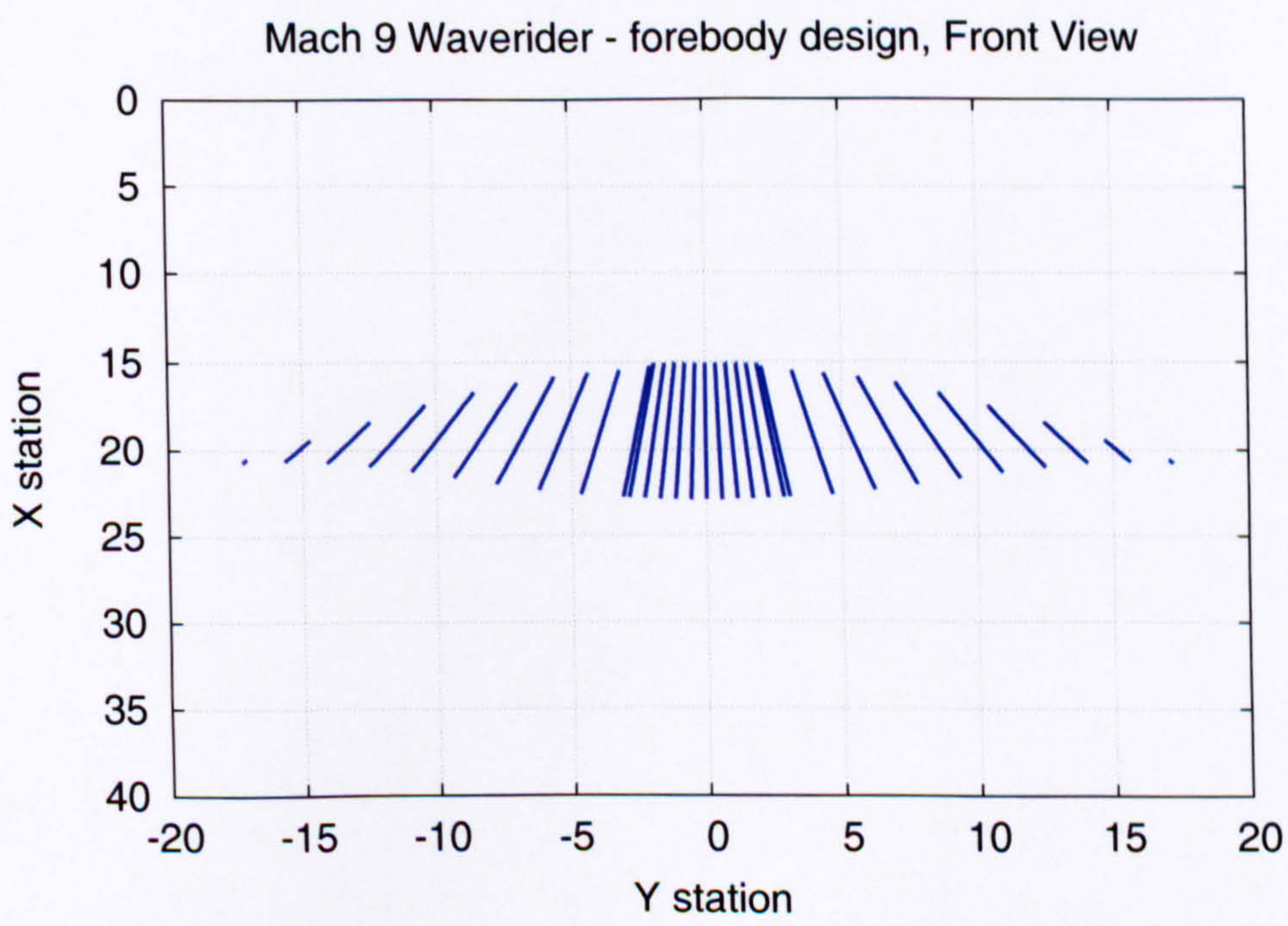


Figure 4.7: Mach 9 example of waverider shape, Front View.

interactions/reflections; an in-depth discussion of which is presented by Van Wie (2000).

More emphasis on internal compression is placed on scramjet inlets contrary to ramjet/turbojet inlet systems where a high degree of external flow turning is required. An important part of the scramjet compression is achieved through internal oblique shock compression in a constant-area duct called an *isolator*. Details of this internal compression process will be presented in Chapter 5 and emphasis on external compression will be made here.

The axisymmetric flowfield produced by the conical shock is transformed into two-dimensional flow by using a single planar inlet ramp. The ramp is integrated with the lower surface of the waverider; forward of the cowl lip and with the same width as W_{eng} in the inlet plane. This maintains flow uniformity inside the combustor minimising the three-dimensional effects especially at the inlet/combustor interface. In addition to uniform flow at the combustor face, the ramp reduces calculation complexity compared to isentropic inlets that are, however, known to produce no total pressure loss.

The forebody thermodynamic variables are mass-averaged to enable a two-dimensional oblique shock calculation to be carried out to maintain a shock-on-lip condition at the engine design Mach number. These shocks are illustrated using dashed red lines on Figure 4.8.

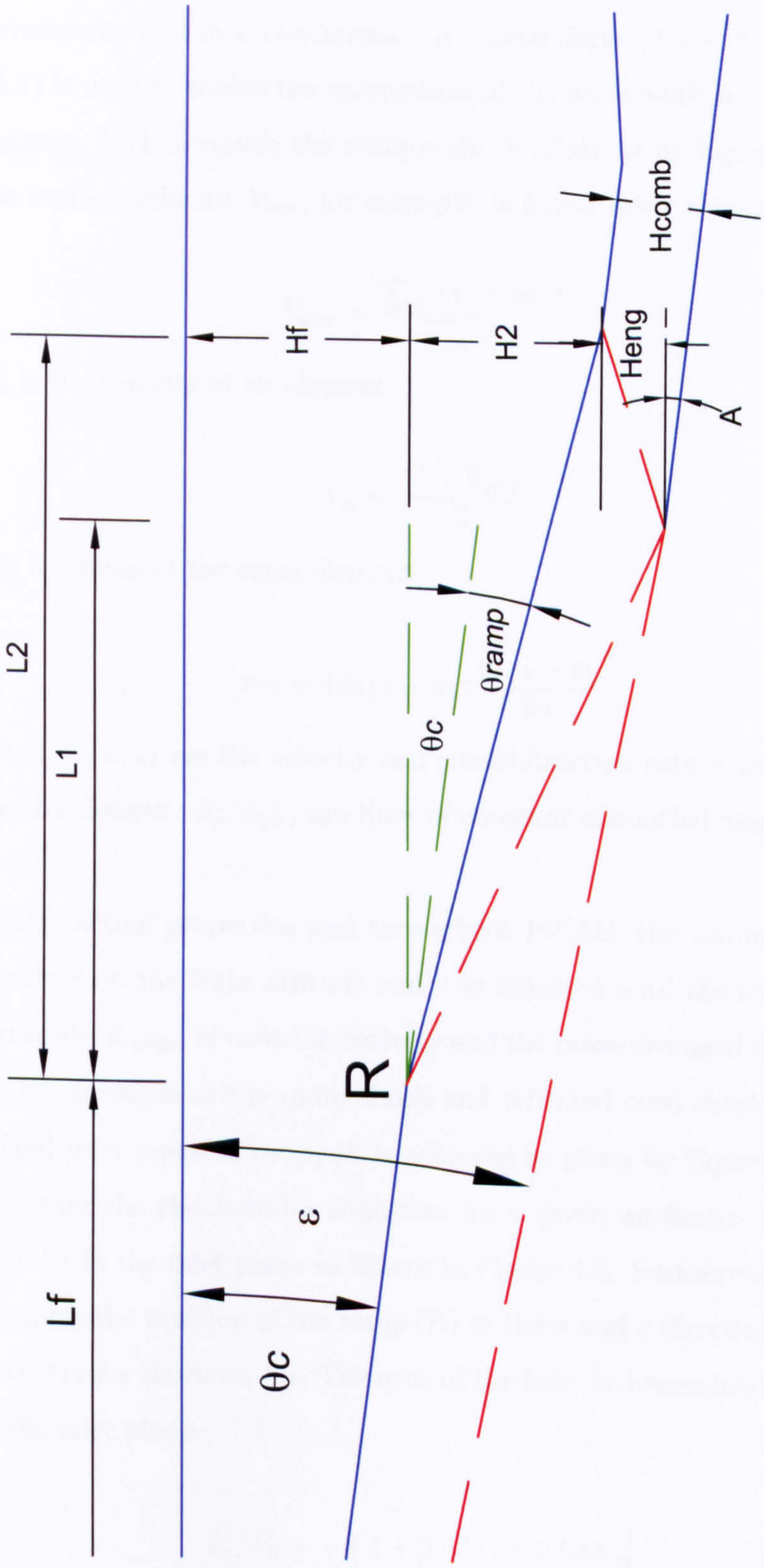


Figure 4.8: Single two-dimensional planar ramp for additional compression. Shocks are shown with dashed lines.

Mass-averaged forebody flowfield properties for the pressure, temperature and velocity are used to facilitate a two-dimensional oblique shock calculation in order to determine ramp and combustor entrance conditions. A closed form of the $\theta - \beta - M$ equation (Equation A.1) is used to enable the calculation of the wave angle for a given ramp angle given by Equation A.11 alongside the oblique shock relations by Equations A.3 to A.7.

The mass average velocity, V_{ave}, for example, is found using Equation 4.4

$$V_{ave} = \frac{\sum_n (V_n * m_n)}{\sum_n m_n} \tag{4.4}$$

where V_n is the velocity of an element,

$$V_n = \frac{V_i + V_{i+1}}{2} \tag{4.5}$$

and m_n is the mass of the same element

$$m_n = (\psi_{i+1} - \psi_i)\frac{\phi_{j+1} - \phi_j}{2\pi} \tag{4.6}$$

V_i, V_{i+1} and ψ_i, ψ_{i+1} are the velocity and streamfunction values along constant radial lines defining the element. ϕ_j, ϕ_{j+1} are lines of constant azimuthal angle on either side of an element.

To determine actual properties and throughout HICAD, the combustor requirements are also dependent on the flight altitude and it is adjusted until the conditions are met.

The ramp angle, θ_{ramp}, is varied iteratively and the mass-averaged flow values are used to determine the strength of the ramp shock and reflected cowl shock. This is repeated until the desired inlet pressure ratio, P, is achieved as given by Equation 4.7 from Billig (1993) to maintain the shock-on-lip condition for a given on-design M_0. This sets the height of the inlet in the inlet plane as shown in Figure 4.8. Furthermore, dimensions are indicated to enable the position of the ramp (R) in the x and z direction to be determined using trigonometry for shock-on-lip. The area of the inlet is determined by setting a value for W_{Eng} at the inlet plane.

$$P_i/P_0 = -8.4 + 3.5M_0 + 0.63M_0^2 \tag{4.7}$$

where i is the inlet face, and M_0 is the Mach at freestream conditions (0). Other useful

Equations based on analytical models to validate a particular design by Billig, include the the inlet contraction ratio similarly for $3 \leq M_0 \leq 25$

$$A_0/A_i = -3.5 + 2.17M_0 - 0.017M_0^2 \tag{4.8}$$

and the air capture ratio for the design Mach number, M_D

$$A_0/A_i = \begin{cases} 1 - (M_D - M_0) \times (0.155 - 0.94 \times 10^{-2} M_D \\ +1.8 \times 10^{-4} M_D^2) & \text{for } M_D < M_0 \\ 1 & \text{for } M_D \geq M_0 \end{cases} \tag{4.9}$$

where A_i now remains fixed at the value of A_0 in Figure 4.1 and A_0 will decrease according to off-design operation. These equations provide a wealth of information that can be estimated for inlet compression.

Note that the height of the engine relative to the freestream direction, H_{eng}, is not the same as the local height of the combustor, H_{comb} due to the deflection of the cowl, with an angle A.

The ramp oblique shock produces, at least, the same pressure ratio as the bow shock and has the effect to minimise combustor length and reduce inlet drag. The ramp is positioned such that a second generating shock impinges on the cowl lip, as with the bow shock, which reflects and this reflection cancels on the shoulder of the combustor upper wall.

The reflected shock cancels on the upper wall of the combustor while turning the flow parallel to the cowl. Its angle (labelled A on Figure 4.8), is kept the same as the angle the streamline makes with the freestream flow once it passes through the bow shock to avoid formation of complex shock/expansion processes inside the combustor.

Table 4.1 shows the on-design flow properties after the inlet shock system. A moveable cowl can be used to maintain a shock-on-lip condition for off-design considerations but that is not considered in this study.

Temperatures at the combustor face are constrained between $1000 \leq T_4 \leq 2200K$ as recommended by Billig (1990) to enable auto-ignition of hydrogen and to avoid dissociation of oxygen respectively.

the vehicle are numerically integrated by using average values for the pressure and shear stress acting on the vertices of that element. A vector product determines the area and orientation of each element. The top surface merely produces skin friction drag.

The method is appropriate for streamlines with straight lines as they are for waveriders. The superscript (*) denotes conditions at the reference temperature. The wall shear stress, τ_{turb}, for turbulent flow is calculated given conditions at the edge of the boundary layer denoted by subscript (e)

$$\tau_{turb} = \frac{1}{2}\rho^* V_e^2 C_f \tag{4.10}$$

where C_f is the skin friction coefficient

$$C_f = \frac{0.0592}{(Re_x^*)^{0.2}} \tag{4.11}$$

at a Reynolds number, Re, based on a length x along a streamline from the leading edge

$$Re_x = \frac{\rho^* V_e x}{\mu^*} \tag{4.12}$$

and the density at the reference temperature is given by

$$\rho^* = \frac{P}{RT^*} \tag{4.13}$$

where P is the pressure, $R = 287.04 J/kg.K$ is the gas constant. The reference temperature, T^* is calculated using the Mach number, M_e and wall temperature, T_w

$$T^* = T_e \left(1.0 + 0.032 M_e^2 + 0.58 \left(\frac{Tw}{Te} - 1\right)\right) \tag{4.14}$$

The wall temperature is estimated to be $1000K$ and has been used throughout this work. The dynamic viscosity μ^* is determined by Sutherland's law

$$\mu^* = \mu_{ref} \left(\frac{T^*}{T_{ref}}\right)^{1.5} \frac{T_{ref} + S}{T^* + S} \tag{4.15}$$

where $\mu_{ref} = 1.789 \times 10^{-5} kg/m.s$ and $S = 110K$, a characteristic temperature for air and $T_{ref} = 288K$ for air.

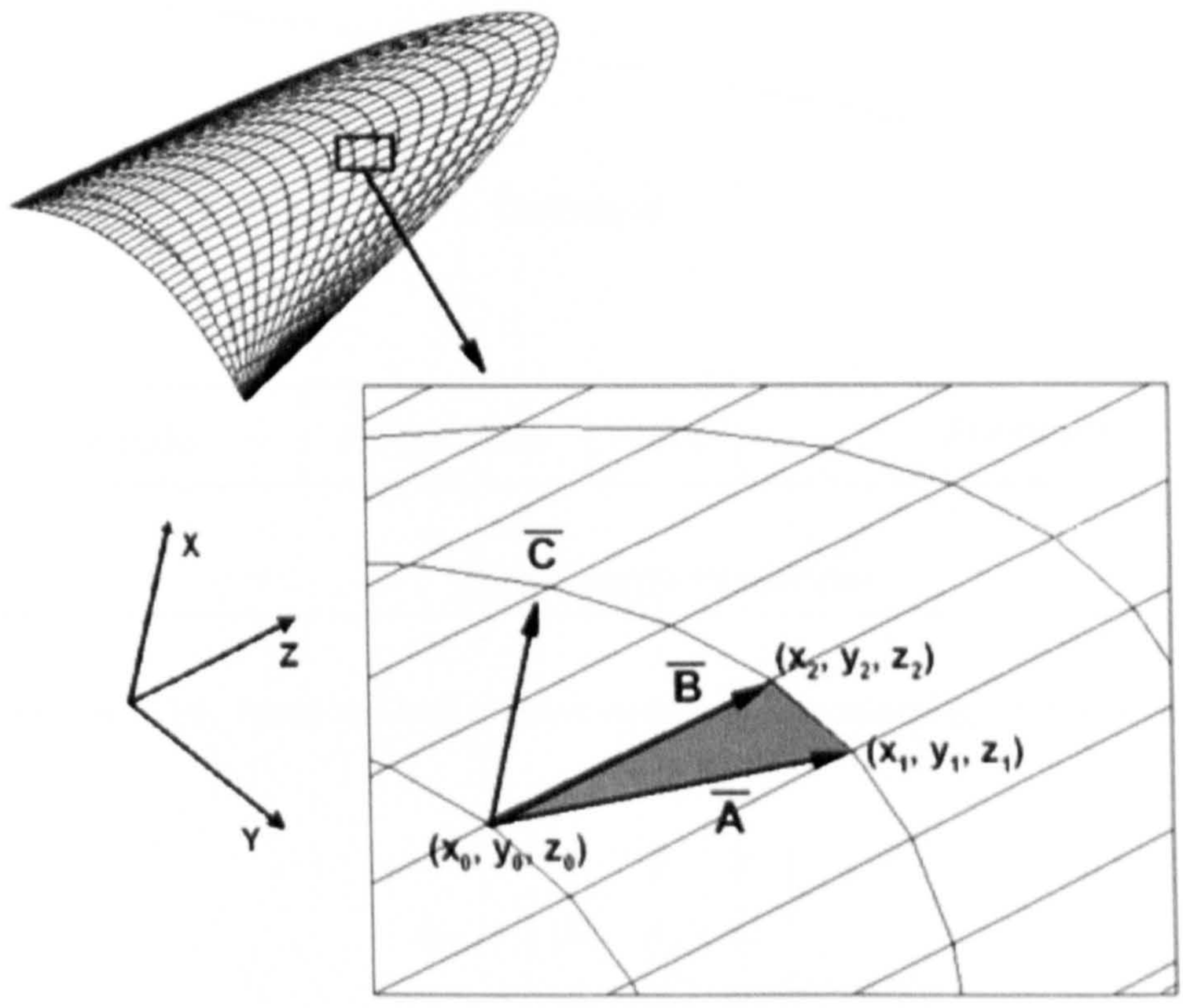


Figure 4.9: Force estimation procedure by integrating forces on cells adapted from Starkey (2000).

4.4.2 Vehicle Force

If the surface of the waverider can be discretised into small cells made of grid points, then the pressure, temperature and density are known from the generating flowfield. By calculating the area of each cell, lift and drag can then be calculated by numerically integrating the pressure and shear stress on each surface element. Figure 4.9 illustrates this method.

Using the vector product of $\overrightarrow{A}$ and $\overrightarrow{B}$, the area of a triangular element is calculated by

$$A_w = 0.5|\overrightarrow{A} \times \overrightarrow{B}| = 0.5|\overrightarrow{C}| \tag{4.16}$$

which can be written in determinant form

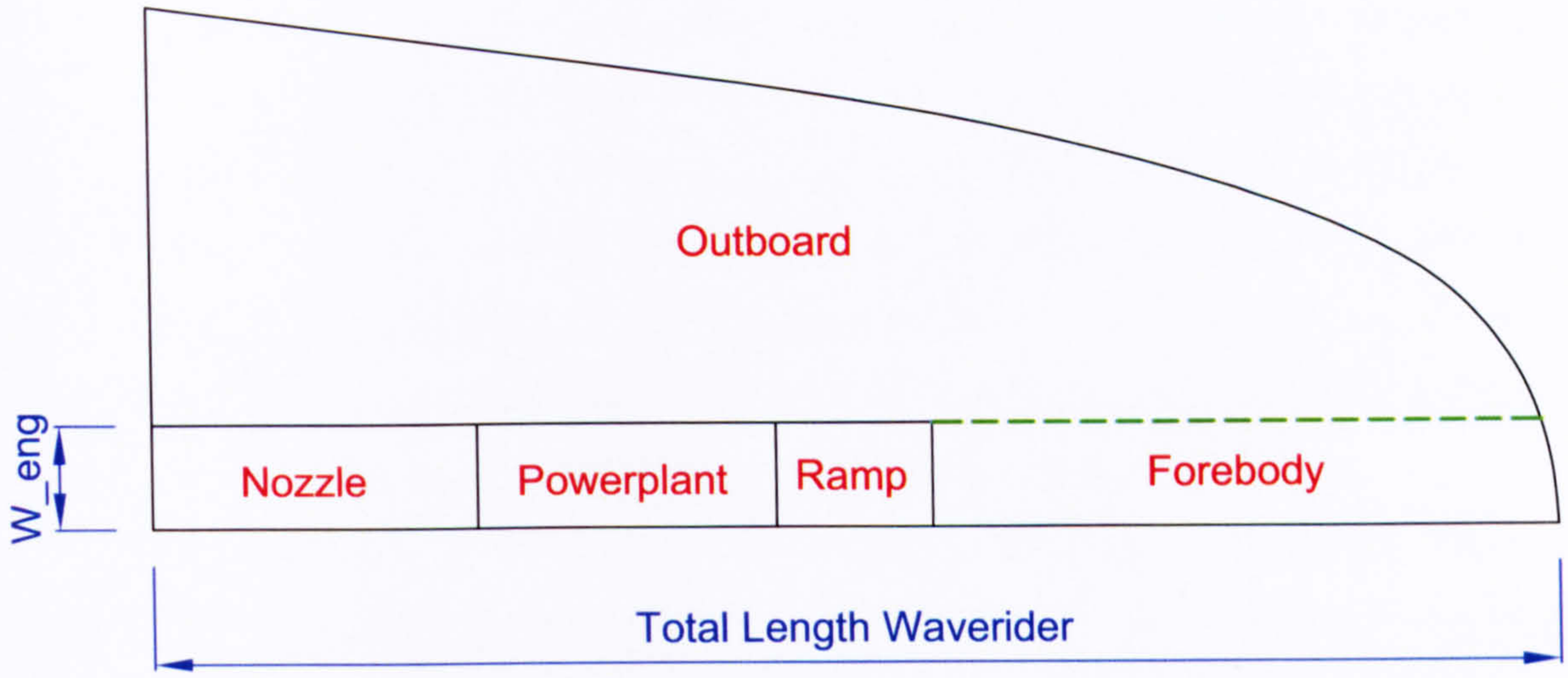


Figure 4.10: Areas involved in lower-surface force accounting. Not to scale.

$$\mathbf{A_w} = \begin{vmatrix} i & j & k \\ A_x & A_y & A_z \\ B_x & B_y & B_z \end{vmatrix}$$

The lift and drag equations can then be formulated as follows

$$L = P_{avg} A_w \frac{C_y}{|\vec{C}|} + \tau_{avg} A_w \frac{B_y}{|\vec{B}|} \tag{4.17}$$

$$D = P_{avg} A_w \frac{C_z}{|\vec{C}|} + \tau_{avg} A_w \frac{B_z}{|\vec{B}|} \tag{4.18}$$

where the pressure and shear stress are averaged from the 3 vertices

$$P_{avg} = \frac{P_0 + P_1 + P_2}{3} \tag{4.19}$$

$$\tau_{avg} = \frac{\tau_0 + \tau_1 + \tau_2}{3} \tag{4.20}$$

To simplify the force estimation procedure, certain areas of the vehicle are not accounted. All directional drag forces, however, are accounted. These assumptions are based on the findings of O'Neill (1992) and are used in this study with an aim to reduce both the computational steps and time taken for computation. The ramp is considered to add a large contribution to the total drag of the vehicle.

Referring to Figure 4.10, the forces may be summarised as follows. The forebody includes the lower surface forward of the ramp towards the leading edge and complete upper surface (not shown here). The ramp is shown in Figure 4.8 and extends up to the combustor face and also shown is the cowl interior and exterior, which is the inside surface downstream of the combustor. Nozzle is the upper surface expansion section aft of the combustor. The lift and drag forces of the combustor have not been accounted for in this study. The outboard section consists of the remaining vehicle lower surface.

The lift generated by the forebody and ramp for the engine span section (W_{eng}) is cancelled by the negative lift on the inside entrance of the cowl. However, the nozzle generates positive lift whereas the cowl exit produces negative lift due to the pressure acting on that surface. The outboard section contributes to both lift and drag. The top surface equates to a zero lift as it is parallel to the freestream.

It must be noted, that no heat transfer study was conducted as part of this work.

4.5 Optimisation

One of the most important aspects of a vehicle design of this nature is to incorporate optimisation into the analysis. This can account for the non-linear interaction between aircraft components. Multidisciplinary Optimization (MDO) has been shown Bowcutt (2003) to produce significant performance benefits over non optimum concepts.

The term optimisation is used to describe the process for the automated selection of values for a number of independent design variables that lead to an optimum (maximum or minimum) value for a given merit function. To run through all possible combinations of each design variable, would be a very time consuming and inefficient task. The merit function needs to be selected carefully so that it encompasses the desired outcome.

4.5.1 Design Variables and Constraints

A good figure of merit for cruise-type applications is to maximise the product of I_{sp} and L/D. This has been used in several previous studies such as by O'Neill and Lewis (1993), Takashima and Lewis (1999) and Bowcutt (2001) and is useful during maximum range calculations given by the Breguet equation B.2.

Several variables remained fixed during optimisation. The total vehicle length was kept

Variable	Constraint
y_7	$Ye_t + 0.2(Rs_{tail} - Ye_t) \leq y_7 \leq Ye_t + 0.9(Rs_{tail} - Ye_t)$
y_4	$Ye_t + 0.2(y_7 - Ye_t) \leq y_4 \leq Ye_t + 0.9(y_7 - Ye_t)$
y_5	$y_4 + 0.2(y_7 - y_4) \leq y_5 \leq y_4 + 0.9(y_7 - y_4)$
y_6	$y_5 + 0.2(y_7 - y_5) \leq y_6 \leq y_5 + 0.98(y_7 - y_5)$
x_4	$0.2(Rs_{tail}) \leq x_4 \leq 0.8(Rs_{tail})$
x_5	$0.2(Rs_{tail}) \leq x_5 \leq 0.8(Rs_{tail})$
x_6	$0.2(Rs_{tail}) \leq x_6 \leq 0.8(Rs_{tail})$
ϵ	$10° \leq \epsilon \leq 14°$
W_{eng}	inlet plane dimensions

Table 4.2: Optimisation design variables and side constraints.

constant, the cowl was parallel to the streamlines crossing the conical shock to reduce drag, the altitude was also kept constant for a given run. No upper surface expansion is required as the top surface is designed parallel to the freestream. Also the cowl length remained fixed at a minimum distance, which will be described later.

Currently, nine parameters are used in optimisation. These include the generated conical shock angle, scramjet intake size in the inlet plane and the seven geometric wing-curve variables. The geometric constraints are based on O'Neill (1992) and will be described briefly here.

Two types of constraints as highlighted by Takashima (1997) were used. These are design side constraints and geometric constraints. Side constraints are implemented as a pair of inequalities and if violated the routine returns a penalty value. Geometric constraints exist to ensure the design is feasible. Table 4.2 summarises the side constraint variables.

The parameter Ye in this table corresponds to point 3 on the inlet curve and Ye_t is this point traced back towards the trailing edge of the vehicle, that is at the tail station. Points 1-3 are known from the inlet plane and the x, y points 4-7 are subject to the following constraints. Rs_{tail} is the shock radius at the tail station. x_7 is required to sit on Rs_{tail} and can easily be computed using y_7.

In terms of geometric constraints, the semi-minor a_e and semi-major parameter b_e

were not included in the optimisation. However, changing a_e will affect the length of the forebody and is constrained by not exceeding a given total length of vehicle. Changing b_e affects the curvature of the inlet curve at the inlet plane. The following inequality is observed $a_e \leq b_e$. The cowl radius for the cruise vehicle is set close to R_{shock} to maximise air capture.

Upper and lower limits on the selection of 7 wing-curve variables include the shock angle and corresponding cone surface respectively. If these values fall outside the shock angle then the vehicle will be prone to excessive heating and drag and if within the cone surface then that will represent a non-real design space. The engine width must be non-zero and less than the width of the waverider in the inlet plane. The conical shock was constrained between a minimum and maximum of 10° and 14° respectively.

Several behaviour constraints also exist that encompass the design space.

- The lower surface at any point must not exceed the geometric upper surface.
- The streamline produced at each point on the generating curve should not exceed the length of the central streamline for the span of the engine. This is to prevent a concave surface as viewed in the planform view.
- The nozzle upper wall expansion angle has a maximum set at 18° to prevent thermal choke.
- The combustor entry pressure and temperature must meet allowable limits as mentioned in a previous chapter.

4.5.2 Method

To find the optimum combination on N parameters, the objective function mentioned above is used, which reflects the effects of variation of each parameter. A range of numerical optimisation methods are available but a robust and widely accepted method for severely constrained waverider optimisation is the non-linear downhill simplex method in multi-dimensions by Nelder and Mead (1965). Advantages of this method are that it does not require calculation of derivatives, allowing it to handle functions that are not written as regular analytic expressions. Restarting the process using converged values, is recommended to ensure the solution is not contained within a local minimum. Also, many

optimisation schemes require an analytical function to minimise but this is not possible in this case and the simplex method readily handles a complete function. A disadvantage of this method is that a large number of function evaluations may be necessary before an optimum solution is achieved.

The simplex method operates upon an initial selection of starting values, that is an n-vector of independent variables and the method travels downhill through the n-dimensional topography until it encounters a local minimum.

A simplex is defined as a geometric object that has $n + 1$ points or vertices for a n-dimensional problem. In two dimensions, for example, the simplex represents a triangle and in three-dimensions, the simplex is a tetrahedron. Nondegenerate simplexes are used in this method, which means that they should encapsulate a positive, finite inner n-dimensional volume.

Starting with an initial simplex, the objective function to be minimised is evaluated at each vertex. The vertex with the highest value undergoes transformation and moves so that an optimal improvement is made in the function value at the vertex. The process is repeated many times until the simplex contracts on itself and surrounds the lowest optimum point (minimum).

The transformations performed in the downhill simplex method are illustrated in Figure 4.11 for a tetrahedron. The top diagram shows the start of the step and towards the end, the simplex can either be a reflection, reflection and expansion or contraction in one or all dimensions from the highest point. This is the process of converging to a minimum.

The minimum value found for the objective function may not be the global minimum so the method allows for adaptation to the environment to achieve a minimum. For example, in a long narrow valley, the simplex will become long and thin and will make large steps down along the valley. The amoeba algorithm (so called due its behavioural similarities) given by Press (2002) has been integrated within HICAD to enable computations without relying on external applications. The source code `amoeba.cpp` is given in §B.4.

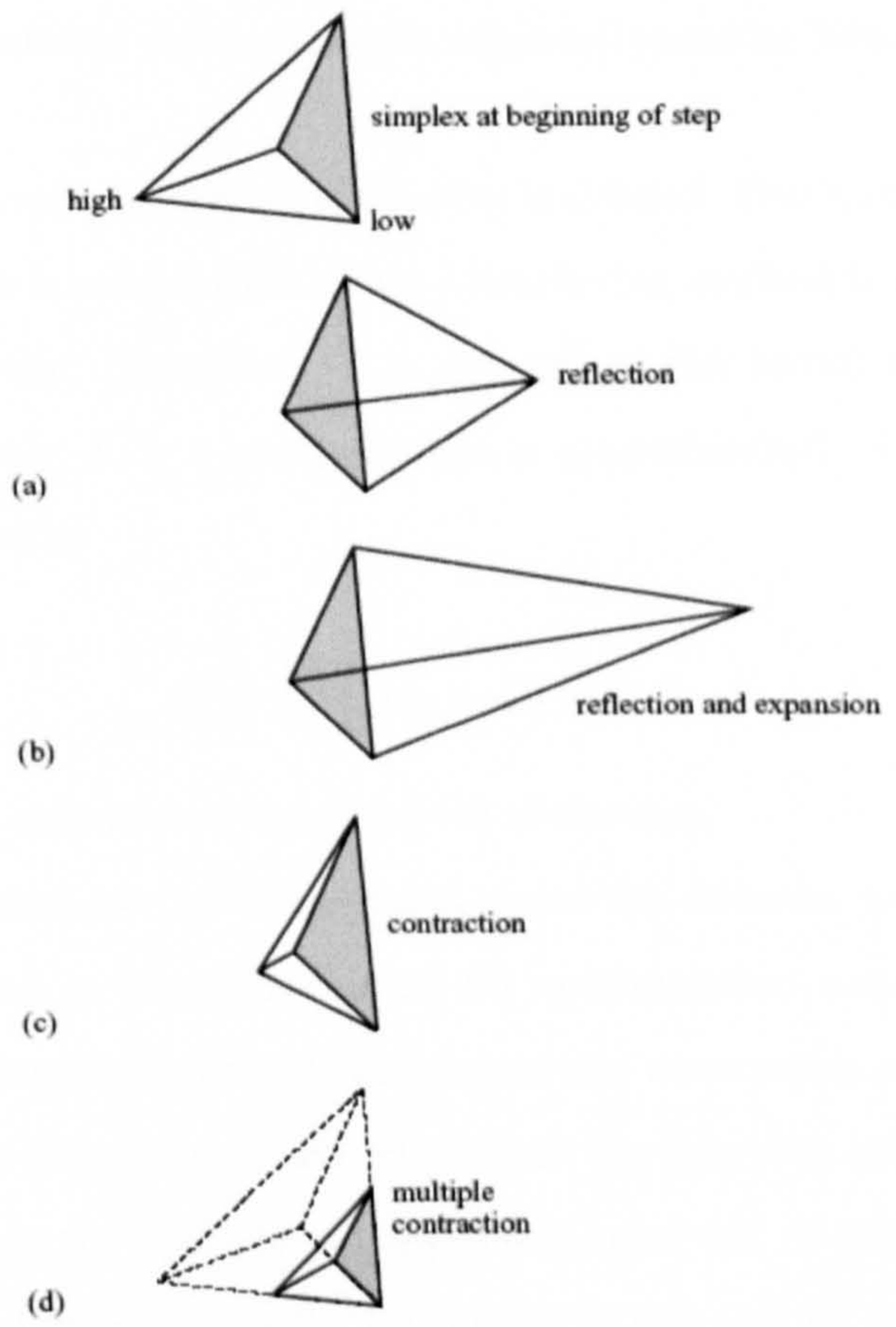


Figure 4.11: The series of steps in the downhill simplex method for converging to a minimum. Figure adapted from Press (2002).

Step	Inequality	Value
reflection (α)	$-1 < \alpha < 0$	-1
reflection and expansion (γ)	$\gamma < 1$	-2
contraction (β)	$0 < \beta < 1$	0.5

Table 4.3: Characteristic length scale, λ possibilities in the simplex method. The final column labelled *value* represents suggested values by Nelder and Mead.

Starting with $n+1$ vertices, the initial simplex is defined. Due to the multidimensional nature of the problem, it is not possible to use a bracketing method to ensure the minimum exists between two points. Therefore P_0 is guessed as the initial starting value and a characteristic length scale, λ, is a constant that is approximated. A good choice for the other n points is defined by

$$P_i = P_0 + \lambda e_i, i = 1, \ldots, n \tag{4.21}$$

where each e_i is an unit vector along the ith dimension.

Table 4.3 offers choices for the values for λ under the different transformations.

The simplex method is originally aimed for configuration unconstrained problems, however it can be adapted for both side and behaviour constraints as encountered in this study. A large penalty value can be returned from the function call if any constraint is violated, which will have the effect of moving the simplex out of the invalid design space. As given by Shoup and Mistree (1987), a value of 20,000 can be used. This large value would contract, expand or reflect the simplex as appropriate.

The stopping criterion is based on a tolerance value. The method was tested on a test problem called Rosenbrocks parabolic valley with excellent agreement. The reader may be interested in the equation and solution given in §B.4.1.

5

High-Speed Propulsion

This chapter deals with the formulation of the scramjet combustor model and a discussion of important concepts affecting combustion in a supersonic stream. The differences between ramjet and scramjet cycles will be analysed before continuing with a description of the model employed in this study. To generate thrust, the combustor exit flow is expanded through a two-dimensional nozzle, the details and design of which are considered in this chapter. Supporting references in preceding chapters suggest the viability of a dual-mode scramjet for practical airbreathing flight and its qualities have been demonstrated during airframe-integration. In general, the length of the high-speed propulsion system is key to establishing the overall vehicle length.

5.1 Scramjet

An airbreathing hypersonic vehicle must fly a profile that withstands high structural heat load and provide sufficient airflow for efficient combustion. A ramjet can operate when the freesream hypersonic flow can be decelerated to subsonic speeds in the combustor. At higher flight speeds, the flow inside the combustor can not be decelerated sufficiently and a supersonic stream exists, hence the need for a scramjet.

During ramjet operation, two physical throats are required, first at the inlet to decelerate the flow from supersonic to subsonic and the second at the nozzle to accelerate the flow back to supersonic for the expansion. For scramjet operation, no throat is necessary

as the flow remains supersonic throughout. It is advantageous to use ramjets up to Mach 5/6 as the specific impulse is favourable over scramjets as shown in Figure 2.7 (Anderson *et al.* (2000)).

At increasing flight speeds, transition to a scramjet mode from ramjet becomes necessary when the total pressure loss becomes too great across the terminal normal shock due to the large contraction ratio. Oblique shocks are used instead to decrease the dependency on the external compression system and this is coupled with an internal compression process. Scramjets, however, suffer from increased Rayleigh losses, short residence times for flow inside the combustor length and difficulty in mixing.

To operate over a wide range of flight conditions, an engine needs to operate in both modes. The dual-mode ramjet/scramjet engine is so-called as it satisfies both these modes by using a constant area duct that operates like a diffuser and contains the precombustion shock train (normal or oblique) to prevent undesirable inlet-combustor interactions during combustion. This shock/stabilising duct is known as an *isolator* and is positioned between stations 2 and 3 as shown on Figure 4.1 and also in the schematic of Figure 2.12. This permits both subsonic and supersonic combustion streams in one engine geometry and without the need for a variable geometry design.

Heiser and Pratt (1994) present Figure 5.1 to demonstrate the purpose of the isolator in the dual-mode concept. Station 2 shows the inlet/combustor junction, 2-3 represents the isolator and station 4 is the combustor exit/nozzle entrance. The flow at station 2 has been compressed by the bow, ramp shock and the reflected shock off the cowl lip. Station 3 also corresponds to the axial location of the most upstream fuel injector. Between station u and d, a region of separated flow exists due to existence of an adverse pressure gradient and station s is where the flow reattaches itself. Furthermore, s, is the location of the lowest Mach number in the combustor. Station 10 represents the end of the nozzle expansion.

5.1.1 Isolator

An isolator is central to the design of the dual mode combustion system, which is able to cope with subsonic and supersonic combustion streams. Incorporating an isolator into the combustor geometry permits dual mode ramjet / scramjet operation by coping with

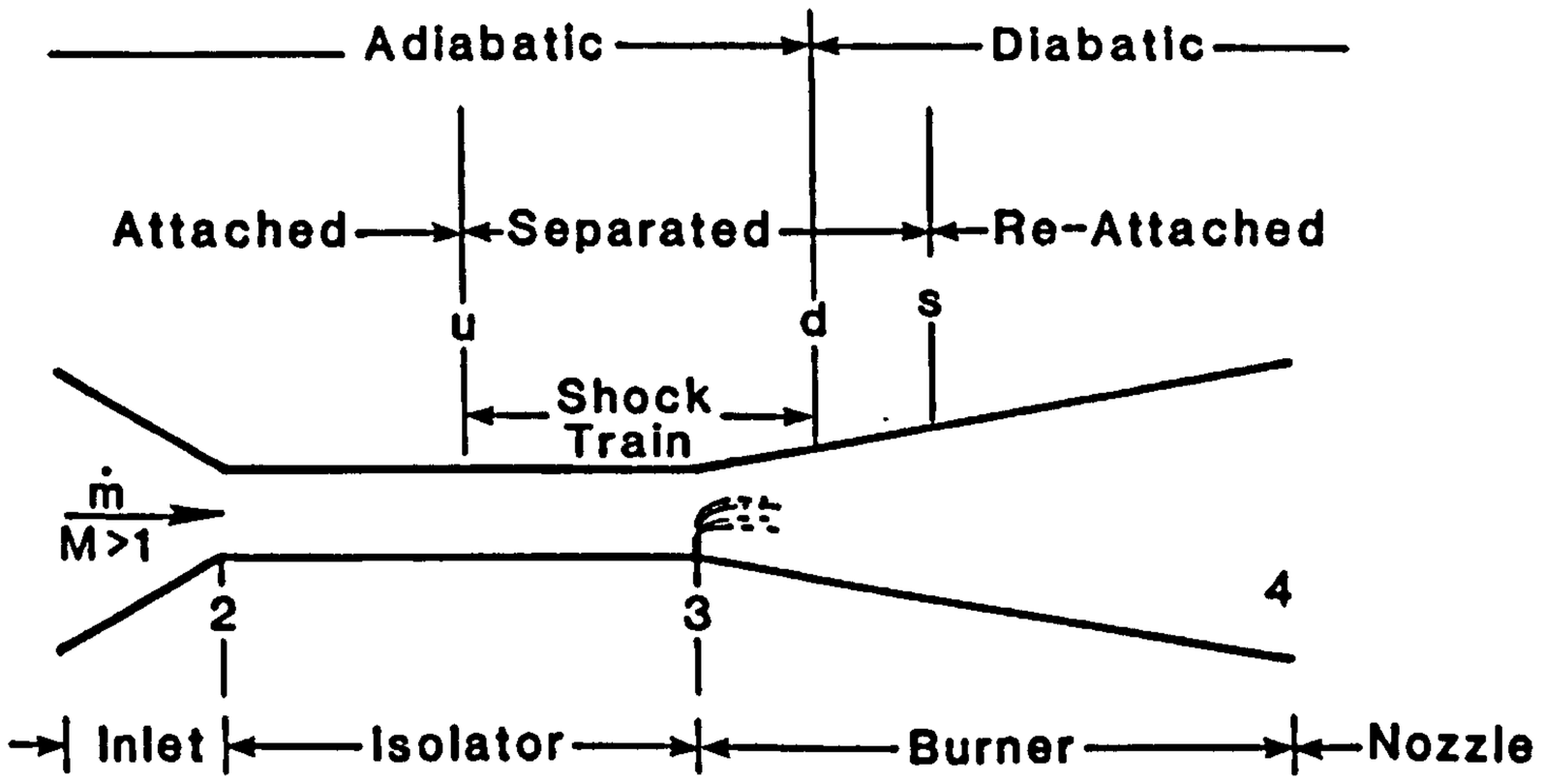


Figure 5.1: Simple schematic of a dual mode ramjet / scramjet with station numbers representing separate parts of the design. Heiser and Pratt (1994).

subsonic and supersonic combustion streams.

In ramjet mode, heat addition (combustion) causes the core flow to become thermally choked (Mach = 1) and therefore subsonic. A normal shock develops and travels upstream where a normal shock train exists in the isolator. The back pressure, P_3, at burner entry must not exceed the isolator pressure, P_2, otherwise the inlet can unstart thereby dislodging the normal shock. The second ramjet throat is a choked thermal throat, which exists for the correct choice of the area distribution, A_x, fuel-air mixing and total temperature distribution from combustion, T_{tx}.

In scramjet mode the isolator still serves a purpose by containing an oblique shock train if an adverse pressure gradient occurs. This can result if there is a rapid pressure rise during combustion causing the boundary layer to separate (thermal occlusion). This is an area of significant research. In this situation, the isolator prevents inlet unstart by containing an oblique shock train assuming that the isolator exit has a supersonic confined core flow surrounded by a region of separated flow (Waltrup and Billig (1973)). The core flow re-attaches at the axial location of maximum pressure and a control volume analysis is carried out, illustrated in Figure 5.2. The height of the isolator is given by H_i and the length of the shock train from u to station 3 is given by L.

There are two main regions in an isolator. The first is the core flow that has increasing area contraction in a supersonic stream and expansion of this area during subsonic flow.

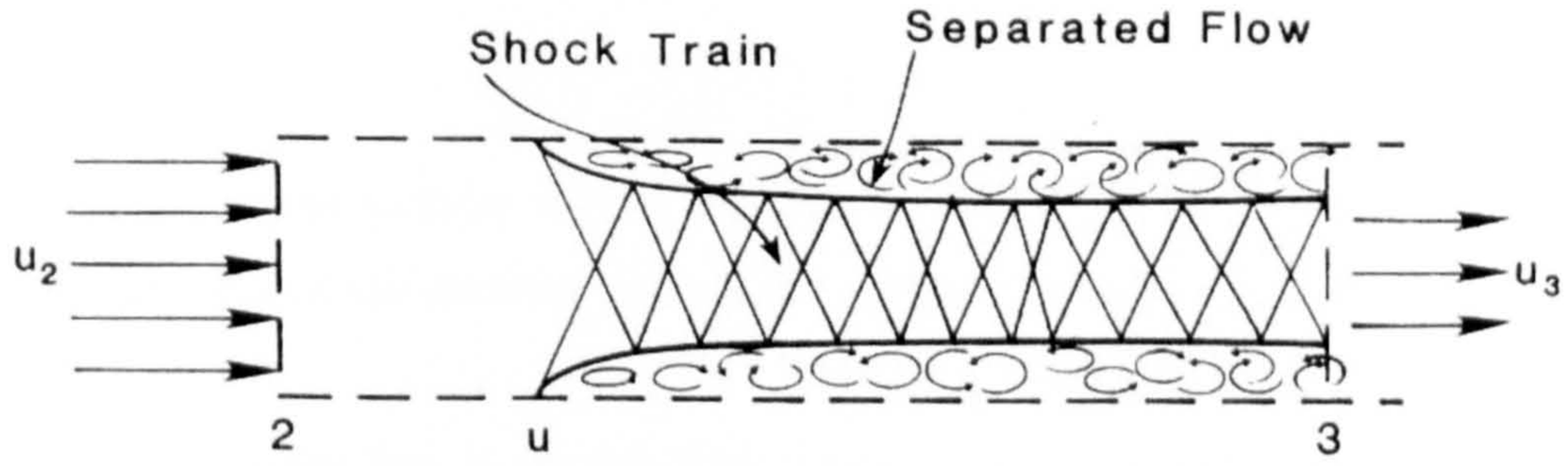


Figure 5.2: Region of core flow in the isolator. Heiser and Pratt (1994).

This results in a pressure gradient. The second region is the separated flow at the boundary that has a thickness dependent on the balance of the pressure gradient from the shear stress in this boundary.

Whether a normal or oblique shock train develops depends on the Mach number in the inlet and boundary layer thickness. The strength of the shock system will dictate flow exiting the inlet at subsonic or supersonic speeds (Van Wie (2000)). At $M_0 > 8$, the heat release is not sufficient to choke the flow and the shock train disappears.

The prediction of a shock train is not a simple affair due to complexities associated with separation, shock-shock and shock-boundary layer interactions and three-dimensional effects. Instead, a simple empirical relationship given by Equation 5.1 is used to find the shock train length, S_t, for given inlet conditions based on experimental data (Billig (1993)).

$$\frac{S_t(M_2^2 - 1)Re_\theta^{1/4}}{H(\theta/H)^{1/2}} = 50(P_s/P_4 - 1) + 170(P_s/P_4 - 1)^2 \tag{5.1}$$

where, θ is the inlet boundary-layer momentum thickness, Re_θ is the inlet Reynolds number and H is the duct height. Typical S_t/H are of the order about 10. The existence of the shock train is dependent on the character of the boundary layer and whether or not separation occurs. The equation is applied to the design of the isolator and combustor.

If during the analysis, the isolator is required, then the Mach number at station 3, M_3 can be calculated as a function of M_2 and back pressure ratio p_3/p_2 by

$$M_3 = \left(\frac{\gamma_b^2 M_2^2 \left(1 + \frac{\gamma_b - 1}{2} M_2^2\right)}{(1 + \gamma_b M_2^2 - p_3/p_2)^2} - \left(\frac{\gamma_b - 1}{2}\right) \right)^{-1/2} \tag{5.2}$$

and the core flow (c) area ratio, $A_{3c}/A_2 < 1$, as shown in Figure 5.2 is given by

$$\frac{A_{3c}}{A_2} = \frac{1}{\gamma_b M_3^2}\left[\frac{p_3}{p_2}(1+\gamma_b M_2^2) - 1\right] \tag{5.3}$$

The length of the isolator should be long enough so that the shock train does not migrate upstream of the isolator due to the adverse pressure gradient and cause inlet unstart.

Inlet start is when flow in the internal portion of an inlet* does not affect the capture characteristics of the inlet. Inlet unstart occurs when flow chokes at the throat due to over-contraction or combustion back pressure causes an adverse pressure gradient. During scramjet inlet unstart, the ratio of the boundary layer to inlet flow is large resulting in supersonic flow spillage whereas in a ramjet, the opposite is true.

For the dual-mode engine to remain started, the design should incorporate area expansion in the combustor to delay thermal choke, an isolator and axial fuel injection.

5.1.2 Quasi-One-Dimensional Combustor Model

Combustion occurs between station 3 and 4 and fuel is injected at station 3. The variation of Mach number through the combustor, M_x, is modelled using quasi-one dimensional analysis based on a formulation by Shapiro (1953) for frictionless flow. The following ordinary differential equation for frictionless flow without mass addition but with a change A and T_t due to heat addition is solved step by step using a fourth order Runge-Kutta technique

$$\frac{dM_x}{dx} = M_x\left(\frac{1+\frac{\gamma_b-1}{2}M_x^2}{1-M_x^2}\right) \left\{-\left(\frac{1}{A_x}\frac{dA_x}{dx}\right) + \frac{1+\gamma_b M_x^2}{2}\left(\frac{1}{T_{tx}}\frac{dT_{tx}}{dx}\right)\right\} \tag{5.4}$$

This is based on calorically perfect gases † with prescribed specific heat ratios, frictionless flow without mass addition and constant pressure heat addition. Specific heat values at freestream was assumed to be $\gamma = 1.4$. The inlet ramp, isolator, and combustor held $\gamma = 1.36$; and the nozzle flow was assumed to be at $\gamma = 1.24$ given that a larger number of

*applies to turbojet, ramjet or scramjet

†Ratio of specific heats is a constant throughout component

molecular degrees of freedom exist in the exhaust flow. Given that combustor undergoes a user-defined change in A_x and an increase in T_{tx} due to heat addition, then Equation 5.4 can be used to calculate the variation of thermodynamic properties. T_{tx} is determined by a rational function, τ_x

$$\tau_x = \frac{T_t(x)}{T_{t2}} \tag{5.5}$$

The thermophysical properties such as pressure, temperature, velocity are obtained using Shapiro's useful integral relations for axial variation of Temperature $T(x)$, pressure $p(x)$, total pressure $p_t(x)$ and velocity $V(x)$.

$$\frac{T(x)}{T(2)} = \frac{T_t(x)}{T_{t2}} \left[\frac{1 + \left(\frac{\gamma_b - 1}{2}\right) M_2^2}{1 + \left(\frac{\gamma_b - 1}{2}\right) M^2(x)} \right] \tag{5.6}$$

$$\frac{p_x}{p_2} = \frac{A_2}{A_c(x)} \frac{M_2}{M(x)} \sqrt{\frac{T(x)}{T_2}} \tag{5.7}$$

$$\frac{p_t(x)}{p_{t2}} = \frac{p(x)}{p_2} \left[\frac{T_2}{T(x)} \frac{T_t(x)}{T_{t2}} \right]^{\frac{\gamma_b}{\gamma_b - 1}} \tag{5.8}$$

$$\frac{V(x)}{V_2} = \frac{M(x)}{M_2} \sqrt{\frac{T(x)}{T_2}} \tag{5.9}$$

These are determined from $A(x)$, $T_t(x)$ and M_x based on a non-dimensional rational function given by Heiser and Pratt (1994).

Other assumptions made in the combustor analysis similar to Small *et al.* (1976) include the following. The engine is a rectangular modular engine that attaches directly to the vehicle undersurface to simplify integration issues. The area change of the combustor, A_x, is a linear divergent section of constant angle with an expansion ratio of 2:1. Heat addition occurs at constant pressure. The concept is likely to use swept compression surfaces and fuel injector struts to provide inlet starting at low-speed and good internal performance throughout the scramjet operating speed range. Instream fuel injection is used to minimise combustor length and heat flux to the internal surfaces. The heat released during combustion is based on complete combustion occurring from initial conditions.

Uniform two-dimensional flow exhausting from a single combustor exit was assumed to represent the engine package, with frozen nozzle flow and reaction kinetics for supersonic

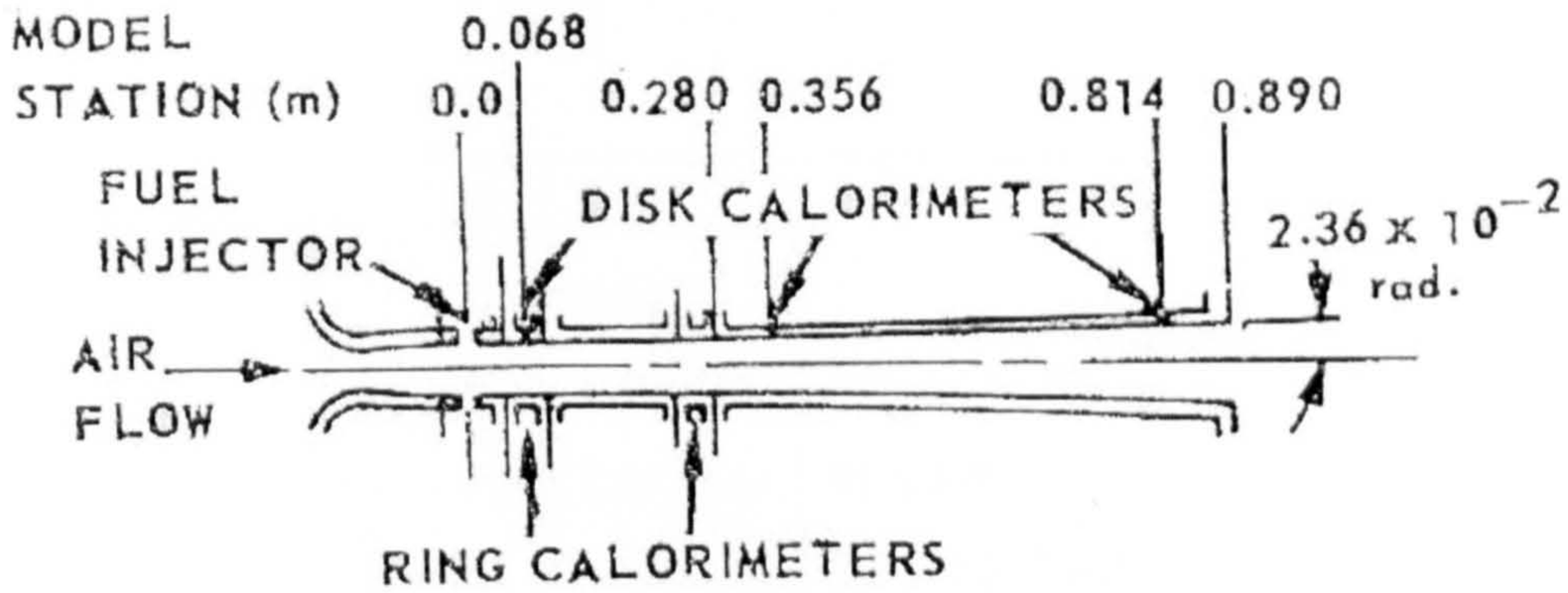


Figure 5.3: The experimental hydrogen-fuelled combustor geometry specifications of Billig and Grenleski (1970) with a 0.28m constant area section.

combustion and nozzle expansion. The combustion efficiency is assumed to be 0.98 and the vehicle flies a constant dynamic pressure trajectory of $1000psf$.

The one-dimensional model with effects of finite-rate chemistry has previously been shown by O'Brien and Lewis ($2001a$) to generate sufficiently accurate results for preliminary vehicle analysis with a relatively short computational time. The primary objective on such design codes remains on the ease of computation.

5.1.3 Model Validation

Many existing quasi-one dimensional models have been validated using experimental wall pressure measurements on scramjets obtained by Billig and Grenleski (1970) for hydrogen-air combustion. See Takashima and Lewis (1999) for similar correlations. The initial conditions for the cylindrical combustor illustrated by Figure 5.3 are shown in Table 5.1. This table shows the entry Mach number and combustor efficiency denoted by η_c. SI units for the flow quantities have been provided where appropriate although the validation was kept in the base units (in) of the experiment. The schematic shows a variable-area diffuser, which produces an oblique shock train.

Figure 5.4 illustrates the ratio of wall pressure to total pressure (P_w/P_{T_0}) as a function of distance from the fuel injector. The quasi-one dimensional model used in this investigation with regards to the above assumptions agrees well with the scatter data and produced an average error of 9.3%. The model has been shown from the point of heat addition and assumes constant pressure heat addition in the confined flow within the constant area segment of the combustor.

M_a	3.23	
η_c	0.94	
T_a	1570 $^\circ R$	872 K
P_a	7.47 $psia$	51.5 kPa
A_a	5.89 in^2	3.8×10^{-3} m^2

Table 5.1: Billig's experimental pressure measurements, initial conditions.

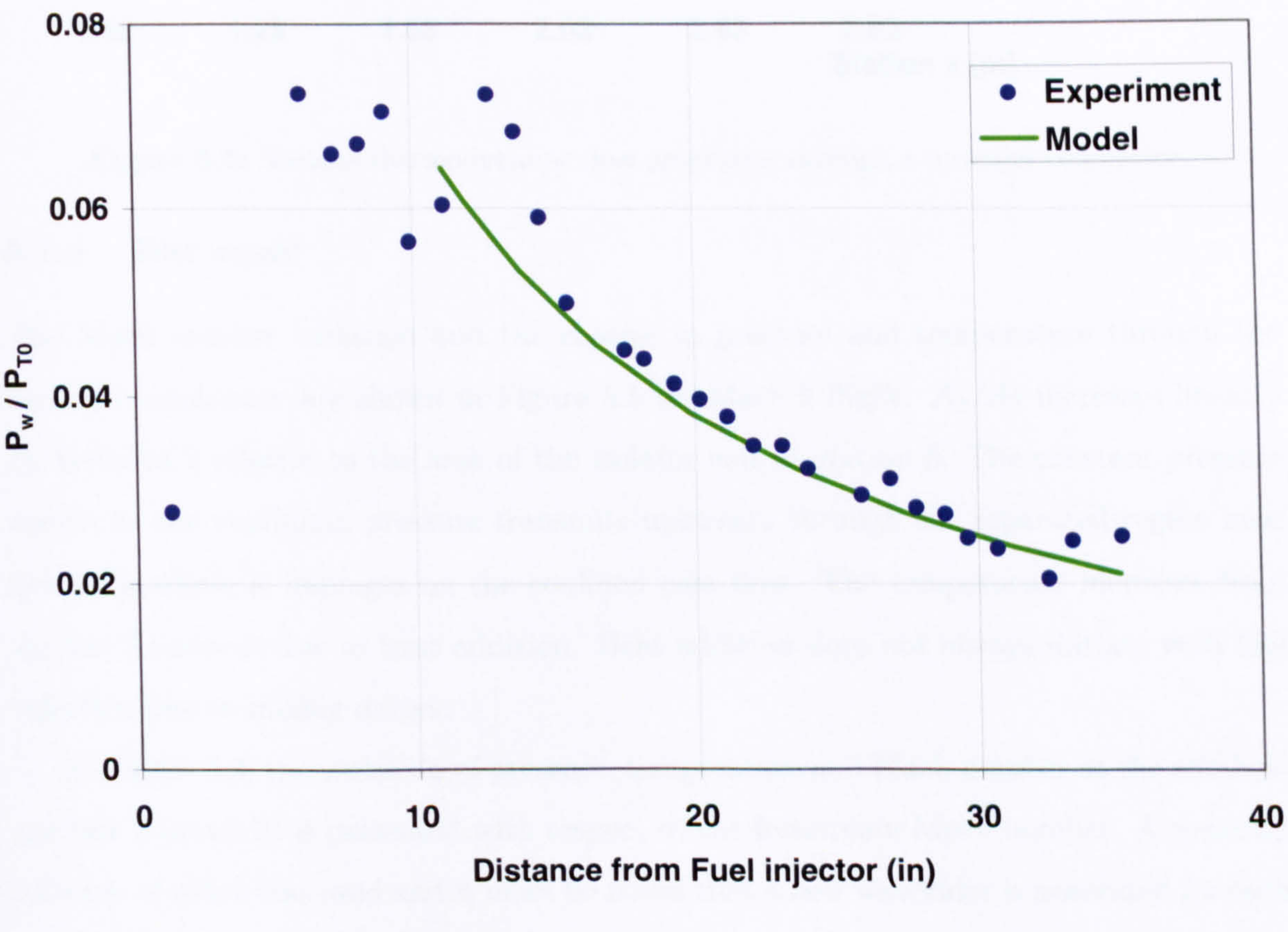


Figure 5.4: Comparison of HICAD's combustor model with the axial pressure distribution from wall pressure measurements of Billig in a cylindrical hydrogen-fuelled scramjet combustor model.

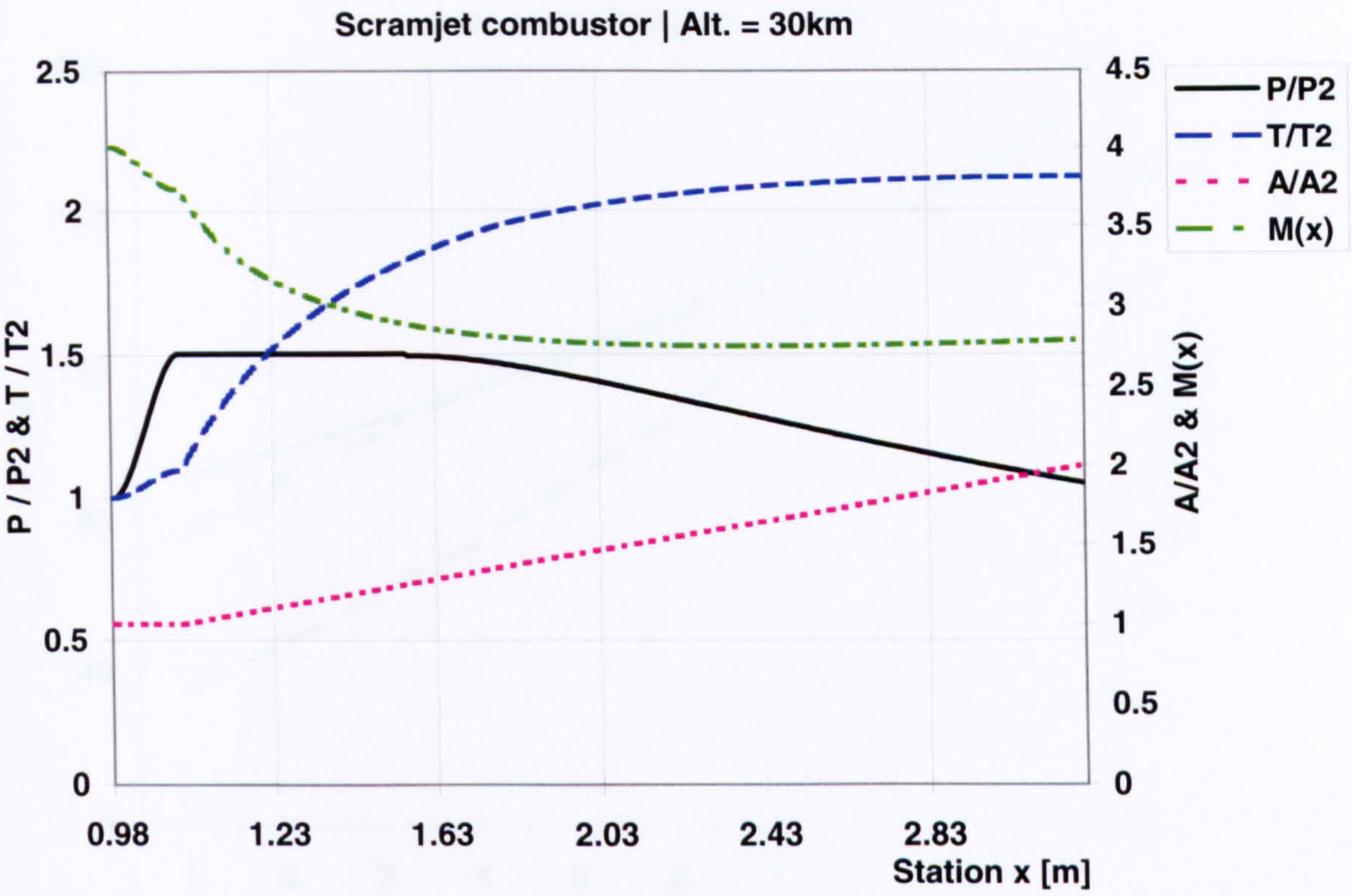


Figure 5.5: Various thermodynamic flow properties through a scramjet combustor.

5.1.4 Test cases

The Mach number variation and the change in pressure and temperature through the scramjet combustor are shown in Figure 5.5 for Mach 9 flight. A_x/A_2 increases linearly by factor of 2 relative to the area of the isolator exit at station 3. The constant pressure occurs as the maximum pressure transmits upstream through the separated region near the walls where it impinges on the confined core flow. The temperature increases from station 3 onwards due to heat addition. Heat addition does not always initiate with fuel injection due to mixing delays.

In Figure 5.6, the variation of pressure, temperature and Mach number at the combustor face (station 3) is presented with respect to the freestream Mach number. A constant altitude of $30km$ was used and it must be noted that a new waverider is generated for each Mach number on the figure such that the points represent on-design, shock-on-lip conditions. The three variables increase with increasing freestream Mach number as expected.

This trend has been extended for a range of Mach numbers and altitudes to represent the variation of combustor entrance pressure and temeperature in the three-dimensional

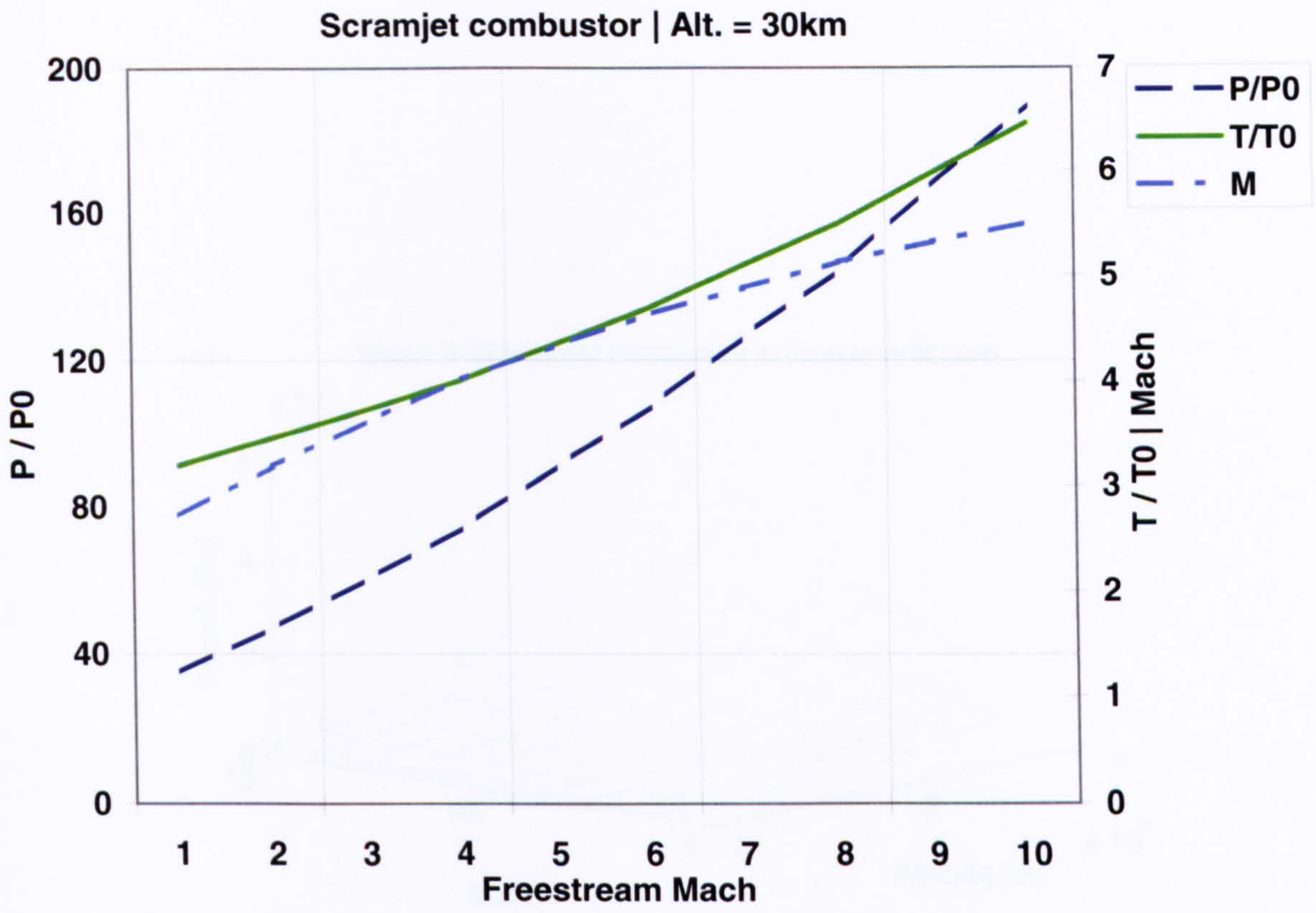


Figure 5.6: On-Design variation of thermodynamic variables and Mach number at a constant altitude at the scramjet combustor face (station 2).

plots in Figures 5.7 and 5.8 respectively.

The entry pressure in Figure 5.7a is shown to increase with increasing Mach number and as expected with the pressure at a maximum at the lower end of the altitude range, that is at sea level. Figure 5.7b shows a contour plot of the maximum pressure occurring at the highest Mach number and lowest altitude. Similarly for the scramjet entry temperature in Figure 5.8a & b, an increase in temperature is noted for increasing Mach numbers with a curvature noted in the contour plot, the minimum of which occurs in the mid-altitude range. As mentioned in §3.4.1, these quantities are constrained to satisfy efficient combustor entrance conditions.

The main components of a scramjet engine include the isolator, combustion chamber and divergent section of the combustor. The inlet and nozzle are then integrated to these components. The isolator determines the cycle efficiency and fuel schedule in a dual-mode scramjet. Practically, the combustor is likely to incorporate a step change in area to accommodate mixers and flame holding devices.

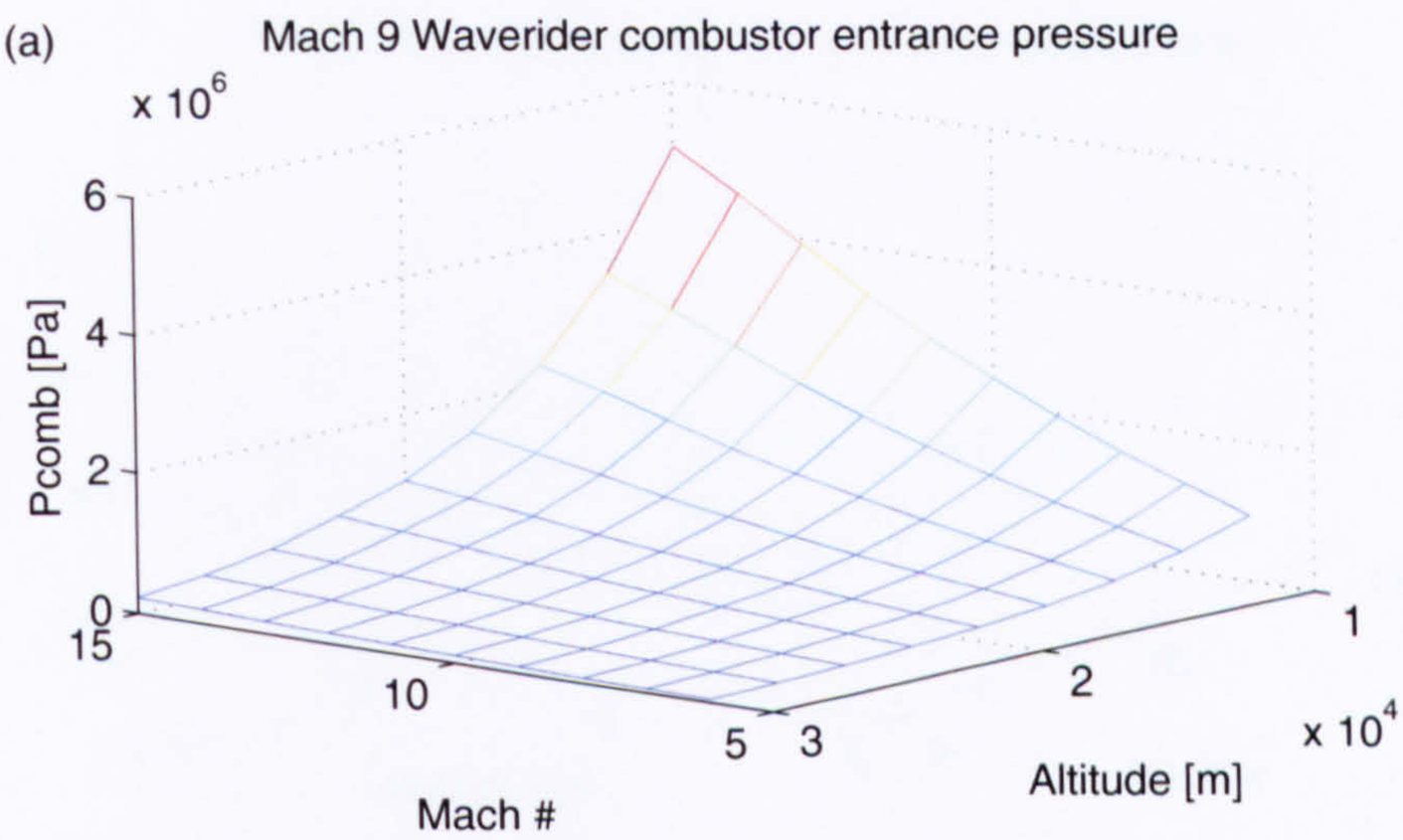
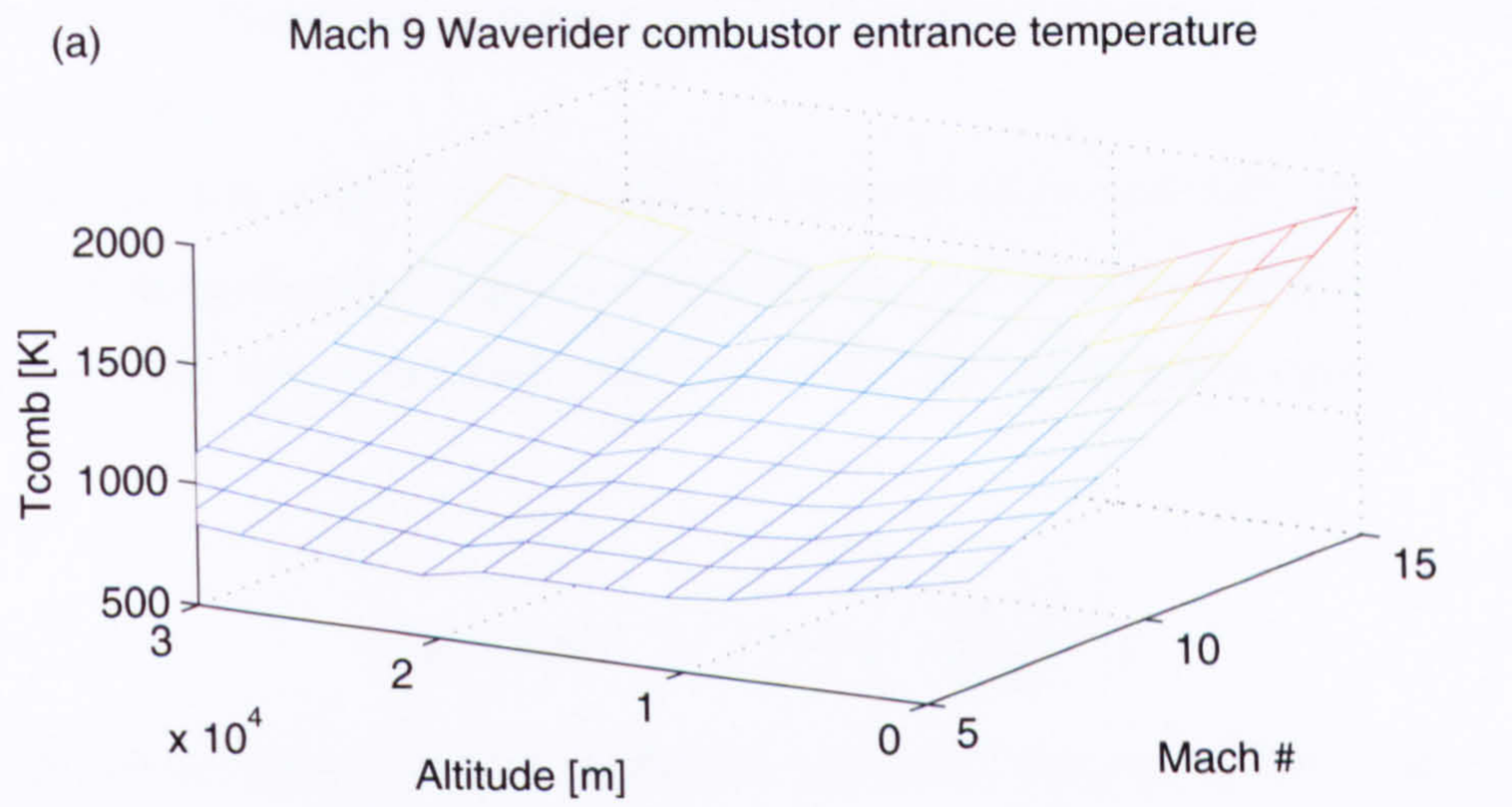


Figure 5.7: a) The variation of combustor entrance pressure, P_2 with a range of Mach numbers and altitudes, b) a contour plot for improved visualisation.



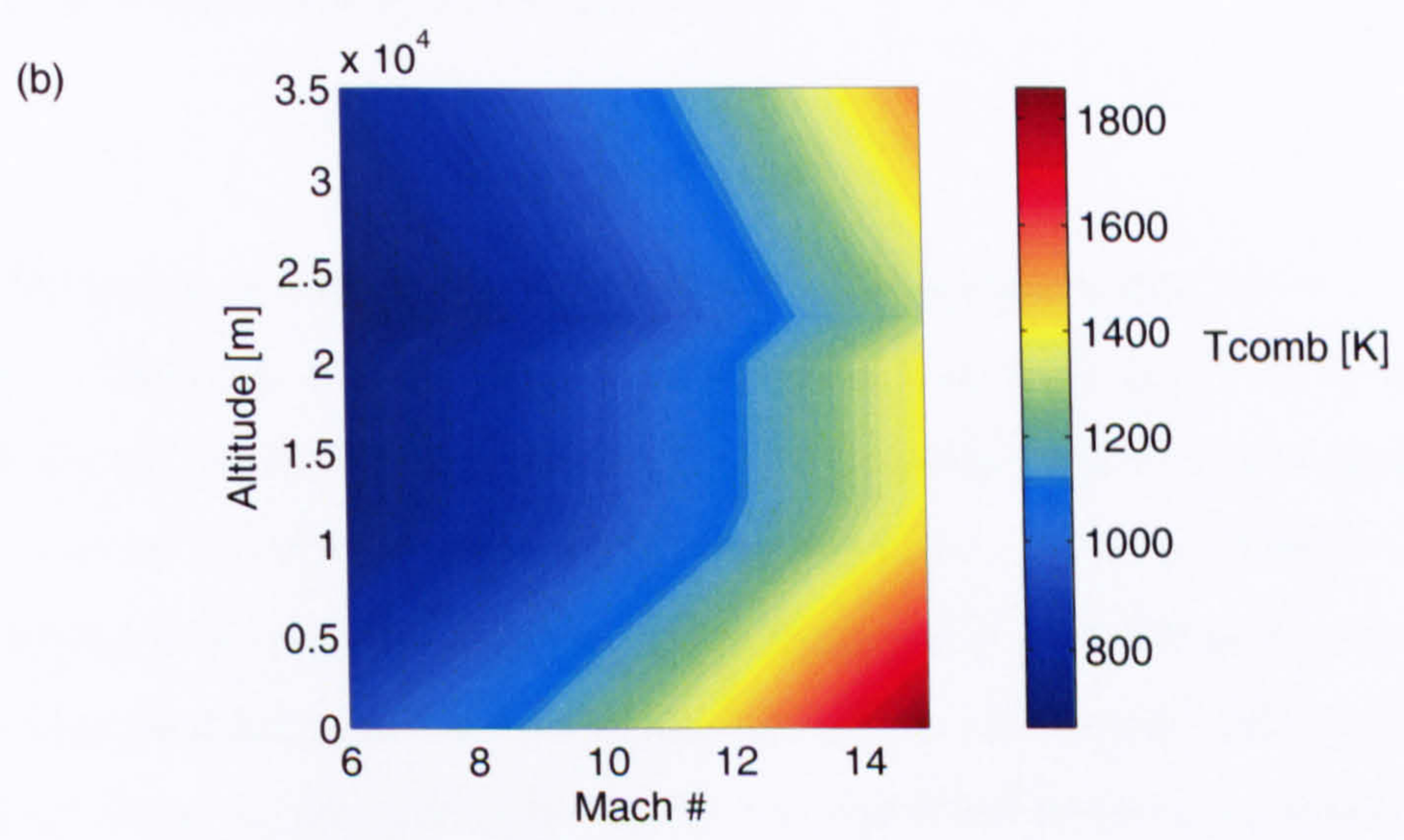


Figure 5.8: a) The variation of combustor entrance temperature, T_2 with a range of Mach numbers and altitudes, b) a contour plot for improved visualisation.

5.2 Fuel-Air Reaction

Achieving useful thrust characteristics in the scramjet combustor hinges upon the proper mixing of hydrogen fuel and high-speed air before the mixture exits the vehicle. The time taken for fuel to be injected, mixed and burned at supersonic speeds is very short; of the order of $1ms$. The study of mixing and reaction is an extremely complex problem in supersonic streams.

The reaction time is given by an empirical correlation proposed by Rogers and Schexnayder (1981) using chemical kinetics. The burning time following self ignition was defined as the time to raise the temperature from 5% to 95% of equilibrium temperature rise given by

$$\tau_R = 3.25e^{-4}p^{-1.6}exp\left(\frac{-0.8 * T_0}{1000}\right) \tag{5.10}$$

Oblique shocks present in the combustor can cause separation, and this can be predicted by using boundary layer separation criteria

$$\frac{M_d}{M_u} < 0.762 \tag{5.11}$$

This relationship is used to approximate for turbulent boundary layers as shown by Billig (1993). Sufficient thrust must be produced to overcome the drag of the vehicle and mixing should occur within a combustor of reasonable length. The length required for mixing can be estimated using empirical correlations given by O'Brien and Lewis ($2001a$). A turbulent boundary layer can cope better with an adverse pressure gradient than a laminar boundary layer before separation occurs (Anderson (1989)). The length for mixing to occur is therefore governed by the condition between separation and the subsequent reattachment process. As described by Ortwerth (2000), ramp mixing is a promising method of dissociating mixing rate from fuel momentum effects. This method uses coaxial jets that develop counter-rotating vortices thereby enhancing mixing. The length of which becomes independent to the freestream conditions. Ortwerth goes on to explain how the base of the ramp can be used as a flame holder.

Fuel injection into the airstream can include either protuberances from the wall (strut-jets or hypermixers) or flush mounted injectors (Anderson and Gooderum (1974)). Both

of which work on the principle of generating strong vortices to expedite mixing. In-stream injection is a better choice even though they lead to increased drag (Ben-Yakar and Hanson (2001)). Fuel is assumed to be injected in the first 10% of the combustor. Flame holding is most challenging at lower Mach numbers around three where the recirculation temperatures are the lowest. This temperature is proportional to the square of the Mach number.

The length of the combustor is calculated based on work by O'Neill (1992) for the time taken for ignition and reaction plus the mixing length. If the combustor length is too long, the takeoff weight increases and specific impulse decreases. The length can not be shorter than required for establishing complete mixing of fuel and air to produce the desired stoichiometric conditions. Since the flows within these combustors are supersonic, the mixing and residence time available for reaction are reduced compared to subsonic combustors. Its length is estimated using an analytical expression for the reaction time as a function of combustor entrance conditions O'Brien and Lewis (2001*b*).

Given that hydrogen fuel is cryogenically stored on the vehicle, it can provide convective cooling to achieve a constant wall temperature of $1000K$ as assumed in this study. Hydrogen is passed through channels from the storage tanks around the leading edges of the hot structure and combustor walls as it provides a good heat sink capacity.

Reliable combustor operation requires continuous ignition to effect flame holding. Ortwerth (2000) mentions that flame holding is provided by a recirculation zone from the separation around a fuel jet.

The compressed air prior to combustion has to be mixed with the fuel injected from protuberances in the wall from a combustor of reasonable length scale. These injectors, however, incur drag and have cooling issues. The requirement of cooling is alleviated by reducing the wetted area inside the combustor and this can be achieved by using multiple fuel-injection struts which will decrease the time for mixing and keep the combustor length to a minimum.

Energy loss in scramjets can occur from the shock wave in terms of the total pressure loss, wall friction and cooling. There are also inherent losses associated with fuel injection, mixing and incomplete combustion and the coupling of them in the scramjet. These, however, have not been adequately modelled in this study due to its increased complexity.

5.3 Supersonic Nozzle

5.3.1 Theory

A nozzle is designed to expand and accelerate the exit combustor flow to static freestream pressure. This provides the forward thrust for the vehicle, which must be equal to or greater than the drag. As with the forebody and combustor, the nozzle is highly integrated with the waverider airframe and two-dimensional designs are chosen for computational simplicity. The length and height of the nozzle, referring again to Figure 4.1, are determined by subtracting the dimensions of the forebody and combustor length from the total vehicle length.

The flowfield of a half-nozzle contour configuration is designed for shock-free, isentropic flow using the two-dimensional Method of Characteristics. The combustor exit flow is treated as steady and irrotational and considered to be uniform across the span of the engine; maintained by holding a constant spanwise upper wall angle.

The contour of the thrust surface of the nozzle is defined by a third order polynomial given by Equation B.6 and is calculated using the available geometric information from the nozzle (See §B.3 for solution), z is the direction along the waverider axis (parallel to combustor exit flow), and x is oriented perpendicular to z. In addition, the contour is dependant on setting the initial and final wall angles. The method is repeated spanwise to complete the exit configuration.

This method calculates a flowfield defined by a mesh composed of characteristic lines which propagate at the Mach wave angle relative to the local flow direction. Along the characteristics, flow properties (P, T, ρ) are continuous and the derivatives are indeterminate. This study considers the on-design flowfield only. Off-design operation includes overexpanded ($p_4/p_0 < Design$) and underexpanded ($p_4/p_0 > Design$). A sharp nozzle corner with angle θ_{wall} at station 4 ensures the nozzle is a minimum length design. The exit angle, θ_{exit} is specified by the user.

Consider the steady, adiabatic, two-dimensional, irrotational flow that is governed by hyperbolic ($M > 1$) [‡] partial differential equations as shown by Anderson (1990). We find

[‡] $M = 1$:parabolic, $M < 1$:elliptic

that two characteristics exist through each point and the slope of the characteristic lines is

$$\left(\frac{dx}{dz}\right)_{C_\pm} = \tan(\theta \pm \mu) \tag{5.12}$$

where θ is the deflection angle of the streamline in xz space and μ is the Mach angle given by $\mu = sin^{-1}(1/M)$. Flow properties are indeterminate along characteristic lines and the algebraic compatibility equation holding along a $C+$ or $C-$ characteristic is

$$K_\pm = \theta \mp \upsilon(M) \tag{5.13}$$

where $K_\pm$ are constants along their respective characteristics, analogous to Riemann invariants Anderson (1990), and $\upsilon(M)$ is the Prandtl-Meyer function at the local Mach number given by .

$$\nu(M) = \sqrt{\frac{\gamma+1}{\gamma-1}} tan^{-1} \sqrt{\frac{\gamma-1}{\gamma+1}(M^2-1)} - tan^{-1}\sqrt{M^2-1} \tag{5.14}$$

At each node along a characteristic line, unit processes govern the nature of the down-stream flowfield depending on where the flowfield is being calculated. The M, θ, $\nu(M)$ are determined using Equations 5.13 and 5.12. This information is used to find the spatial coordinates of x and z using trigonometry. A detailed and informative description of the method is given by Zucrow and Hoffman (1977). The streamline deflection is illustrated in Figure 5.9 for an internal node, showing the characteristic + and − lines. The streamline is curved due to the curvature in the characteristic lines from varying θ and μ.

The exhaust flow is often underexpanded due to the losses incurred during the inlet compression and eventual combustion. To achieve high thrust, correct trim and low system weight, the shape of the nozzle/aftbody needs to be optimised for the available height and length. This is possible within HICAD by varying the nozzle upper wall angle such that the pressure and Mach exiting the nozzle geometry produces a high thrust value.

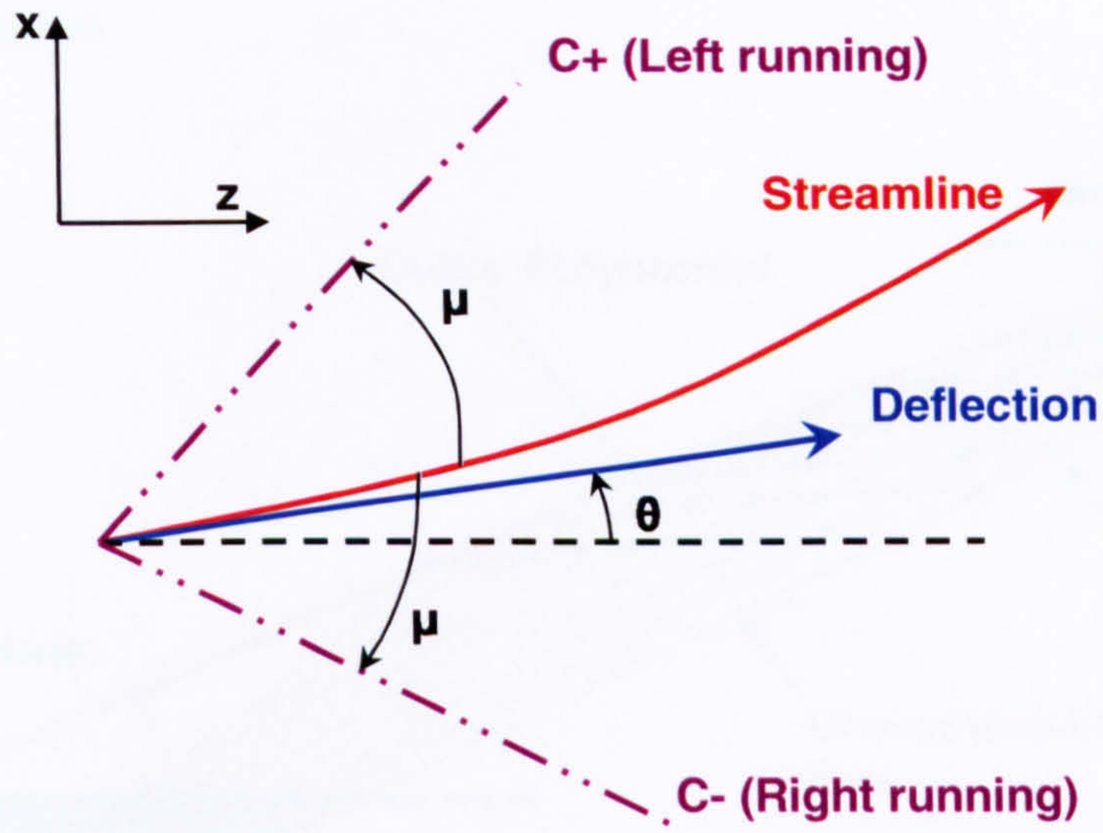


Figure 5.9: Internal unit process of a streamline that has left and right running characteristics lines.

5.3.2 Method

An implementation of `IMOC` - Interactive Method of Characteristics, developed by Jacobs (2004), has been used in the present work to enable calculation of an expansion flowfield. A user-script is required, which should specify the length and orientation of the thrust- and lower surface, entry Mach number, specific heat ratio etc. A flowfield of a mesh of nodes evolves progressively downstream using initial conditions at the sharp corners and adjacent $C-$ and $C+$ characteristic directions until the trailing edge is reached. A dynamic linked library (`.dll`) in `IMOC` handles the data storage, house-keeping and unit processes.

`IMOC`'s technical routines are written in `C` and the `Tcl` language is used to wrap these functions. The `Tcl/Tk`[§] interpreter allows customisation of the user-specified input script to provide a convenient form for additional functions. A GUI front end is provided in `IMOC` that provides a menu selection and data-entry fields and results in a visual representation of the mesh as it evolves.

For the present study, the original `C` files have been integrated within `HICAD` to bypass the GUI such that inflow conditions can be automatically computed in `HICAD` without reverting to an additional compiler/software. This prevents breaking the design cycle and

[§]http://www.tcl.tk/scripting/

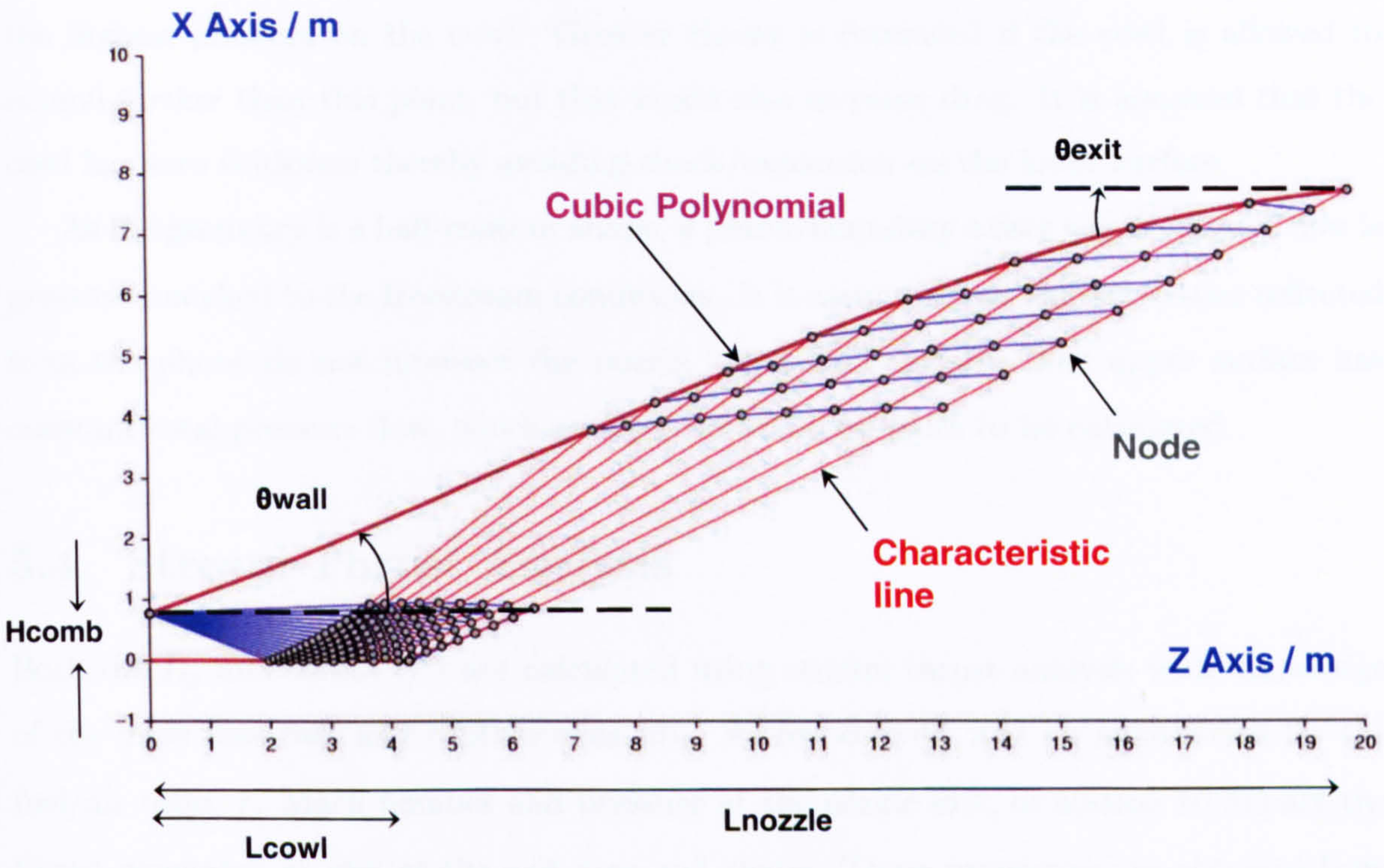


Figure 5.10: Expansion net comprising nodes and characteristic lines.

enhances computational flexibility by using `HICAD` as the base operator.

An example two-dimensional mesh for a Mach 9 waverider using `IMOC` as a standalone code is illustrated in Figure 5.10. The nozzle has an entry Mach number of 2.77 and specific heat value of 1.24. The nozzle length was $19.2m$ for a $64m$ waverider and upper wall expansion angle was 19°.

By maximising H_{nozzle} and L_{nozzle}, the greatest thrust for that geometry is produced. In addition, θ_{exit} can be changed to vary the trailing edge parameters. θ_{wall} is varied iteratively until the maximum available height is achieved. The performance of the propulsion system can be determined in terms of thrust and I_{sp}.

Two centred expansion fans will later be shown to define the nozzle flowfield; one emanating from the upper wall (shown above) and the other is the cowl chamfer with a set angle of 6° as given by Small *et al.* (1976). For mathematical simplicity, it is assumed that the exhaust flow is perpendicular to station 4 and 10. The upper wall angle is allowed to vary iteratively until the boundaries of the nozzle are achieved. The location of the cowl extension into the nozzle is set by the first characteristic emanating from the upper wall. This is the minimum distance the cowl can extend into the nozzle flowfield and maintains

the highest pressure on the cowl. Greater thrust is produced if the cowl is allowed to extend further than this point, but this would also increase drag. It is assumed that the cowl has zero thickness thereby avoiding shock/expansion on the lower surface.

As the geometry is a half-contour shape, a plume boundary exists where exhaust flow is pressure-matched to the freestream conditions. It is assumed that characteristics reflected from the plume do not intersect the nozzle upper wall surface. The upper surface has constant total pressure flow, which enables the static pressure to be calculated.

5.4 Stream-Thrust Analysis

Both the I_{sp} and thrust (F) are calculated using stream thrust analysis with knowledge of the mass flow rate and capture area, $\dot{m}_0$, A_0 respectively and an assumption for the fuel/air ratio, f. Mach number and pressure at the nozzle exit, or station 10 impact the thrust generated as well as the exit area and shape. These properties are obtained from the Method of Characteristic analysis.

Hydrogen will, however, require a larger volume for storage due to its lower density. Combustor length is estimated using an analytical expression for the reaction time (O'Brien and Lewis (2001*a*)) and complete mixing must occur within this length (reduced compared to subsonic flow).

The following quantities at the entrance to the nozzle include the Mach number, pressure, temperature and velocity at station 4 according to Figure 4.1. In addition, the Mach number at the exit to the nozzle is known at station 10 from the nozzle method of characteristics analysis. Using M_{10}, the pressure, temperature and velocity can be determined using isentropic relations given in Appendix A, at station 10. The stream thrust analysis then follows accordingly using the formulation of Heiser and Pratt (1994).

The stream-thrust function, S_a, uses the boundary between internal and external flow, which coincides with maximum mass capture and maximum exhaust flow area as represented in Figure 5.11.

The installed thrust is found from eliminating total vehicle surface drag that will be presented later. Stream thrust function, Sa_0 at the compression stage is given by

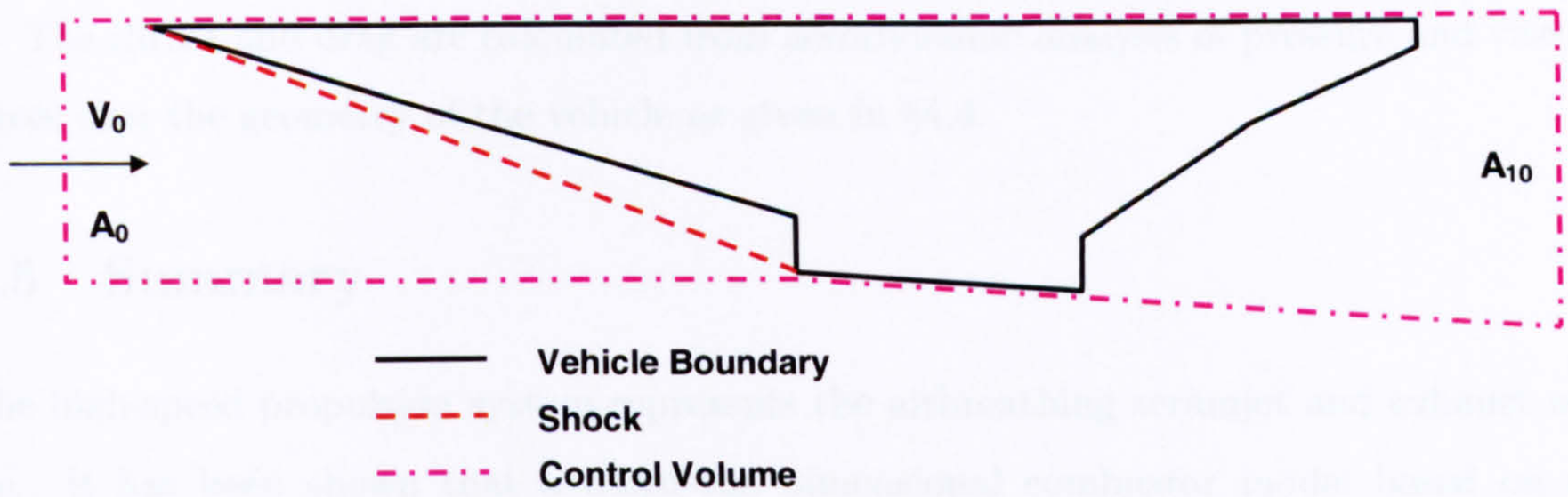


Figure 5.11: Control Volume for uninstalled performance estimation where $A_{10} > A_0$.

$$Sa_0 = V_0\left(1 + \frac{RT_0}{V_0^2}\right) \tag{5.15}$$

where $R = 289(m/s)^2/K$ and similarly at station 10

$$Sa_{10} = V_{10}\left(1 + \frac{RT_{10}}{V_{10}^2}\right) \tag{5.16}$$

The specific thrust, $F/\dot{m}_0$, can then be calculated using the following equation

$$\frac{F}{\dot{m}_0} = (1+f)Sa_{10} - Sa_0 - \frac{R_0T_0}{V_0}\left(\frac{A_{10}}{A_0} - 1\right) \tag{5.17}$$

where the symbols have their usual meaning and $g = 9.81m/s^2$; the gravitational acceleration. The specific impulse is calculated using

$$Isp = \frac{F/\dot{m}_0}{f * g} \tag{5.18}$$

I_{sp} is the amount of thrust you get for the weight of fuel you burn, and has been introduced to describe propulsive efficiency of engine units, which generate thrust by expelling mass. It is an order of magnitude greater for airbreathers than rocket engines. Hydrogen is the preferred fuel at hypersonic Mach numbers due to its high performance yield, low molecular weight, producing high I_{sp} due to the higher heating value compared to hydrocarbon fuels and rapid ignition, reaction and combustion. `HICAD` could potentially incorporate different fuels by allowing the user to change the heating value.

Thrust is generated by burning hydrogen inside the scramjet. At a particular flight velocity, drag is incurred on the vehicle as a function of altitude.

The thrust and drag are calculated from aerodynamic analysis of pressure and viscous forces over the geometry of the vehicle as given in §4.4.

5.5 Summary

The high-speed propulsion system represents the airbreathing scramjet and exhaust nozzle. It has been shown that a quasi-one dimensional combustor model based on the continuity equation, is used to determine the axial variation of flow properties through a linearly-expanding scramjet system. An oblique shock train is contained by the isolator to prevent inlet unstart and its length is estimated using an empirical correlation. The isolator permits dual-mode operation of a ramjet/scramjet cycle depending on flight altitude and speed. A constant-pressure combustor with a 2:1 expansion ratio represents the burner with $\gamma_b = 1.36$. Its length is based on complete mixing of air and fuel. The design of the nozzle is facilitated by an implementation of the two-dimensional method of characteristics routine, `IMOC`, whose module functions have been integrated within `HICAD`. This enhances flexibility of the geometry-specification due to the highly integrated nature of the propulsion system. In the next chapter, the main components of the low-speed propulsion system will be addressed.

6

Low-Speed Propulsion

The principal components of a turboramjet will be addressed in this chapter, with regards to the flowpath and inlet required to generate sufficient thrust. It has been mentioned previously, that a TBCC engine is required to address the low-speed flight regime, that is, between takeoff / landing and Mach 5. As a comparison, consider also the ram-effect of the P&W J-58 engine, which employed bypass flaps to block the flow from the turbine during high-speed operation thereby operating like a ramjet. This engine powered the SR-71 to Mach 3+ speeds.

The design characteristics of the inlet are mainly determined by whether the aircraft will fly at subsonic or supersonic speeds, the required flight envelope and off-design angles-of-attack the aircraft will experience. The inlet should compress oncoming air for high total pressures with small variations in total temperature and pressure. A four-ramp variable geometry planar inlet is used to compress the freestream air for efficient combustion.

6.1 Turboramjet

A turboramjet combines the best features of a turbojet and ramjet into a single engine with potential capability of Mach 5+ flight. The performance was calculated using one-dimensional idealised cycle analysis based on the formulation by Heiser and Pratt (1994) that assumes no friction or heat transfer to the walls and the flow is treated as steady and compressible. The turboramjet generates static thrust at takeoff and subsonic speeds by

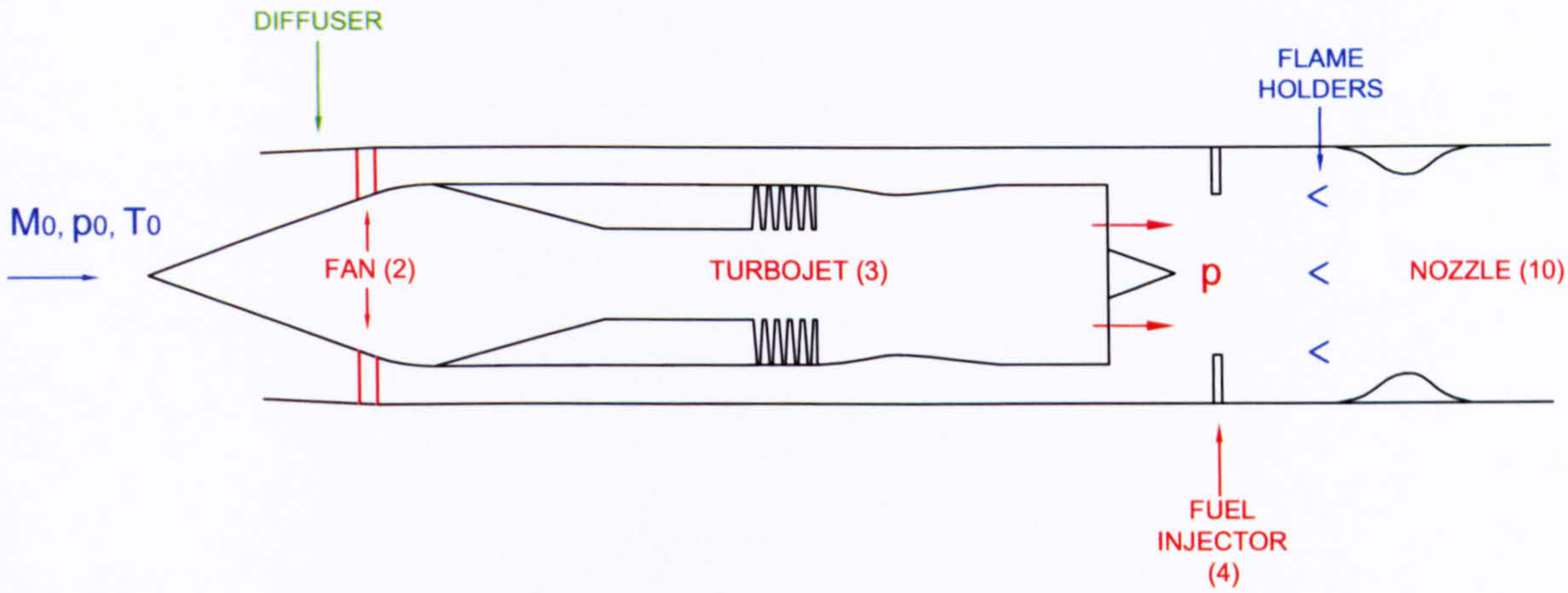


Figure 6.1: Schematic of an axisymmetric turboramjet.

mechanically compressing the air for stable combustion of fuel. The principal components of the axisymmetric turboramjet, are illustrated in Figure 6.1. This level of analysis is deemed suitable for the preliminary level of design especially during the development stage of the `HICAD` methodology.

A turbojet is positioned in the core of the turboramjet, which produces high temperature and pressure gases. The flow here is referred to as the primary stream, p, and its operation is independent to the flight altitude. The turbines provide the power to the fan inlet to enable compression of the freestream air. The flow is treated as isentropic without losses. Complete mixing of the outer airflow and primary stream occurs at the turbine exit when additional unreacted fuel is injected as shown, before it reaches the burner and flameholders. The injection of fuel can be considered analogous to afterburning in Turbojets. The total temperature of the flow increases and expands isentropically to the freestream static pressure.

6.1.1 Cycle Analysis

The static pressure of the airflow and primary flow through the turbojet are equal. By equating the mixer with the main burner, fuel can be burned from the primary flow. The influence of the fan on the airflow is defined by the total pressure ratio

$$\pi_F = \frac{p_{t3}}{p_{t2}} \tag{6.1}$$

The method requires inputs in `HICAD` for total pressure and temperature p_{tp}/p_0 and

T_{tp}/T_0, as a function of the primary flow respectively, where 0 represents freestream flow. The choices of these variables form part of an optimisation procedure that results in suitable values until the desired I_{sp} and thrust are achieved for the $M_0 = 5$ scramjet transition speed.

The bypass ratio, α, defined as the ratio of the airflow from the fan to the primary flow, is determined using the following Equation

$$\alpha = \frac{T_{tp}}{T_0}.\frac{T_0}{T_{t0}}\left(\frac{1-(\pi_F.\frac{p_{t0}}{p_0}.\frac{p_0}{p_{tp}})^{\frac{\gamma-1}{\gamma}}}{\pi_F^{\frac{\gamma-1}{\gamma}}-1}\right) \tag{6.2}$$

When the M_0 becomes large, α eventually reaches zero as shown in Figure 6.2. Values for p_{tp}/p_0 and T_{tp}/T_0 are indicated on the figure for conditions at sea-level. It is assumed that π_F remains constant for the turboramjet analysis from given literature. This occurs when the quantity $\pi_F(p_{t0}/p_0) = p_{tp}/p_0$ in the numerator of Equation 6.2. At this point the device is considered to behave like a rocket as the flow is entirely due to the primary flow and so airbreathing performance measures such as $F/\dot{m}_0$ are no longer valid. For the purpose of this study, this is considered to be the operating limit of the turboramjet model.

To delay α reaching zero and to achieve $M_0 = 5$, the military specification (MIL-E-5008B), given by p_{t2}/p_{t0} in Equation 6.3, for total pressure recovery is applied to the analysis for the range of supersonic Mach numbers.

$$\frac{p_{t2}}{p_{t0}} = 1 - 0.075(M_0 - 1)^{1.35} \tag{6.3}$$

With reference to Figure 6.2, the bypass ratio is non-zero for longer when p_{tp}/p_0 and T_{tp}/T_0 are increased. This permits better airbreathing performance for higher Mach numbers. The corresponding values are indicated in the insert of this Figure.

A similar favourable effect on the performance is achieved during the diminishing P_0 that accompanies flying at increasing altitudes. This further increases the value of p_{tp}/p_0 and T_{tp}/T_0 and has a favourable effect for higher Mach numbers under turboramjet power. For a given thrust generated by the scramjet, an equivalent thrust must be produced by the turboramjet to ensure a continuous transition when sizing the turboramjet. This is achieved by varying the low-speed engine parameters within specified constraints, which include a peak value of $I_{sp} = 4000s$ from available literature.

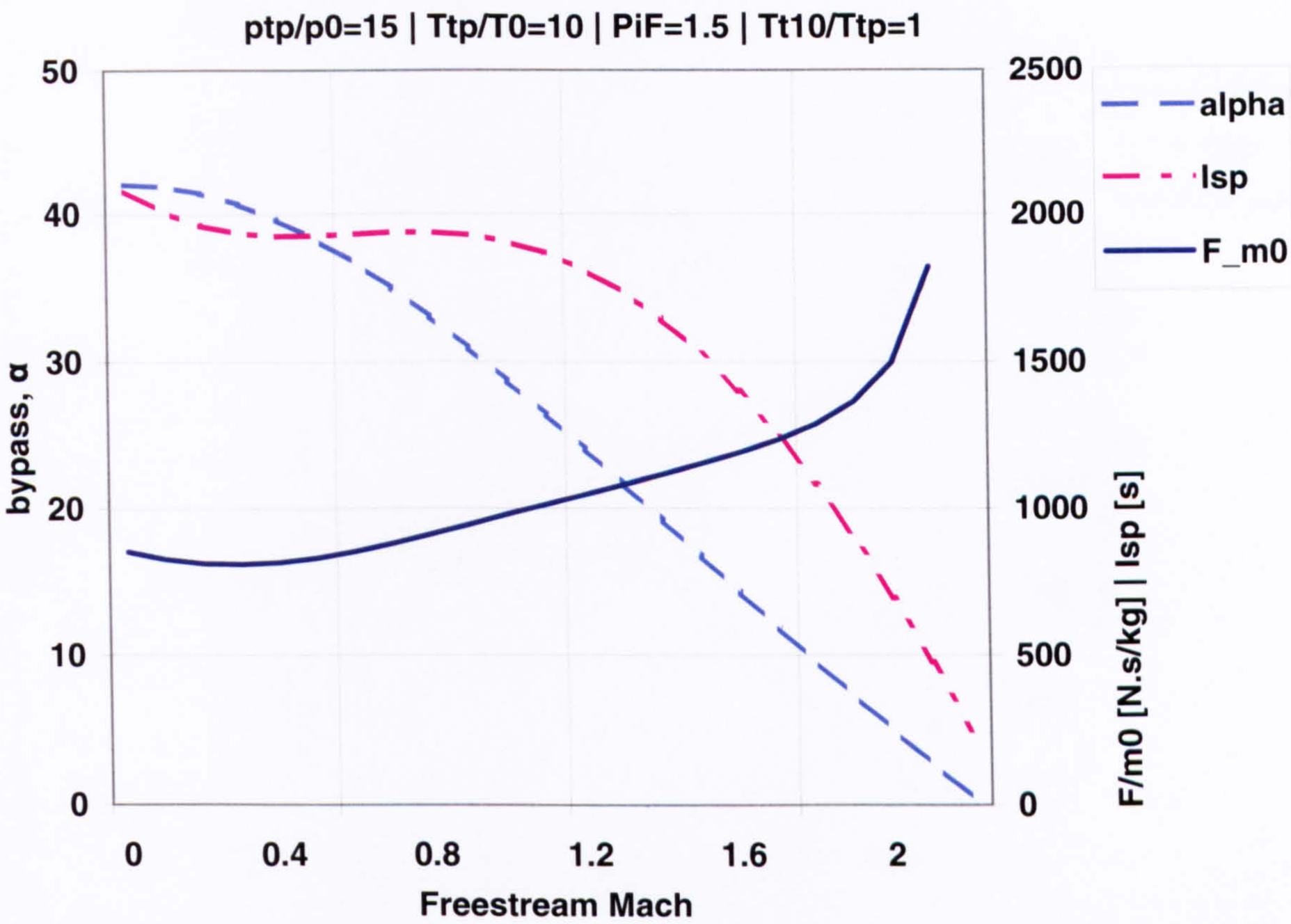


Figure 6.2: Performance of an idealised turboramjet at sea level: α tends to zero around Mach 2.

This in turn provides data for $F/\dot{m}_0$ as a function of h. The turboramjet $F/\dot{m}_0$ is found at the desired scramjet transition point at $M_0 = 5$ and $h = 30km$ and a value for $\dot{m}_0$, is determined in order to achieve the desired thrust in Newtons for the scramjet, which is also dependent on the number of engines. As a result of the optimisation that will be discussed later, the bypass ratio can be made to be non-zero up to Mach 5 by allowing the pressure to change by flying along a constant dynamic pressure trajectory of 1000 lbf/ft^2 ($47880N/m^2$) for example. See Figure 6.4.

The design $\dot{m}_0$ can not be too large else the inlet size $A_{0_{ref}}$ becomes excessive. I_{sp} is a function of the specific thrust given by Equation 6.4 where g_0 is the gravitational acceleration.

$$I_{sp} = \frac{1}{g_0\left(f + \frac{1}{\alpha}\right)} \cdot \frac{F}{\dot{m}_0} \tag{6.4}$$

HICAD calculates $F/\dot{m}_0$ between $0 \leq M \leq 5$ at the hypersonic cruise altitude, h, which determines a value for the $\dot{m}_0$ required for smooth thrust transition at Mach 5 to

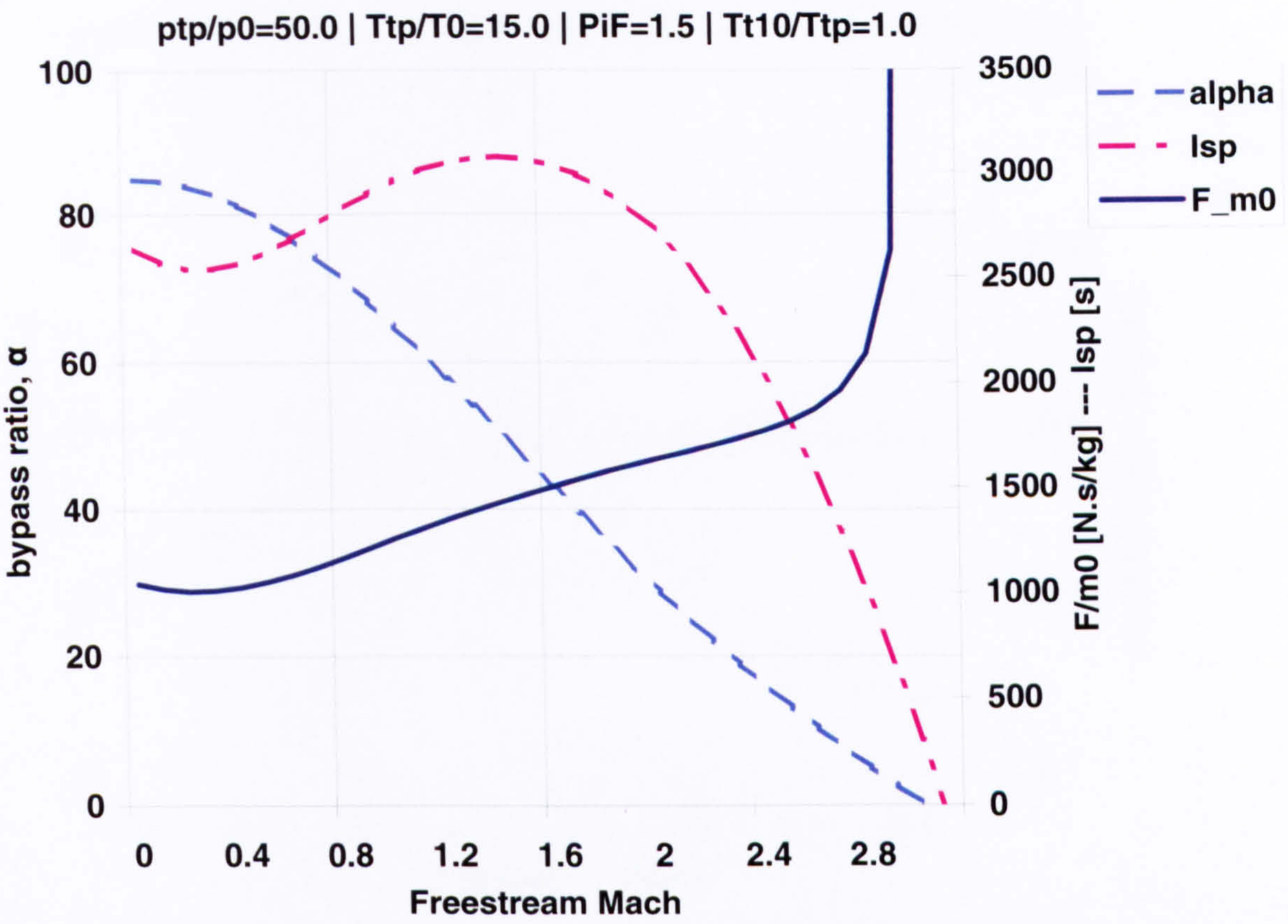


Figure 6.3: Performance of an idealised turboramjet at sea level: α remains positive for longer thereby permitting airbreathing operation to higher Mach numbers.

the scramjet. An inlet must be designed that incorporates variable geometry producing good total pressure recovery according to Equation 6.3 over the Mach range from brakes release to Mach 5 transition point. The inlet size is determined from the design M_0, h and $\dot{m}_0$ variation with h, using an external code that is integrated with `HICAD`. The required area ratio with respect to the design A_0 is plotted for different altitudes, and the most demanding $\dot{m}_0$ and h values are used to size the inlet. For the majority of cases studied that point was at Mach 5 / cruise altitude transition to scramjet mode. Once the inlet size and ramp angles are determined for the off-design conditions, fuel and other systems are accommodated into the vehicle's volume.

Several parameters can be adjusted within `HICAD` for desired results thereby demonstrating the codes flexibility. These include, number of turboramjet engines, compressor pressure ratio, inlet total temperature, specific heat ratios and various component efficiencies. Any changes to these parameters significantly influences the performance. The reference area is constrained to not exceed the waverider forebody limits.

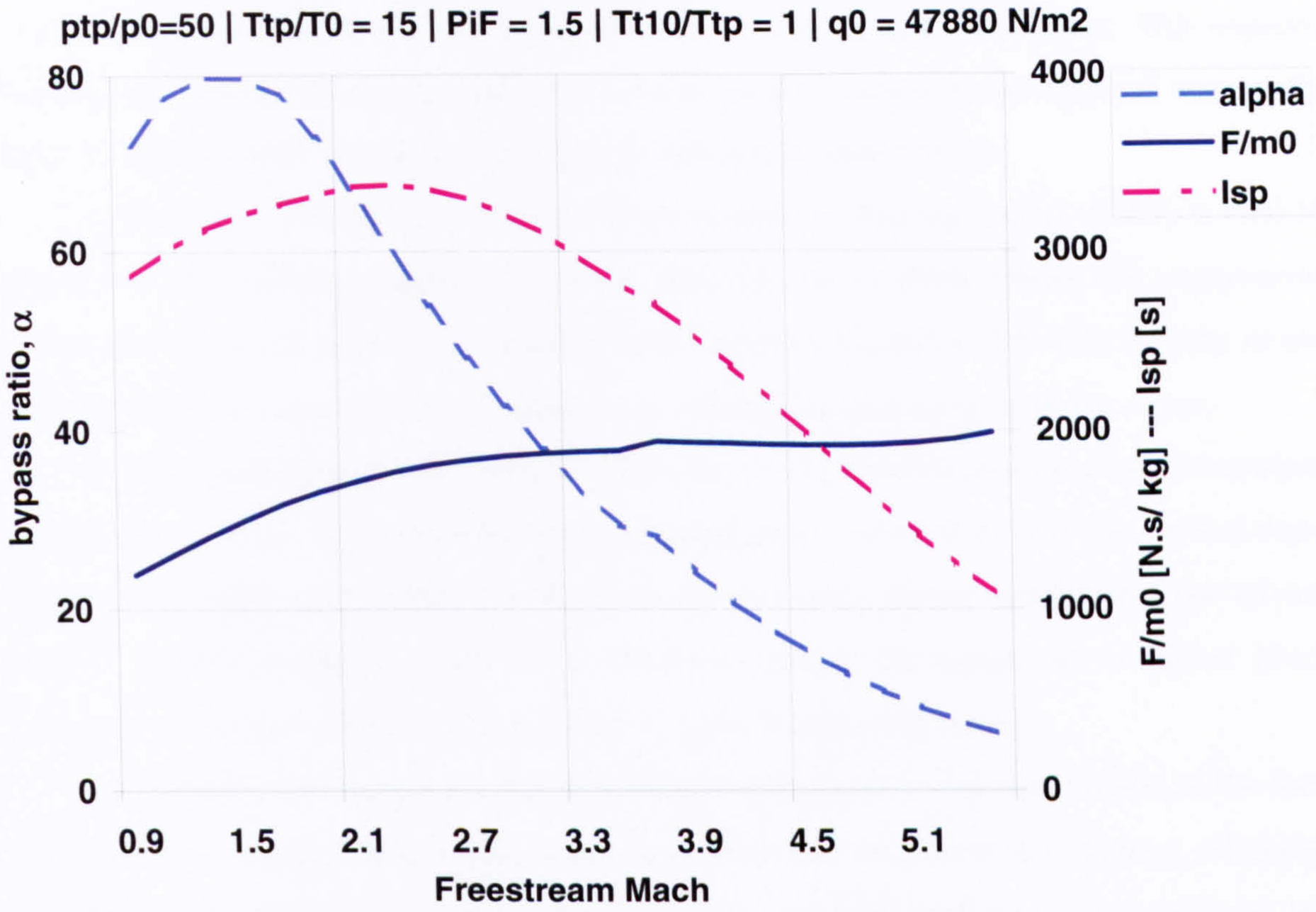


Figure 6.4: The limit of the air-breathing segment indicated by the bypass ratio tending to zero at Mach 5 and a higher altitude.

6.2 Low-Speed Inlet Design

Once the performance data of both the high-speed and low-speed propulsion system have been acquired, it is necessary to design a low-speed inlet system that will deliver sufficient air flow for smooth transition between the two engines. A range of Mach numbers will be encountered during low-speed operation and a variable-geometry inlet system will need to account for changes in inlet area to maintain shock-on-lip for maximum mass capture. As thrust is directly related to the quantity of air ingested by the engine, inlet size and operation directly affects turboramjet performance.

The external compression inlet should: a) provide the necessary airflow for the turboramjet from low subsonic to high supersonic flight conditions at all altitudes considered, (b) deliver high inlet total pressure recovery, η_R, over the desired flight speed range while maintaining shock-on-lip and sonic throat conditions (c) ensure off-design conditions are fully met and (d) minimise losses. In particular, the defined inlet should provide the nec-

essary mass flow, $\dot{m}_0$, to achieve the desired thrust for scramjet transition. This requires variable geometry, which may increase vehicle weight, although this type of supersonic inlet design can take advantage of simple compressible flow theory.

An off-design cycle analysis code, `OFFX` developed by Mattingly *et al.* (1987) is used to determine the corrected engine air flow vs. both M_0 and h. `OFFX` defines the requirement of the inlet in terms of its total pressure ratio based on Equation 6.3. The validity of the code, is based on assumptions of component efficiencies and total pressure ratios.

The low-speed inlet system consists of four successive variable geometry two-dimensional compression ramps. This was selected to generate good values of η_R over the desired flight speed range while maintaining the shock-on-lip and sonic throat conditions. The advantage of variable geometry inlets is the ability to reduce the bypass air at higher Mach numbers by sizing a lower engine leading to lower installation losses.

An additional two ramps provide preliminary compression and they consist of the forebody and subsequent ramp angle, which are illustrated in Figure 4.1. During off-design operation, the variable geometry ramps move to maintain minimum flow spillage and increased pressure recovery thereby preventing boundary layer separation and excessive heating as explained by Seddon and Goldsmith (1985). The width of the inlet is set by W_{eng} and the length is a function of the ramp angle and calculated using trigonometric relations. A planar inlet system is considerably simpler to design and analyse over axisymmetric types and was therefore selected in this study.

The arrangement of the ramps and corresponding shocks are illustrated in the schematic of Figure 6.5, where the shock at station 5 is a terminating normal shock.

This figure represents on-design operation or critical mode, where the fraction of air spilled around the inlet is a minimum. During this condition, the normal shock sits just inside the cowl lip. During off-design operation, the area $A_{0_i} < A_1$. The shock angles can be determined using Equation A.11.

During off-design operation, the shocks are no longer attached to the cowl lip and variable geometry becomes necessary. In the unstart condition, a normal shock appears in front of the inlet, leading to increased flow spillage and reduced stagnation pressure inside the throat, this is known as subcritical operation. Supercritical operation occurs when the corrected mass flow as the design point, is not sufficient and the normal shock is pushed

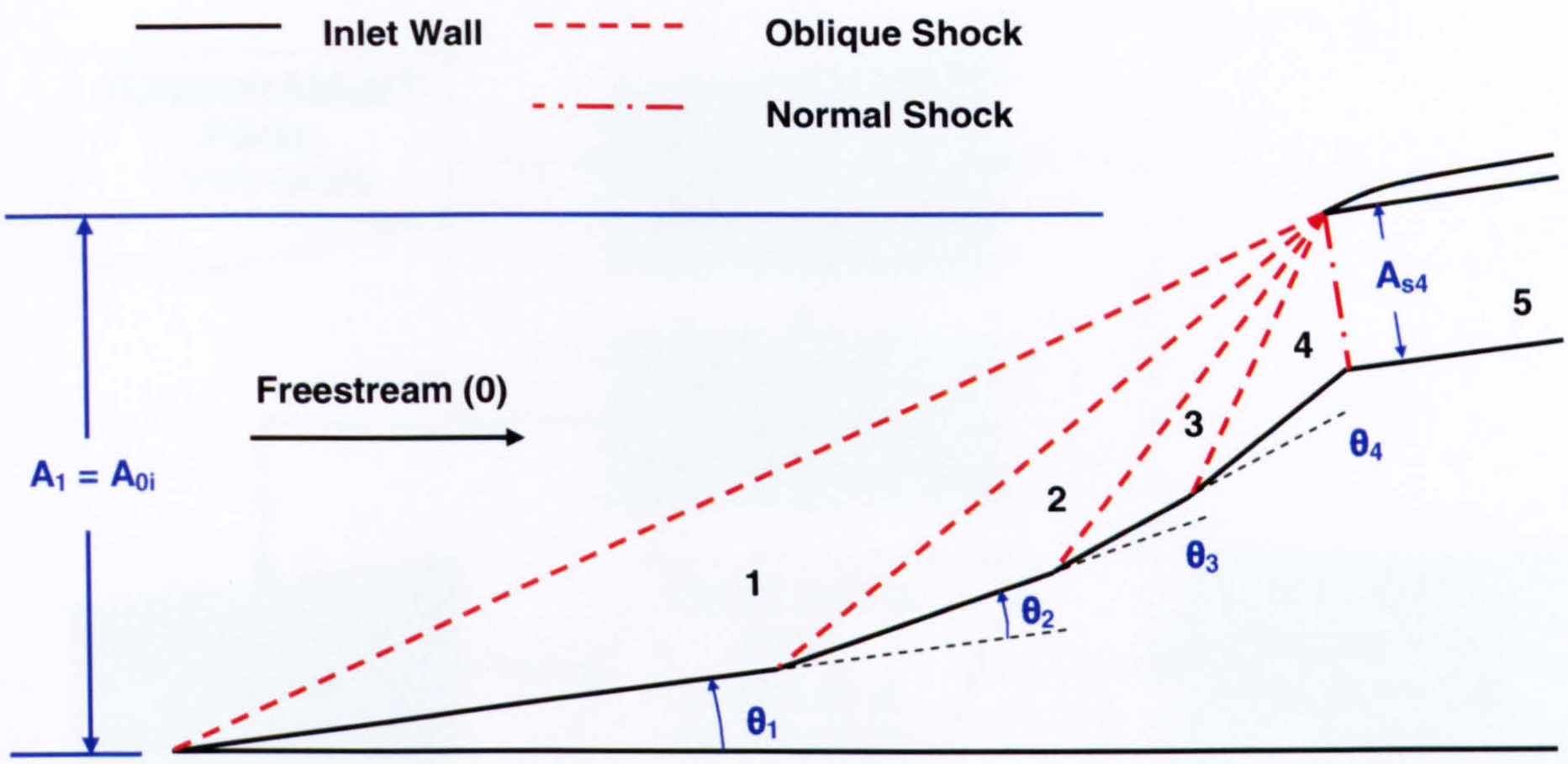


Figure 6.5: On-Design operation of a turboramjet inlet system (not to scale) illustrating a four-ramp arrangement that generates four-oblique shocks and a terminating normal shock at station 5.

downstream of the throat leading to poor engine performance.

An excessive inlet turning angle will be prone to an adverse pressure gradient causing separation and undesired boundary layer/shock interactions. This would lead to reduced performance and inlet unstart.

6.2.1 Calculation Procedure

Figure 6.6 illustrates the computational steps required to design the low-speed inlet.

After initialising the user-interface, first the on-design properties must be selected that includes inputs, for Mach number, altitude, compressor pressure ratio amongst many others. The first stage of the calculation then invokes the Turboramjet subroutine for a single design-point calculation. The calculated performance attributes are then written to a reference file that forms the input to operate the off-design cycle analysis code, `OFFX` by Mattingly *et al.* (1987). The reference file is made up of about 150 variables. Additional user-selected variables include $\dot{m}_0$, which determines the reference area, A_{0ref}.

Through `HICAD`'s interface, the user can select the off-design options and for the purpose of inlet design, this will include a selection for the off-design altitude and range of Mach numbers to be tested. Along with these selections accompanied by the reference file, `OFFX` calculates several quantities, the most important of which is the variation of mass flow.

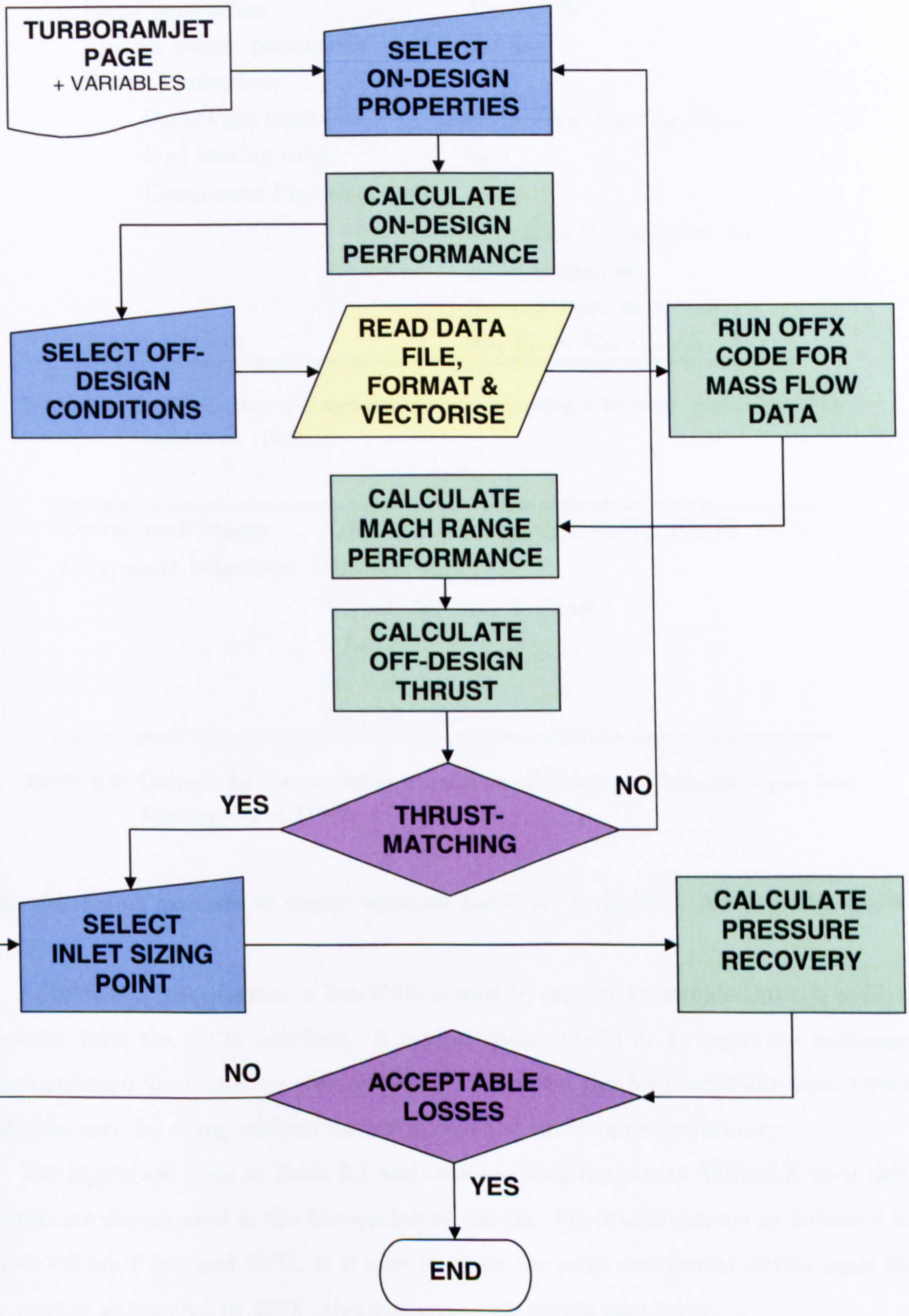


Figure 6.6: Program flow chart for thrust-matching and low-speed inlet design.

Flight parameters	M_0, T_0, P_0
Aircraft system parameters	β, C_{TO}
Design Limitations	
Perfect gas constants	γ_c, γ_t, γ_{AB}, C_{pc}, C_{pt}, C_{pAB}
Fuel heating value	h_{PR}
Component Figures of merit	ϵ_1, ϵ_2
	π_b, π_{dmax}, π_{Mmax}, π_{AB}, π_n
	$\varrho_{c'}$, ϱ_{cH}, ϱ_{tH}, ϱ_{tL}
	η_b, η_{AB}, η_{mL}, η_{mP}, η_{mH}
Design Choices	$\pi_{c'}$, π_c, α, T_{t4}, T_{t7}, M_5, P_0/P_9

Table 6.1: Inputs for the on-design calculation addressing a Turbojet engine from Mattingly *et al.* (1987).

Overall performance	F/m_0, SFC, f_0, η_p, η_{TH}, V_9/V_0, P_{t9}/P_9, T_9/T_0
Component behaviour	π_{tH}, π_{tL}, π_M
	$\tau_{c'}$, τ_{cH}, τ_{tH}, τ_{tL}, τ_λ, $\tau_{\lambda AB}$
	f, f_{AB}
	$\eta_{c'}$, η_{cH}, η_{tH}, η_{tL}
	$M_{5'}$, M_6, M_9

Table 6.2: Outputs for the on-design calculation addressing a Turbojet engine from Mattingly *et al.* (1987).

This calculation assumes an engine selection based on Turbojet + Afterburning engine equations.

As OFFX is a DOS program, a batch file is used to capture keystrokes through options available from the HICAD interface. A typical option would be to input the minimum plus maximum Mach number and step size and to repeat this for several altitudes. Other variables used for sizing analysis include π_c and the fan compressor ratio, $\pi_{c'}$.

The inputs are given in Table 6.1 and corresponding outputs in Table 6.2; their definitions are documented in the Nomenclature section. Important outputs as indicated in Table 6.2 are $F/\dot{m}_0$ and SFC. It is important for the order and format of this input file be exactly as required by OFFX otherwise erroneous results may occur.

Continuing with the calculation procedure, the Turboramjet subroutine is called to

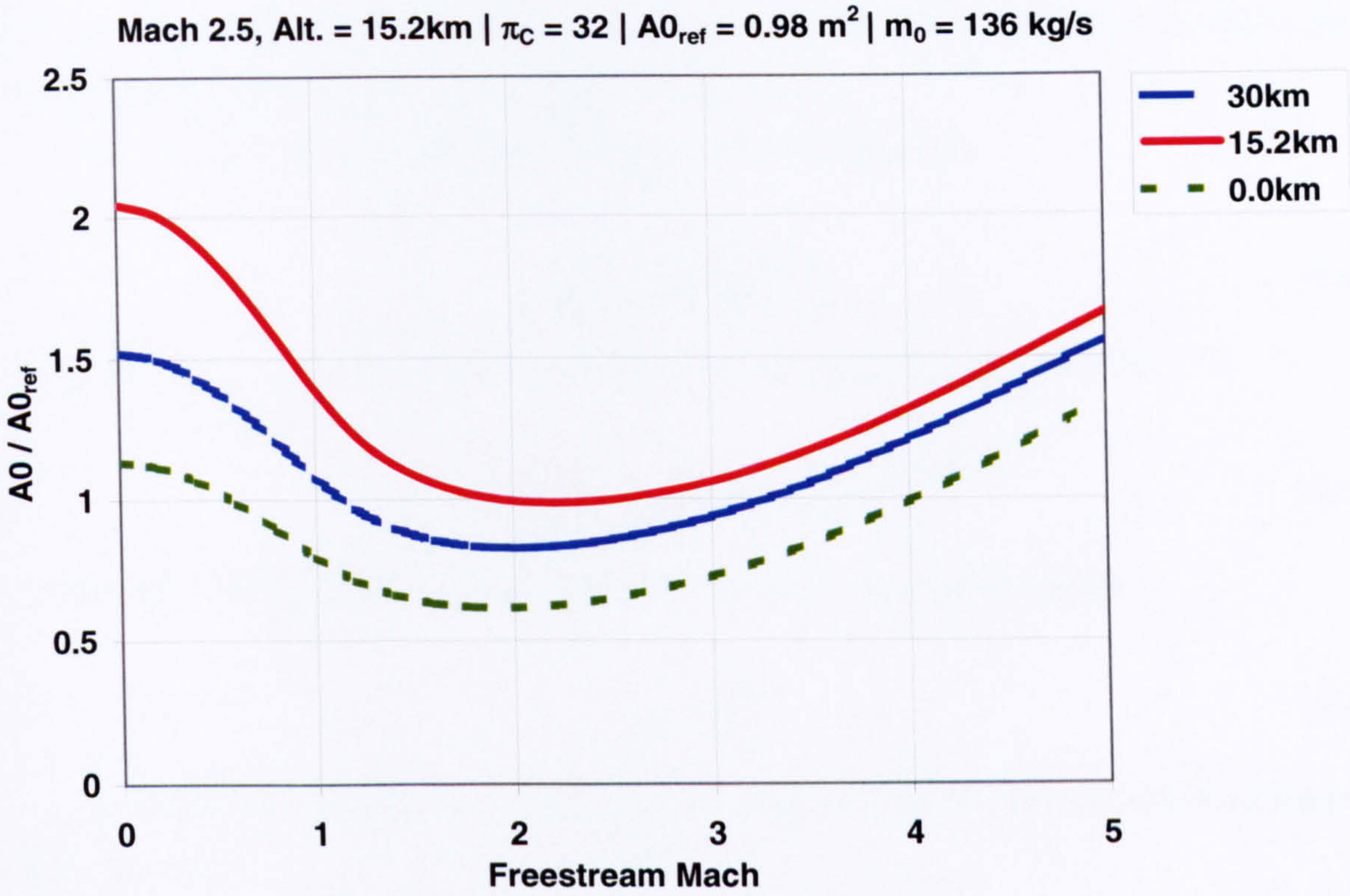


Figure 6.7: Required inlet airflow at various altitudes.

output data for an the on-design Mach range between Mach 0 and 5. The $F/\dot{m}_0$ coupled with $\dot{m}_0$ obtained from `OFFX` enables the thrust to be calculated for this Mach range. Thrust-matching is next performed for both thrust and specific impulse.

Finally, the inlet design can begin by first generating a plot for the air flow requirement at various altitudes, A_0/A_{0ref}, based on a reference area, A_{0ref} which is given by

$$A_{0ref} = \frac{R_c T_0 \dot{m}_{0ref}}{p_0 V_0} \tag{6.5}$$

where $\dot{m}_{0ref}$ is the mass flow rate input in `HICAD` and $R_c = 287 J.kg/K$.

To illustrate the area flow requirement, a example design point of Mach 2.5 at $h = 15.2km$ with $\dot{m}_0 = 136.1$ kg/s is used. The area distribution requires `OFFX` data for $\dot{m}_0$ vs. M_0 and the resulting graph for A_0/A_{0ref} is shown in Figure 6.7 with a minimum around Mach 2. The flight conditions are shown in the insert of the figure.

This figure presents information to select the flight condition at which the mass flow requirement at a particular Mach number is the greatest with a corresponding area given by $A_{0_{ireq}}$. m_i represents the air that enters the inlet whereas $\dot{m}_0$ is the air minus the boundary layer bleed as stated by Mattingly *et al.* (1987) for a mixed compression inlet.

The engine airflow is corrected for a 4% safety margin and boundary layer bleed that varies linearly from 0% at Mach 0.8 and 4% at Mach 2.

The area ratio A_{0_i}/A_{s4} is then determined by the following

$$\frac{A_{0_i}}{A_{s_4}} = \eta_R \frac{A/A^*|_{M_0}}{A/A^*|_{M_5}} \tag{6.6}$$

where A/A^* is a compressible area flow function given by Equation 6.7

$$\frac{A}{A^*} = \frac{1}{M}\left\{\frac{2}{\gamma+1}\left(1+\frac{\gamma-1}{2}M^2\right)\right\}^{\frac{\gamma+1}{2(\gamma-1)}} \tag{6.7}$$

and the total pressure ratio is the sum of the individual shock jumps

$$\eta_R = \frac{P_{t5}}{P_{t0}} \tag{6.8}$$

For individual total pressure ratio across a single normal shock, the following expressions are used

$$\frac{P_{ty}}{P_{tx}} = \left\{\frac{\frac{\gamma+1}{2}M_x^2}{1+\frac{\gamma-1}{2}M_x^2}\right\}^{\frac{\gamma}{\gamma-1}} \left\{\frac{2\gamma}{\gamma+1}M_x^2 - \frac{\gamma-1}{\gamma+1}\right\}^{-\frac{1}{\gamma-1}} \tag{6.9}$$

where M_x is the upstream Mach number and M_y is the downstream given by

$$M_y = \left\{\frac{M_x^2 + \frac{2}{\gamma-1}}{\frac{2\gamma}{\gamma-1}M_x^2 - 1}\right\}^{\frac{1}{2}} \tag{6.10}$$

The required throat area A_{s_4} can then be determined from

$$A_{s_4} = \frac{A_{0_{ireq}}}{A_{0_i}/A_{s4}} \tag{6.11}$$

Finally A_1 is calculated from geometry for a given value of A_{s_4}. The value of A_1 is a function of the geometric ramp angle configuration and its final value is found when the highest value of η_R is achieved and the M_4 is greater than unity thus providing subsonic flow for the combustor. To accommodate subsonic operation, A_1 is corrected for Mach 0.8 operation where $A/A^* = 1.038$ for $\gamma = 1.4$.

The installation losses can be determined using the following equation

$$\phi_{inlet} = \left(\frac{A_{0i}}{A_0} - 1\right)\left\{M_0 - \left(\frac{2}{\gamma+1} + \frac{\gamma-1}{\gamma+1}M_0^2\right)^{1/2}\right\}\left(\frac{Fg_c}{m_0 a_0}\right)^{-1} \tag{6.12}$$

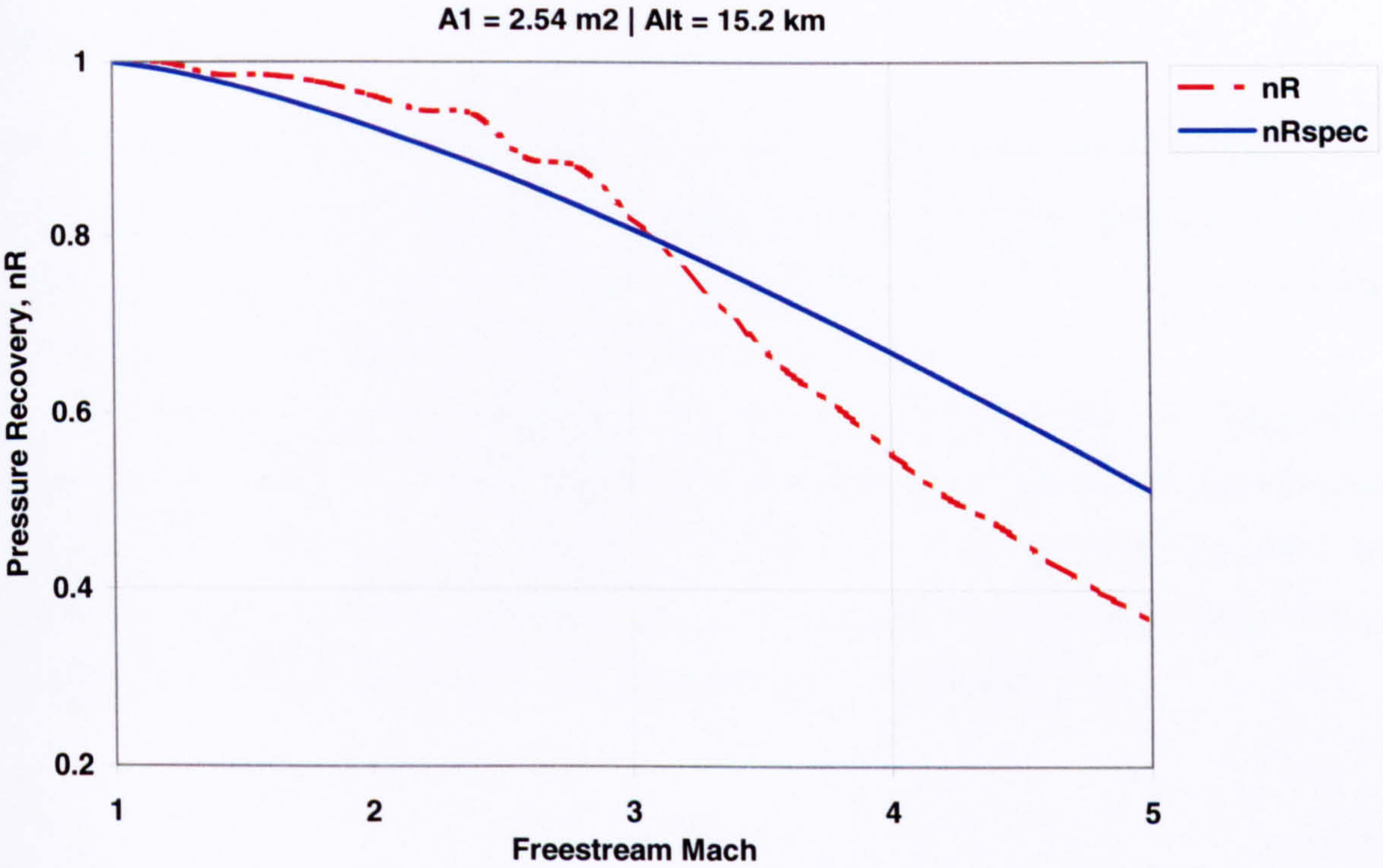


Figure 6.8: Intake loss associated with a four-ramp inlet system.

Having determined A_1, subsequent ramp angles for the range of Mach numbers that lead to the best overall pressure recovery can be found.

The large number of possible combinations are constrained by choosing ramp angles that have equal strength shock jumps between the four ramps. In other words, the total pressure ratio across each shock is the same and achieved by a larger ramp angle with respect to the upstream ramp due to the reduced Mach number. The pressure recovery at the design point should, at least, exceed Equation 6.3. The selected inlet configuration has been illustrated in Figure 6.8 over the Mach range for low-speed operation at the transition altitude of $15.2km$.

The model assumes intake operation with five shocks to define the total pressure recovery factor. Since additive spillage drag forces and effects of ingested vehicle forebody boundary layer have not been accounted for, the model may appear a little optimistic.

The pressure recovery graph shown in Figure 6.8 for this example, has a total flow turning angle of 36° degrees at Mach 5 and $30km$. The pressure recovery can be improved by allowing a greater turning angle at this case but this will increase drag. Once acceptable losses are accrued, the design of the low-speed inlet is completed.

6.3 Summary

Idealised analysis of a turboramjet has been carried out using quasi-one-dimensional analysis. Performance of the engine can be calculated by means of direct methods based on a bypass ratio. When this value reaches zero, the engine no longer behaves as an airbreathing system and that is considered to be the limit of the engine.

The first step in conceptual design is to vary the inlet contraction (or compression) ratio and the combustor area ratio and examine the sensitivity of performance as a function of component efficiencies. The results serve to guide the selection of the geometry flow path. The next step is an investigation of possible geometric shapes to produce the wave structure to yield the desired inlet compression and contraction ratios.

7

Airframe-Propulsion Integration Results

7.1 Introduction

The interdependence of the airframe and propulsion system for hypersonic cruise vehicles is analysed in this chapter and it will be shown that the success of a proposed vehicle concept is strongly linked to their tight integration. In most cases presented in the results below, an example waverider design point is selected to illustrate the capacity of HICAD in achieving valuable insight into the hypersonic aircraft design process. Three main areas of investigation are considered as summarised below.

1. Thrust-matching of a low-speed and high-speed engine for smooth transition between the powerplants. The associated principal performance parameters such as thrust and specific impulse will be presented as a result of this procedure using the quasi-one dimensional cycle analysis discussed in previous chapters.

2. The notable challenges with regards to the airframe-propulsion integration of the turboramjet and scramjet and their flowpaths with a waverider airframe. The practical operation of the variable geometry / multiple inlet system will be discussed.

3. Results of optimising multiple variables to produce aerodynamically efficient vehicle configurations.

7.2 Propulsion System Performance

7.2.1 Nozzle

Engine performance relies heavily on the design of the supersonic nozzle. Using IMOC developed by Jacobs (2004), results were obtained for a two-dimensional nozzle whose height and length are defined from a consideration of the overall vehicle length set at 60m and subtracting the dimensions of the forebody, inlet and propulsion. The programmatic routines require an entry Mach number, ratio of specific heats and freestream conditions. It then computes the expansion net until the nozzle dimensions are reached.

Given a nozzle entry Mach number of 2.8 at station 4, an expansion flowfield is illustrated in Figure 7.1 for a dimensionally unconstrained linear expansion nozzle. This nozzle also has a second expansion fan resulting from a cowl chamfer set at 6°, which produces greater gross thrust at station 10 than a nozzle configuration with no lower surface expansion.

A close-up image of this nozzle showing the cowl expansion, is illustrated in Figure 7.2. These visualisations are based on the original IMOC code whereas HICAD only performs the calculation with an output based on thrust and specific impulse. These quantities are calculated using equations from the stream thrust analysis explained in chapter 4. If desired, the data can be exported into the IMOC code for later visualisation and the images here offer an insight into the nozzle shock structure.

As the upper wall angle is increased, the thrust increases in a linear fashion as shown in Figure 7.3 and similarly for the specific impulse in Figure 7.4. This plot is for a Mach 9 waverider with constant nozzle entry Mach number and linear upper thrust surface. Linear interpolation is used to find the Mach number at the trailing edge of the vehicle, i.e. the length of the nozzle. In HICAD, a maximum upper wall angle is set at 18° with reference to Small *et al.* (1976).

As shown in this analysis, there is a strong interaction between the nozzle cowl surface and the expansion flowfield. Although, the expansion effect of extending the cowl into the nozzle flowfield has not been considered in this study.

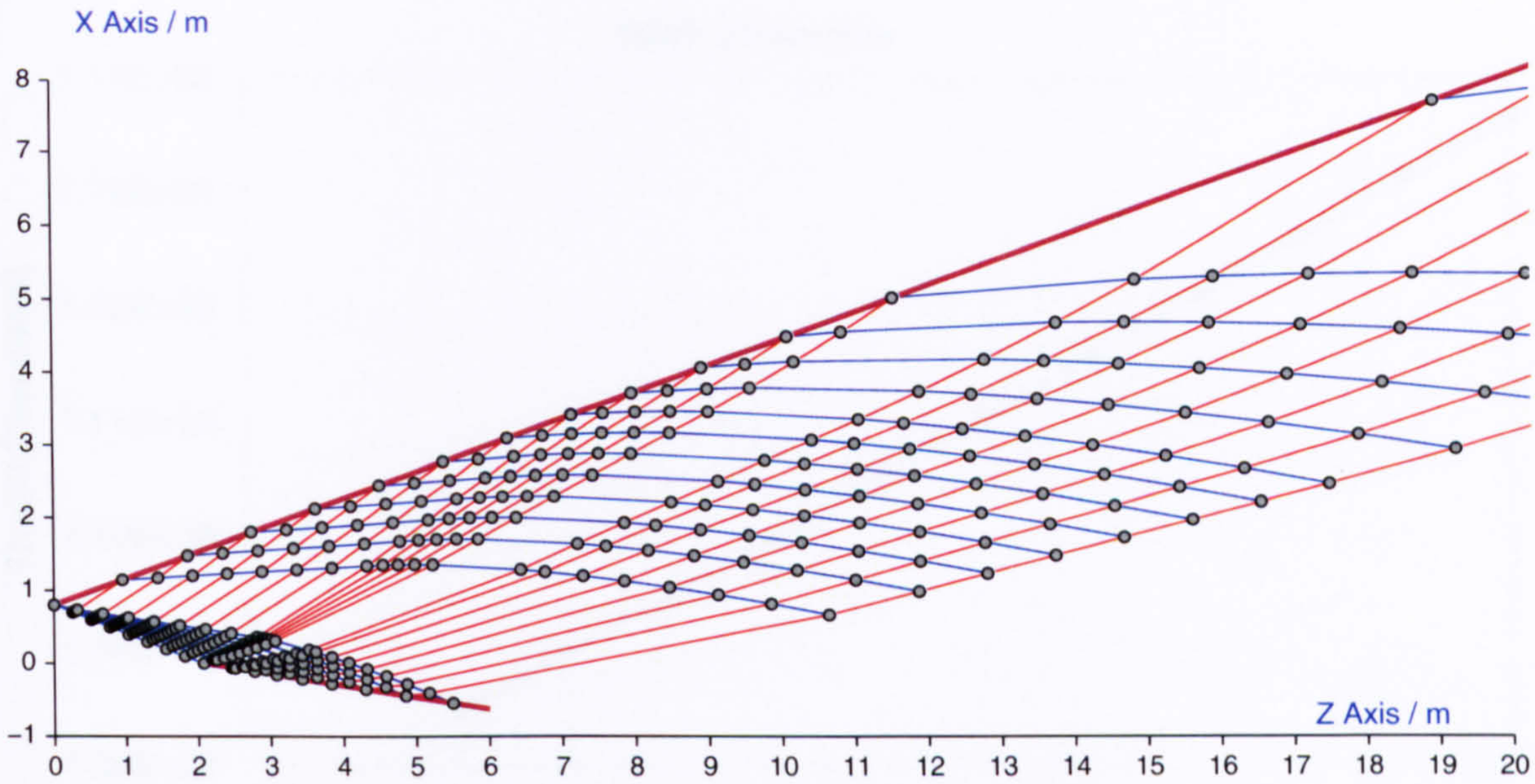


Figure 7.1: An example expansion net of a Mach 9 waverider using IMOC for the visualisation. This nozzle has an entry Mach number of 2.8, cowl chamfer of 6° and thrust wall angle is 20°.

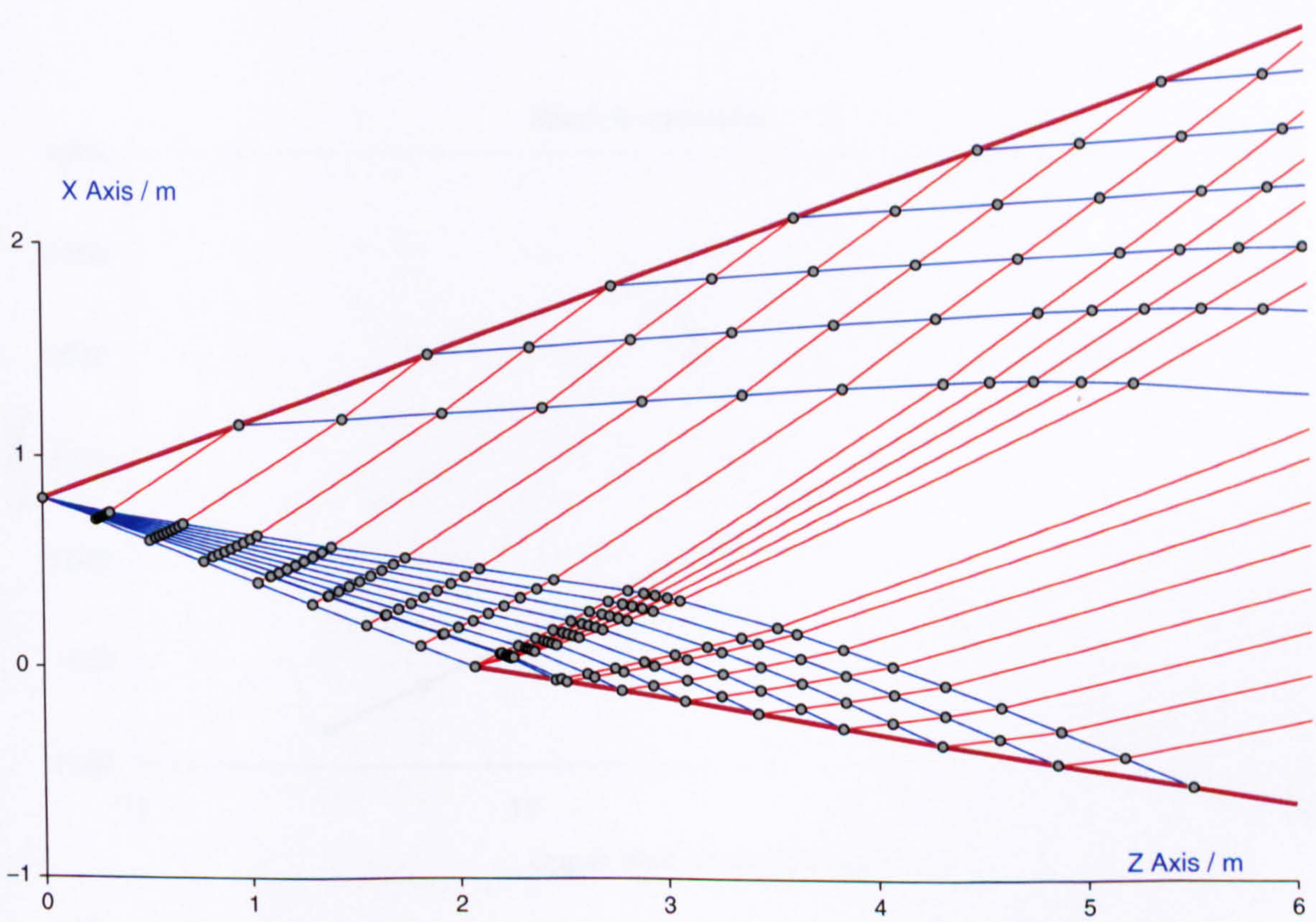


Figure 7.2: A close-up version of Figure 7.1 showing the cowl expansion.

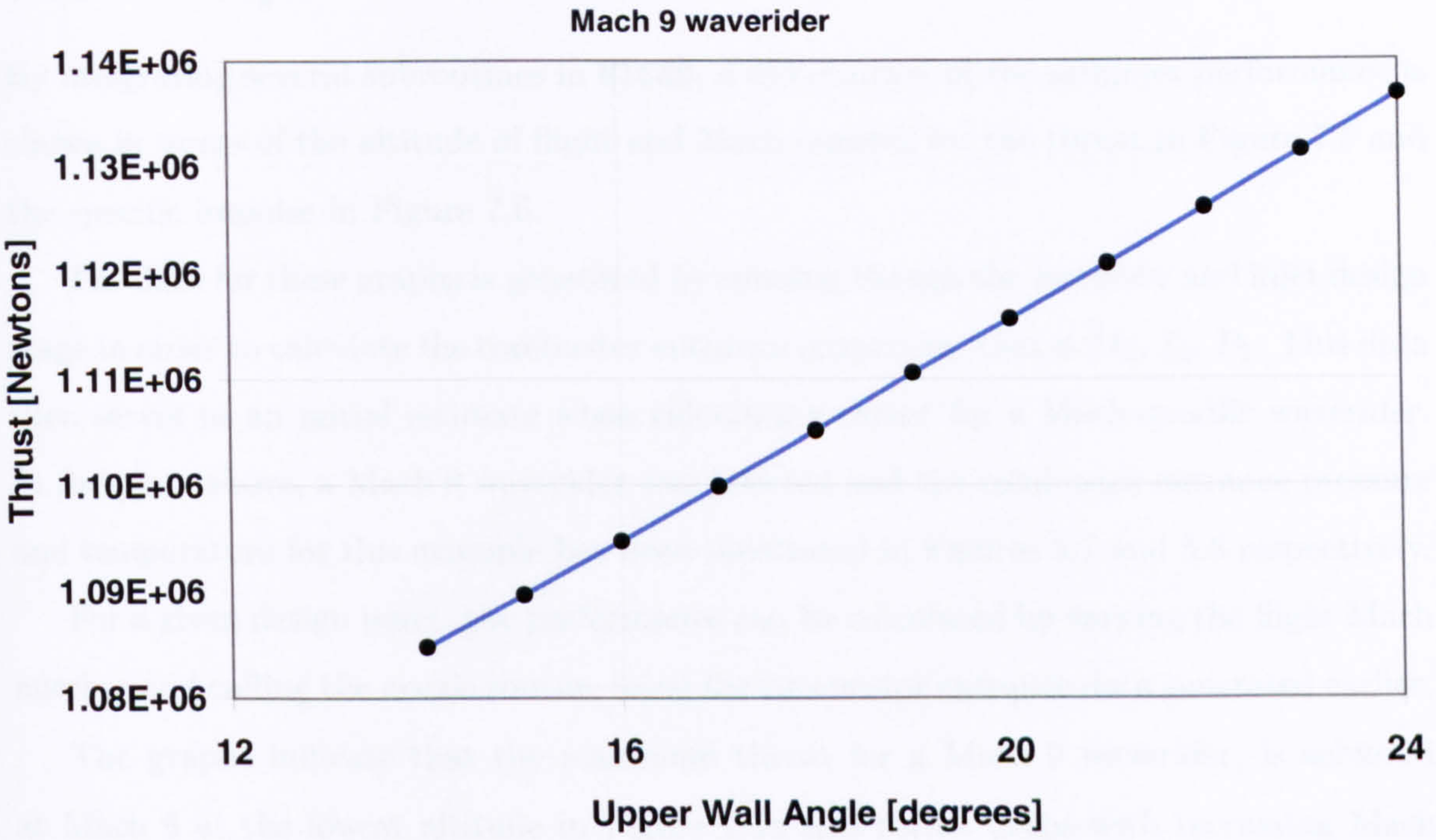


Figure 7.3: Nozzle thrust output as a function of the upper wall angle for a Mach 9 waverider

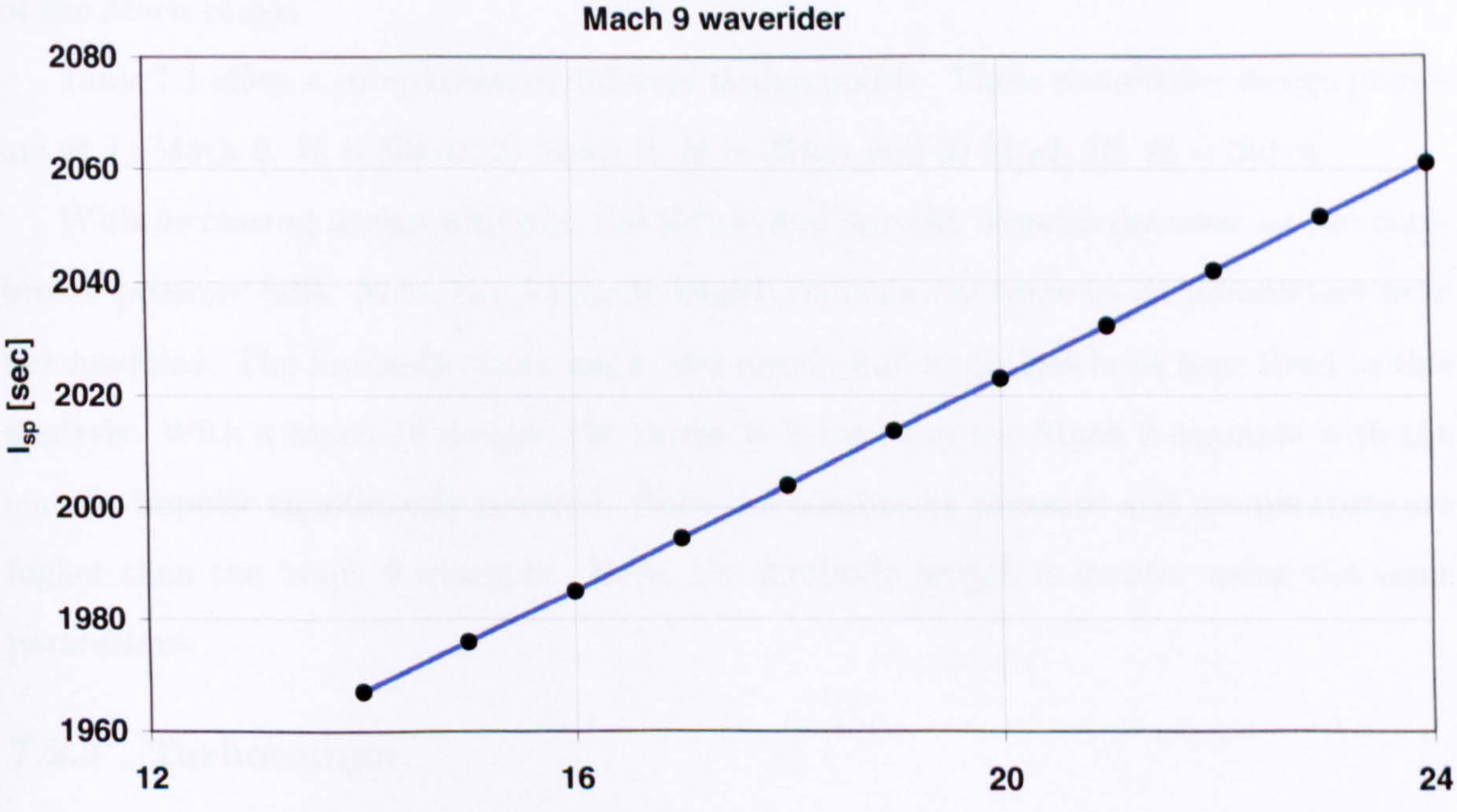


Figure 7.4: Nozzle Specific Impulse output as a function of the upper wall angle for a Mach 9 waverider

7.2.2 Scramjet

By integrating several subroutines in HICAD, a distribution of the scramjet performance is shown in terms of the altitude of flight and Mach number for the thrust in Figure 7.5 and the specific impulse in Figure 7.6.

The data for these graphs is generated by running though the forebody and inlet design stage in order to calculate the combustor entrance properties, that is M_2, T_2, P_2. This data then serves as an initial estimate when calculating thrust for a Mach-specific waverider. In the plots above, a Mach 9 waverider was selected and the combustor entrance pressure and temperature for this example has been illustrated in Figures 5.7 and 5.8 respectively.

For a given design point, the performance can be calculated by varying the flight Mach number and calling the nozzle routine using the combustor entrance data generated earlier.

The graphs indicate that the maximum thrust for a Mach 9 waverider, is achieved at Mach 6 at the lowest altitude in Figure 7.5a and thrust drops with increasing Mach numbers and altitude as shown in Figure 7.5b. The specific impulse is approximately constant with an increasing altitude as shown in Figure 7.6a and as expected in the contour plot of Figure 7.6b, the maximum specific impulse is attainable at the lower end of the Mach range.

Table 7.1 offers a comparison of different design points. These waverdider design points are at 1) Mach 9, $H = 30km$; 2) Mach 9, $H = 35km$ and 3) Mach 10, $H = 30km$.

With increasing design altitude, the thrust and specific impulse decrease as the combustor pressure falls. Note, the forebody length remains the same as its parameters were not modified. The forebody shock angle and nozzle wall angle has been kept fixed in this analysis. With a Mach 10 design, the thrust is lower than the Mach 9 example with the specific impulse significantly reduced. Both the combustor pressure and temperature are higher than the Mach 9 example. Here, the forebody length is greater using the same parameters.

7.2.3 Turboramjet

Before thrust matching can be performed, the turboramjet system performance is investigated with regards to some of the core flow variables. Specific thrust, specific impulse and specific fuel consumption as a function of Mach number will by analysed in turn by

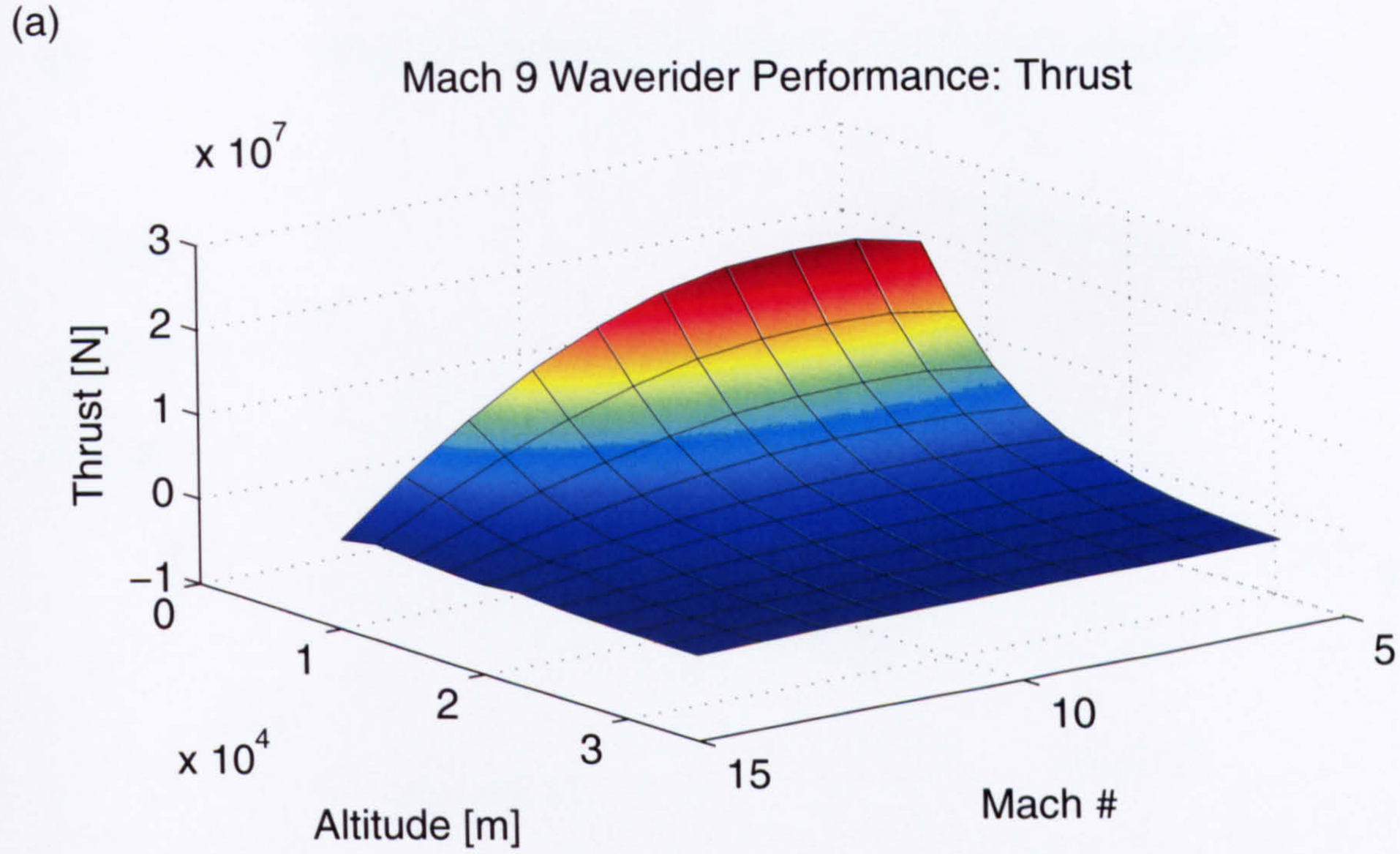


Figure 7.5: Thrust variation as a function of Mach number and altitude for a Mach 9 waverider.

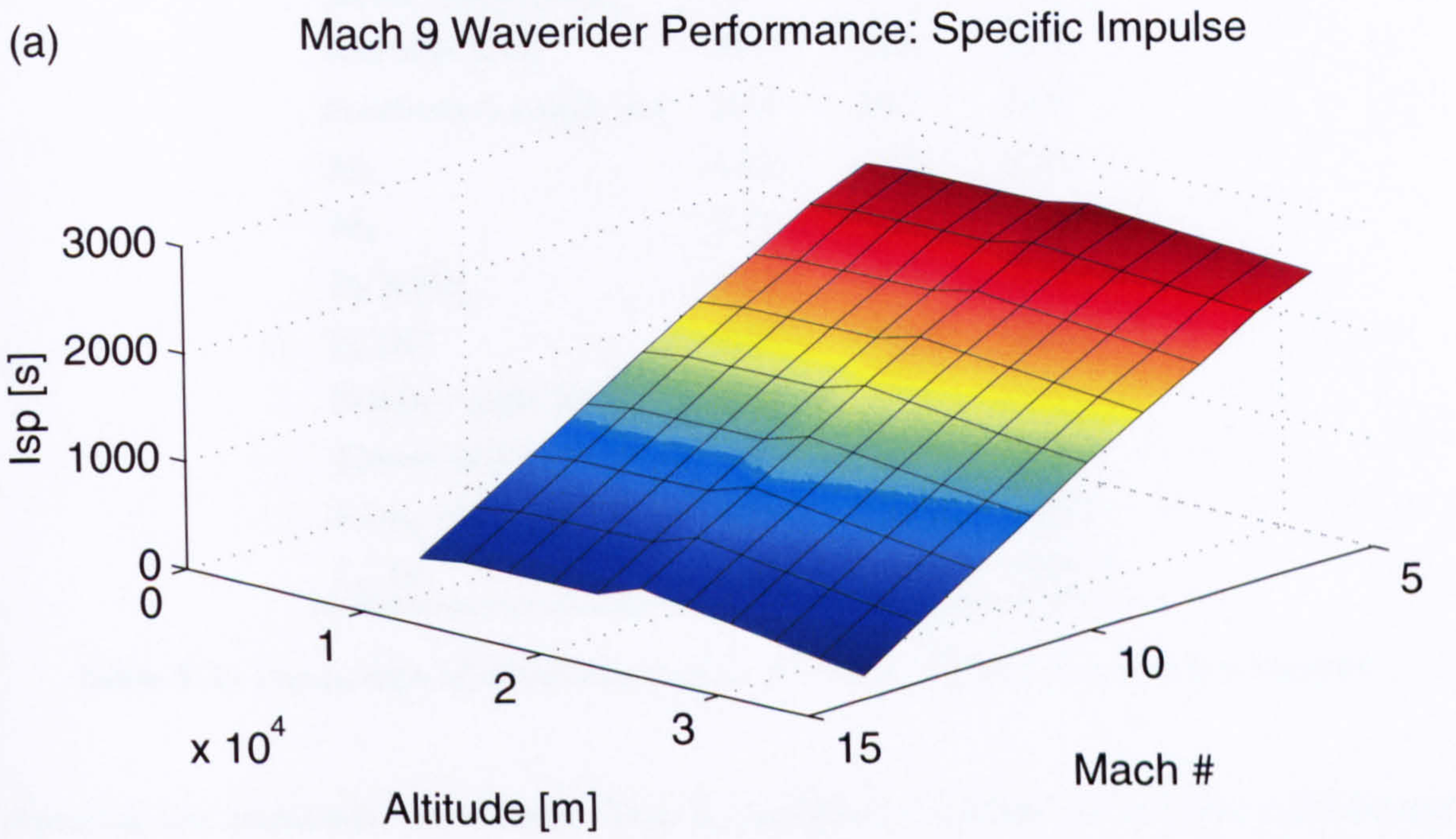


Figure 7.6: Specific Impulse variation as a function of Mach number and altitude for a Mach 9 waverider.

Property	Value		
Mach	9	9	10
Shock Angle [*deg.*]	11.4	11.4	11.4
Altitude [km]	30.0	35.0	30.0
Forebody Length [m]	39.3	39.3	46.9
M_2	4.01	4.01	4.34
M_4	2.79	2.79	2.90
P_2 [kPa]	87.1	41.4	105.8
T_2 [K]	893.2	949.3	966.8
Nozzle Angle [*deg.*]	18.0	18.0	18.0
Thrust [kN]	107.1	49.1	100.2
F/m_0 [$N.s/kg$]	554.6	529.5	391.2
I_{sp} [s]	1942.6	1854.9	1370.2

Table 7.1: Comparison of initial data and performance of different waverider examples.

changing one parameter at a time. This is possible by calling the HICAD's turboramjet loop subroutine for a range of on-design Mach numbers. In all figures in this section, the analysis proceeds by maintaining all variables fixed except for the variable in question. Furthermore, the graphs are plotted for the limit of normal operation, that is when the model appears to break down.

7.2.3.1 Variation of ptp/p_0

First the bypass ratio is analysed for three different ptp/p_0 values for fixed $Ttp/T_0 = 10$ at sea-level in Figure 7.7. The graph shows that with an increasing ptp/p_0, the bypass ratio tending to zero can be delayed until a higher Mach number. This translates as a better specific thrust with increasing ptp/p_0 as shown in Figure 7.8 again for the same conditions. Similarly, both the specific impulse and SFC curves observe the same trend in Figures 7.9 and 7.10 respectively. Therefore a conclusion from this may be drawn that the greater the ptp/p_0, the better the turboramjet performance for a given set of design conditions.

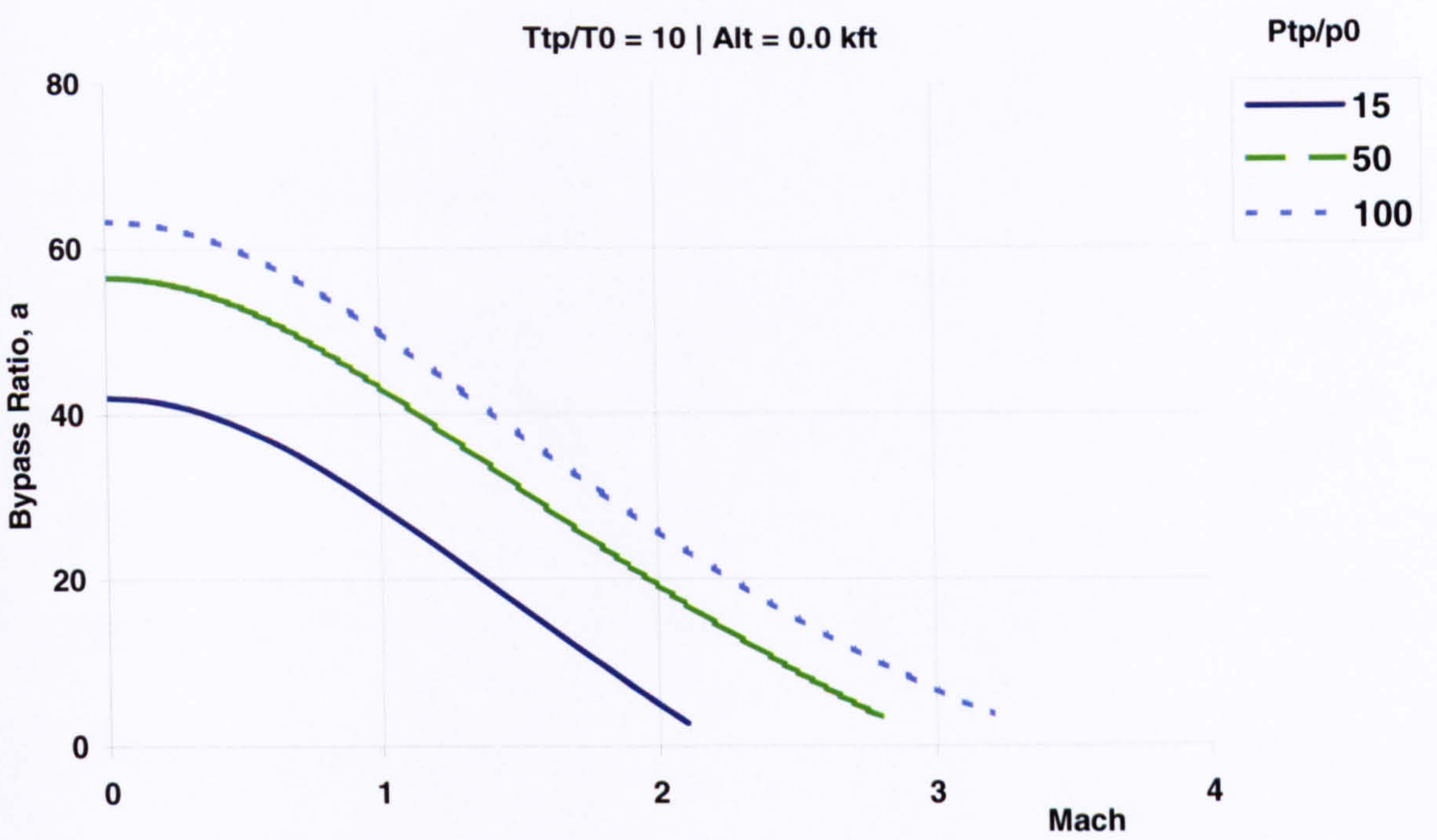


Figure 7.7: Variation of bypass ratio as a function of ptp/p_0 for a range of Mach numbers.

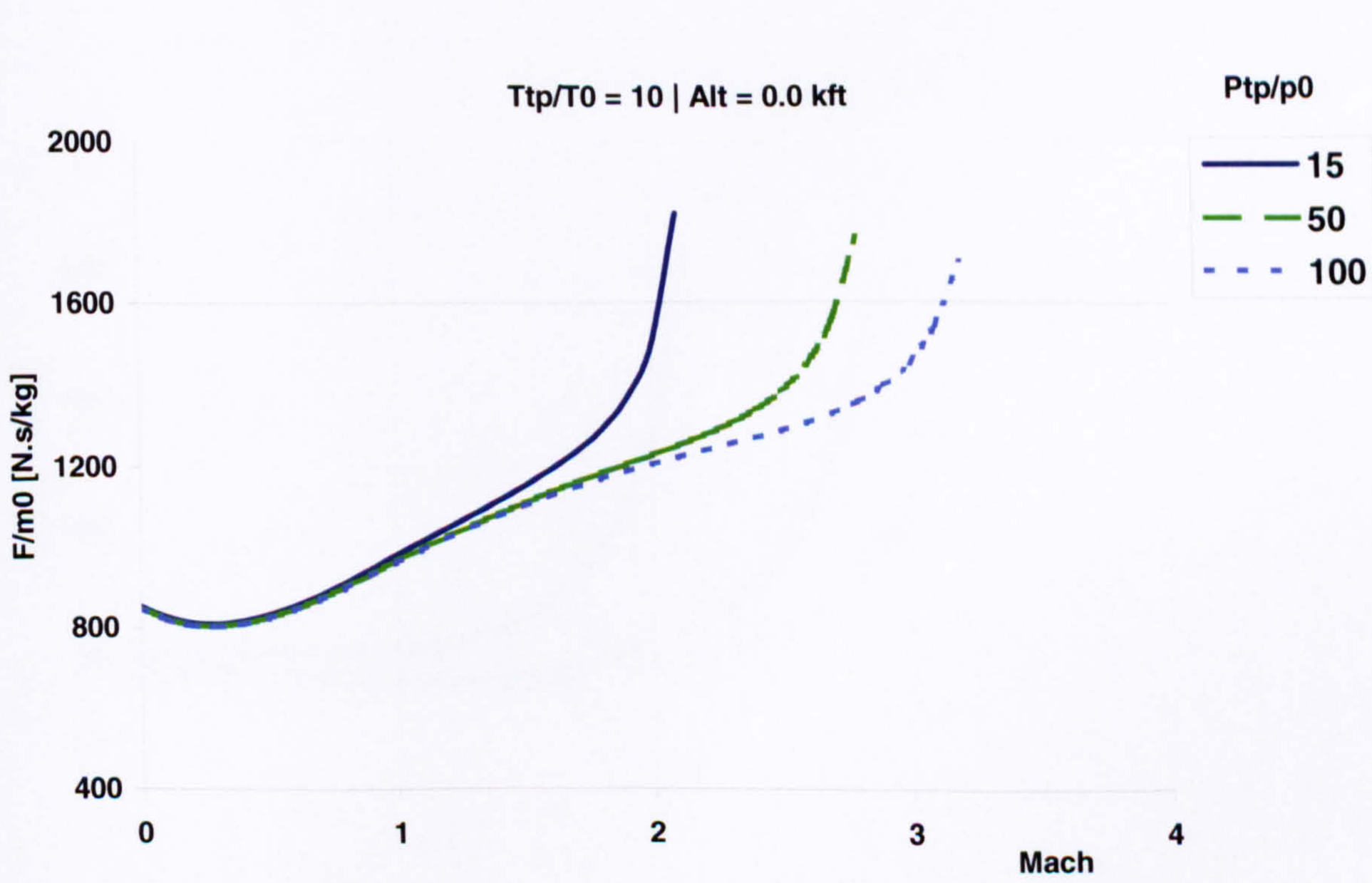


Figure 7.8: Variation of specific thrust as a function of ptp/p_0 for a range of Mach numbers.

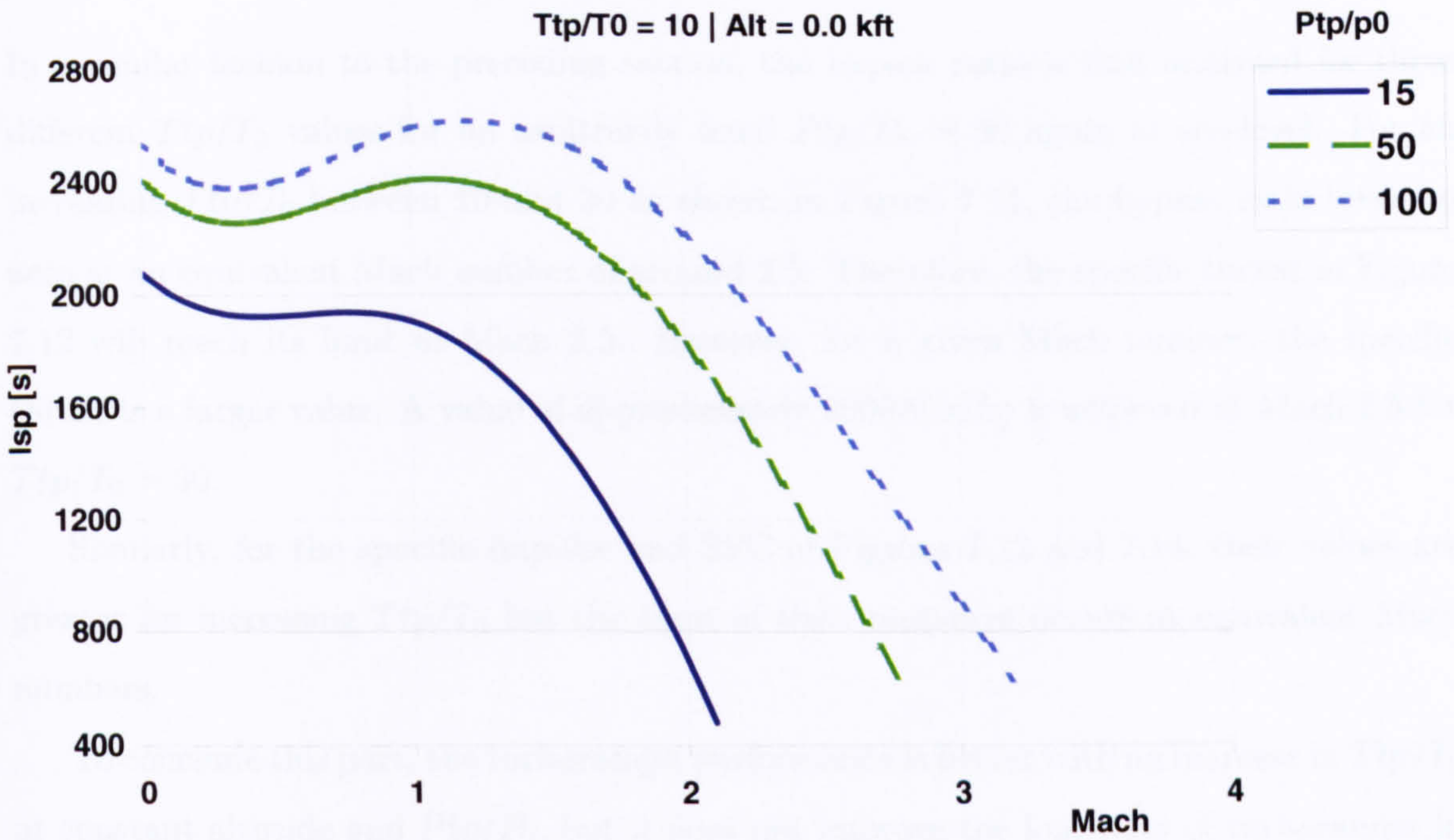


Figure 7.9: Variation of specific impulse as a function of ptp/p_0 for a range of Mach numbers.

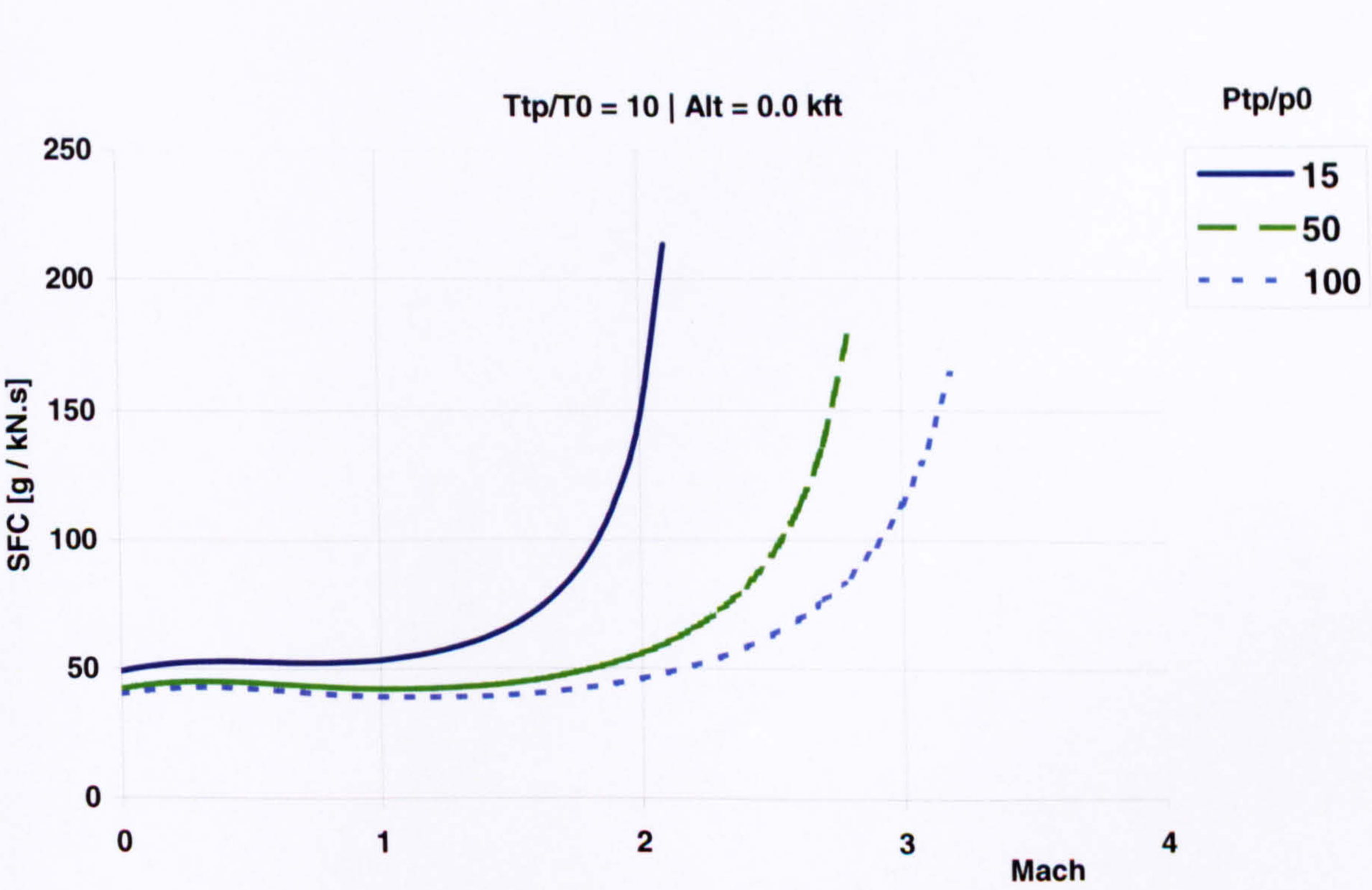


Figure 7.10: Variation of specific fuel consumption as a function of ptp/p_0 for a range of Mach numbers.

7.2.3.2 Variation of $Ttp/T0$

In a similar fashion to the preceding section, the bypass ratio is first analysed for three different Ttp/T_0 values for an arbitrarily fixed $Ptp/P_0 = 30$ again at sea-level. For an increasing Ttp/T_0 between 10 and 30 as shown in Figure 7.11, the bypass ratio tends to zero at an equivalent Mach number of around 2.5. Therefore, the specific thrust in Figure 7.12 will reach its limit at Mach 2.5. However, for a given Mach number, the specific thrust is a larger value. A value of approximately $3000N.s/kg$ is achieved at Mach 2.5 for $Ttp/T_0 = 30$.

Similarly, for the specific impulse and SFC of Figures 7.13 and 7.14, their values are greater for increasing Ttp/T_0 but the limit of their measures occurs at equivalent Mach numbers.

To conclude this part, the turboramjet performance is better with an increase in Ttp/T_0 at constant altitude and Ptp/P_0, but it does not improve the longevity of turboramjet in terms of its bypass ratio.

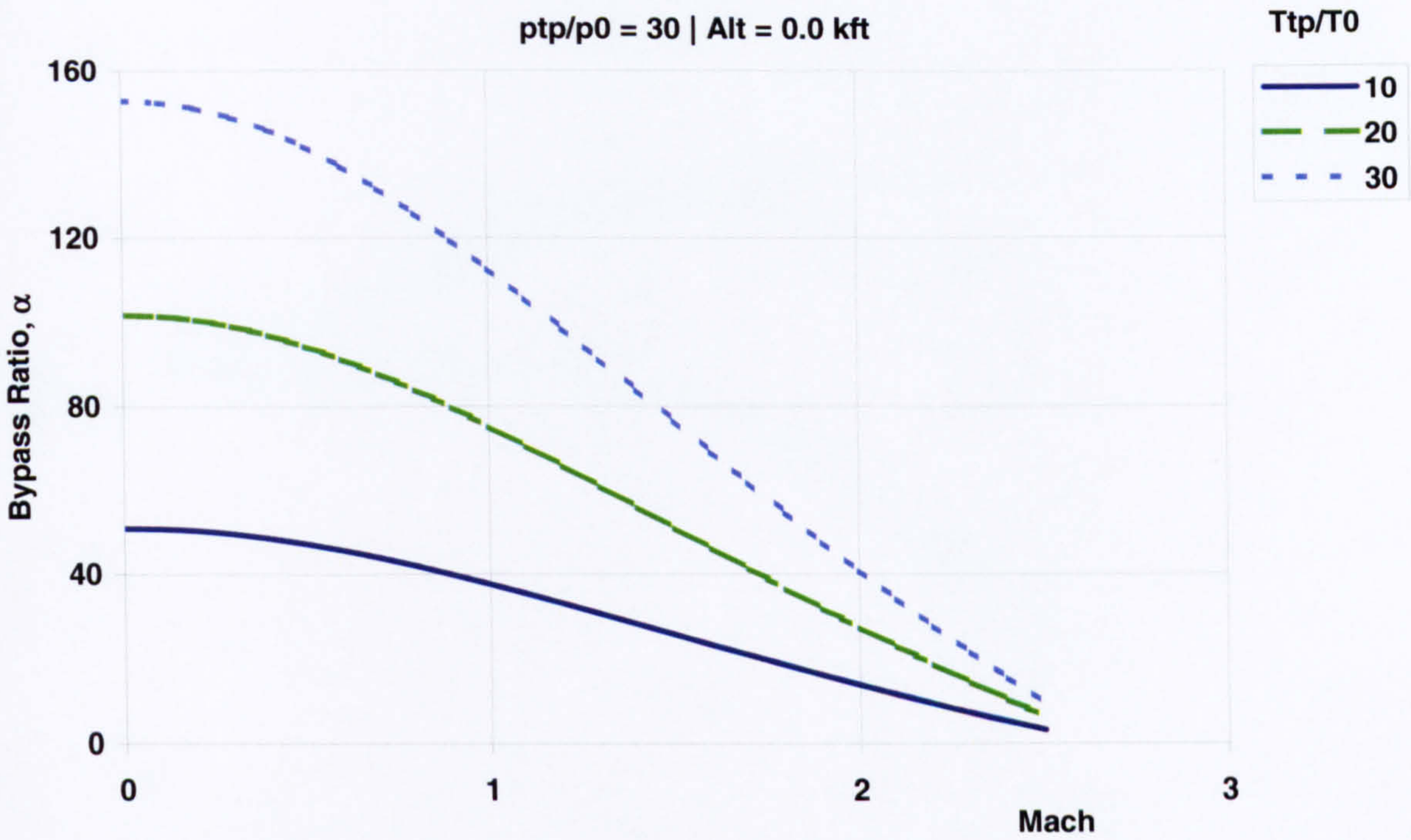


Figure 7.11: Variation of bypass ratio as a function of Ttp/T_0 for a range of Mach numbers.

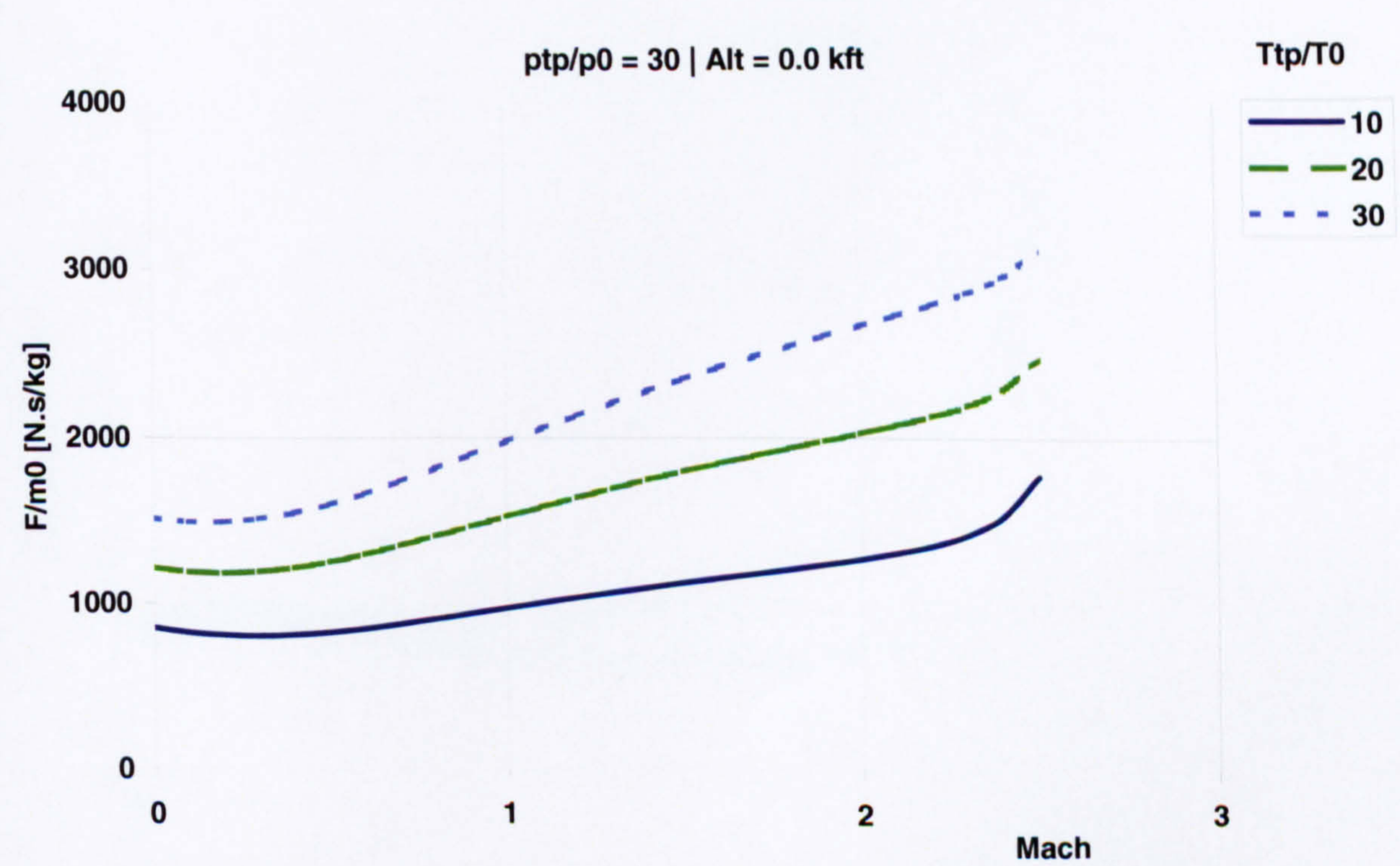


Figure 7.12: Variation of specific thrust as a function of Ttp/T_0 for a range of Mach numbers.

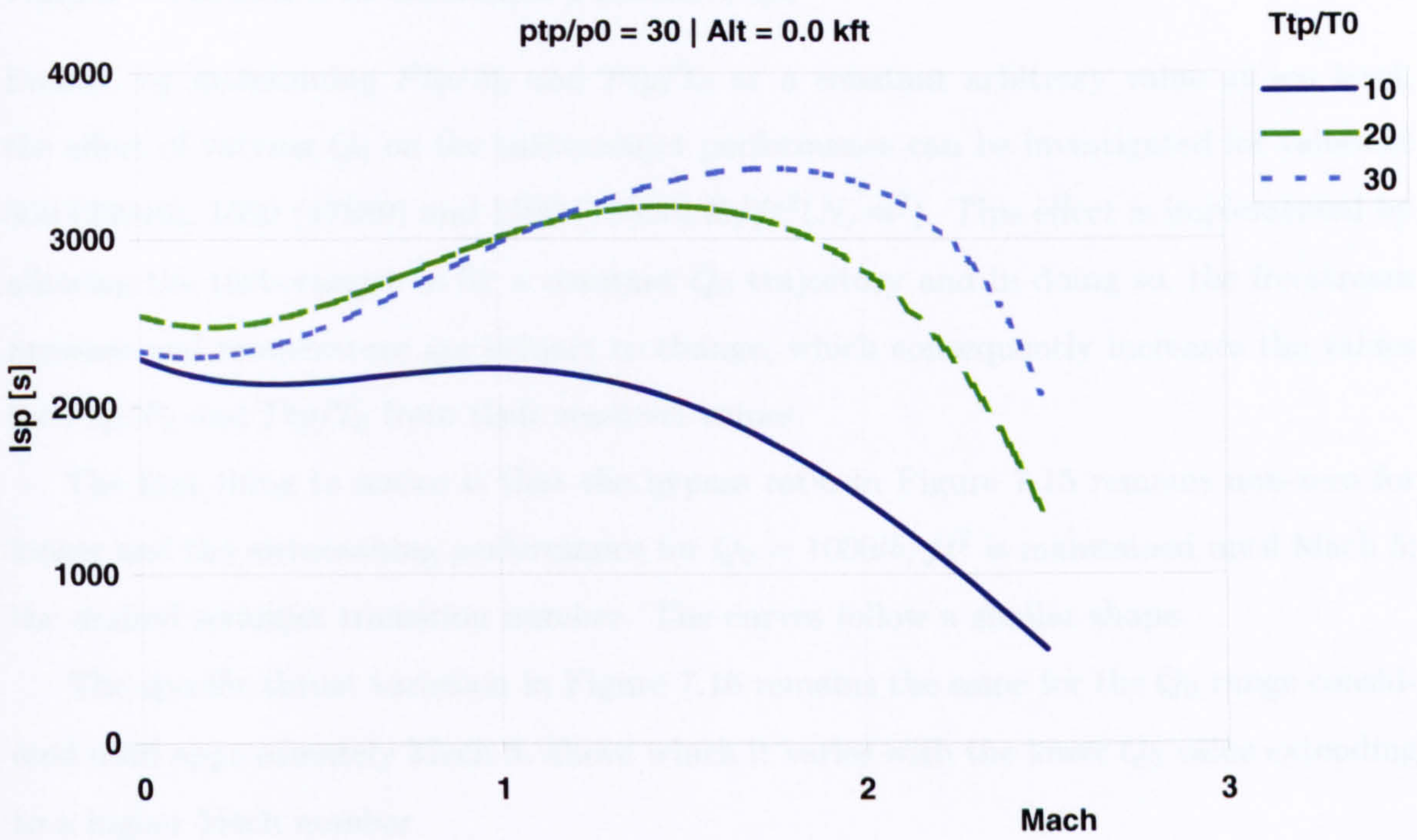


Figure 7.13: Variation of specific impulse as a function of Ttp/T_0 for a range of Mach numbers.

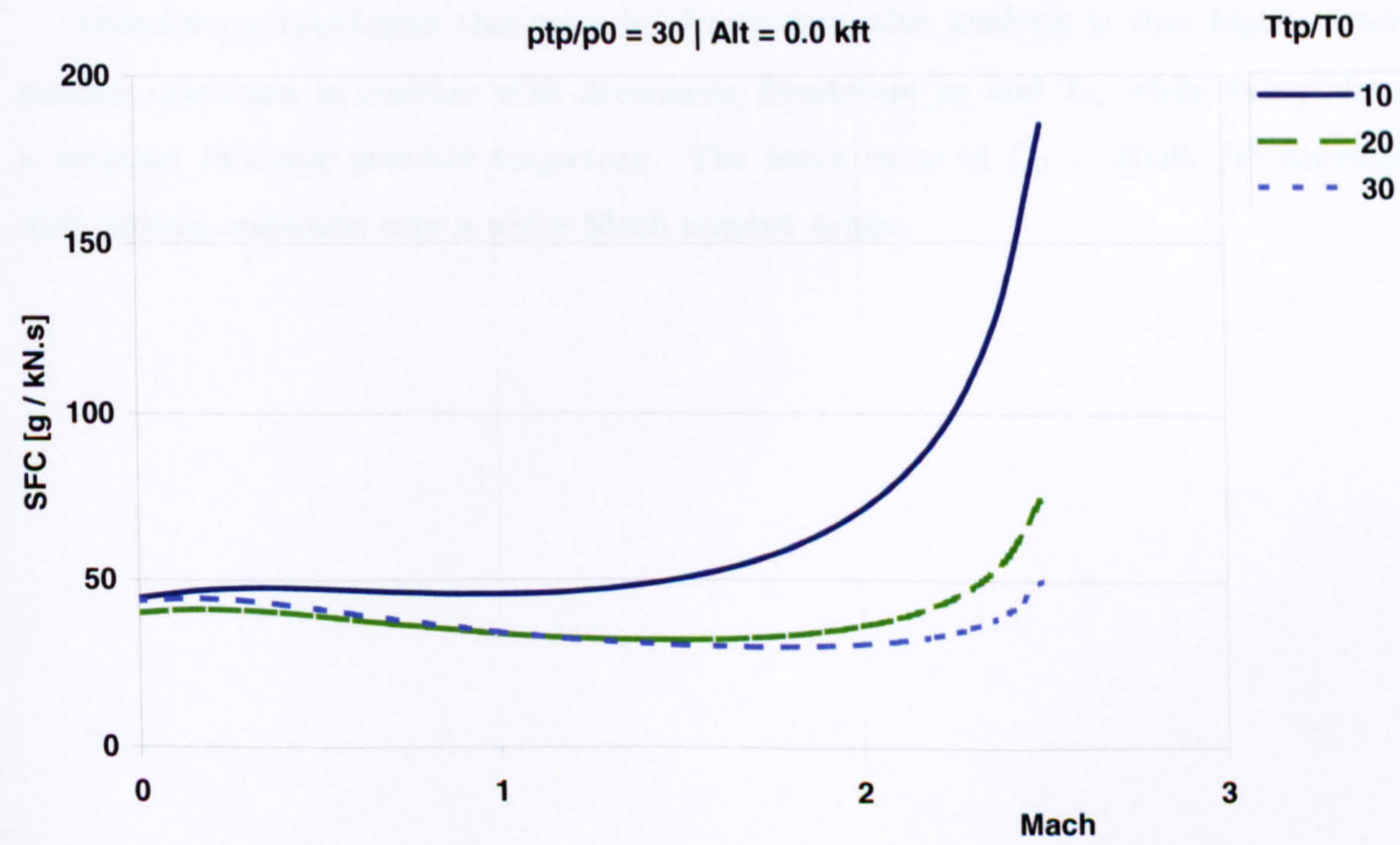


Figure 7.14: Variation of specific fuel consumption as a function of Ttp/T_0 for a range of Mach numbers.

7.2.3.3 Variation of Dynamic Pressure, Q_0

Finally, by maintaining Ptp/P_0 and Ttp/T_0 at a constant arbitrary value at sea level, the effect of varying Q_0 on the turboramjet performance can be investigated for values of 500 (23940), 1000 (47880) and 1500 (71820) $lb/ft^2(N/m^2)$. This effect is implemented by allowing the turboramjet to fly a constant Q_0 trajectory and in doing so, the freestream pressure and temperature are subject to change, which consequently increases the values for Ptp/P_0 and Ttp/T_0 from their sea-level values.

The first thing to notice is that the bypass ratio in Figure 7.15 remains non-zero for longer and the airbreathing performance for $Q_0 = 1000lb/ft^2$ is maintained until Mach 5; the desired scramjet transition number. The curves follow a similar shape.

The specific thrust variation in Figure 7.16 remains the same for the Q_0 range considered until approximately Mach 3, above which it varies with the lower Q_0 value extending to a higher Mach number.

The higher Mach number operating range is also illustrated in the specific impulse and SFC variation in Figures 7.17 and 7.18 respectively. Specific impulse is highest for $Q_0 = 500lb/ft^2$.

Therefore, a conclusion that may be drawn from this analysis is that higher Mach number operation is possible with decreasing freestream p_0 and T_0, while flying along a constant dynamic pressure trajectory. The lower value of $Q_0 = 500lb/ft^2$ provides airbreathing operation over a wider Mach number range.

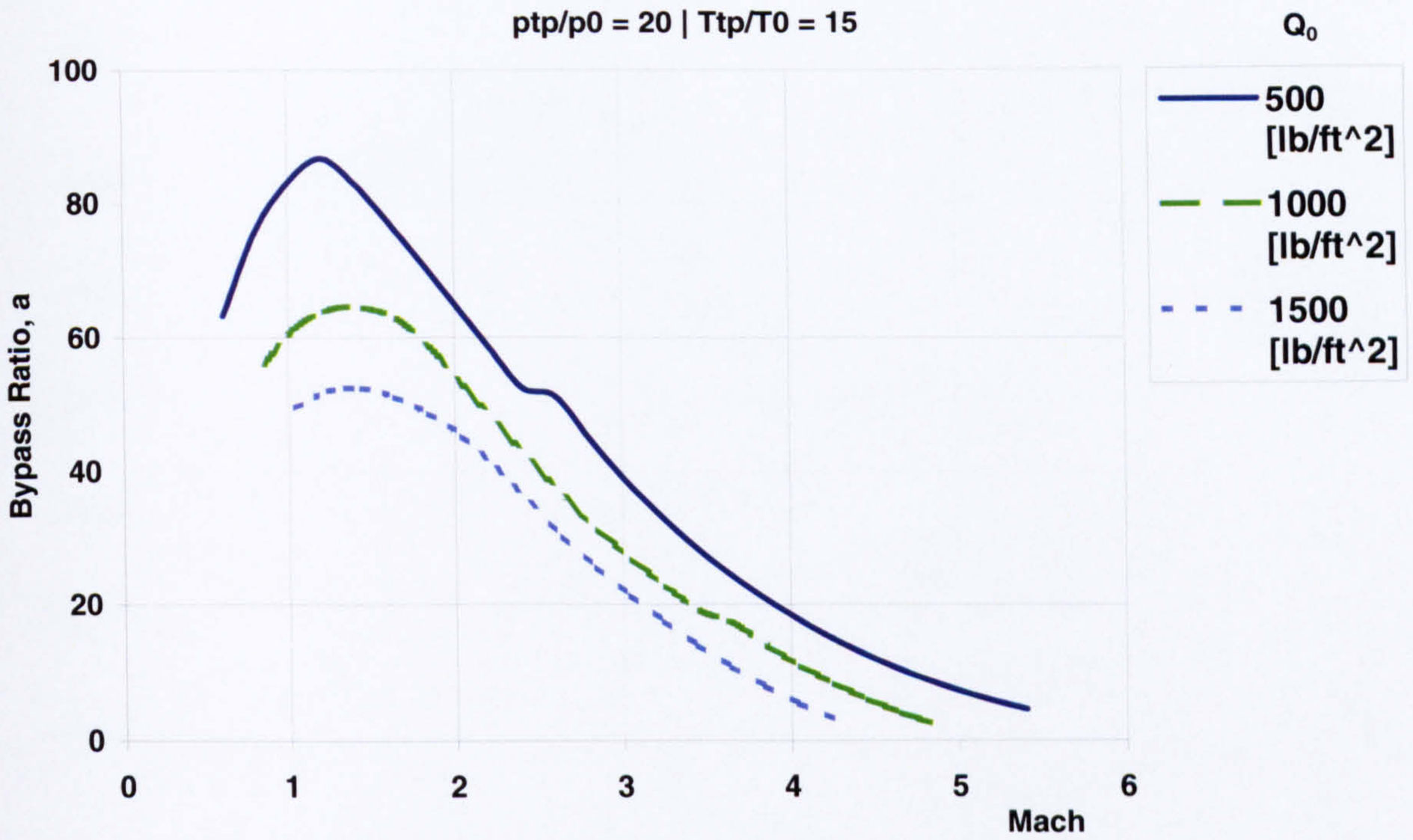


Figure 7.15: Variation of bypass ratio as a function of Q_0 for a range of Mach numbers.

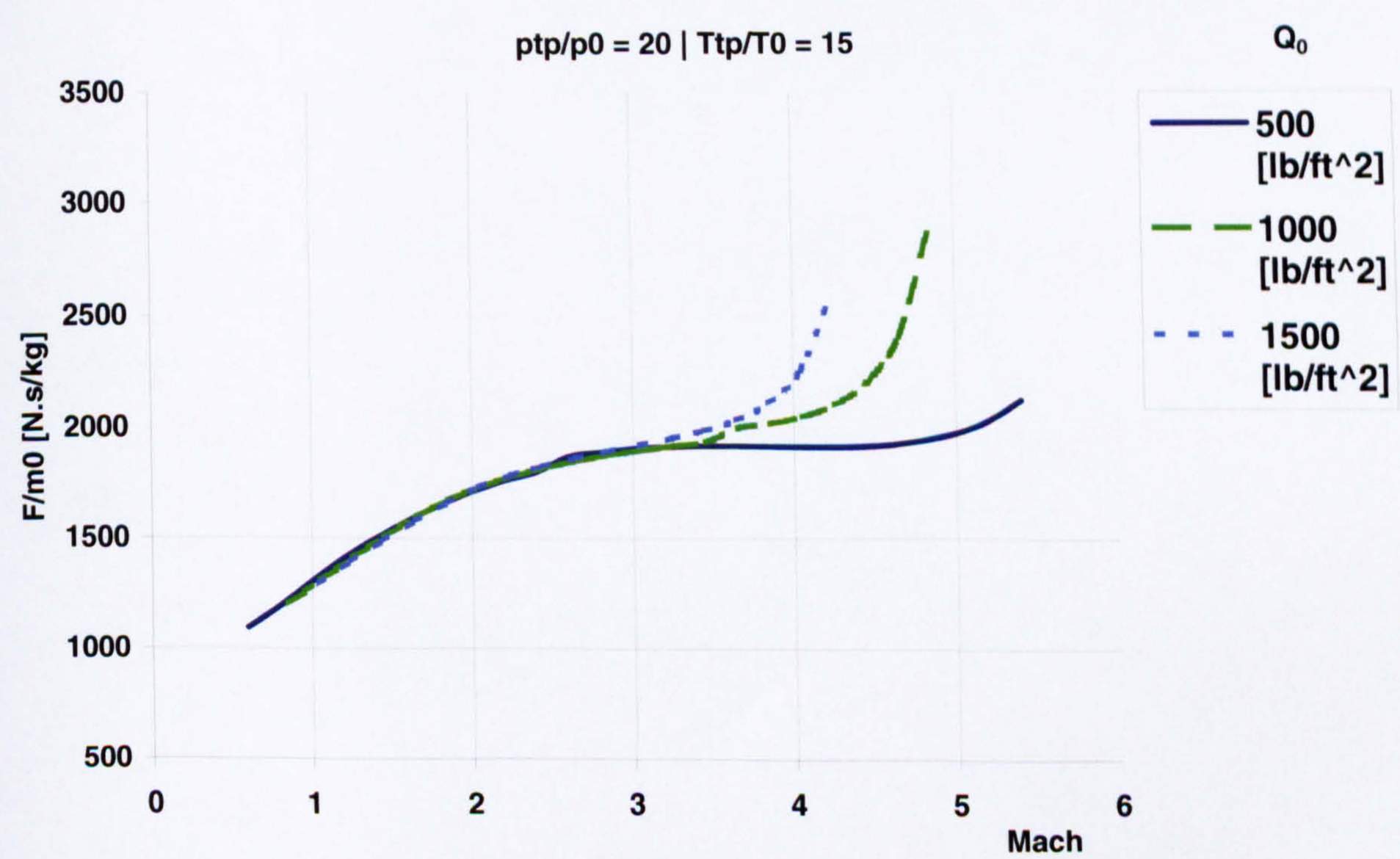


Figure 7.16: Variation of specific thrust as a function of Q_0 for a range of Mach numbers.

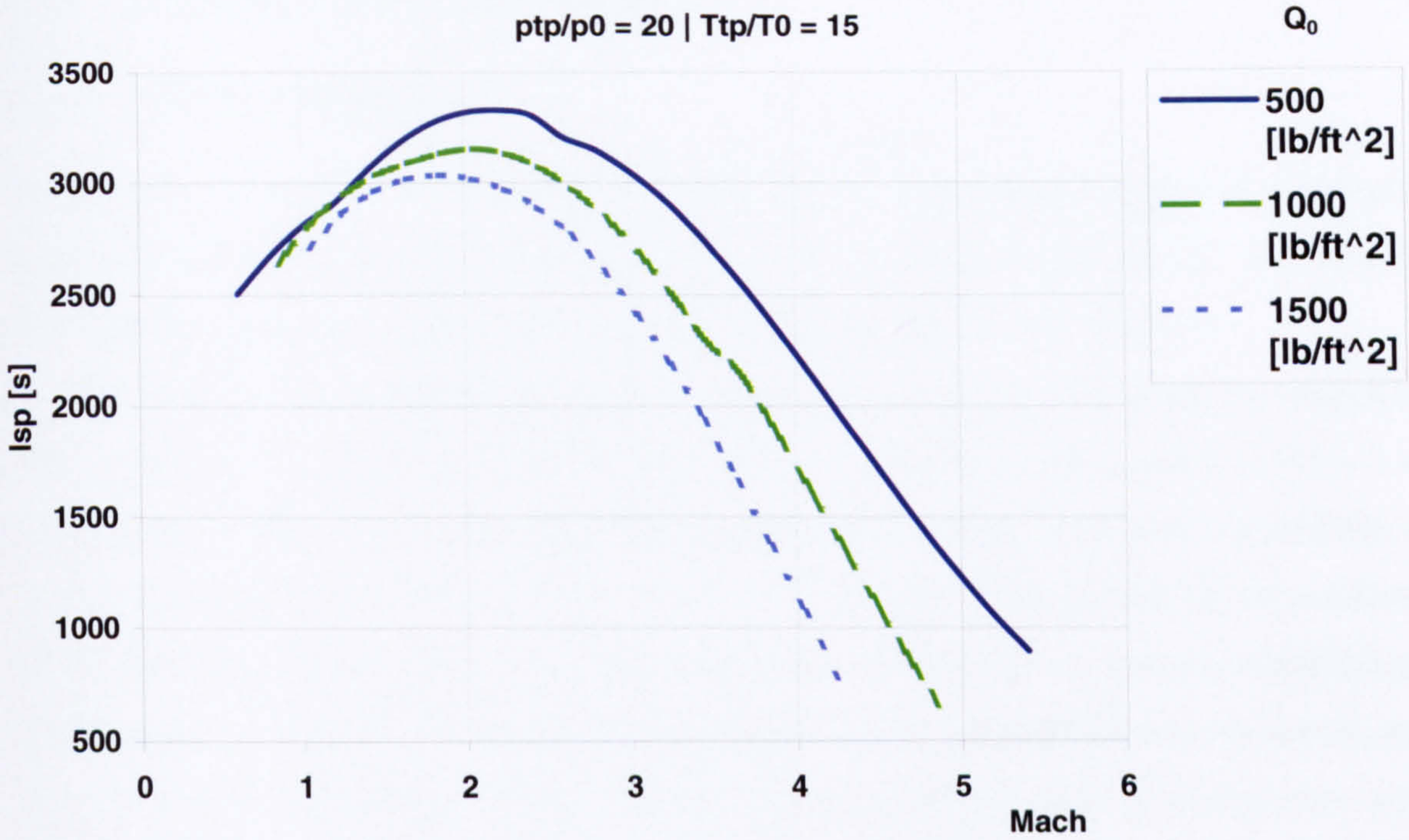


Figure 7.17: Variation of specific impulse as a function of Q_0 for a range of Mach numbers.

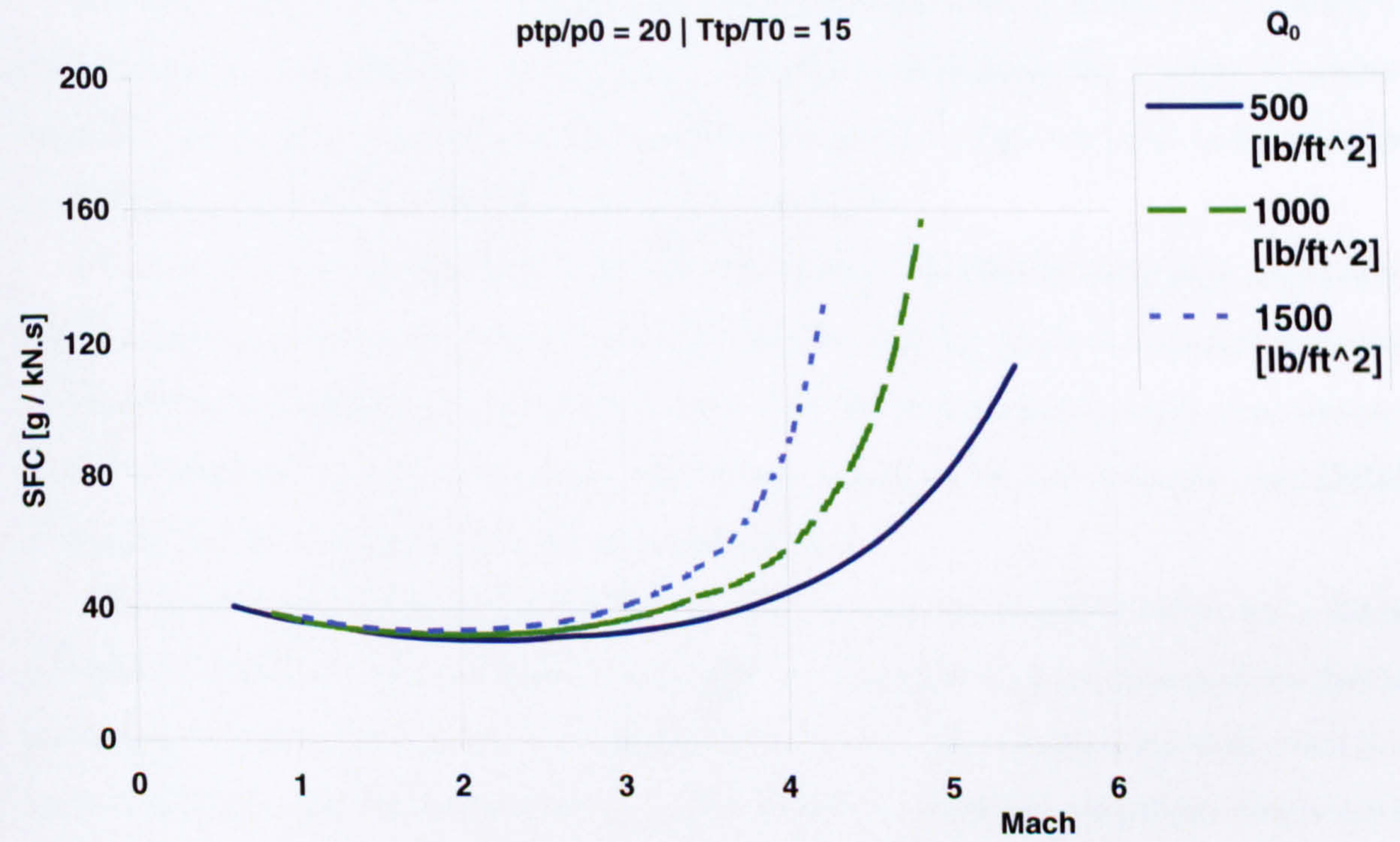


Figure 7.18: Variation of specific fuel consumption as a function of Q_0 for a range of Mach numbers.

7.3 Performance-Matching

7.3.1 Cycle Analysis

Referring to Figure 6.6, the turboramjet performance estimation and analysis is an integral part of thrust-matching with data from the on-design scramjet known a priori and analysis that was based on the simple stream thrust analysis presented in Chapter 4.

The specific thrust graph of Figure 7.19 provides the data to determine the mass flow ratio required to achieve the desired thrust at the scramjet transition speed of Mach 5 at an altitude of $30km$. This graph assumes a design Mach number of 2.5 and an altitude of $15.2km$ arbitrarily as a design point. The plot is obtained using stream thrust analysis, which takes the fuel/air ratio as one of its parameters. It relies on momentum relationships and a control volume that represents the on-design freestream capture area to nozzle exit area. It is assumed that the velocity vector is aligned with the local axial direction with the throughflow area perpendicular to that direction. The thrust produced by the scramjet during constant altitude acceleration is shown in Figure 7.20 along with the thrust curves for the turboramjet at different altitudes shown in the insert.

For this example, four turboramjet units are used, each with a design $\dot{m}_0 = 136kg/s$, that translates to a reference area of $A_{0_{ref}} = 0.98m^2$. Increasing the number of engine modules, will increase thrust but with a penalty of increased weight and cost and reduction in available propellant fraction for a given size of vehicle.

The turboramjet displays high values for the specific Impulse at mid-range supersonic Mach numbers as shown in Figure 7.21. The specific impulse graph is matched with the scramjet through iteration on the primary flow variable as described in a previous section. Any matching of I_{sp} has to maintain the thrust matching for the scramjet and HICAD performs this by undergoing an iteration procedure.

The number of engines is user defined in order to meet the required thrust for a Mach 5 scramjet transition. The number of turboramjets is limited to a maximum of six due to packaging requirements for the example presented later. The design mass flow must not be too large else the reference area $A_{0_{ref}}$ will exceed the allowable waverider dimensions. Using six engines instead of four requires smaller engine diameters, hence inlet depth for a given total thrust and therefore packaging and integration becomes much easier.

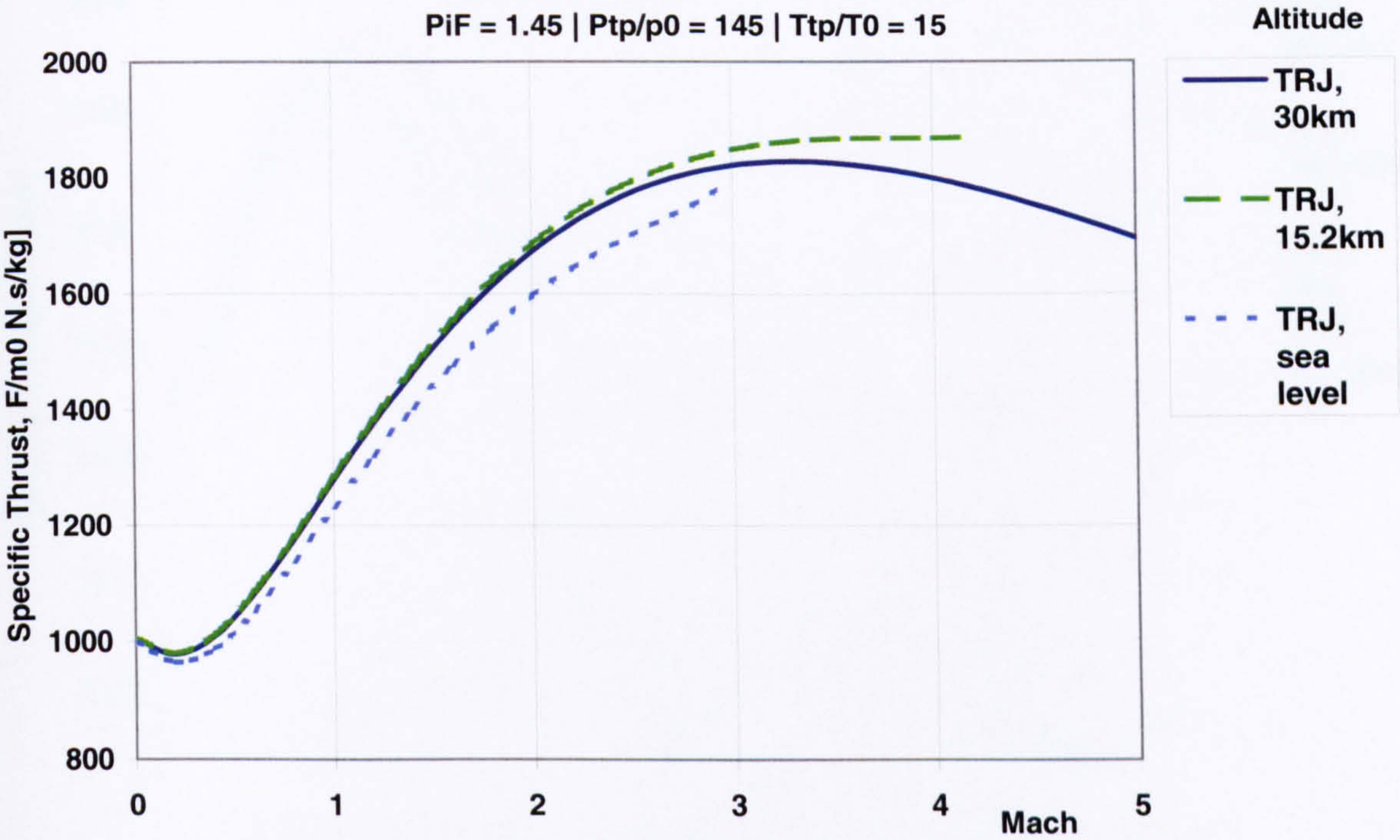


Figure 7.19: Specific Thrust at different altitudes.

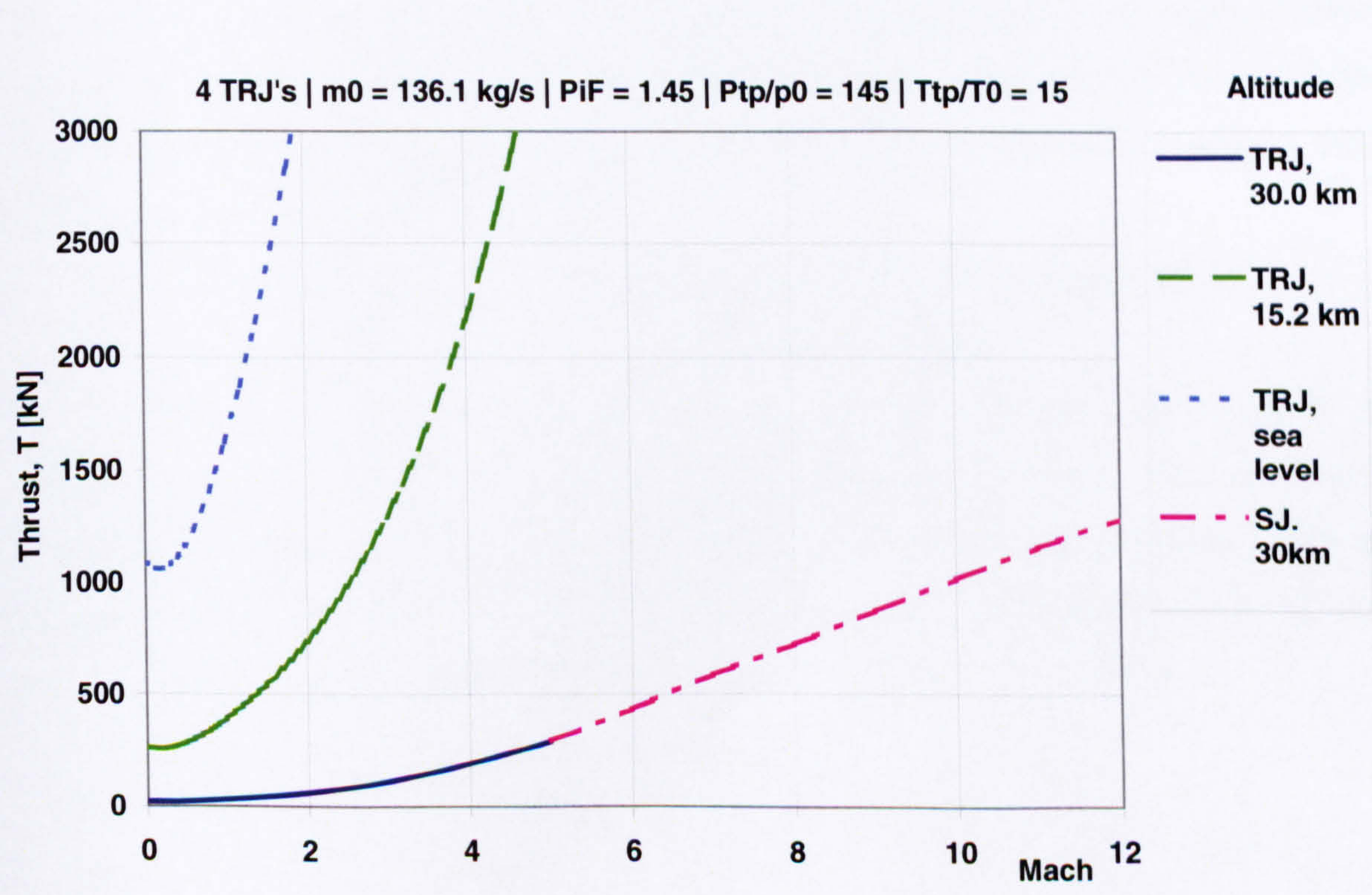


Figure 7.20: Thrust-Matching of low-speed and high-speed engine.

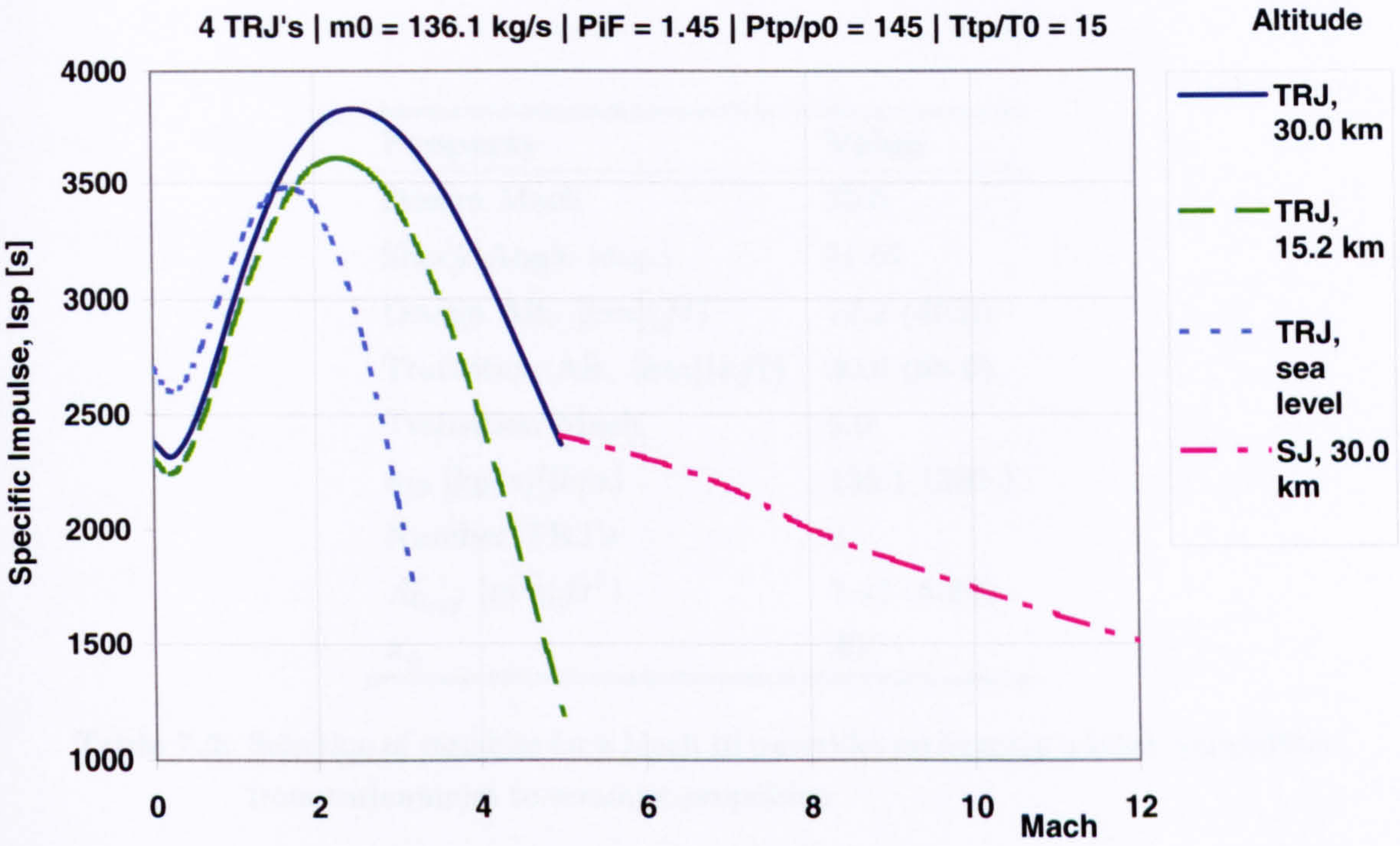


Figure 7.21: Thrust Matching of low-speed and high-speed engine.

7.3.2 Integration of IMOC

In contrast to the nozzle expansion for the performance matching above, which is based on the formulation by Heiser and Pratt (1994), a different sizing point of Mach 2.0 and an altitude of $12.2km$ $(40kft)$, was selected to demonstrate performance-matching using the more advanced nozzle integration.

Here, the salient features of a Mach 10 waverider example are presented.

Table 7.2 summarises the variables selected for this example.

The process automatically changes the values for Ptp/P_0 and Ttp/T_0 and if not matched, the user is prompted to input new variable selections other than these aforementioned variables. Figures 7.22 and 7.23 show the smooth transition between both the thrust and specific impulse for a Mach 10 waverider using the variables given in the table above. A tolerance of 2.5% was used when searching for a break condition.

Property	Value
Design Mach	10.0
Shock Angle $[deg.]$	11.67
Design Alt. $[km](ft)$	12.2 (40.0)
Transition Alt. $[km](kft)$	30.0 (98.0)
Transition Mach	5.0
$\dot{m}_0$ $[kg/s](lb/s)$	136.1 (300)
Number TRJ's	6
$A_{0_{ref}}$ $[m^2](ft^2)$	2.42 (8.26)
π_c	30

Table 7.2: Selection of variables for a Mach 10 waverider undergoing a Mach 5 transition from turboramjet to scramjet propulsion.

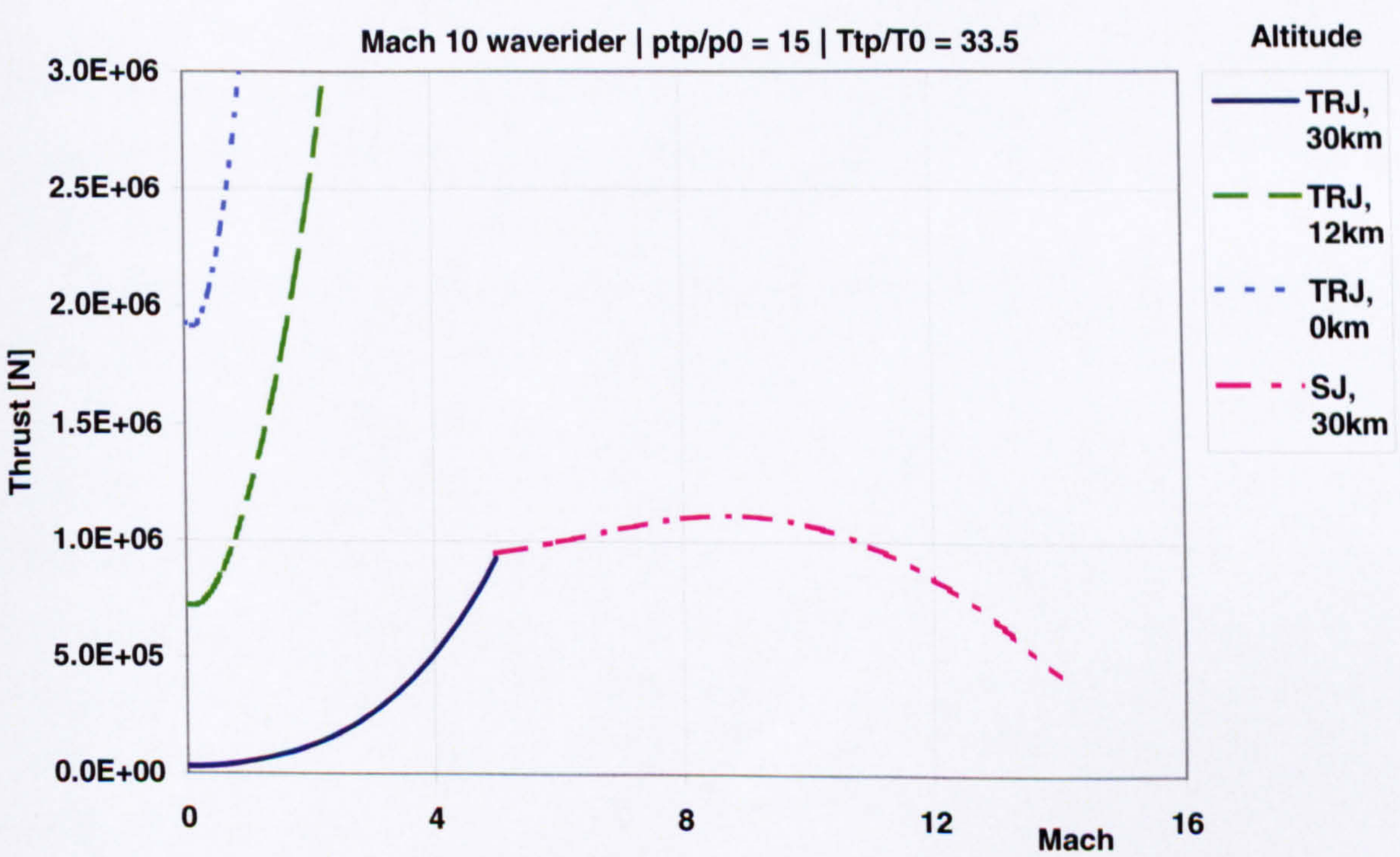


Figure 7.22: Thrust Matching of low-speed and high-speed engine for a Mach 10 waverider.

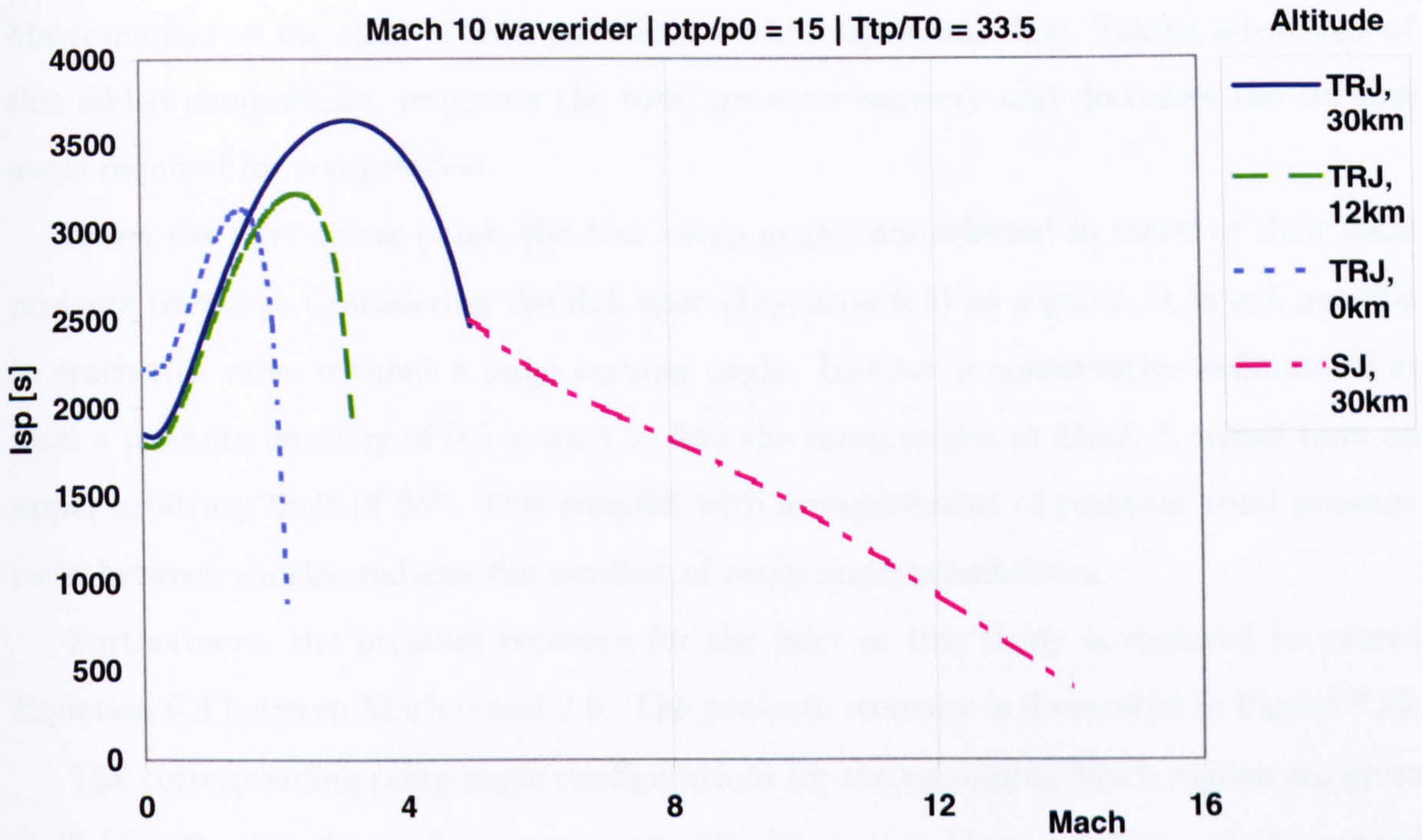


Figure 7.23: Specific Impulse Matching of low-speed and high-speed engine for a Mach 10 waverider.

7.4 Low-Speed Inlet sizing

The mass flow variation with Mach number generated from the off-design analysis above, forms the basis for the low-speed inlet design. The inlet area variation, A_0/A_{0ref}, for the Mach 10 waverider is illustrated in Figure 7.24.

The minimum can be seen to occur at the design point, which is Mach 2, at an altitude of $12.2km$. The fixed inlet capture area (A_1) must exceed the largest required mass flow area at freestream conditions A_0 by incorporating a 4% boundary layer bleed added as a safety factor. Inspection of Figure 7.24 shows the most demanding condition to determine the size of the inlet (A_1), occurs at Mach 5 at an altitude of $12km$. However, it has been assumed earlier that transition occurs at $30km$ and therefore is considered as the most demanding condition instead. Inlet sizing at the hypersonic cruise altitude of $30km$ ($98kft$) in the present example is likely to meet requirements at lower altitudes and off-design Mach numbers.

Prior to the low-speed inlet-ramp system, the freestream flow is compressed and decelerated using first a) the semi-span angle of the forebody and b) the fixed geometry two-dimensional planar ramp. Therefore, the variable-geometry ramps experience a lower

Mach number at the start of their geometry during supersonic flow. Taking advantage of this added compression, improves the total pressure recovery and decreases the turning angle required for compression.

Given the inlet sizing point, the four ramp angles are selected in merit of their total pressure recovery. Considering the MIL spec (Equation 6.3) as a guide, it is not possible to reach this value without a large turning angle. Instead, a conservative estimate of at least a pressure recovery of 0.5 is used to find the ramp angles at Mach 5, which have an upper arbitrary limit of 25°. This coupled with a requirement of constant total pressure ratio between shocks, reduces the number of ramp angle possibilities.

Furthermore, the pressure recovery for the inlet in this study is required to exceed Equation 6.3 between Mach 0 and 2.5. The pressure recovery is illustrated in Figure 7.25.

The corresponding ramp angle configurations for the remaining Mach regime are given in Table 7.3. The first column represents the freestream Mach number and the second represents the Mach number after the flow is compressed through the forebody and inlet ramp shocks. The total turning angle for this configuration is 24°. In this table, one can notice that the ramp angles are the same after a freestream Mach number of 3.2. This is because the total turning angle is initially determined at the sizing point, Mach 5 in this example, and once this turning angle is reached, the ramp angles are fixed at that position in order to comply with the on-design configuration.

To further illustrate the sizing analysis, the area ratio, A_{0i}/A_s is plotted in Figure 7.26 for this inlet. This curve allows the area ratio A_s to be determined. The reference area A_1 is found to be $1.84m^2$, which translates to an inlet size square size of $1.36m$. The diameter will be that corresponding to A_1, which results in a value of $1.53m$.

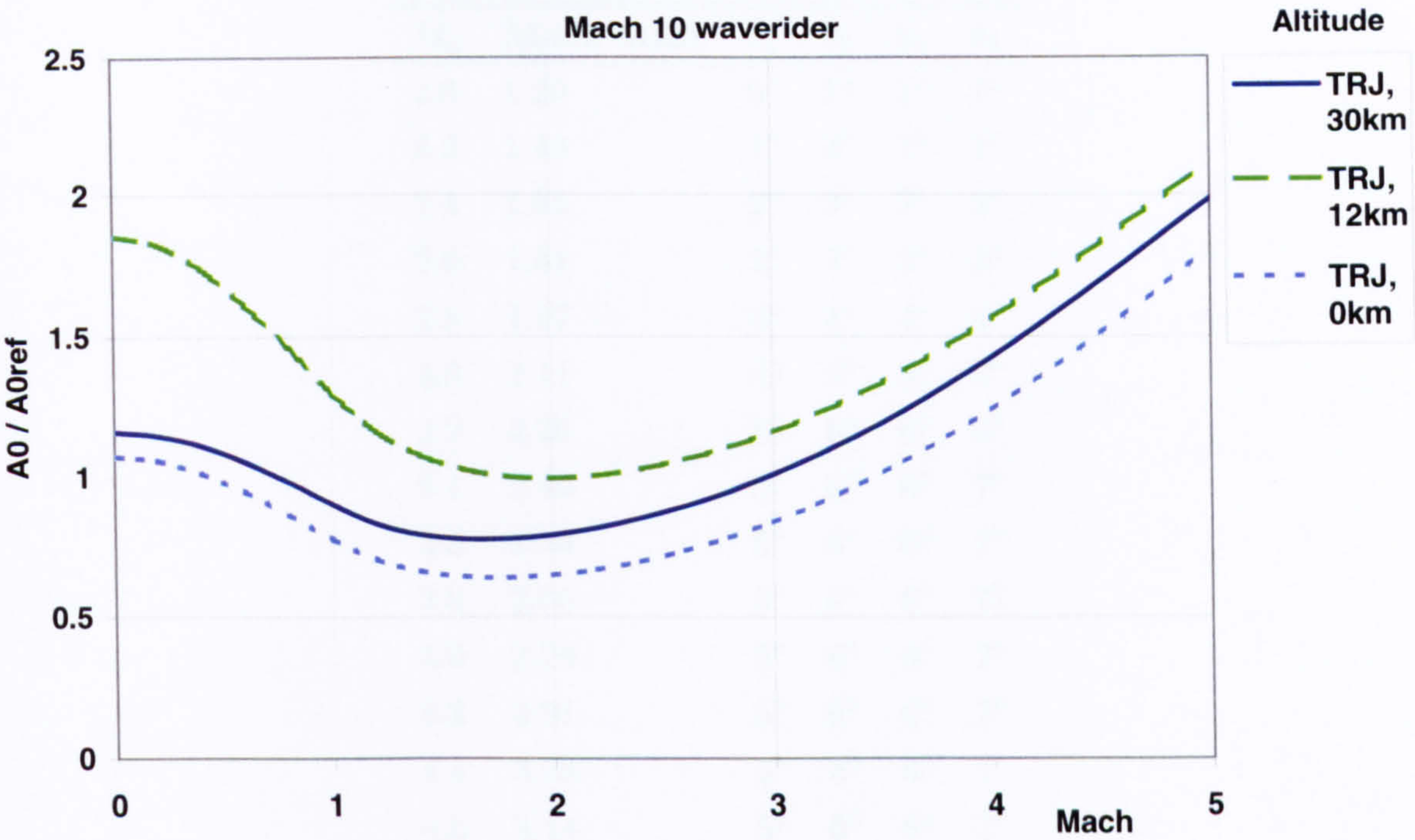


Figure 7.24: Inlet area variation with Mach number for an $A_{0_{ref}} = 2.42m^2$ and minimum occurring at the design point Mach 2, 12.2km.

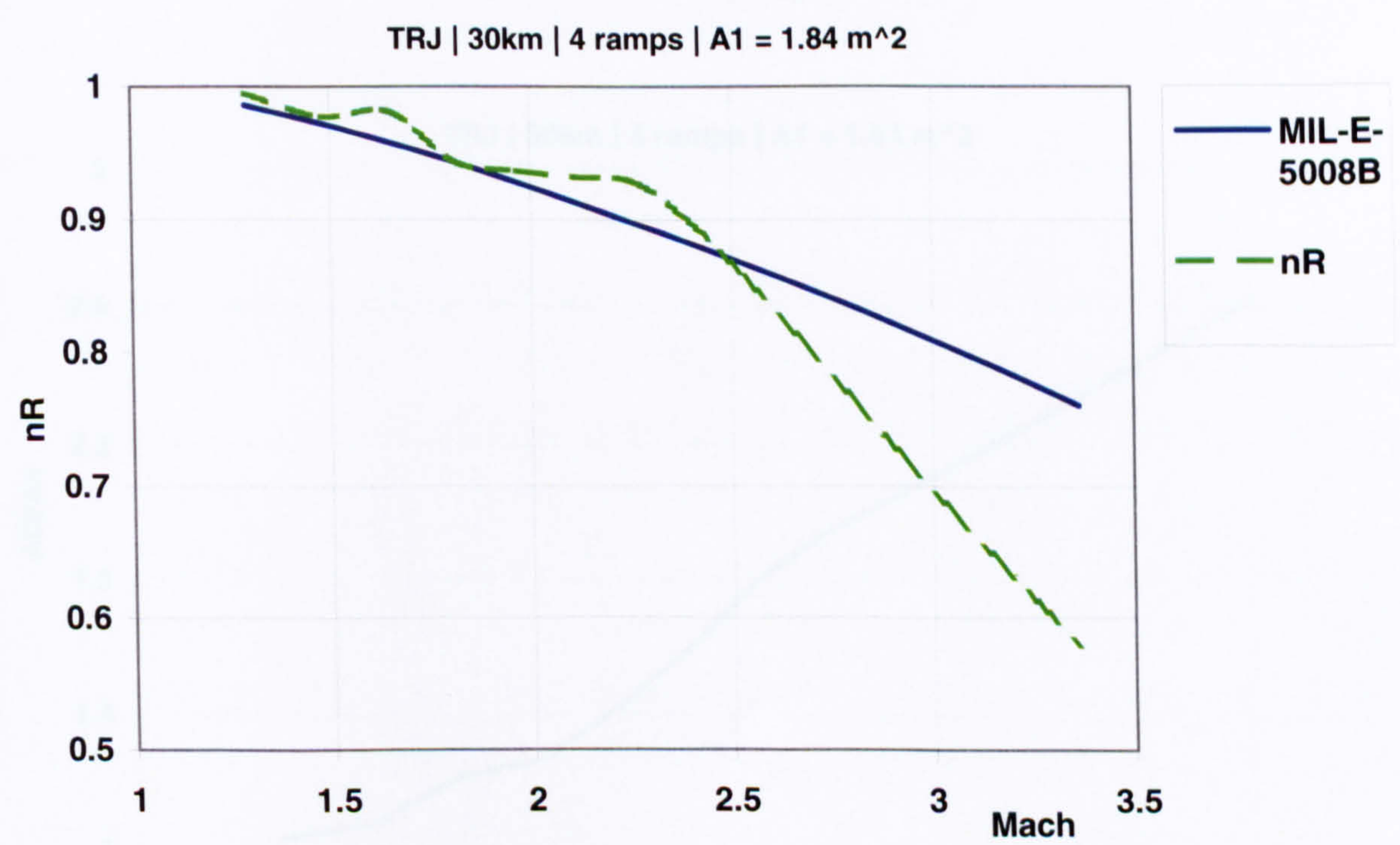


Figure 7.25: Total pressure recovery for a 4-ramp variable geometry external compression inlet. The recovery exceeds the MIL spec up to Mach 2.5 then trails off.

M_0	**Mach start**	θ_1	θ_2	θ_3	θ_4
2.0	1.29	0°	1°	1°	1°
2.2	1.48	1°	2°	1°	1°
2.4	1.65	2°	3°	3°	3°
2.6	1.81	2°	3°	3°	3°
2.8	1.97	3°	4°	4°	4°
3.0	2.11	4°	5°	5°	5°
3.2	2.26	5°	6°	6°	6°
3.4	2.40	5°	6°	6°	7°
3.6	2.53	5°	6°	6°	7°
3.8	2.66	5°	6°	6°	7°
4.0	2.79	5°	6°	6°	7°
4.2	2.91	5°	6°	6°	7°
4.4	3.03	5°	6°	6°	7°
4.6	3.14	5°	6°	6°	7°
4.8	3.25	5°	6°	6°	7°
5.0	3.36	5°	6°	6°	7°

Table 7.3: Inlet ramp angle selections.

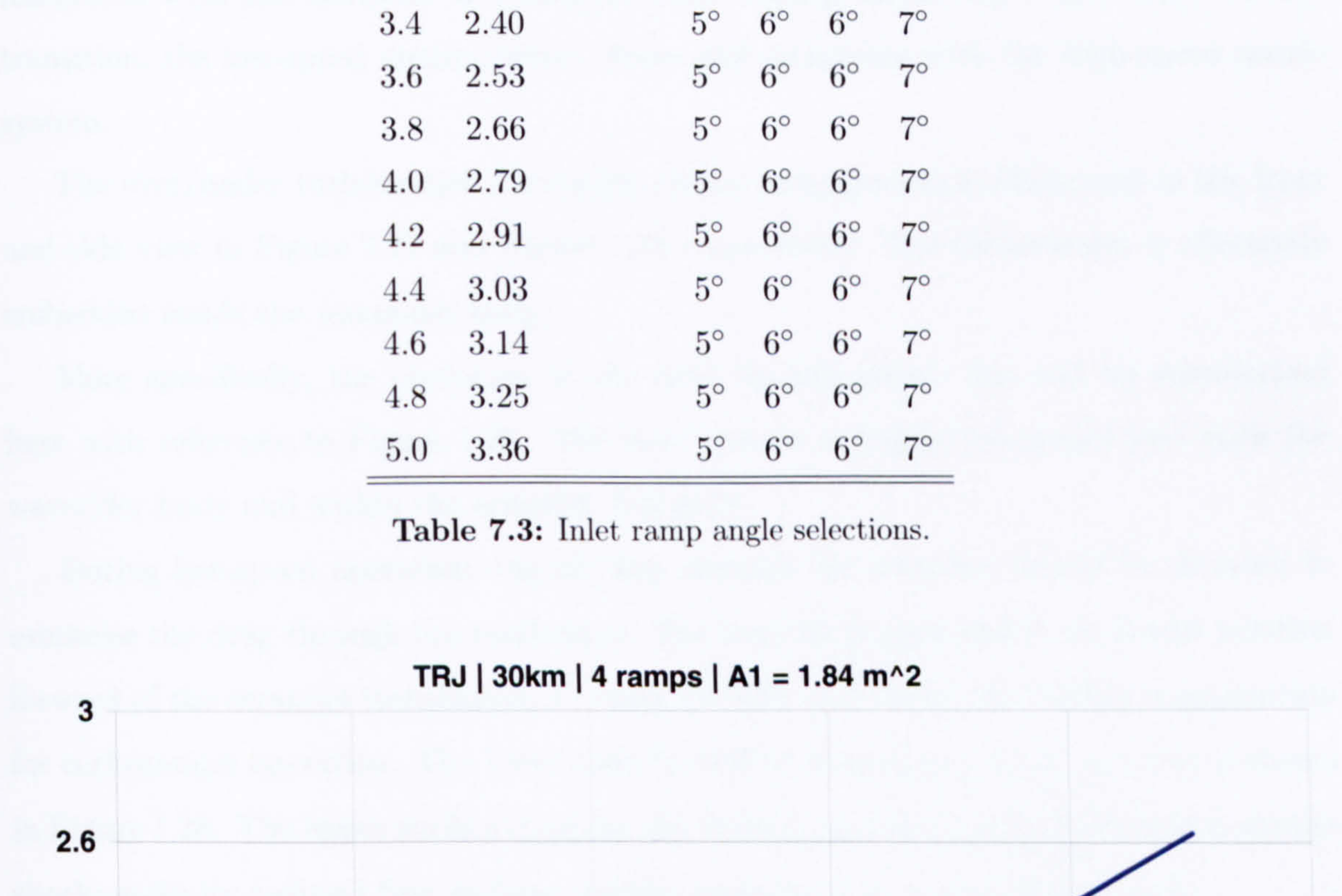


Figure 7.26: Required inlet area ratio variation with Mach number.

7.5 Airframe-Propulsion Integration

The low-speed system should be capable of providing adequate thrust for takeoff and transonic / supersonic acceleration to the high-speed propulsion system transition Mach number. The low-speed system will cease operation above transition so mechanisms need to be employed to prevent the airflow through the low-speed inlet system and divert it to the scramjet during hypersonic flight. The low-speed nozzle system is also highly integrated with the airframe and operates only during turboramjet operation. Above transition, the low-speed nozzle system closes and integrates with the high-speed nozzle system.

The over/under turboramjet / scramjet engine arrangement is illustrated in the front and side view in Figure 7.27 and Figure 7.28 respectively. The turboramjet is effectively embedded inside the waverider body.

More specifically, the operation of the cowl lip and nozzle flap will be summarised here with reference to Figure 7.28. The inlet system is highly integrated into both the waverider body and within the scramjet flowpath.

During low-speed operation, the air flow through the scramjet should be diverted to minimise the drag through the combustor. The cowl lip is deployed to its lowest position forward of the scramjet installation, to open the area and match the airflow requirements for turboramjet operation. The lower cowl lip will be hinged on a pivot and this is shown in Figure 7.28. The upper surface contains the variable geometry ramp system to maintain shock-on-lip for reduced flow spillage thereby ensuring a good pressure recovery.

During transition to a scramjet around Mach 5, the cowl lip retracts upwards to allow the air flow to enter the combustor and becomes an integral part of the high-speed inlet. That stops the air flow to the turboramjet to protect the structural integrity of the fan and turbine blades and to avoid excessive heating. The transition stage of the inlet cowl and nozzle is illustrated in Figure 7.29. In the high-speed mode, the flow is first compressed by the forebody geometry and next by the ramp angle whose selection is based on the discussion of chapter 4. The thrust is entirely due to the scramjet at this point. For high-speed operation the cowl and nozzle are fully retracted as shown in Figure 7.30. The detailed off-design analysis of the cowl lip has not been considered in the present analysis. Only the on-design operation, which is critical for conceptual design, has been defined.

The requirement for variable-geometry for the scramjet inlet can be relaxed as discussed by Henry and Anderson (1972) when considering the excess weight and complexity with only a marginal improvement in performance. However, if a larger range of flight conditions experienced by engine during normal operation then variable-geometry is deemed necessary.

Other important considerations during airframe/propulsion integration include the longitudinal position of the turboramjet. If this is located too forward then the nozzle duct length becomes excessive, which increases the cooling requirement in a long nozzle. A longer inlet is more acceptable, by moving the system further aft. But this changes inlet mass capture and the design of the low-speed inlet will need to modified accordingly. Vertical location is also important for maximising the useful internal volumetric capacity of the vehicle.

Any change in the low-speed system will have a knock-on effect on the scramjet inlet especially in maintaining the shock-on-lip and minimising interference from the low-speed cowl during hypersonic cruise operation. The approach adopted in this study is to primarily design for mission requirements (range, speed, vehicle length) and then adapt the design accordingly to meet the other requirements.

The turboramjet nozzle flap operates in a similar manner to the cowl lip at the inlet plane. During low-speed operation, the nozzle flap opens into the existing nozzle geometry to allow for exhaust flow. At hypersonic speeds, the nozzle flap is closed and becomes part of the high-speed nozzle to ensure streamlined surfaces for expansion from the scramjet combustor. The width of the nozzle must be large enough to accommodate both the scramjet and turboramjet for low-speed thrust adequately up to transition. This is shown in Figure 7.27 for the inlet system, which has a similar width to the scramjet both maintaining flow uniformity and compatibility with the existing inlet system.

The shape of the nozzle upper surface affects the magnitude of lift produced and the cowl needs to be positioned such to maximise the lift. For the present study, the nozzle cowl is at a fixed angle of 6 degrees to generate an expansion fan.

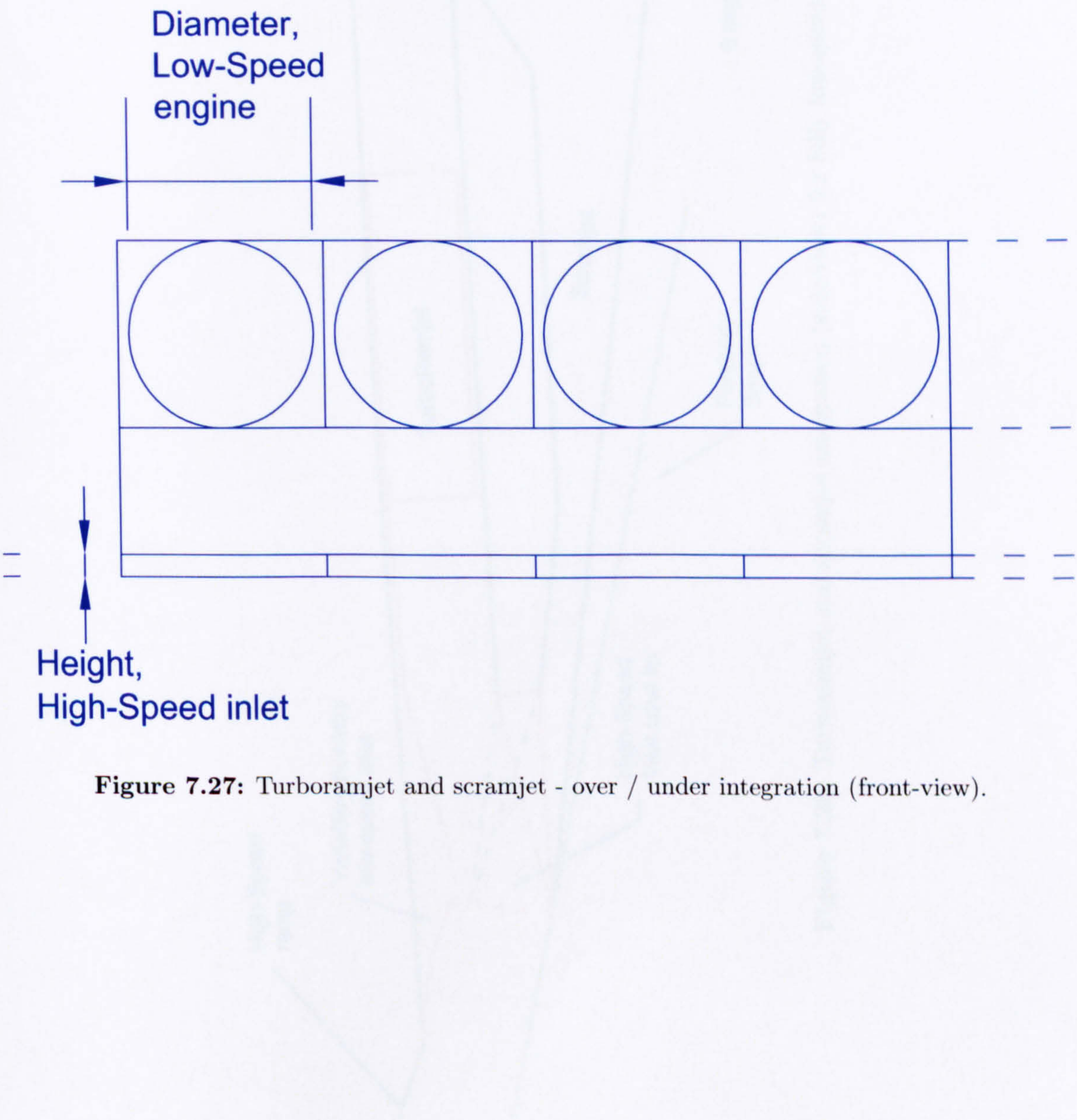


Figure 7.27: Turboramjet and scramjet - over / under integration (front-view).

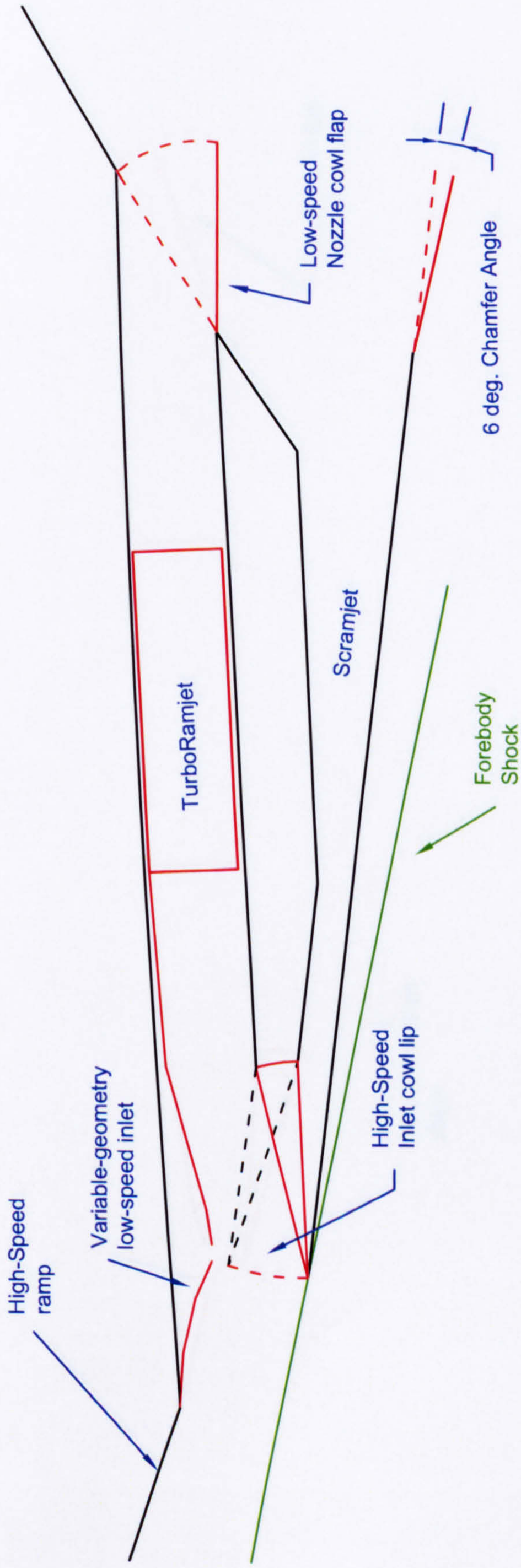


Figure 7.28: Turboramjet and scramjet integration (side-view) for fully low-speed operation.

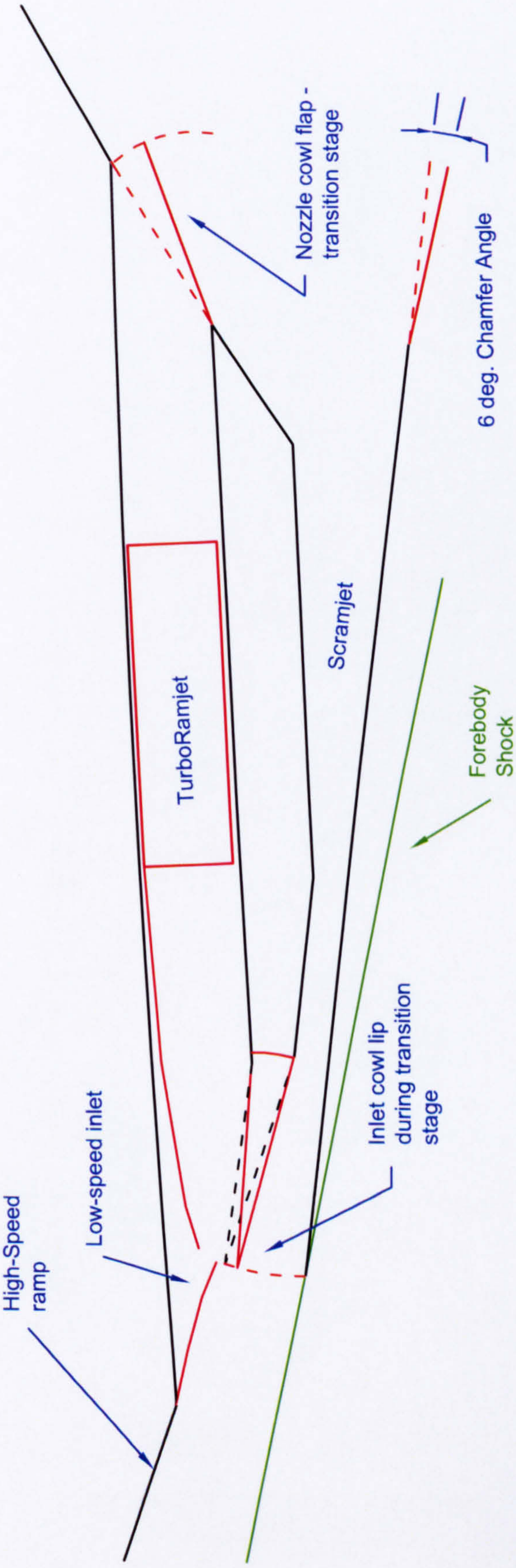


Figure 7.29: Turboramjet and scramjet integration (side-view) for transition stage.

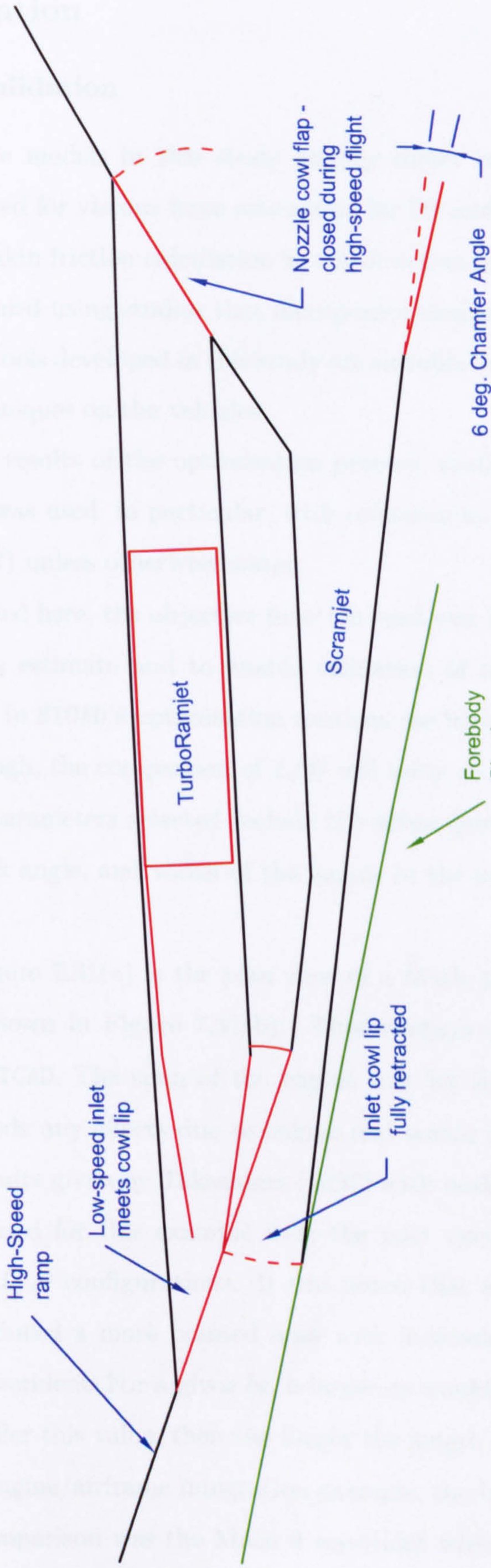


Figure 7.30: Turboramjet and scramjet integration (side-view) for high-speed cruise operation.

7.6 Optimisation

7.6.1 Model Validation

The majority of the models in this study employ direct inviscid methods. Although methods are employed for viscous force estimation for lift and drag using a turbulent flow assumption for the skin friction calculation in the direction of the surface velocity vector. Validation is performed using studies that incorporate similar strategies.

The conceptual tools developed in this study are suitable for considering the application of optimisation techniques on the vehicles.

To compare the results of the optimisation process, available literature on conically-derived waveriders was used, in particular, with reference to work by O'Neill (1992) and Bowcutt *et al.* (1987) unless otherwise stated.

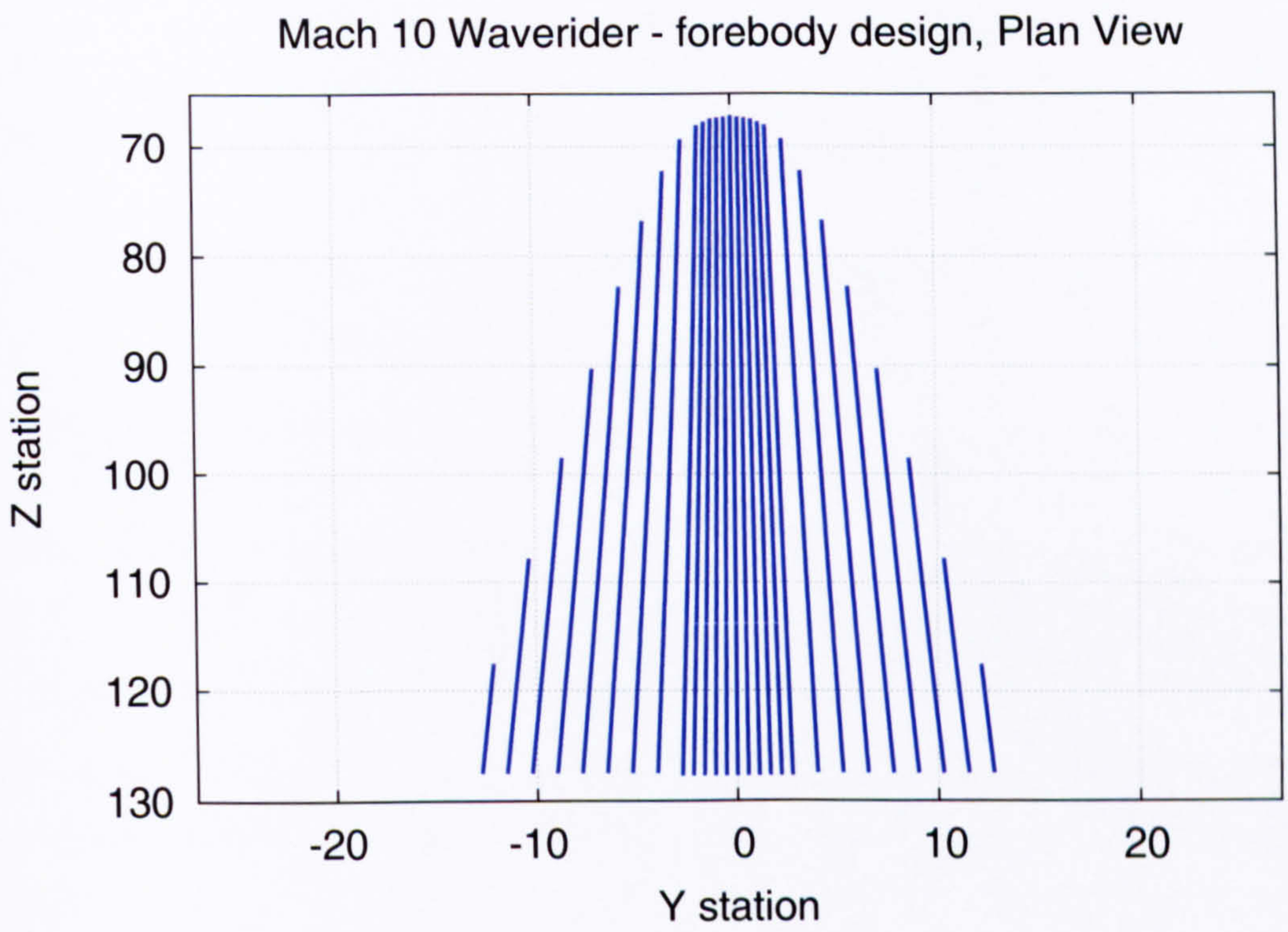
In all cases studied here, the objective function used was $Isp \times L/D$ as this is suitable for an initial design estimate and to enable validation of the results. The number of parameters selected in HICAD's optimisation routines are less than similar studies for this type of work, although, the comparison of L/D will serve as a useful example.

The optimised parameters selected include the seven geometric wing curve variables, the generating shock angle, and width of the engine in the inlet plane as shown in Table 4.2.

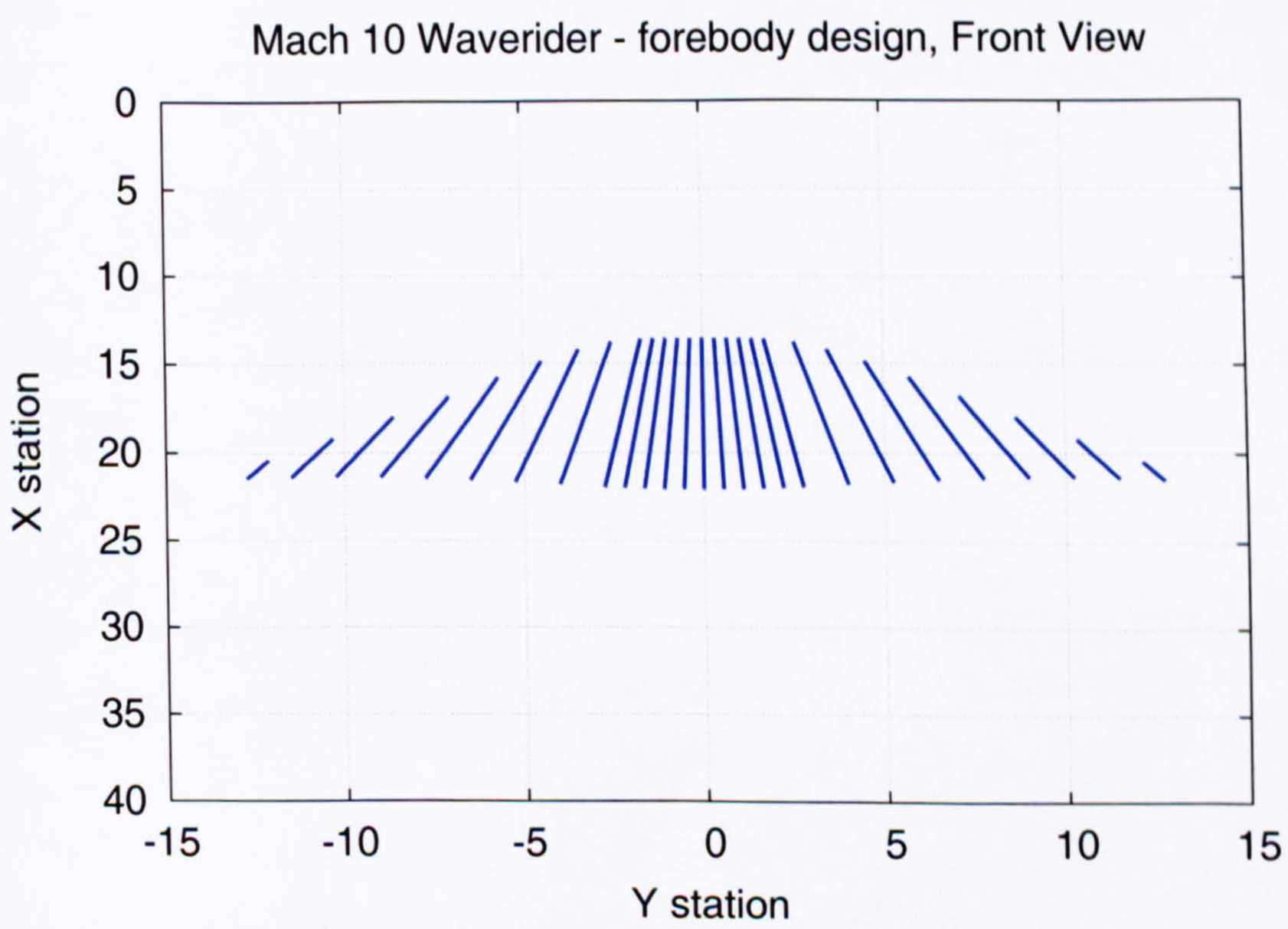
Presented in Figure 7.31(a) is the plan view of a Mach 10 pure waverider shape and the front view is shown in Figure 7.31(b). That configuration geometry produced an $L/D = 7.8$ using HICAD. The span of the engine was $5m$ in the inlet plane. The L/D value does not include any effects due to engine and nozzle integration. This value is in accordance with results given by Takashima (1997) with under 1% error.

Variables optimised for this example were the inlet curve and wing curve shape to produce maximum L/D configurations. It was noted that a change in the ellipticity of the inlet curve produced a more pointed nose with increasing design Mach number for L/D maximised waveriders. For a given be, a larger ae would result in a shorter forebody length and the smaller this value, then the longer the length of the forebody.

In terms of an engine/airframe integration example, the baseline cruise vehicle configuration used for comparison was the Mach 9 waverider with a $60m$ total vehicle length,



(a) Plan view of L/D maximized Mach 10 Waverider.



(b) Front view of L/D maximized Mach 10 Waverider.

Figure 7.31: Multiple views of a Mach 10 waverider.

cruise altitude of $31,900m$ and $ae = 20$. The shock angle constraint had a minimum of $\epsilon_{min} = 11°$, and a maximum set at 14°. The combustor wall temperature was constant at $1000K$ and the altitude ensured the combustor entrance pressure was of the order of $0.6atm$.

As the number of variables differ between the HICAD and validation case, a discrepancy in the results is expected for a particular configuration. For example, the combustor has a large parameter set including the length of combustor and expansion ratio and the values used in HICAD will differ somewhat.

The nozzle was operated using a linear expansion upper surface as the polynomial surface was proving unstable during optimisation. The recurring problem was during computation of Mach numbers towards the trailing edge of the vehicle that would decrease in an unconventional manner. The reason behind this is due to IMOC's bezier curve part of the code, which tries to converge the final cowl expansion characteristics at the value for the computed length of nozzle. That was causing reflections upstream of the nozzle flowfield.

Presented in Figure 7.32, are the optimisation histories of a) the objective function, b) the L/D ratio and in Figure 7.33 is the Isp history. The number of iterations required for a maximised solution is 210 with a specified tolerance of 1×10^{-5}. Each point of the histories represents a simplex operation, that is, a reflection, expansion or contraction to arrive at function minimisation. The effect of λ has not been investigated in this study.

In Figure 7.34, the optimisation histories of 7 geometric wing curve points are shown and similarly in Figure 7.35 for the history of the shock angle and engine width. The number of iterations can be reduced if the tolerance is relaxed. Also the step size when calculating the lower surface has an effect on the number of trials.

The L/D value obtained for this case was 4.52, which is approximately 16% within quoted values for a Mach 9 vehicle as shown in Table 7.4

Routine	L/D
HICAD	4.52
Validation	3.9

Table 7.4: Difference in L/D values compared to HICAD.

This is reasonable given the range of variables possible in HICAD. The Isp value obtained was $1981s$ with a corresponding thrust value of $807491N$. The forebody length was found to be $L_{fore} = 39.5m$, combustor entrance pressure was $P_{comb} = 0.65atm$ and entrance temperature was $T_{comb} = 914K$.

Lift and Drag are shown in Figure 7.36(a) and Figure 7.36(b) respectively. Not all surfaces are required for Lift computation and similarly for Drag. This has been discussed in a previous chapter and saves significant computation time by accounting for force annulation effects. The total lift for this configuration was $4.67 \times 10^6 N$ and total drag was $1.03 \times 10^6 N$.

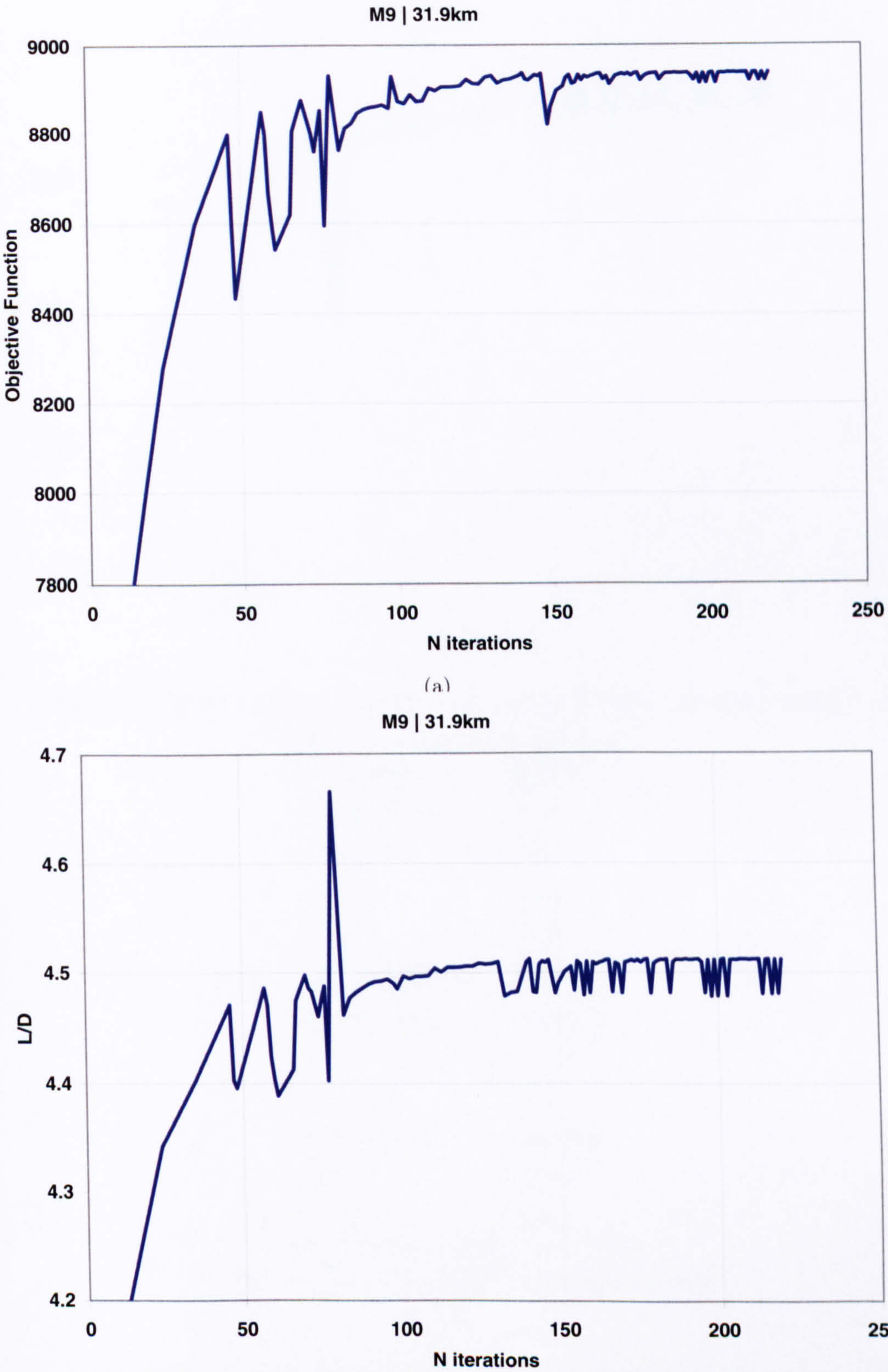
Finally, the front and plan view of this configuration are shown in Figure 7.37(b) and Figure 7.37(a). The half-width of the waverider at the tail station is $y_7 = 17.3m$. Although, not shown clearly on these figures, the top surface is aligned parallel to the freestream direction.

7.6.2 Mach 10 Waverider

For a Mach 10 example waverider cruising at $33km$, optimisation produced a maximum $L/D = 4.26$. The shock angle converged to $12.19°$ and the scramjet resulted in a span of $5.0m$ with a freestream capture area of $40.9m^2$ and $I_{sp} = 1775s$. The combustor entrance pressure was $P_{comb} = 0.69atm$ and entrance temperature was $T_{comb} = 1015K$. These results are summarised in Table 7.5.

The parameter a_e was increased to $20.5m$ from the default value of $20.0m$ as the latter was resulting in a forebody length of $48.6m$, which shortened the forebody length to $37.9m$. This is important once combustor lengths have to be accounted and leaving sufficient length for the nozzle for a given $60.0m$ waverider length.

Optimisation histories for the objective function is shown in Figure 7.38(a) along with the L/D ratio Figure 7.38(b). Figure 7.39 illustrates the history for Isp. The number of iterations required for a maximised solution was 222 with a specified tolerance of 1×10^{-4}.



(a)

(b)

Figure 7.32: Optimisation histories of the (a) objective function and (b) L/D factor for a Mach 9 baseline vehicle.

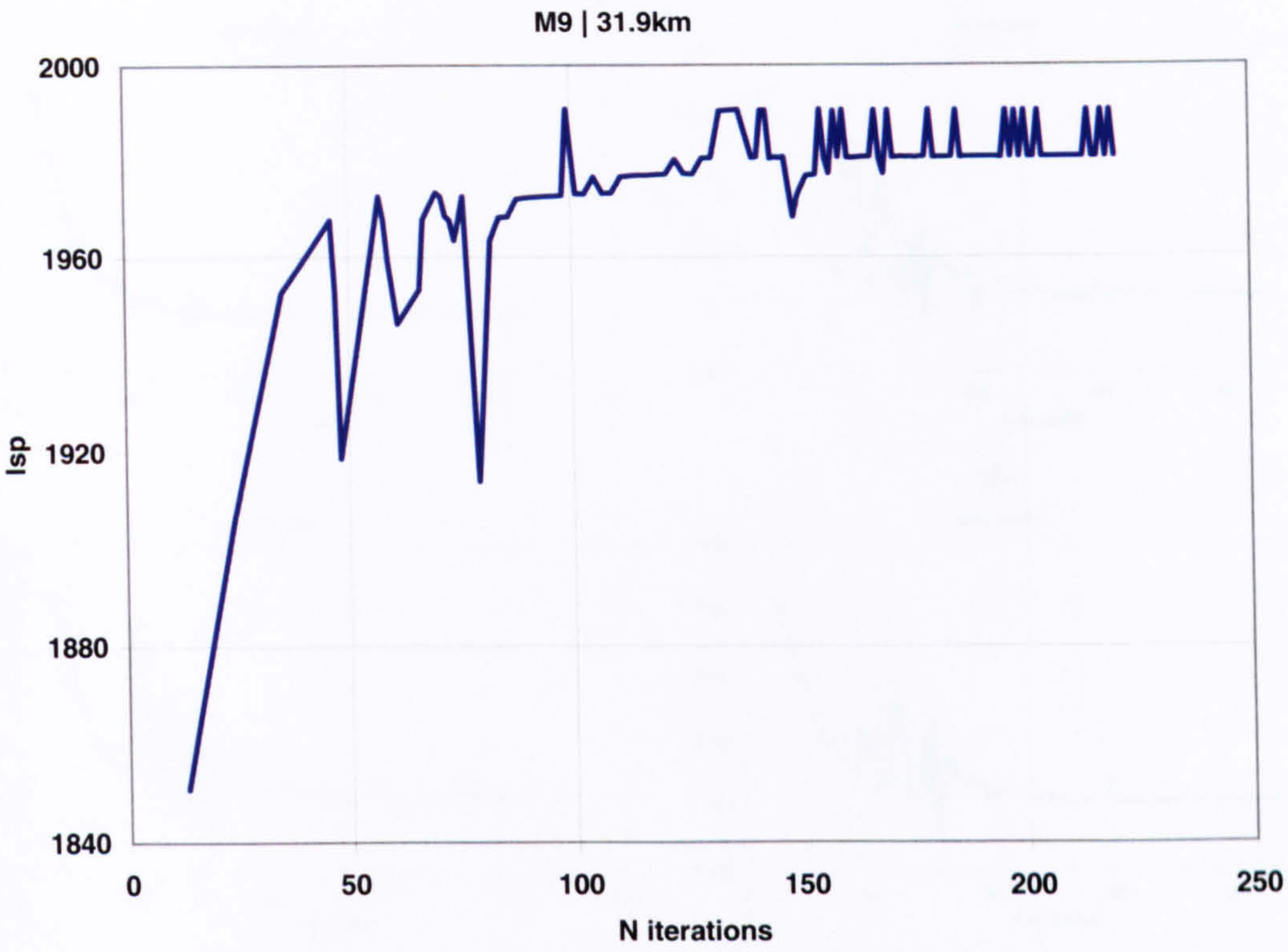
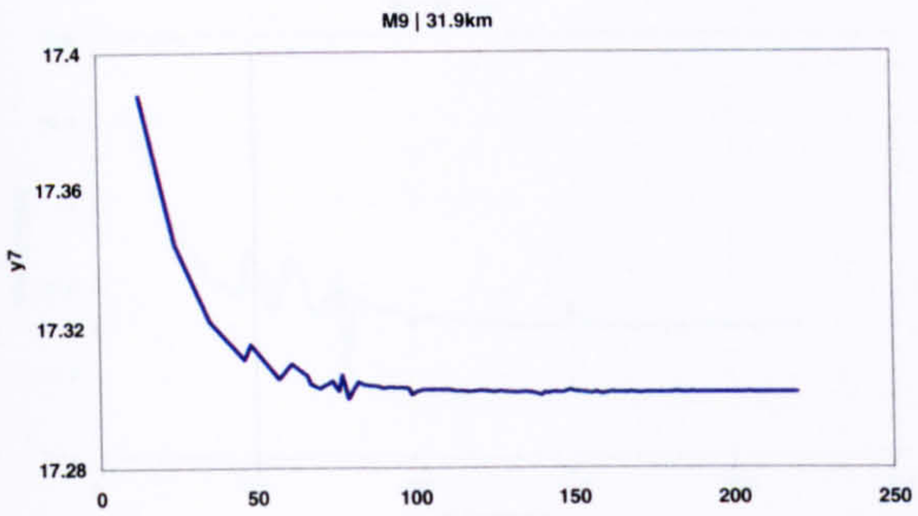


Figure 7.33: Optimisation history of the Isp for a Mach 9 baseline vehicle.

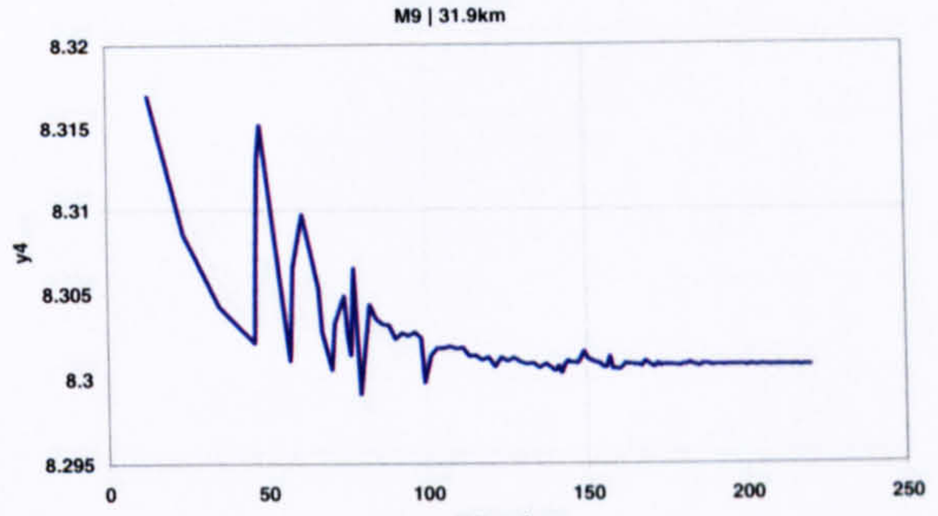
Parameter	**Input**
Design Mach	10.0
Design Alt. $[km]$	33.0
a_e $[m]$	20.5
dZ $[m]$	0.05
Veh. Length $[m]$	60.0
Parameter	**Output**
ϵ°	12.19
W_{eng} [m]	5.0
$Thrust$ [N]	701588
Isp [s]	1775
L/D	4.26

Table 7.5: Inputs and outputs for Mach 10 case.

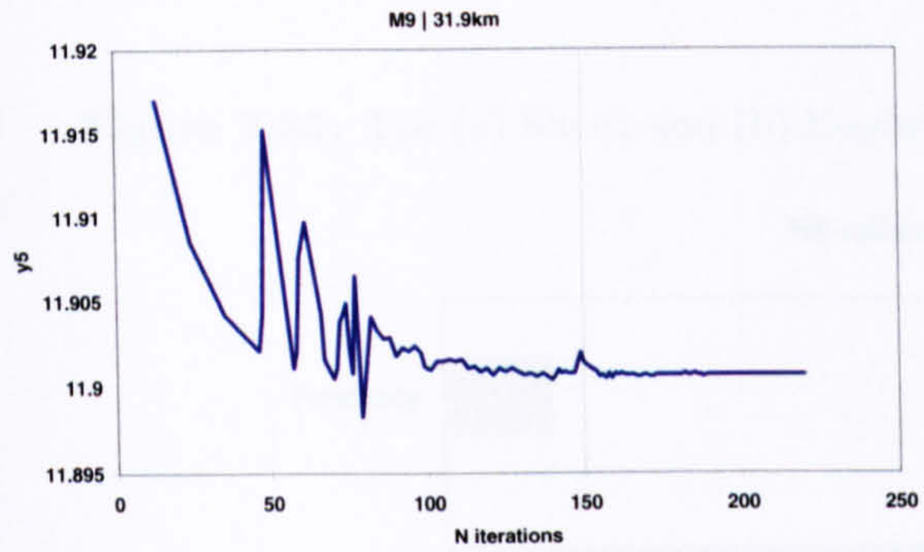
Figure 7.40 shows the optimisation history for the 7 geometric wing curve points and again similarly for the shock angle and engine width in Figure 7.41. The step sizes in the x station and z station were halved from previous runs and this increased the number of



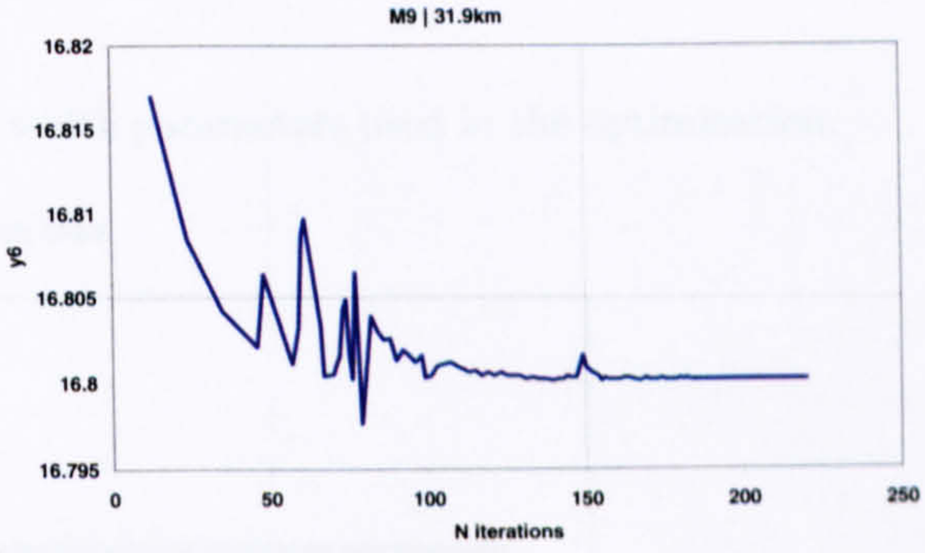
(a)



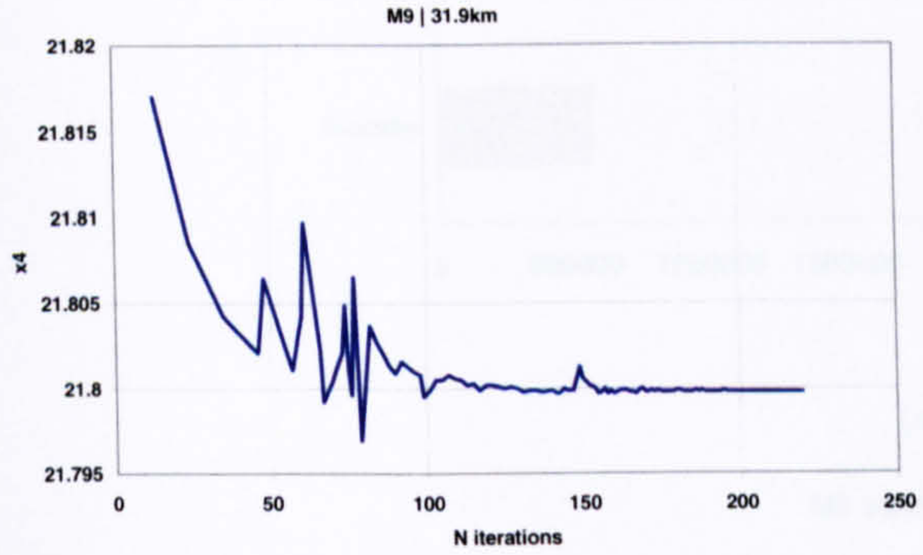
(b)



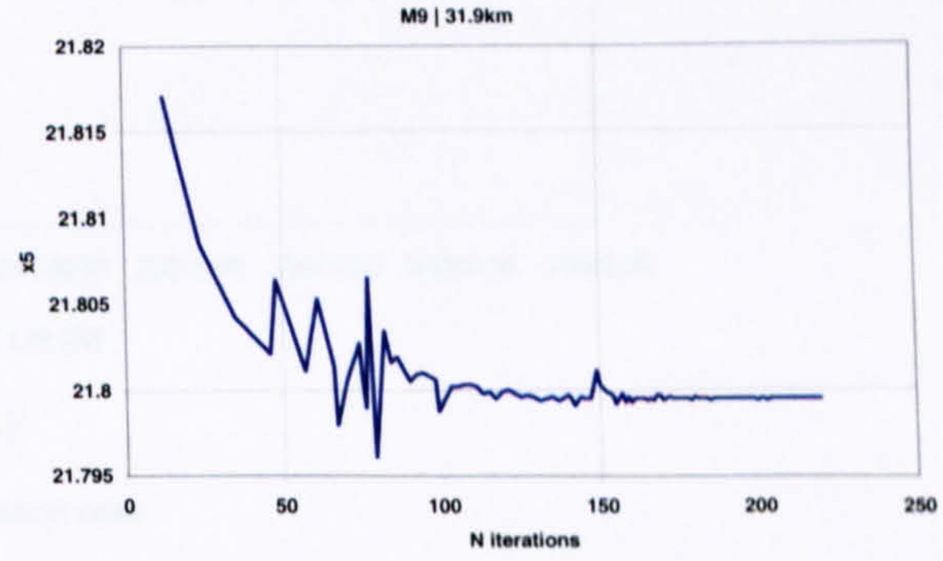
(c)



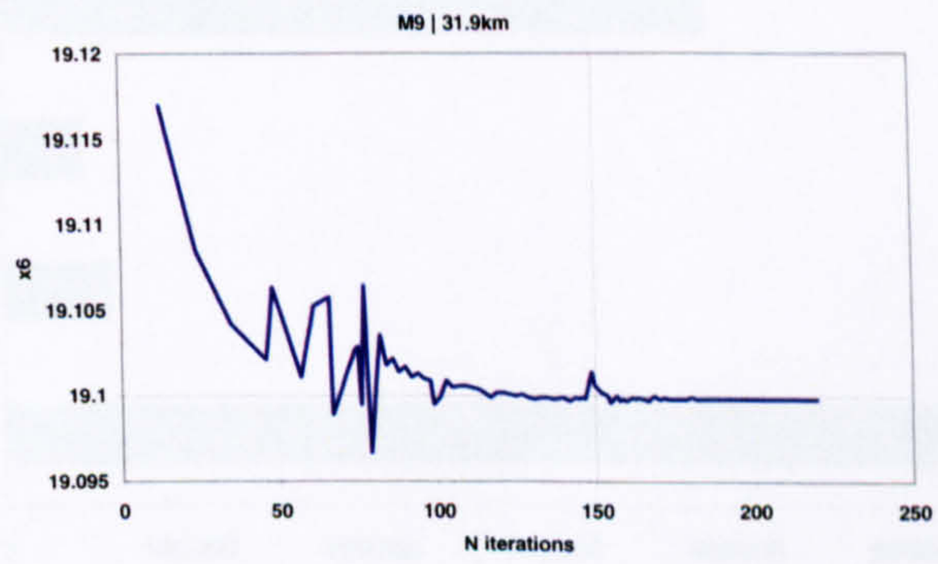
(d)



(e)

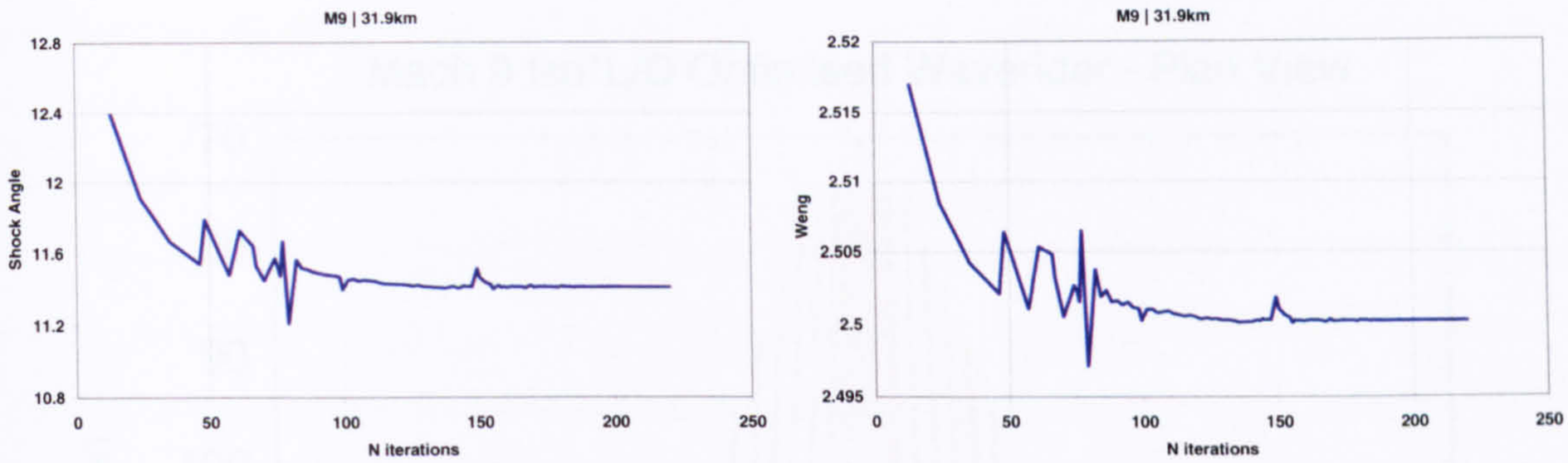


(f)



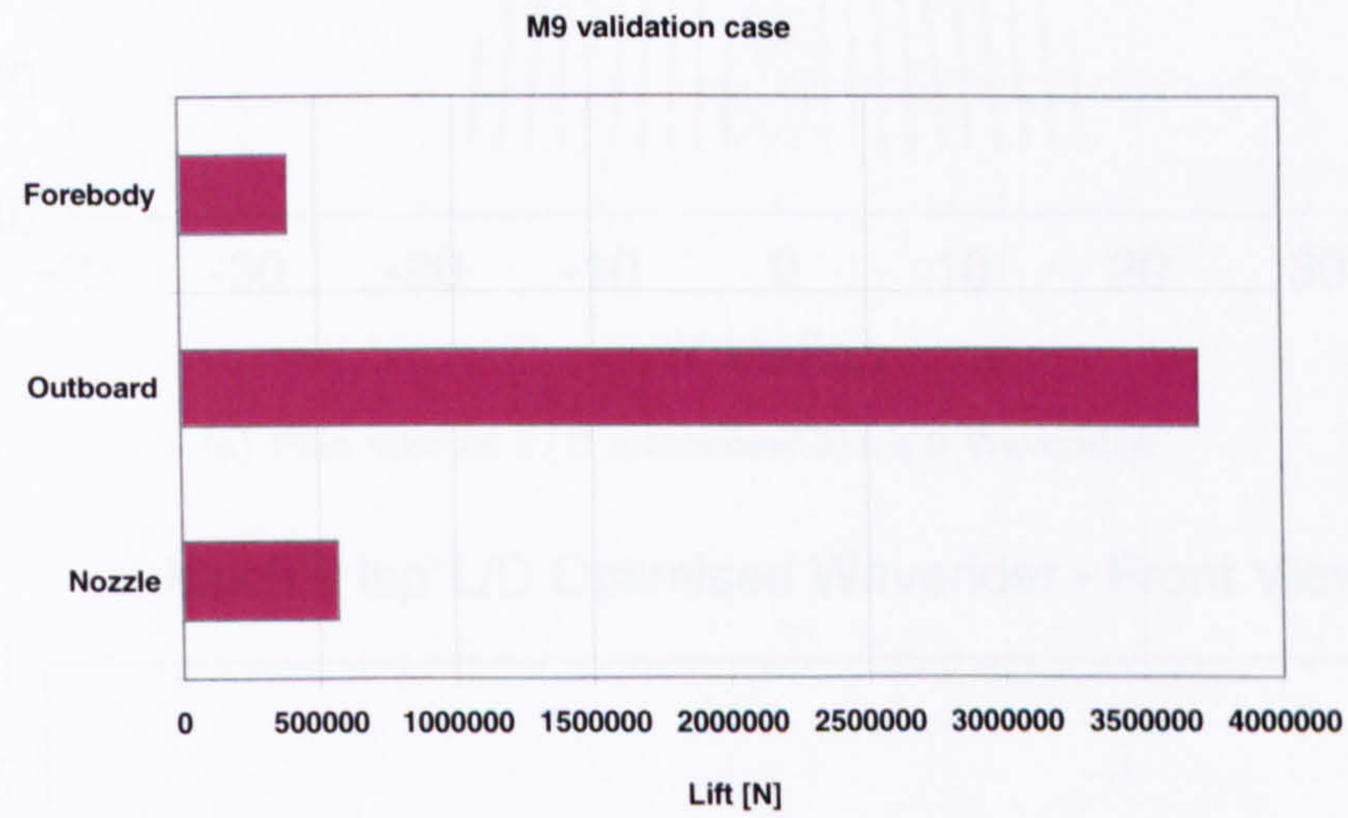
(g)

Figure 7.34: Optimisation history of the seven geometric wing curve variables that exist at the tail station.

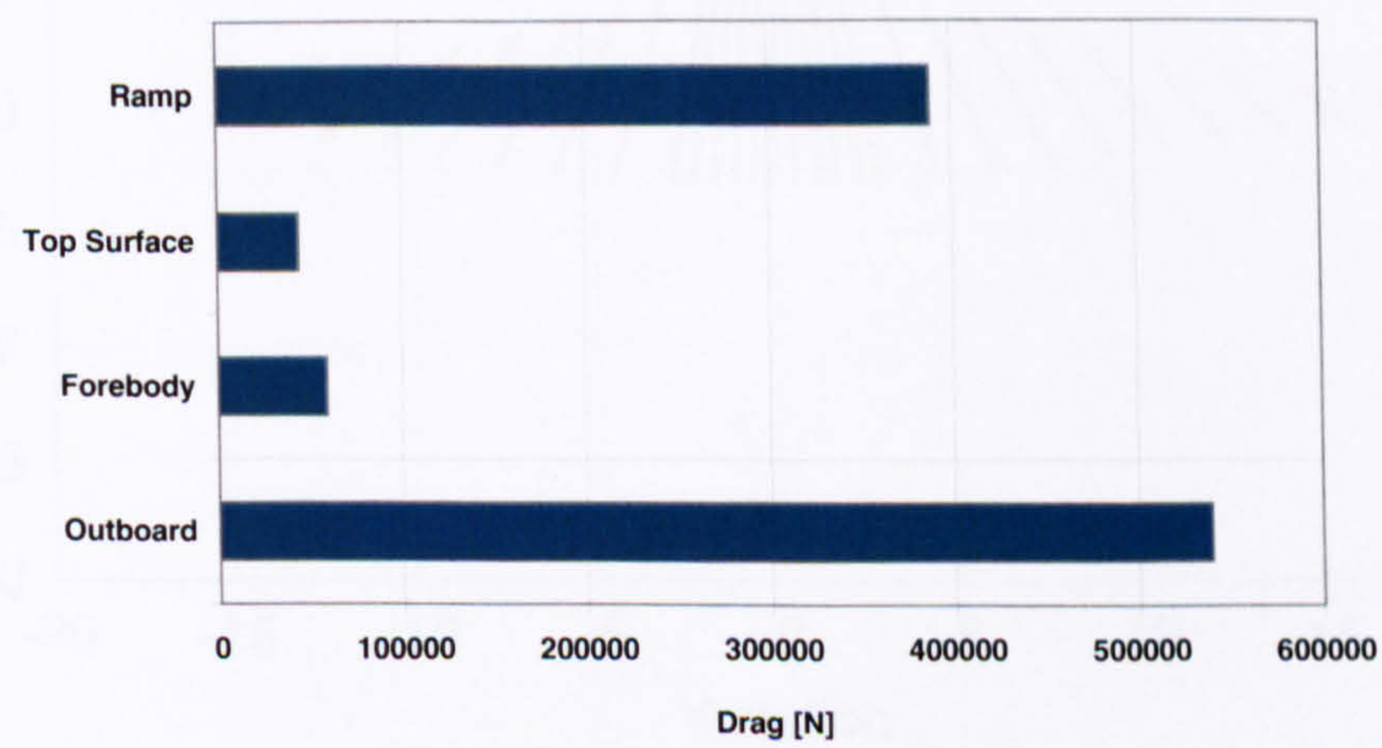


(a) (b)

Figure 7.35: The (a) Shock and (b) Engine width parameters used in the optimisation.

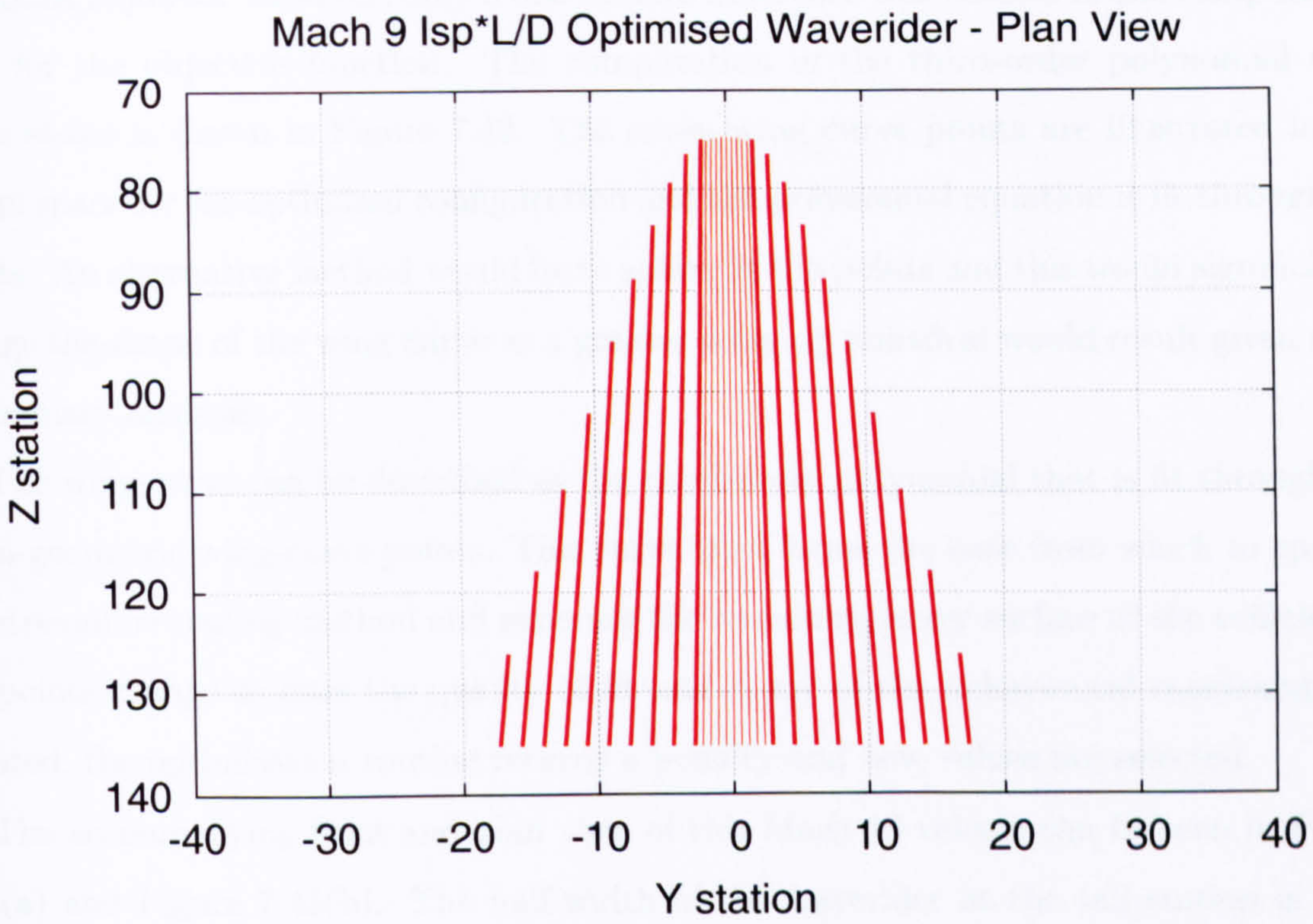


(a)

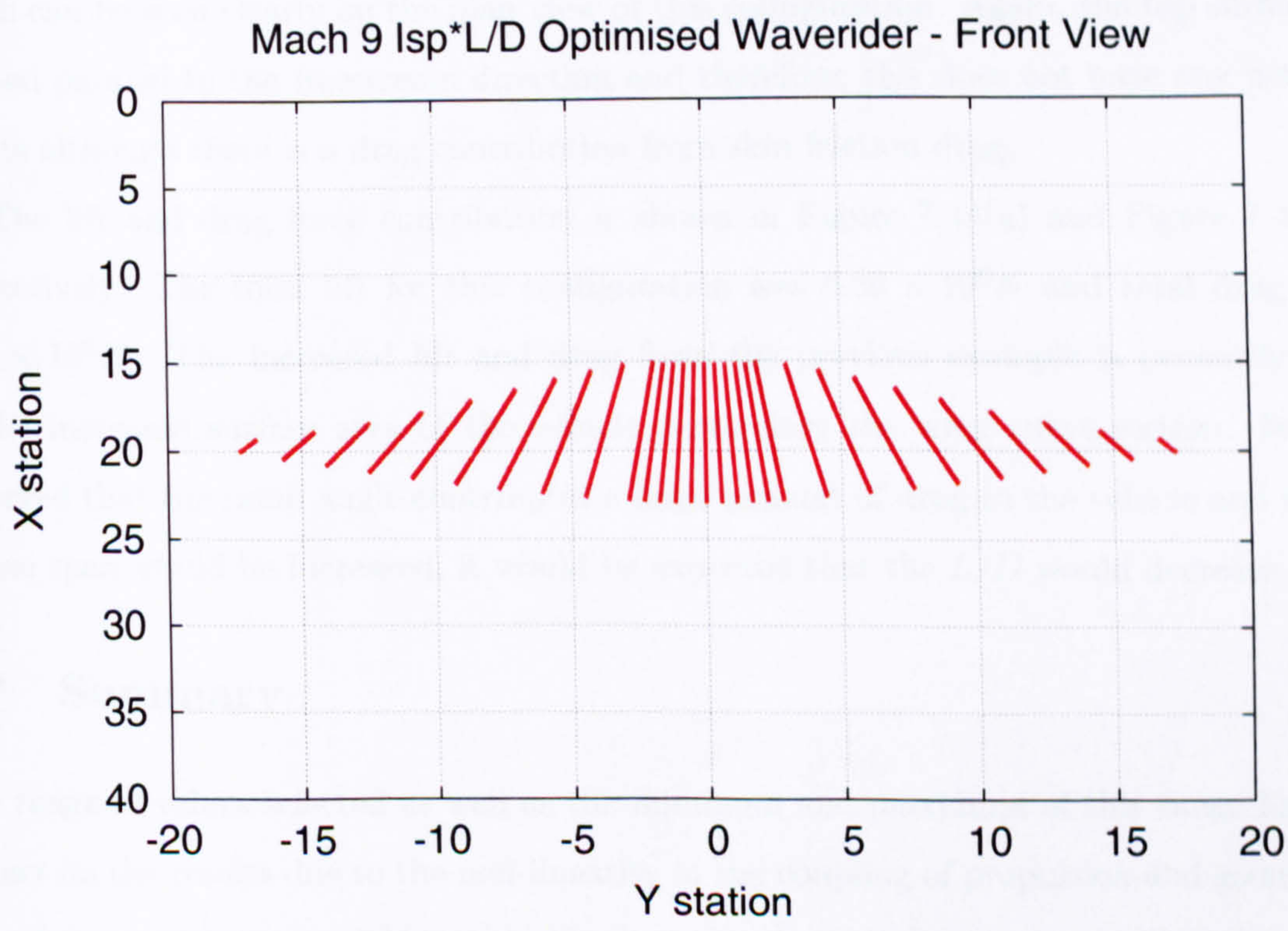


(b)

Figure 7.36: Lift and Drag of the Mach 9 optimised waverider.



(a) Plan view of L/D maximised Mach 9 Waverider.



(b) Front view of L/D maximised Mach 9 Waverider.

Figure 7.37: Front and plan views of Mach 9 optimised waverider.

iterations required. However, only a one-minute difference was noticed in the computation time for the objective function. The computation of the third-order polynomial wing curve shape is shown in Figure 7.42. The seven wing curve points are illustrated in the design space for the optimised configuration and the polynomial equation is fit through the points. An alternative method would be to spline fit the points and this would significantly change the shape of the wing curve as a greater wing tip anhedral would result given some preliminary analysis.

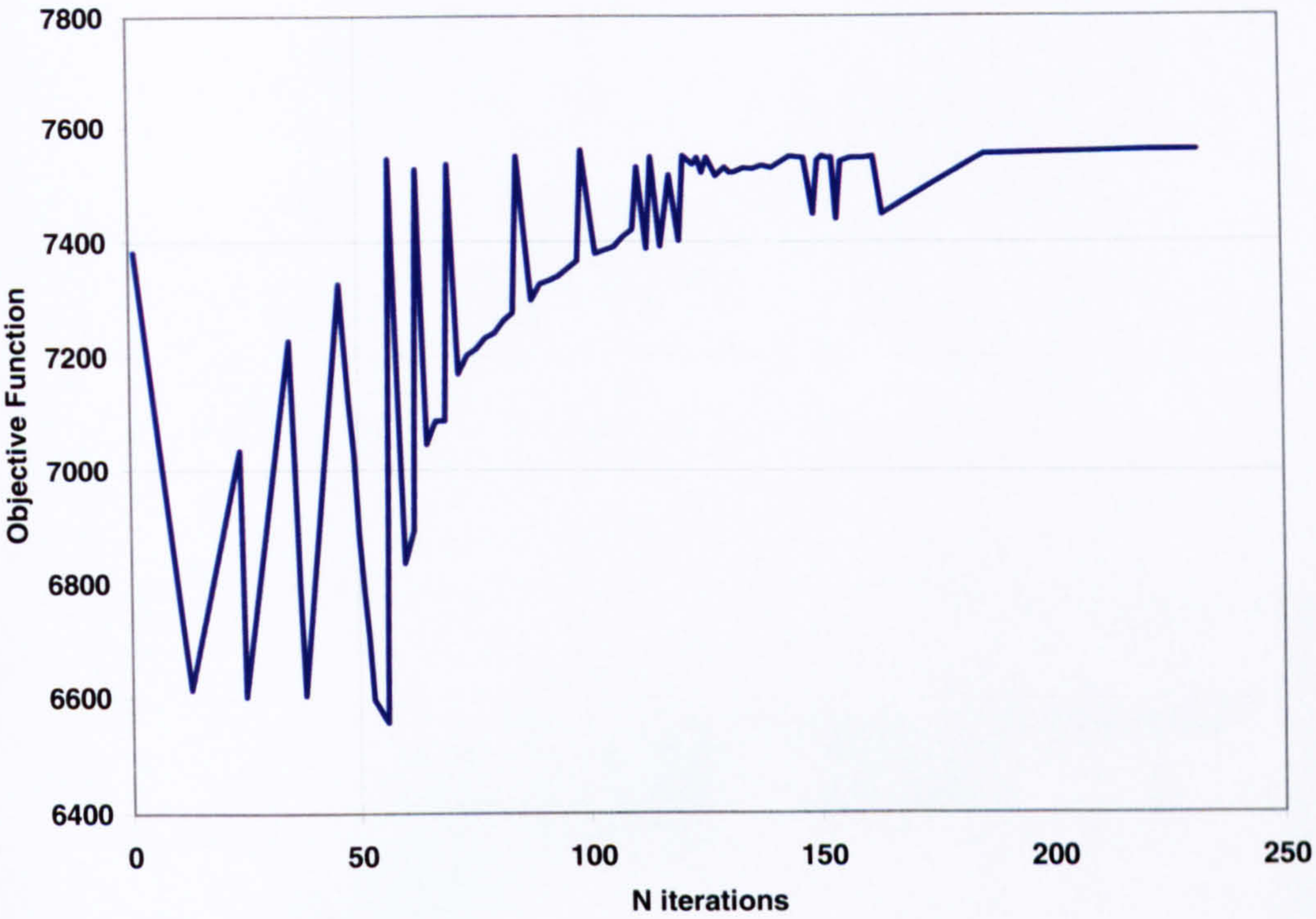
The wing-curve can be described as the third-order polynomial that is fit through the seven-geometric wing-curve points. This curve then forms the base from which to operate the streamline tracing method and generate the remaining lower surface of the vehicle. As the points change so does the quality of fit and if any of the behavioural constraints are violated, the optimisation routine returns a penalty and new values are selected.

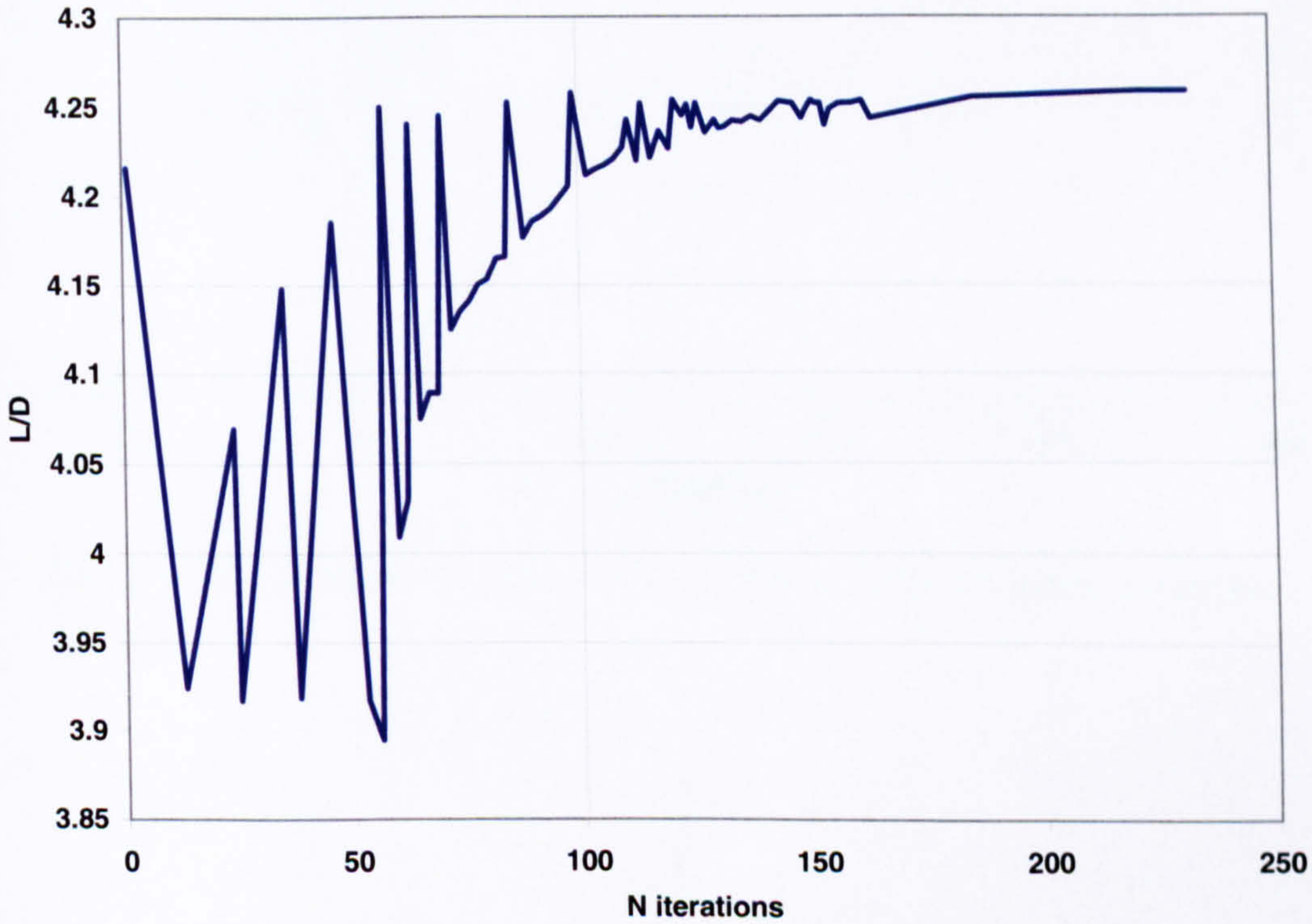
The accompanying front and plan view of this Mach 10 vehicle can be seen in Figure 7.43(a) and Figure 7.43(b). The half-width of the waverider at the tail station is $y_7 = 22.82m$, which is a large value compared to the Mach 9 example above. The increased width can be seen clearly on the plan view of this configuration. Again, the top surface is aligned parallel to the freestream direction and therefore, this does not have any net lift effects although there is a drag contribution from skin friction drag.

The lift and drag force contribution is shown in Figure 7.44(a) and Figure 7.44(b) respectively. The total lift for this configuration was $6.86 \times 10^6 N$ and total drag was $1.61 \times 10^6 N$. The increased lift and drag from the previous example is primarily due to the increased surface area of the vehicle particulary the wing curve section. It was observed that the ramp angle contributes a large amount of drag to the vehicle and if the engine span would be increased, it would be expected that the L/D would decrease.

7.7 Summary

The range of values selected as well as the minimum and maximum of this range had an impact on the results due to the non-linearity in the coupling of propulsion and geometry. One of the most active variables is the shock angle selection. Its range was allowed to vary between 11 and 14 degrees.





(b)

Figure 7.38: Optimisation histories of the objective function and L/D factor for a Mach 10 baseline vehicle.

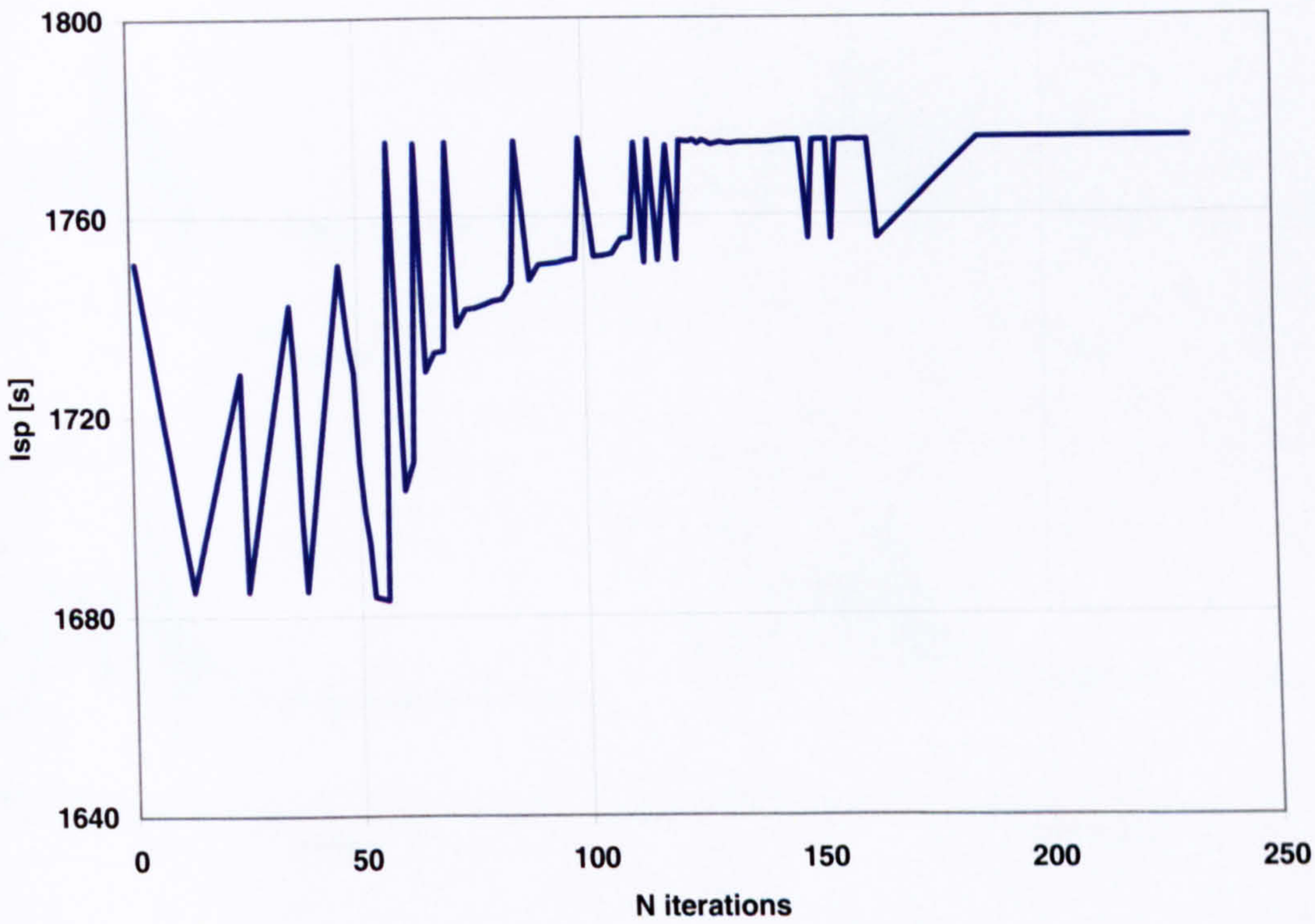
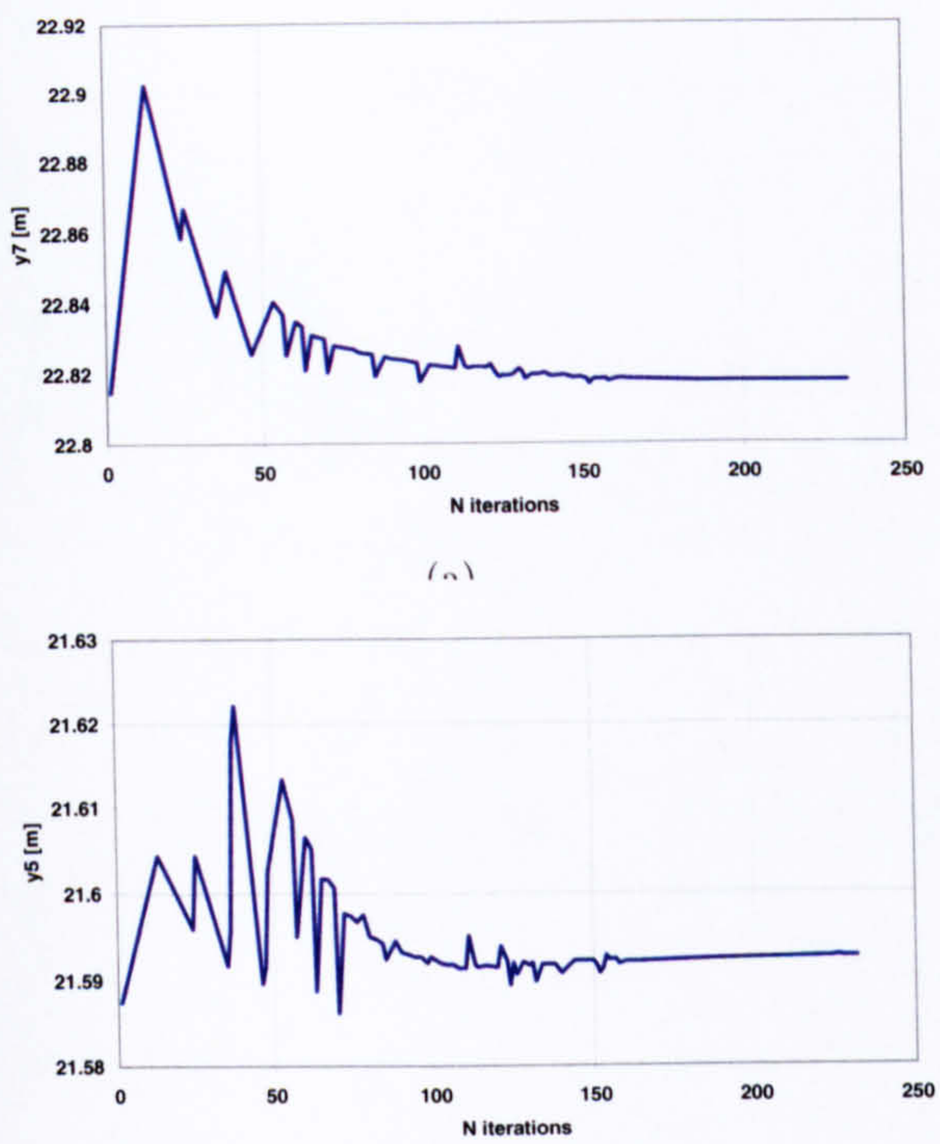
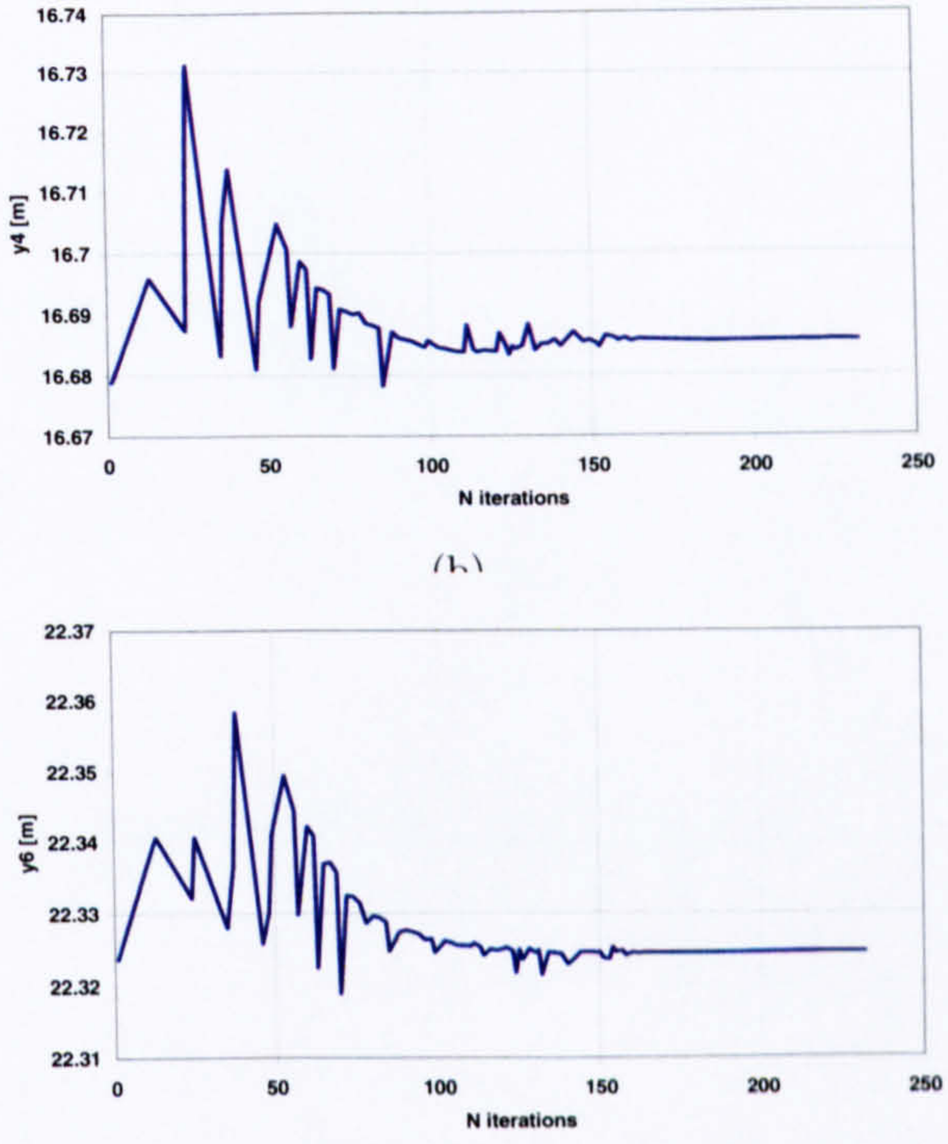


Figure 7.39: Optimisation history of the Isp for a Mach 10 example waverider.



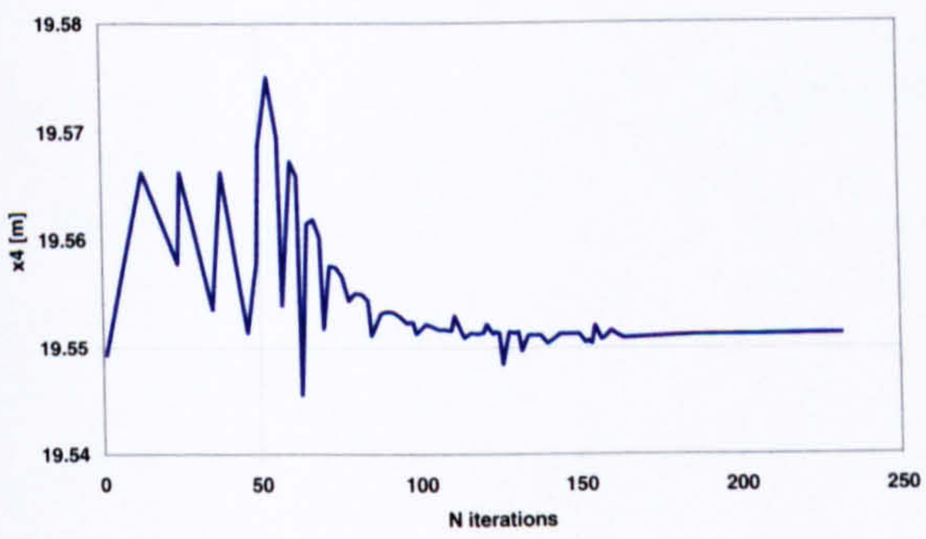
(a)



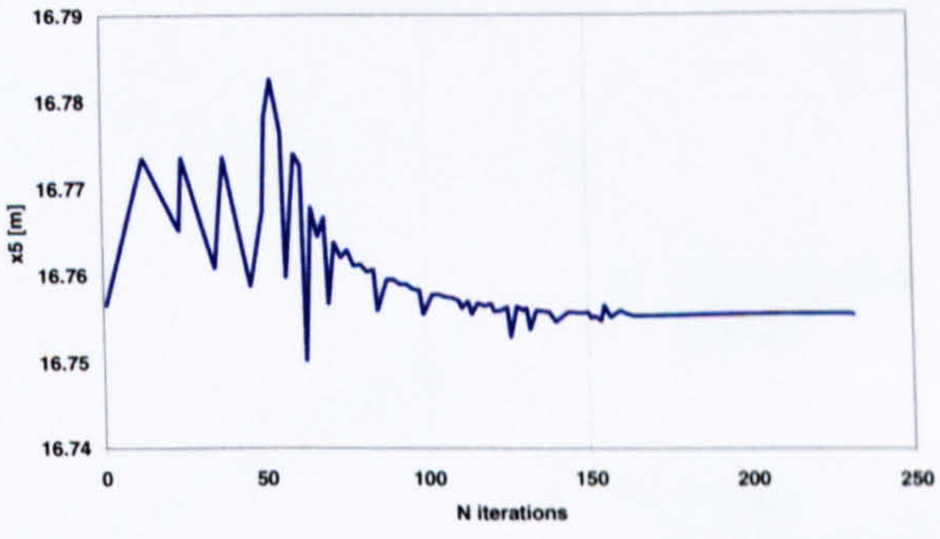
(b)

(c)

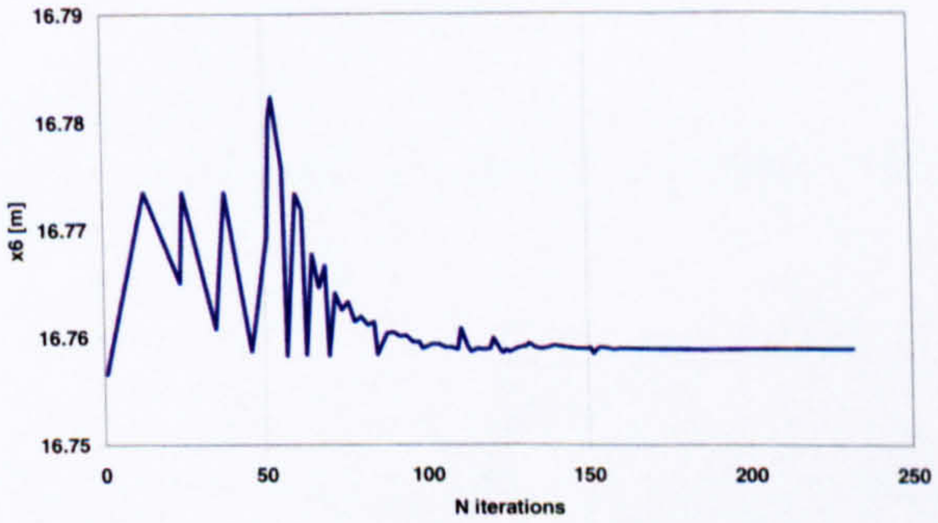
(d)



(e)

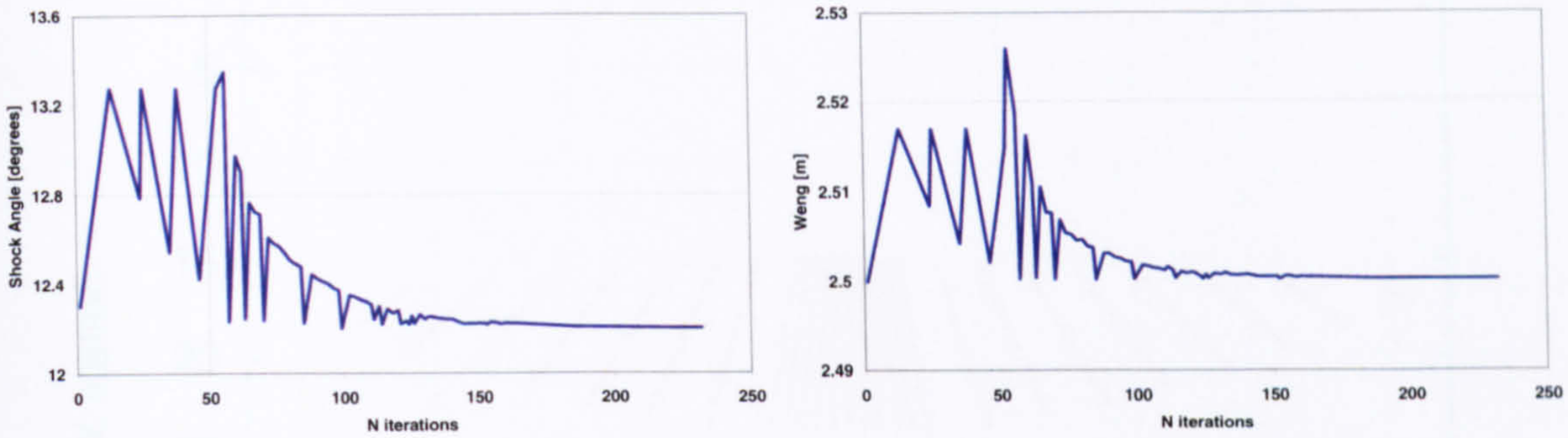


(f)



(g)

Figure 7.40: Mach 10 Optimisation history of geometric wing curve variables.



(a) (b)

Figure 7.41: Mach 10 (a) shock and (b) engine width optimisation histories.

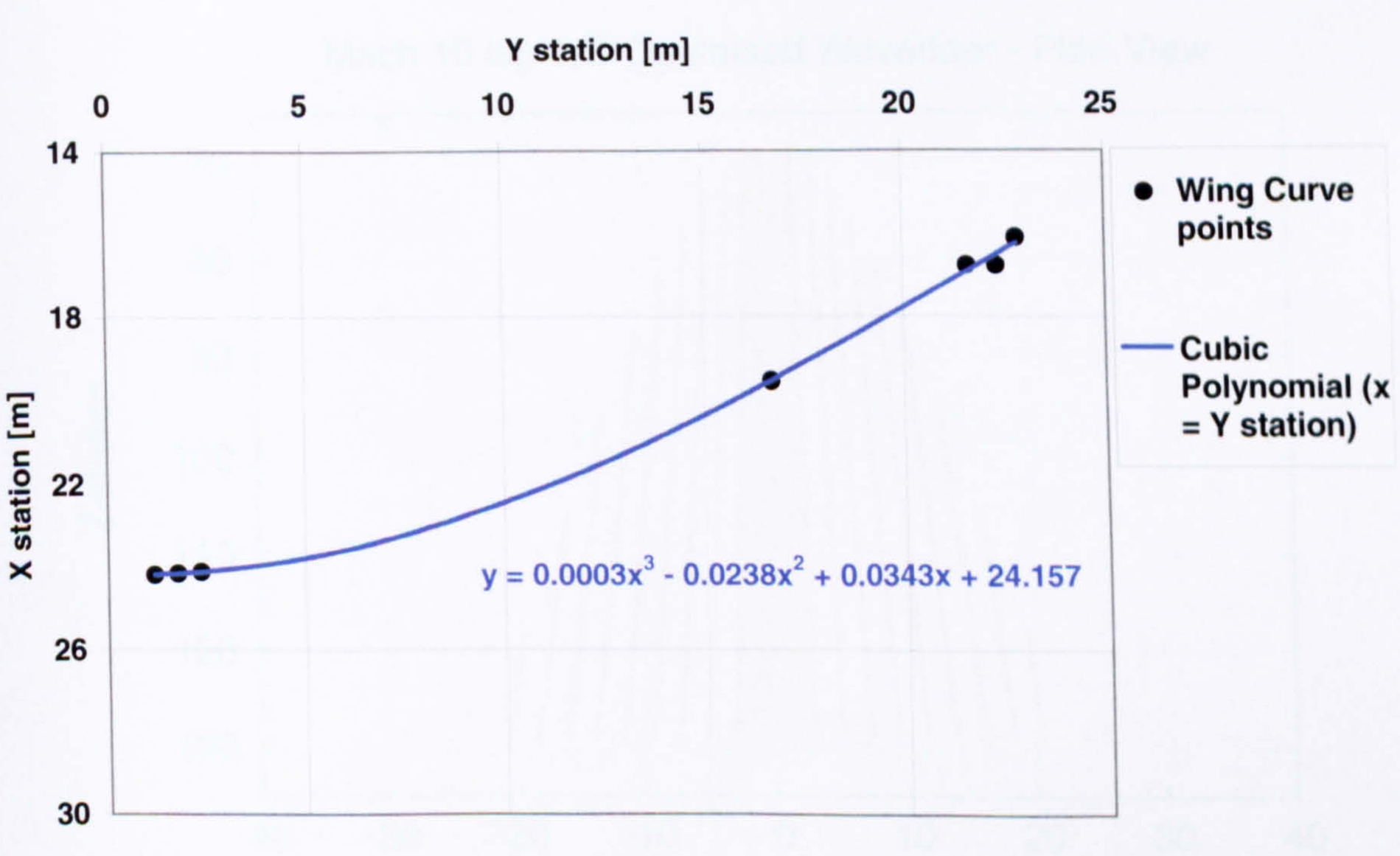
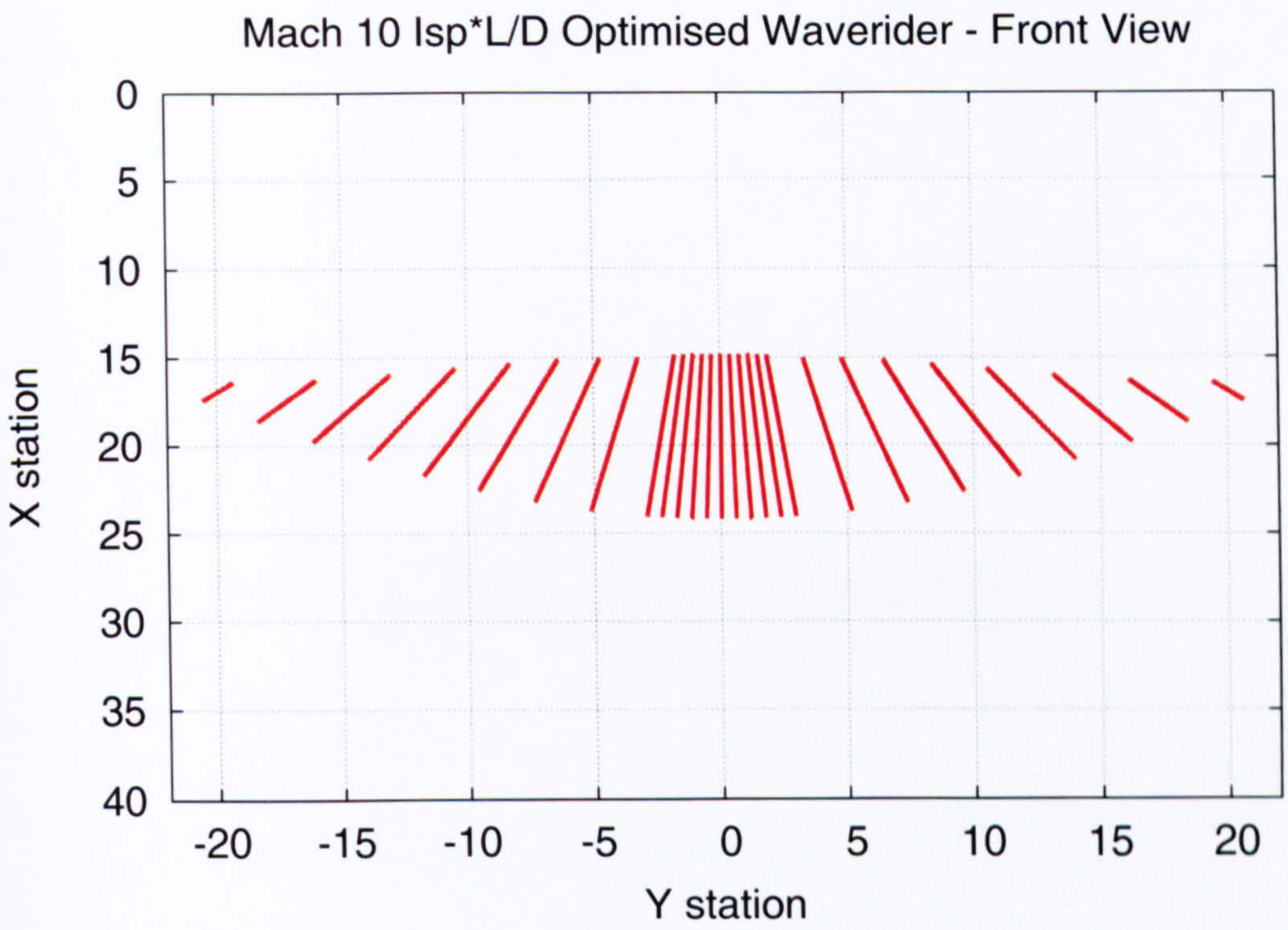
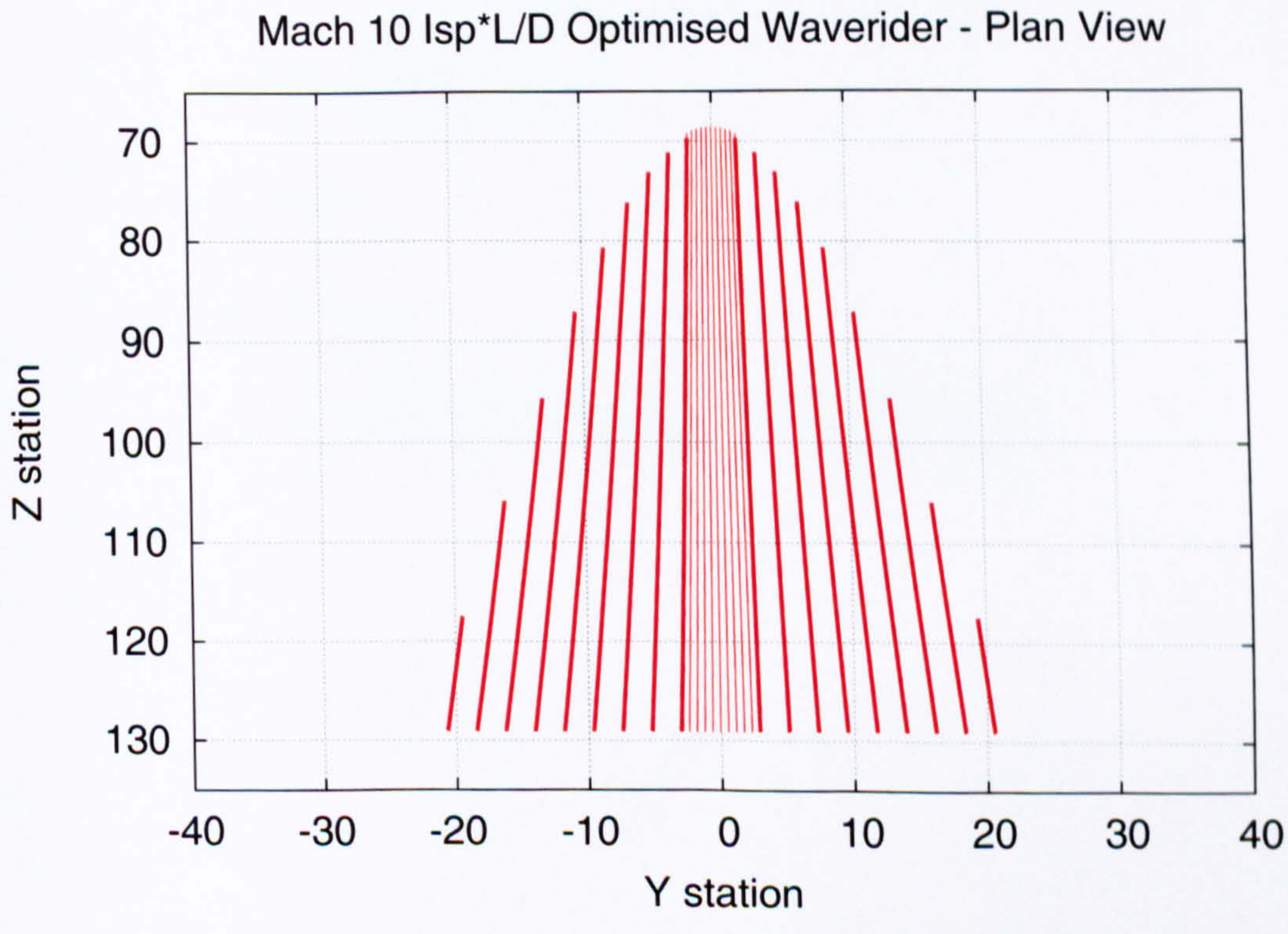


Figure 7.42: A cubic polynomial fit through the wing-curve points that forms the base curve from which to generate the remaining lower surface.

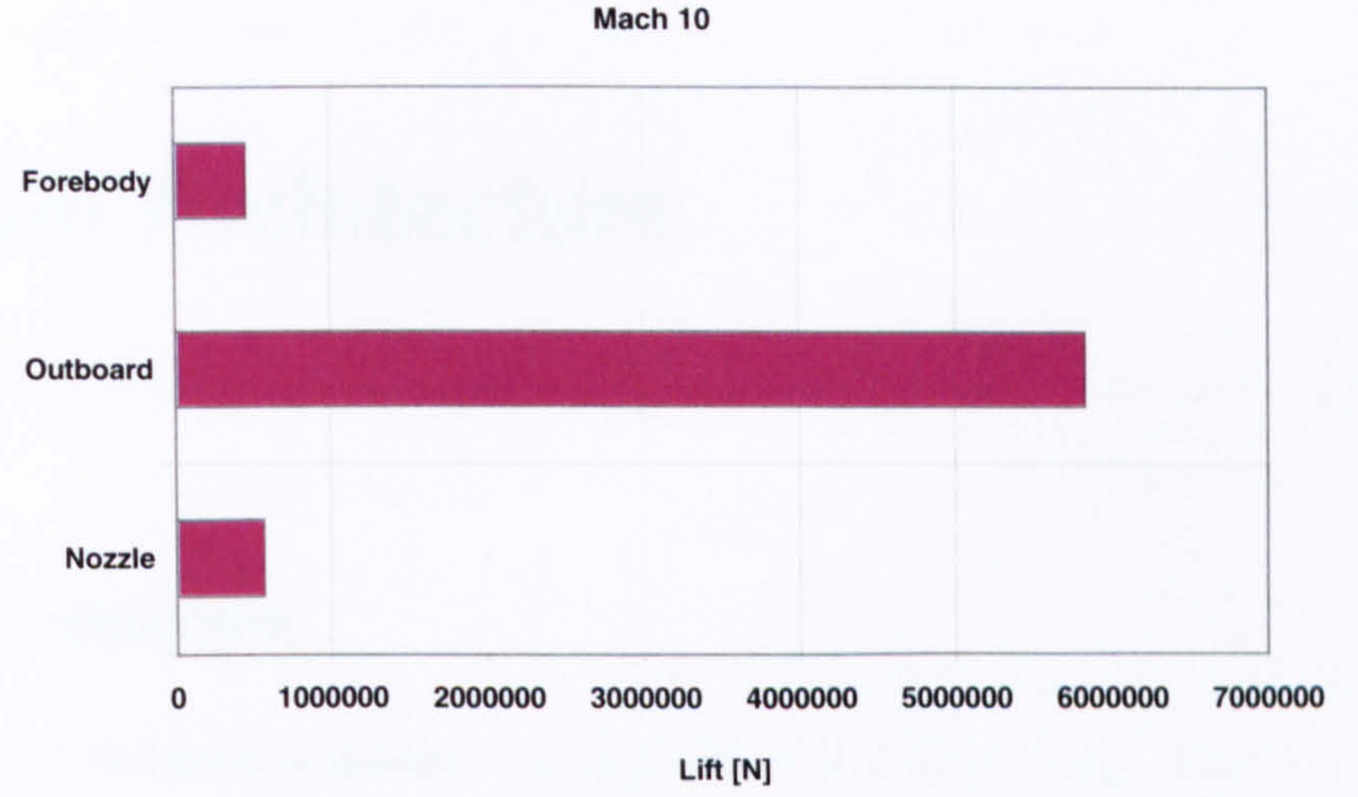


(a) Plan view of L/D maximised Mach 10 Waverider.

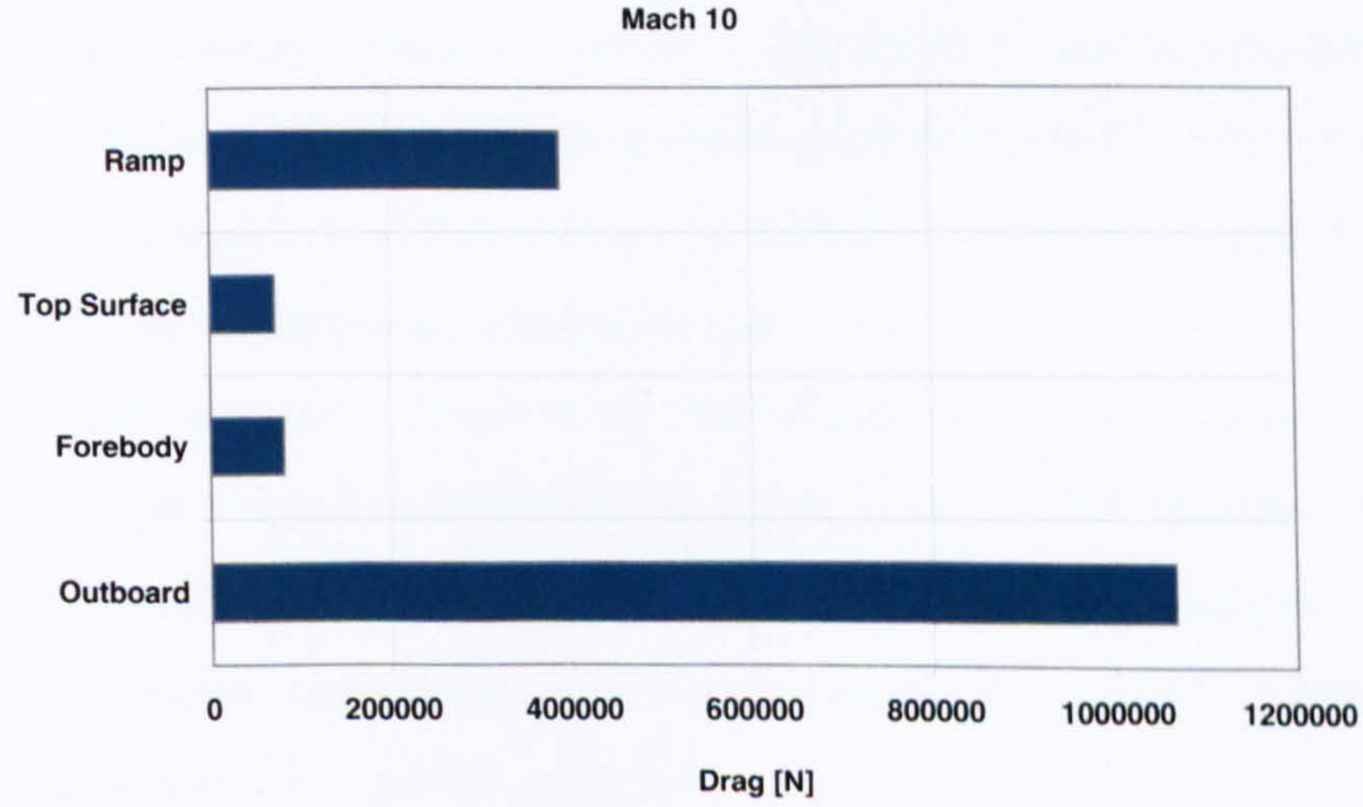


(b) Front view of L/D maximised Mach 10 Waverider.

Figure 7.43: Mach 10 waverider, $Alt = 33km$, $a_e = 20.5m$, $\epsilon_{min} = 11°$.



(a)



(b)

Figure 7.44: Lift and Drag of the Mach 10 waverider.

8

Program Architecture

8.1 Introduction

The purpose of developing design methods discussed in previous chapters of this thesis was to enable their integration into a computational tool for the design, modification and optimisation of hypersonic waverider vehicles. This allows a user to interactively investigate tradeoffs between geometric and propulsion parameter sets to achieve an optimised engine / airframe integrated configuration - essential for a hypersonic vehicle. The results are returned without a significant computational time.

The Hypersonic Interactive Combat Aircraft Design (HICAD) automated methodology has therefore been developed to fulfil this objective. A user is able to enter / modify initial variables using buttons, edit boxes and mouse controls for rapid analysis. This chapter deals with the processes, organisational structure and capabilities incorporated to achieve optimised configurations for specific missions.

8.2 Interface

The methodology is split into two parts. The numerical part of the design is written in C++ using object orientated code, which is an efficient way of encapsulating similar functionality within a class and protects data from unwanted changes. The Graphical User Interface (GUI) is developed using Microsoft's Foundation Class (MFC) that links C++ to a windows environment. The routines were developed using the Microsoft Visual C++®

6.0 software. Therefore, HICAD operates and is compatible with Windows® XP and 2000.

The code is structured in a modular format that takes inputs and either passes outputs by reference, stores data in vectors for later use or writes directly to a data file. Most data files are readable by a variety of software packages for plotting or further formatting. It was intended for the salient features of design variables to be visualised in HICAD via a simple charting class that was modified for the current use.

A multiple document interface (MDI) was used to hold a number of property sheets dealing with different aspects of the design. The computational structure will be presented in forthcoming programmatic flowcharts.

A summary of the different classes developed is provided in Table 8.1. The list does not include the several MFC-own generated classes that handle the mechanics of the GUI. Flowcharts for the formulation will be presented along with screen-shots representing the visual output offered by HICAD. Routines are distinguished by either the numerical part (N) or a dialog box / property sheet denoted by (G) for GUI.

The 1976 Standard Atmosphere model is used, which is made up of statistical correlations. The relationships were easily converted into code and is available directly by calling its subroutine from anywhere within the code. The input is altitude and Mach number and the output is a calculation of freestream conditions including static temperature and pressure. The routine is labelled `Atmosphere(...)`.

The GUI is split into five different pages that handles separate parts of the design. This is illustrated in HICAD's organisational flowchart of Figure 8.1. The pages are programmed as property sheets that include the forebody design, scramjet inlet and combustor performance estimation, vehicle attributes including optimisation, a multiple design-point option Mach dependent performance calculation and a turboramjet inlet design/performance estimation procedure.

8.3 Point-Design

Push buttons and edit controls on each property page call subroutines belonging to classes shown in the previous table. Some operations require activation/calculation of a previous control before the design can proceed and this is clearly illustrated in the sequential order of the point-design process in Figure 8.2. To compute a waverider geometry, establish

Class Name	Function
CChart (N)	Handles 2D plotting functions for a series of data.
CForebody (N)	Design of Forebody lower surface.
CGraphPage (G)	Computes on-design data for a range of Mach numbers by linking subroutines.
CLowSpeed (N)	Turboramjet inlet and cycle analysis.
CLowSpeedPage (G)	Calls CLowSpeed subroutines and OFFX for turboramjet analysis.
CMyPropSheet (G)	Holds pointers to the property sheets on HICAD and initialises them.
COptimisation (N)	Links all subroutines in a `Driver()` subroutine and operates the simplex algorithm.
CScramjet (N)	Design of scramjet inlet, cycle analysis and nozzle calculation.
CScramjetPage (G)	Calls CScramjet subroutines.
CShock (N)	Runge-Kutta calculation for Cone Angle.
CTRJdataDlg (G)	Handles data transfer for OFFX operation from user-selected variables.
CUserInput (G)	Calls CShock and CForebody subroutines for single-point design.
CUserInputViewImage (G)	Display either a graph from GnuPlot computation or design diagrams.
CVehicle (N)	Lift and Drag estimation subroutines and optimisation constraints analysis.
CVehiclePage (G)	Calls CVehicle subroutines for single-point design calculations.

Table 8.1: Class information from MFC ClassWizard in alphabetical order. (N) stands for numerical code and (G) for GUI. A number of numerical subroutines exist within each class.

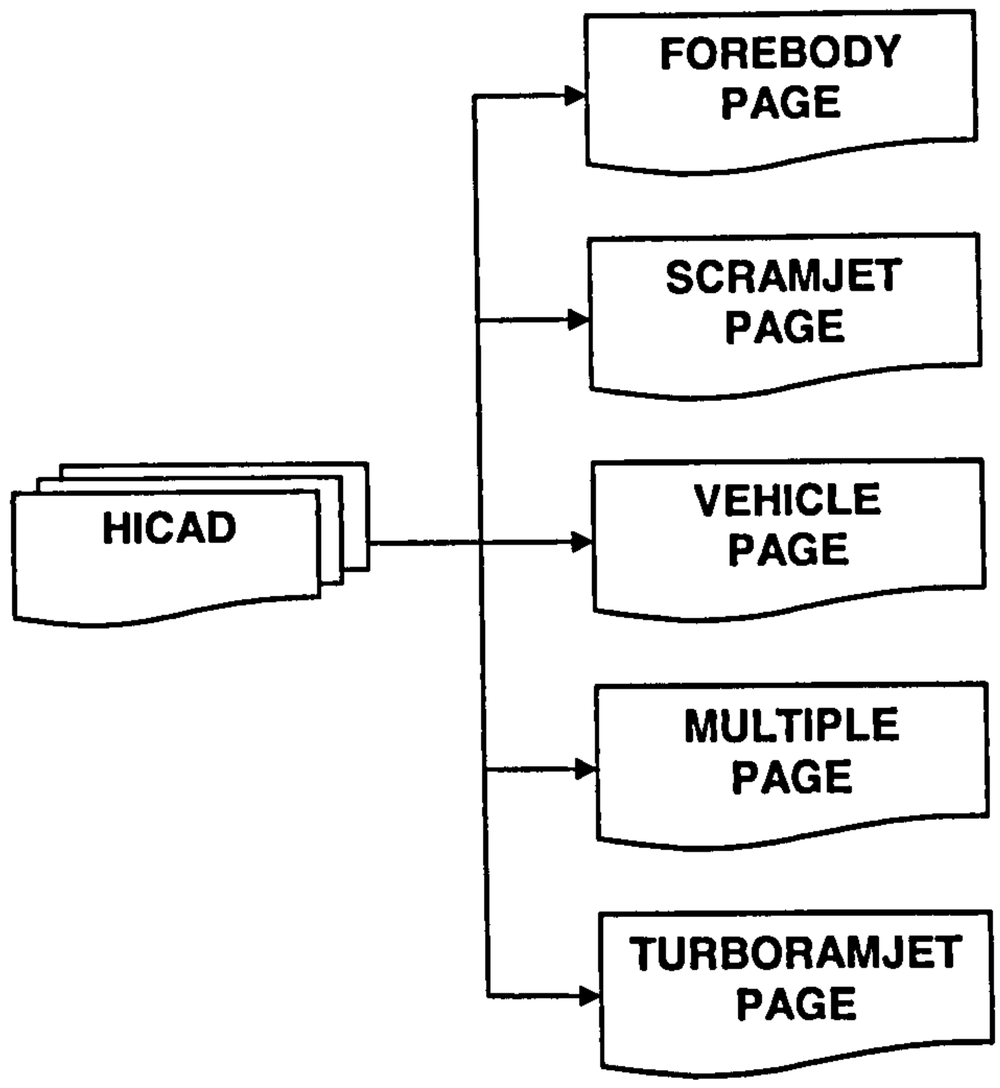


Figure 8.1: Organisational structure of GUI made up of an MDI interface.

multiple engine performance and estimate lift and drag on the vehicle, the first three pages in HICAD are used.

First, variables are input (default values are provided) that includes Mach number, cruise altitude, shock angle etc. onto the first page labelled FOREBODY as shown in the screenshot of Figure 8.3(a). The first button calculates the cone angle using a Runge-Kutta integrator as well as the freestream conditions that are stored on the GUI, also for later use. Values that are output to the GUI can be called and used in functions on separate pages.

Next, the forebody length is calculated (Button 2) using the streamline tracing technique. This calculation depends on *ae* and *be* which can be changed accordingly. Other variables include the half-span of the scramjet and cowl radius in the inlet plane. This function will not operate unless the cone angle is computed.

If desired, the length vs. Mach number relationship can be visually outputted by activating the LOOP button. This runs through a range of Mach numbers, the minimum of which is input in the CRUISE MACH box and maximum in the MAX box.

The design proceeds onto the adjacent page using NEXT. The scramjet inlet ramp angle is determined using the variables shown on Figure 8.3(b) that can be changed from

their default values. Key parameters include the specific heat ratios in various parts of the combustor and component estimates that range from low, mid to high. This change affects the stream thrust calculated, an alternative, simpler method to the IMOC nozzle calculation obtained from Heiser and Pratt (1994).

Upon determining the ramp angle conforming to the desired inlet properties, then the flow through the scramjet can be calculated along with the associated isolator if this is required. Whether or not the isolator is required, the decision is posted onto the screen. This uses data presented in the INPUT part of this page. Data is output to the GUI in the edit box for later analysis or plotting. At any stage in this calculation, the user has the freedom to return to the previous page for modification of variables. The final part of the calculation is the nozzle thrust (Button 3) that calls the IMOC routines. The maximum ramp angle is set at 18 degrees. Thrust and specific impulse are displayed in the appropriate edit boxes on the GUI.

Given the on-design properties, the OPTIMISE page can be called as shown in Figure 8.5 that will generate the remaining wing curve part of the lower surface and complete the design to enable a lift and drag calculation. A wide range of wing curve points are then calculated using the WINGCURVE button that runs through the entire spectrum of values and stores the possibilities in a data file. These values are then fit using the cubic polynomial routine, which finds one parameter set that results in a configuration. The routine is obtained from Press (2002) called `svdfit()`. Then finally, the lift and drag can be calculated by pressing button (2) and includes the relevant surfaces. Separate subroutines represent various wetted surfaces, the forces are summed by outputting values for the lift and drag. This completes a non-optimised point-design calculation.

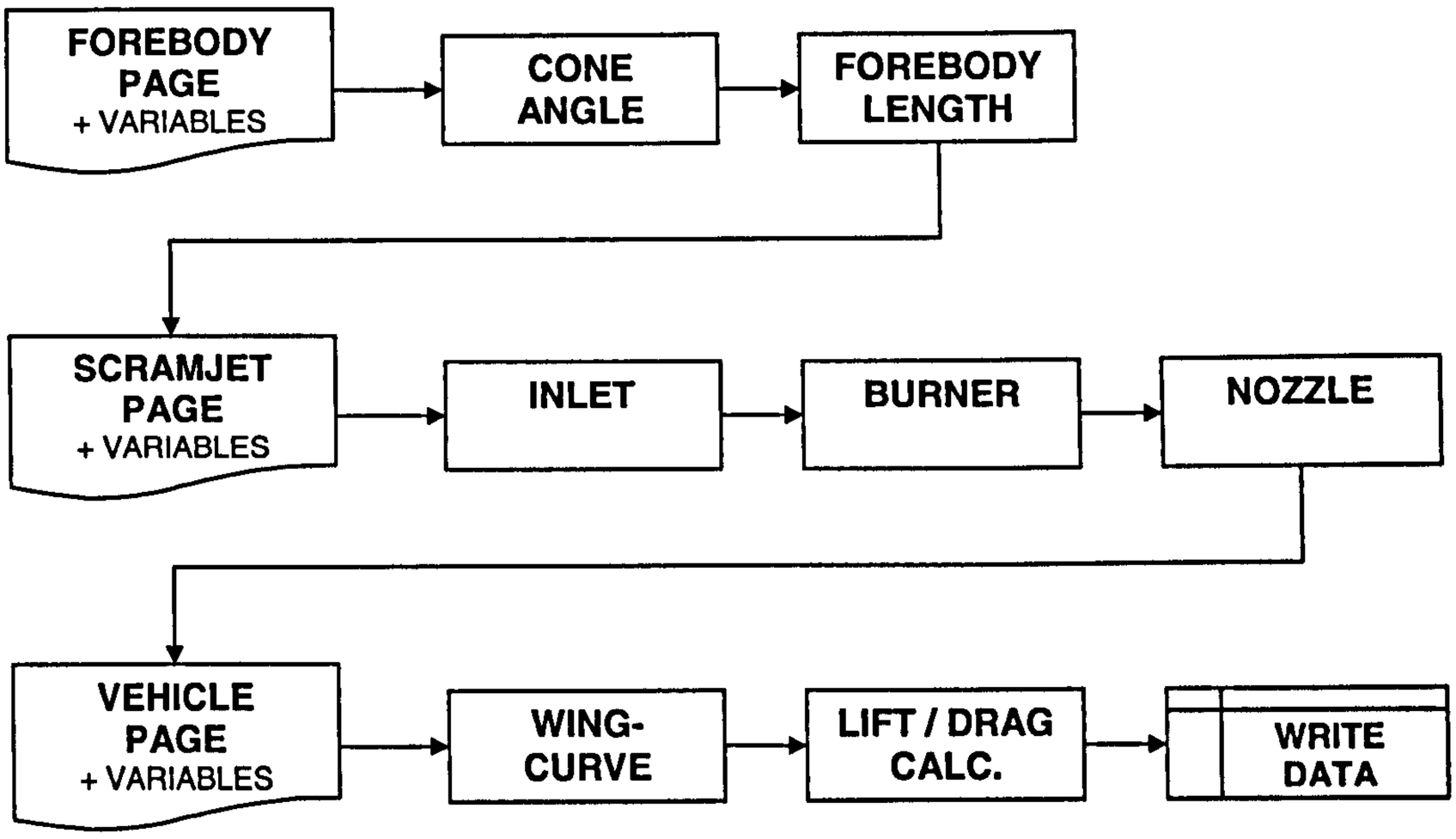


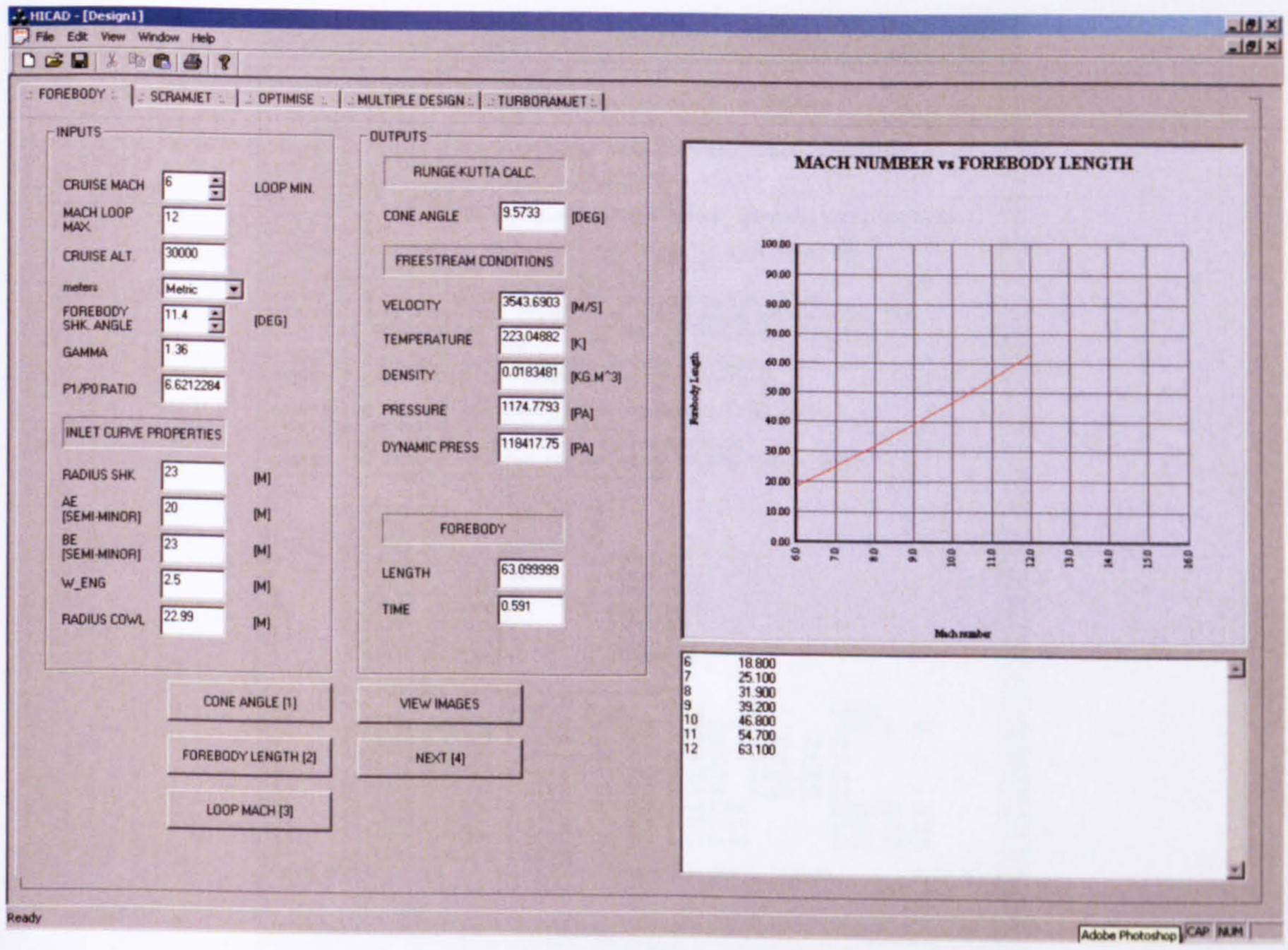
Figure 8.2: Point-design calculation flowchart.

8.4 Multiple Design

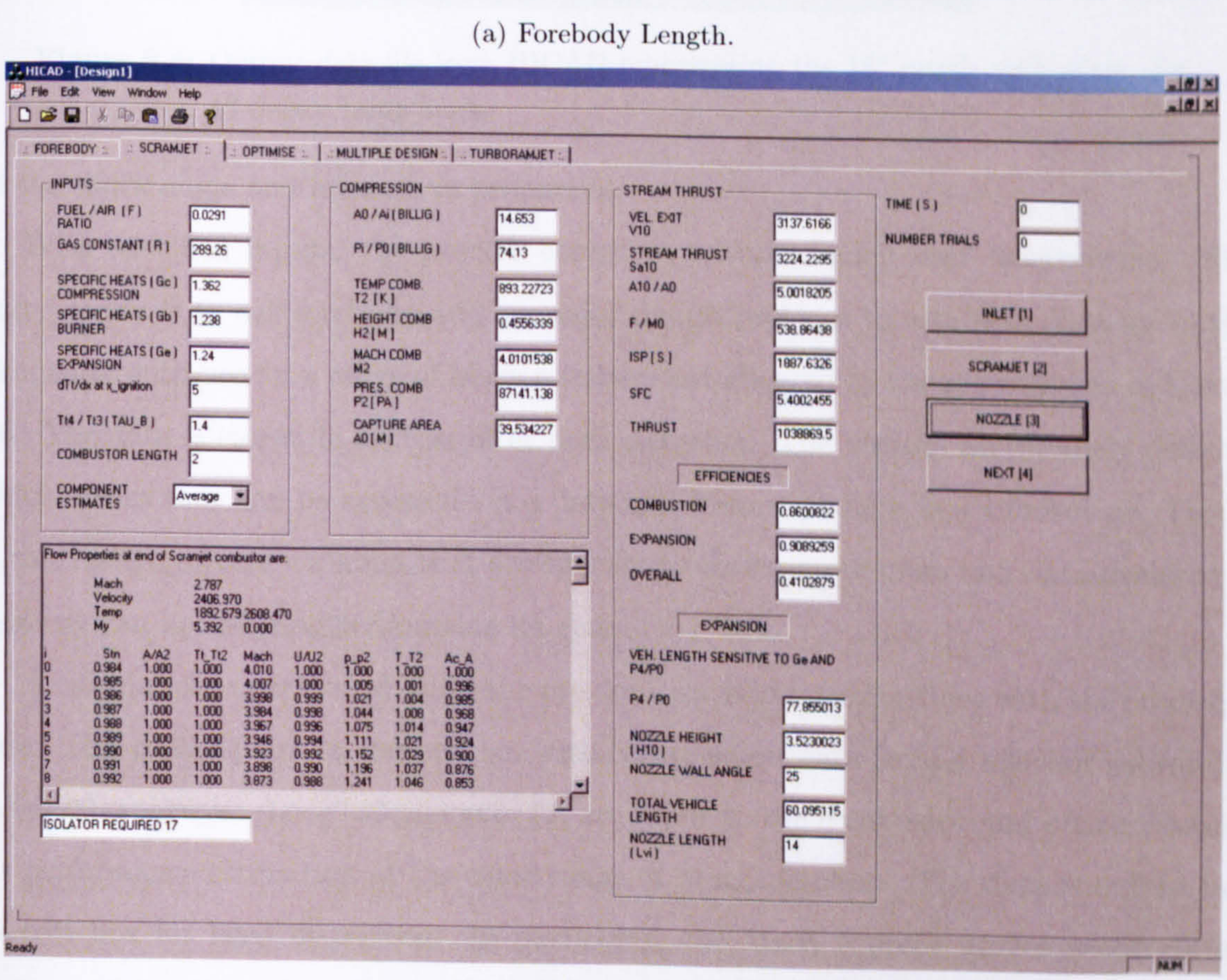
The MULTIPLE design page is used to generate waverider and performance data for a range of Mach numbers. Two processes are involved in this page. Firstly, the entire spectrum of subroutines can be called via the RUN LOOP button to call routines on the previous two pages to generate on-design data vs. Mach number. However, the simplified stream thrust analysis is used to generate thrust. This is useful to see how the waverider properties change when designing for different Mach numbers. This is indicated in the left column of the flowchart in Figure 8.6 with input specifications shown in the screenshot of Figure 8.7.

In addition, the right-hand column in the flowchart of Figure 8.6 represents the performance estimation through incorporation of the IMOC nozzle routine. Here, three-dimensional data for Thrust-Altitude-Mach number can be generated. For this calculation, an altitude and a design Mach number is specified.

Furthermore, a minimum Mach number for the loop range is specified. For Mach 5 transition from turboramjets to scramjets, data at Mach 5 is required and this is input in the relevant edit box. There may be instances where the default values will not converge at a solution for either low Mach numbers (5) or higher numbers (12+). Therefore, values may be modified on the forebody and scramjet property pages. Most noteworthy would



(a) Forebody Length.



(b) Scramjet inlet, combustor and nozzle design.

Figure 8.3: HICAD pages for forebody length and scramjet performance estimation.

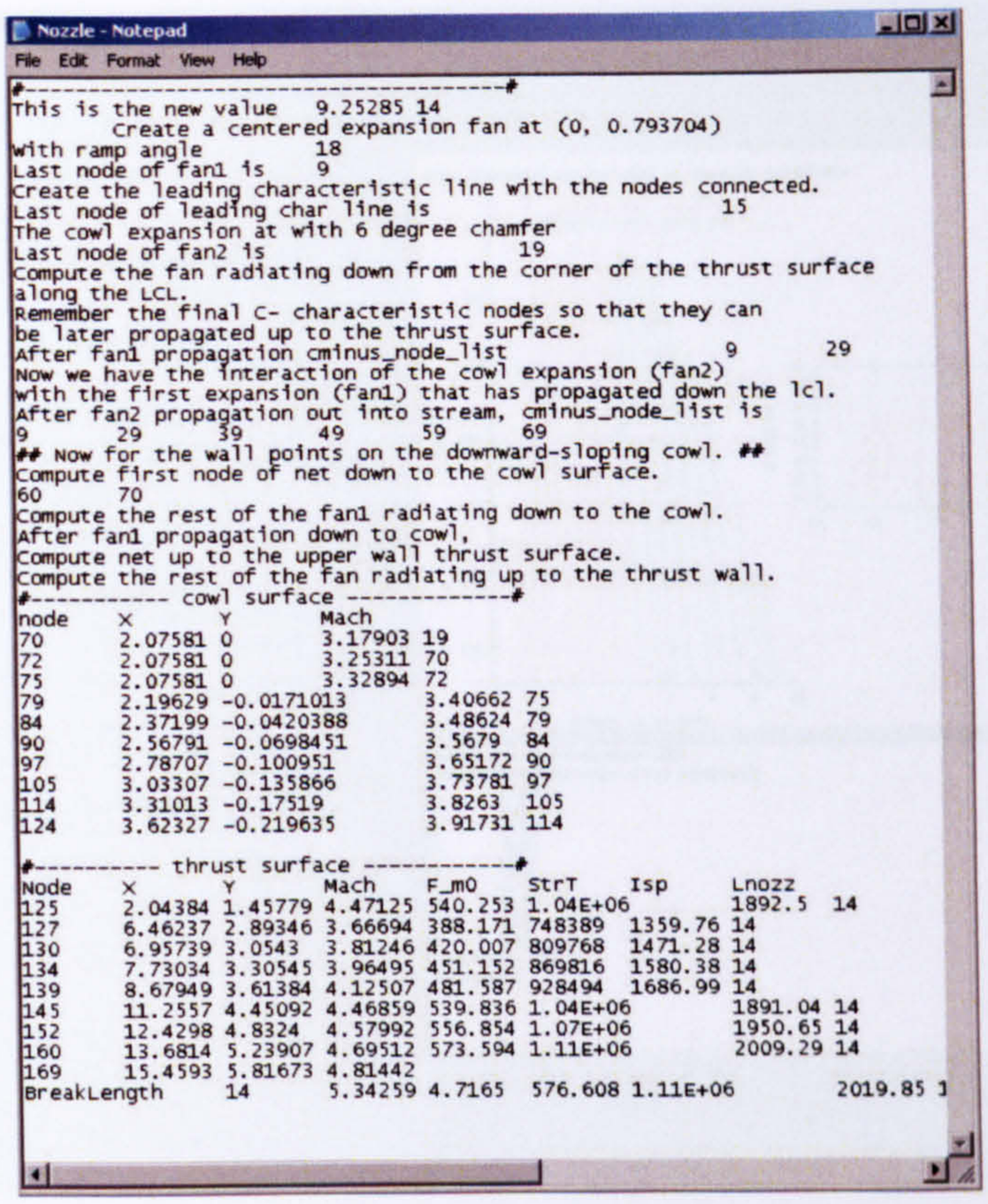


Figure 8.4: Output data file from HICAD representing the 18° nozzle wall angle. for 18 degree ramp angle.

be the shock angle and inlet curve properties.

With specified inputs, the process continues without much user intervention. The next process is to call forebody and scramjet design routines to establish data up to the combustor entrance for a range of Mach numbers as indicated by the relevant box in Figure 8.6. The data is stored in vectors after each iteration. The vectors are publicly defined, which means they can be accessed via a data call from anywhere in a subroutine. This is in contrast to private variables that are specific to their parent class and data declared in this way can not be modified outside its class.

A calculation is performed to fill the previous waverider subroutines with the on-design data. This design-point in conjunction with compression data from a relevant subroutine called `CGraphPage::LoopToCombustor()`, are input to the combustor and nozzle routines for performance estimation at the same range of Mach numbers. The data is output into an edit box for later inspection. In particular, the Mach 5 point proves useful during turboramjet analysis for achieving smooth thrust and Specific Impulse transition.

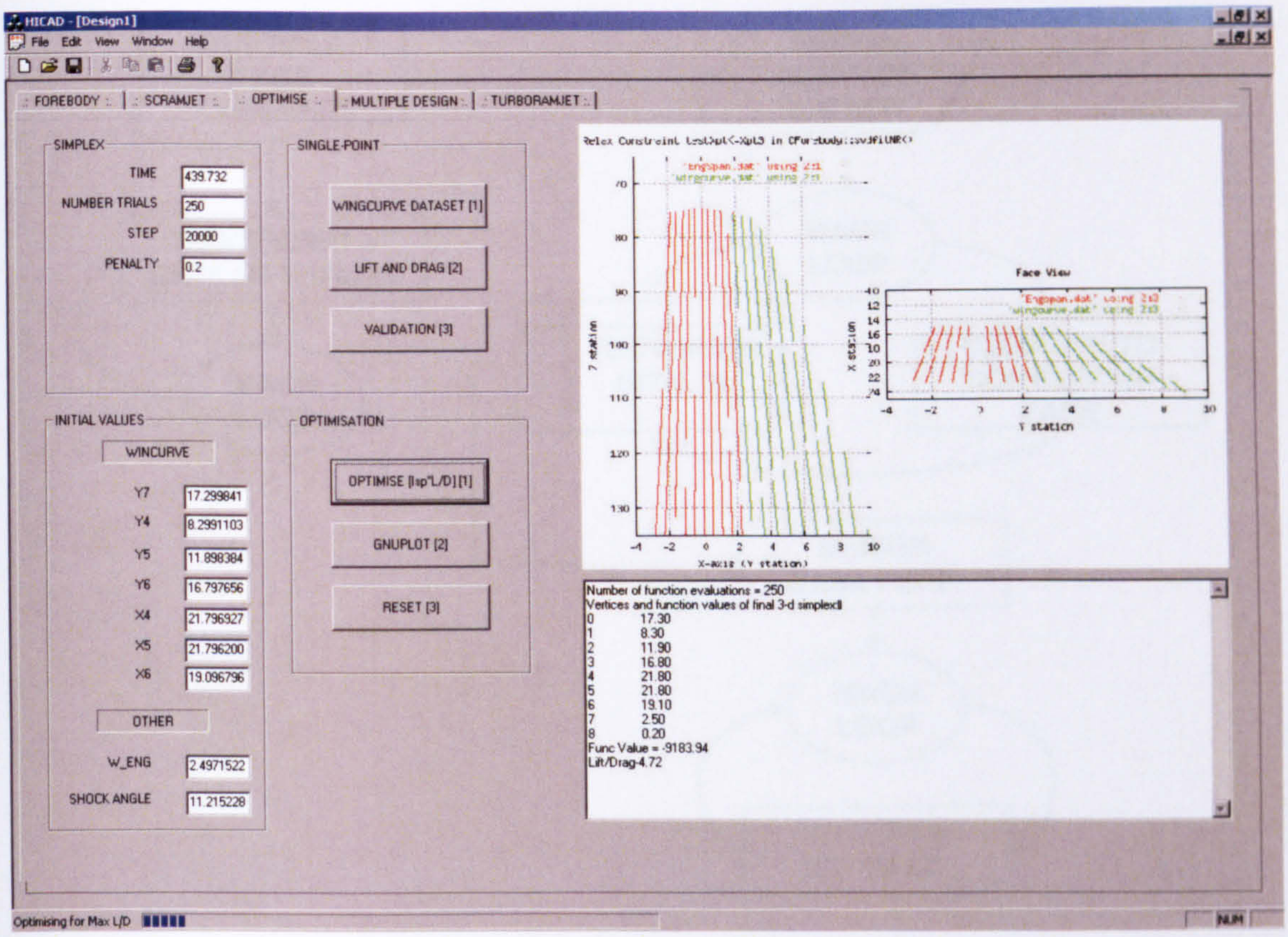


Figure 8.5: HICAD Vehicle analysis, lift and drag plus optimisation.

8.5 Turboramjet

A description and accompanying flowchart for the turboramjet analysis method and thrust-matching was presented in Chapter 6 and Figure 6.6. The associated screenshot is presented in Figure 8.8 and the accompanying `OFFX` program is called using Button 3 as shown in Figure 8.9, after the on-design properties have been calculated (Button 2). Once complete, the user is prompted to confirm successful operation of this code and by pressing Button 4, mass flow data is output to the edit box for later inspection. Similarly, for correct calculation, the order of the sequence of events is important in achieving thrust-matching and the user is prompted via warning flags if a violation has occurred.

An example of the output file from `OFFX` for a range of Mach numbers and off-design selection 3 on Figure 8.8, is shown in Figure 8.10. The data at the top of this file is dependent on user selections of on-design variables that can be modified by calling the `VIEW DATA` dialog box on the `TURBORAMJET` page. It is necessary to open this box to input design point conditions and altitude as required. In some cases, the altitude specified here,

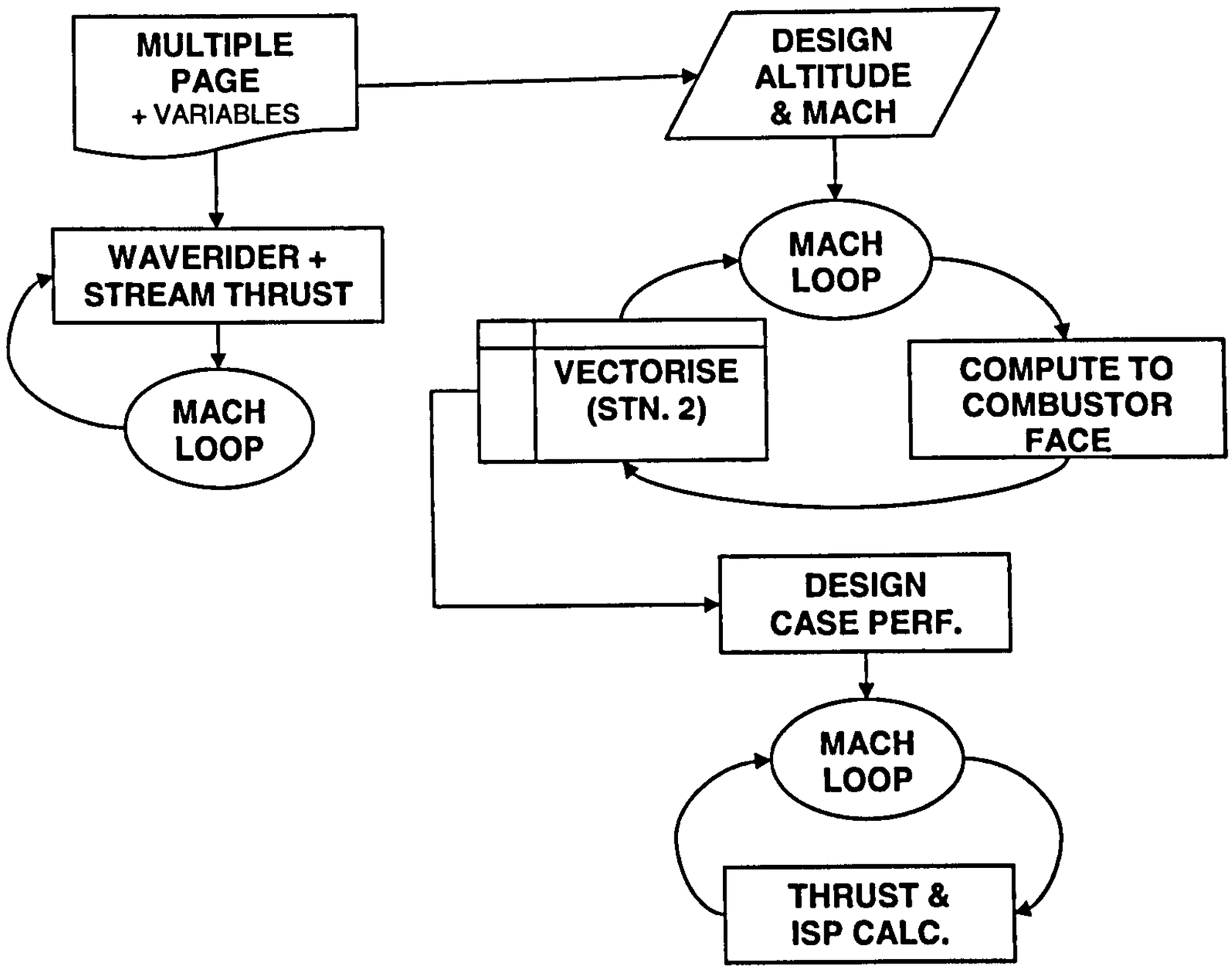


Figure 8.6: Multiple-design calculation flowchart.

is used for off-design calculations. This dialog box is shown in Figure 8.11. The input file is based on the On-Design cycle analysis code `ONX` developed by Mattingly *et al.* (1987) and the data is stored in a separate file called `TRJ.txt` containing exactly 150 variables.

As `OFFX` is a `DOS` executable, the options are selected via key strokes. For the user to avoid repeating this several times, the options can be selected on this page in the `GUI` and the choices are stored in a data file. This file is called using a batch command that sends information to `OFFX`. The `C++ ShellExecute()` command is called in `HICAD` to link the batch file (`.bat`) and is shown in Figure 8.8.

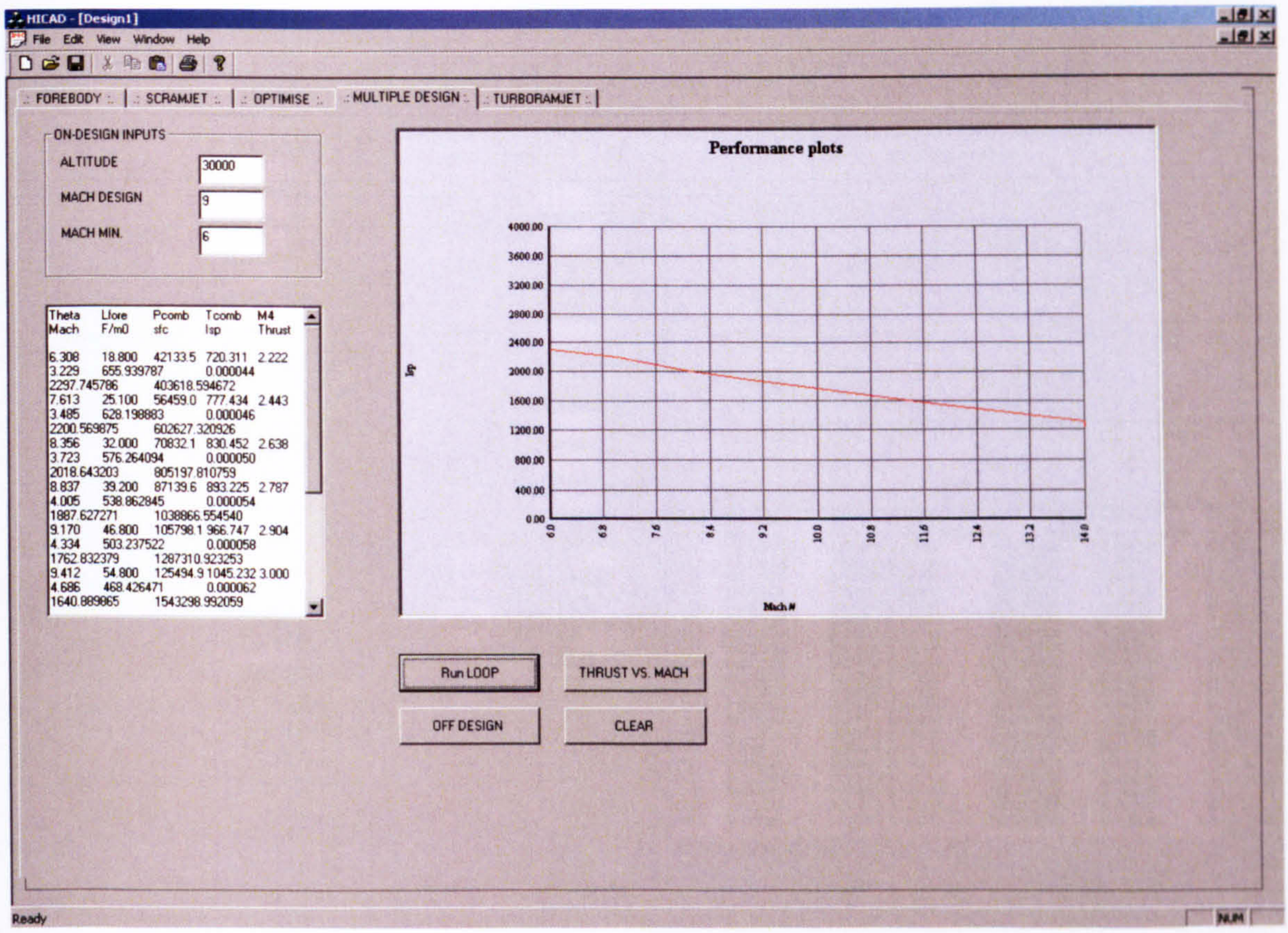


Figure 8.7: HICAD - Iterate on Mach number.

8.6 Optimisation

For optimisation calculations, the user input is minimal if necessary as initial values are suggested by default. The starting values can be modified but as the design space is severely constrained, this may lead to a non-starting process. If user selection fails, an alternative set of initial values can be found by operating the wing-curve button, which loops through all possible combinations as described earlier, tests the values in the lower-surface generation routine and creates a lookup list of the successful outcomes. An example was the Mach 10 waverider case, which had over 40,000 possible combinations of the wing curve points of which 39 produced valid waverider configurations. This is indicated by the first process in Figure 8.12.

The optimisation then performs its task for minimising the objective function and generally follows a three-step procedure 1) determination of I_{sp}, 2) wing-curve selection and 3) L/D estimation and objective function evaluation.

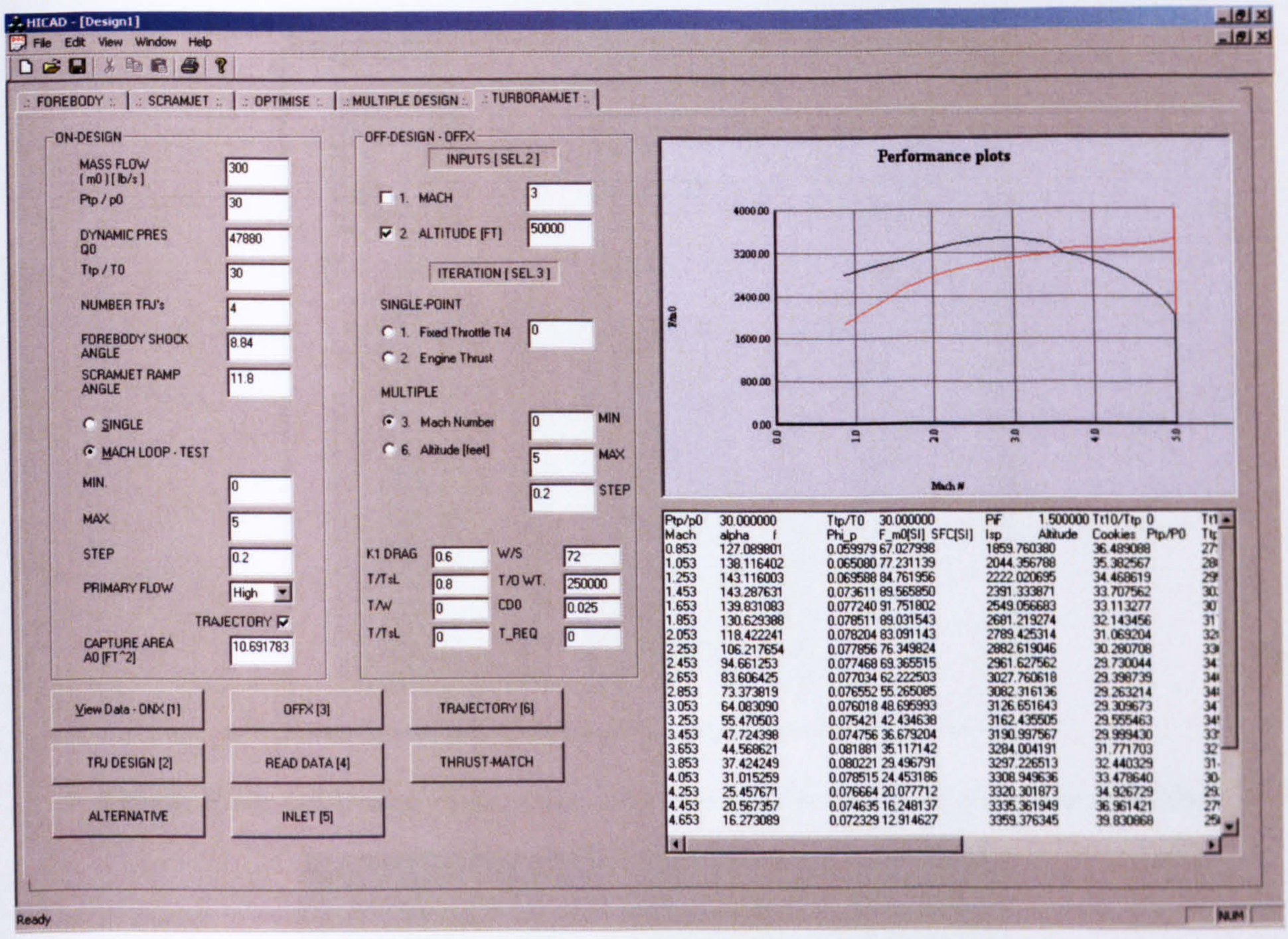


Figure 8.8: HICAD Turboramjet design and analysis.

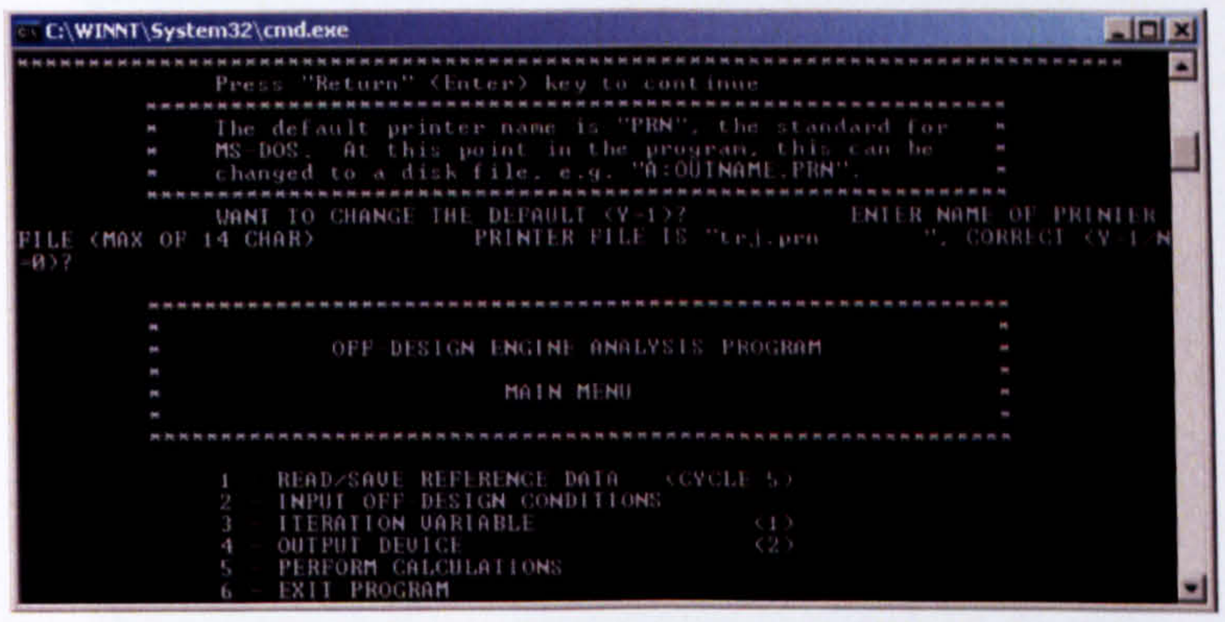


Figure 8.9: OFFX called from Turboramjet Page in HICAD. Inputs are provided by a batch file (.bat).

The `OPTIMISE` button calls a `Driver()` routine, which inputs the initial values into a vector and is sent to the `amoeba()` simplex algorithm as given in Appendix B. `amoeba()` makes a call to a subroutine, which performs the three-steps mentioned above. Following a successful (no side-constraint violation), wing curve points selection, the parameter set is stored in a vector and fed to the cubic polynomial fitting routine. The coefficients of the

TRJ.PRN - Notepad

File Edit Format View Help

```
FILE: trj.txt              OFF-DESIGN CALCULATIONS                PAGE  1

          ***** FIXED AREA TURBINE - TURBOJET ENGINE *****
 INPUT CONSTANTS
 PID MAX = .9700   CP C    = .2380   CP T    = .2950   CP AB   = .2950
 ETA B   = .9800   GAM C   =1.4000   GAM T   =1.3000   GAM AB  =1.3000
 ETA  AB = .9700   PI B    = .9700   PI AB   = .9600   PI N    = .9800
 ETA C   = .8693   ETA CH  = .8769   ETA MH  = .9800   ETA ML  = .9900
 PI TH   = .2920   TAU TH  = .7766   ETA TL  = .9169   ETA MPL = .9800
 BLEED   =  1.00%  COOL #1 =  5.00%  COOL #2 =  5.00%  PTOL(KW)=  294.
 PIM MAX = .9700   TAU M1  = .9758   TAU M2  = .9855   ETA MPH = .9800
 PIC MAX =   .00   PT3 MAX =    .0   TT3 MAX =    0.R  PTOH(KW)=    0.
 RPML MAX=    .0%  RPMH MAX=    .0%

M0  =     .01    ALT =   50000. FT    T0  = 390.00 R
P0  =   1.6920 PSIA  P0/P9 = 1.0000  TT4 = 3200.0 R  TT7   = 3600.0 R

   M0 THRUST  AIR    FUEL   F/MDOT    S    PI C  PT9/P9  V9/V0 L
      (LBF) (LB/S) (LB/H)
  .01 18321. 117.50  24630. 155.92 1.3444 92.63   11.38 495.36 0
  .20 17832. 118.48  24818. 150.50 1.3918 90.85   11.48  24.82 0
  .40 17621. 121.47  25389. 145.06 1.4408 85.78   11.77  12.46 0
  .60 17716. 126.57  26357. 139.98 1.4878 78.23   12.26   8.35 0
  .80 18108. 133.92  27747. 135.21 1.5323 69.27   12.97   6.32 0
 1.00 18798. 143.78  29594. 130.74 1.5744 59.89   13.93   5.10 0
 1.20 19591. 155.10  31667. 126.31 1.6165 50.86   15.03   4.30 0
 1.40 20560. 168.56  34086. 121.97 1.6579 42.69   16.33   3.72 0
 1.60 21746. 184.70  36934. 117.74 1.6984 35.60   17.89   3.30 0
 1.80 23160. 203.92  40257. 113.58 1.7382 29.63   19.76   2.96 0
 2.00 24806. 226.63  44096. 109.46 1.7777 24.69   21.96   2.70 0
 2.20 26683. 253.28  48488. 105.35 1.8172 20.66   24.54   2.48 0
 2.40 28787. 284.37  53464. 101.23 1.8572 17.39   27.55   2.30 0
 2.60 31106. 320.43  59049.  97.08 1.8983 14.75   31.04   2.15 0
 2.80 33620. 362.01  65257.  92.87 1.9410 12.61   35.07   2.02 0
 3.00 36298. 409.71  72088.  88.59 1.9860 10.87   39.69   1.91 0
 3.20 39096. 464.11  79522.  84.24 2.0340  9.46   44.96   1.81 0
 3.40 41956. 525.79  87513.  79.80 2.0858  8.30   50.94   1.72 0
 3.60 44798. 595.29  95986.  75.25 2.1426  7.34   57.67   1.64 0
 3.80 47526. 673.05 104830.  70.61 2.2058  6.55   65.20   1.57 0
 4.00 50019. 759.43 113889.  65.86 2.2769  5.89   73.57   1.50 0
 4.20 52136. 854.57 122961.  61.01 2.3585  5.33   82.79   1.44 0
 4.40 53711. 958.39 131788.  56.04 2.4536  4.86   92.85   1.38 0
 4.60 54559.1070.48 140061.  50.97 2.5672  4.46  103.71   1.33 0
 4.80 54476.1190.02 147411.  45.78 2.7060  4.12  115.29   1.29 0
 5.00 53249.1315.64 153418.  40.47 2.8812  3.82  127.46   1.24 0
```

Figure 8.10: Off-Design Mach range data from OFFX that produces mass flow data

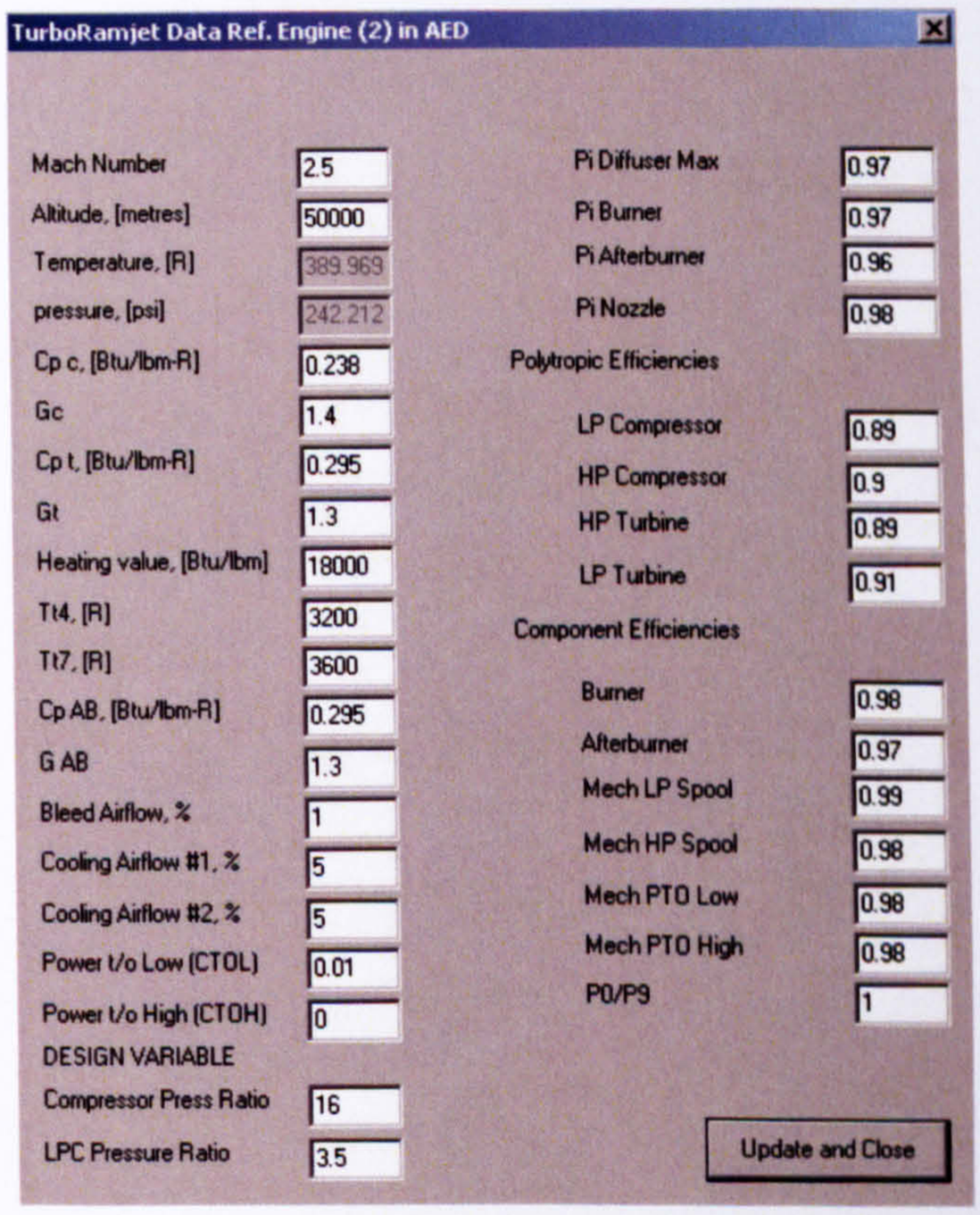


Figure 8.11: Reference file

polynomial are stored and are used to define the wing-curve. The streamline tracing technique then generates the remaining lower surface provided that no behaviour constraint is violated. If so, then the loop restarts by changing the variables and replacing the original input vectors. Output is stored in a separate vector and is called from the GUI. This is illustrated in Figure 8.5.

With a successful iteration, the objective function value is stored and compared to the next successful iteration result and continues to do so until the tolerance is achieved. In doing so the optimisation exits the loop and delivers its output to the vector.

These processes take the form of subroutine calls in the function call routine in the `COptimisation()` class and optimisation uses most of the subroutines presented in HICAD.

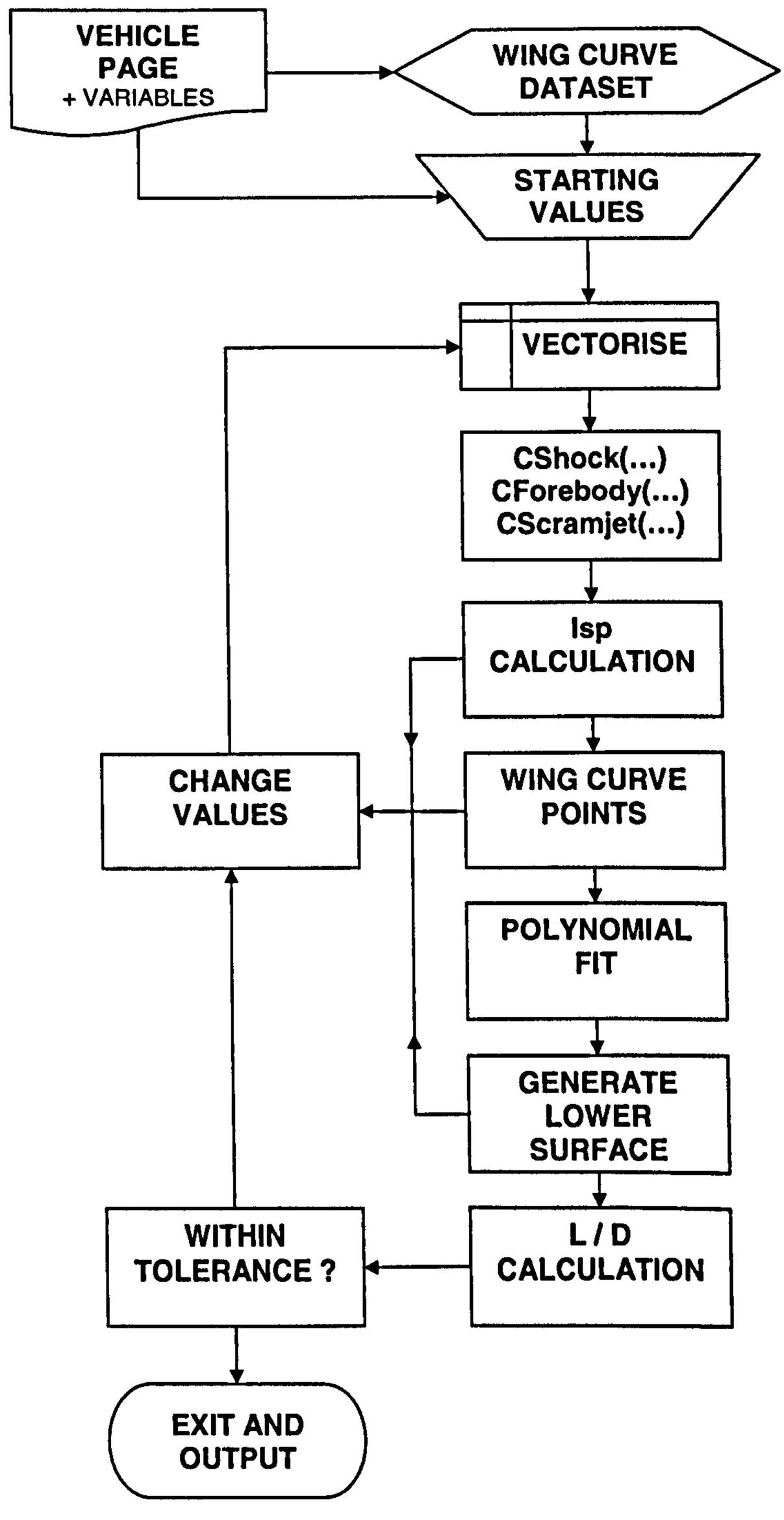


Figure 8.12: The optimisation solution flowchart structure.

9

Discussion

The results that have been demonstrated by the design methodology are discussed according to the objectives laid out at the start of this thesis. This chapter is split into the main component technologies developed in Chapters 3 to 6 and the results that were presented in Chapters 7 and 8. With reference to the full design methodology in Figure 3.2, the biggest part has already been completed within the present research programme as illustrated in Figure 9.1. The tasks that are still outstanding are grayed and these will be addressed in future investigations.

9.1 Waverider

The conically-derived waverider was selected for this study and is generated using an inverse design process. This means the shock structure is defined at the inlet station and the lower surface is carved from the resulting flowfield.

The results show that for a constant set of inlet-curve generating parameters *ac* and *bc*, the forebody length increases with an increasing on-design Mach number. This is because streamlines of constant streamfunction value are traced forward until the shock structure is intercepted. This occurs further forward than lower Mach numbers. For a given length of waverider, the remaining length for the scramjet combustor and nozzle are therefore reduced. The inlet-curve is constrained by limits imposed by the generating cone as the minimum and the conical shock as the maximum limit.

A change in the elliptical parameters; *ae* and *be*, offers different shaped forebodies. For

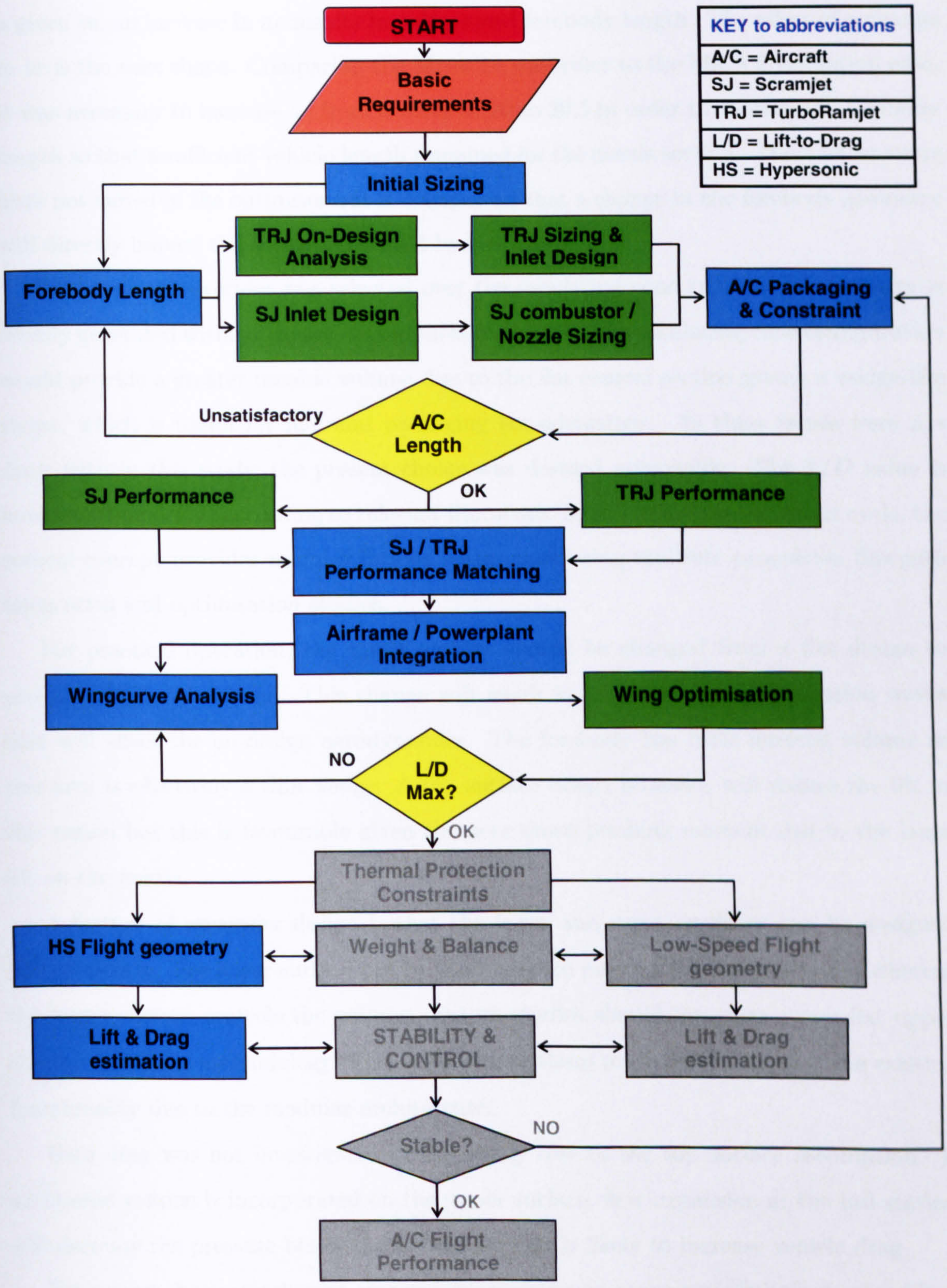


Figure 9.1: Completed models of HICAD shown in colour. Refer also to Figure 3.2 for the complete methodology.

a given *be*, an increase in *ae* results in a decreased forebody length. The effect of a change in *be* is the nose shape. Comparing the Mach 10 waverider to the Mach 9 validation case, it was necessary to increase *ae* from a value of 20 to 20.5 in order to shorten the forebody length so that a sufficient vehicle length remained for the nozzle section. These parameters were not varied in the optimiser but it is expected that a change in the forebody geometry will directly impact the thrust generated by the nozzle.

This type of waverider was selected over the osculating cone type as the geometry is readily generated without excessive computational time. The osculating cone configuration would provide a greater useable volume due to the flat central section giving a wedge-like shape, which is useful for fuel and packaging considerations. As these issues were not dealt with in this study, the present choice was deemed acceptable. The L/D value is however, comparable according to relevant literature. In this initial development cycle, the conical concept provides useful solutions when considering multiple propulsion flowpath integration and optimisation studies.

For practical operation, the upper surface should be changed from a flat design to provide additional volume. This change will result in compression and expansion waves that will affect the on-design aerodynamics. The forebody has little internal volume as this area is effectively a thin wedge. A top surface bulge, however, will reduce the lift in this region but this is favourable given the nose down pitching moment due to the large lift on the nozzle.

A feature of waverider design is that the lower and upper surfaces can be designed independently. The lower surface can be attributed to most of the lift generation whereas the upper surface controls the volume. Future studies should integrate a non-flat upper surface within the methodology. This is possible without much modification of the existing functionality due to the modular architecture.

Base drag was not investigated in this study due to the top surface assumption. If additional volume is incorporated on the upper surface, flow expansion at the tail station will decrease the pressure below the freestream and is likely to increase vehicle drag.

For perfect shock attachment, waveriders are designed assuming infinitely sharp leading edges. For practical reasons, a certain degree of leading-edge blunting will be required to alleviate aerodynamic heating. It is known that heat dissipation at the leading edges is

proportional to the inverse of the square-root of the leading-edge radius. In other words, the greater the blunting, the lower the heating values. A tradeoff is required between the optimum level of blunting to the reduced performance due to flow spillage.

9.2 Scramjet

The nose-to-tail high-speed propulsion model consists of an inviscid, quasi-two-dimensional, real gas, shock wave model that is coupled to a quasi-one-dimensional dual-mode scramjet combustor analysis code.

The shock wave model solves the flowfield for a given forebody shock angle and high-speed ramp angle using information from the freestream Mach number, cruise altitude and cowl position.

The waverider forebody is providing the precompression for the scramjet combustor. In addition, a two-dimensional ramp is required to augment the compression for effective combustion, which raises both the temperature and pressure at the combustor face. This ramp is highly-integrated with the lower surface. Its angle is selected based on both a shock-on-lip condition at the cowl lip and cancellation of the shock on the combustor shoulder at station 2 shown in Figure 4.1. Furthermore, the flow properties must meet the pressure ratio given by Equation 4.7. This process is iterative. The highest temperature and pressure at station 2 was shown in the 3D plots to occur at the higher end of Mach numbers and at the lowest altitude

There are cases where a solution does not exist and the code returns a null value in order to restart the process with a new angle. During analysis, oblique shock relations are used to determine the flow properties after each shock. The cowl is positioned such that it is parallel to the streamlines after the flow passes the reflected / cancelling shock. The cowl surface oriented in this manner does not incur compression or expansion as the relative angle of attack at the on-design condition is zero. Deviations from this arrangement will result in increased lift but also greater drag. As on-design Mach number increases, the pressure and temperature at station 2 increases but to avoid exceeding flow property limits, the altitude of cruise can be adjusted manually. The conical flowfield is mass-averaged to enable a one-dimensional oblique shock calculation.

The heat release schedule is calculated stepwise in the scramjet burner using quasi-

one-dimensional analysis. The model was compared with available experimental data and shown to have good agreement. The validation was based on a cylindrical scramjet design. This validation is similar to other scramjet-waverider integration studies. A constant pressure design and linear-divergent combustor section is used for design of the scramjet. An isolator is required if the separation criteria of Equation 5.11 is satisfied. The isolator permits dual-mode scramjet operation.

An increasing value for the specific heats capacity, γ_c was shown to increase the temperature and pressure at the exit of the combustor for a given design and Mach number at station 4 was a lower value. Default values for the combustor were $\gamma_c = 1.362$ for compression, $\gamma_b = 1.238$ for burning and $\gamma_e = 1.24$ for expansion. Increasing the fuel-air ratio has a positive effect on the performance of the scramjet as expected with a default value set at $f = 0.0291$.

Hydrogen was selected as the main fuel as it offers good heat-sink capacity and high-energy content. Fuel is injected at station 3 and the combustor length is estimated using an analytical relationship that accounts for the reaction time. Similarly, the length of the precombustion shock train (isolator), is estimated using Equation 5.1.

Continuing with the propulsion flowpath, the aftbody acts as an extension to the nozzle. Stations 4 to 10 represent the expansion surface and this generates thrust for the vehicle. The two-dimensional Method of Characteristics in conjunction with numerical routines provided by `IMOC`, are used to design the upper surface by incrementing the upper surface angle until the geometric limits enforced by the remaining length of vehicle are attained. The method computes an expansion net based on the upper wall angle and lower nozzle cowl lip. The cowl chamfer angle was maintained fixed at 6 degrees. Flow properties are calculated at nodes based on positive and negative characteristic lines.

A problem-specific script was written to call the routines to enable this complex calculation with the bookkeeping handled automatically. The script is significantly more complicated than a single expansion ramp due to the vector-handling. The visualisation of the expansion net comes from the `Tcl/Tk` interpretator and currently `HICAD` offers a data file, which outputs the performance at station 10 for a particular wall angle.

The combined effect of the two centred-expansion nets resulted in a greater thrust at the tail station. For $M_4 = 4.01$, an exit Mach number of $M_{10} = 5.34$ was achieved for a

nozzle length of $14m$ and exit height of $H_{10} = 5.8m$. This resulted in a thrust of $1MN$. The performance from the simplified stream thrust analysis applied to same problem did not achieve the performance levels of the more accurate nozzle solution.

At high-thrust levels, the nozzle will be overexpanded and this will be a dominant consideration at transonic speeds. It may also separate shortly after the combustor exit leading to a large rise in base drag and changes in pitching moment.

Pitching moment has not been calculated in this study but it is an important consideration for further research work, as moment forces are likely to be large.

There are limitations to cycle analysis in the combustor as opposed to CFD analysis. For example the side walls are assumed to have zero thickness, which results in no pressure drag, whereas viscous analysis would demonstrate an increase in drag due to three-dimensional effects.

9.3 Turboramjet

The TBCC turboramjet provides low-speed performance and was modelled using one-dimensional cycle analysis. Its performance depends on the prescription of compressor pressure ratio, total pressure and temperature ratios. Their values were selected in accordance with requirements for a Mach 5 transition point to scramjet propulsion. The scramjet performance should therefore be determined prior to attempting transition performance matching. A bypass ratio parameter was used to investigate the upper limit of turboramjet performance. The value tends to zero at higher Mach numbers at which point the engine reaches its useful airbreathing performance limits. The zero value can be delayed up to the desired hypersonic cruise altitude by including effects of reduction in ambient conditions associated with a constant dynamic pressure trajectory.

A detailed inlet design study was performed to supply a required air mass flow for effective turboramjet operation. A Mach 2.0 design-point at an altitude of $12.2km$ was selected in the inlet presented in Chapter 7 and `OFFX` generated mass flow data for an off-design Mach range between standstill and Mach 5. This produced an inlet area of $A_1 = 1.84m^2$ with pressure recovery of a minimum of 0.5 that was set in the code. This analysis assumed flow was compressed by the forebody and scramjet ramp before approaching the low-speed inlet. This is why Mach 3.2 is displayed in the upper range of Figure 7.25. The

total flow turning angle was 24 degrees using a four-ramp design.

Compare this then to the inlet of a design point of Mach 2.5 and altitude of $15.2km$. An inlet area of $A_1 = 2.54m^2$ was achieved with a corresponding pressure recovery of 0.35 at Mach 5. The total flow-turning angle was also greater. It is important to note that this earlier analysis did not account for the compression achieved by the forebody and ramp angle prior to the inlet design.

The ramp angles are selected on their total pressure recovery merit, whose values should compare favourably up to at least, the design point with reference to the prescribed military specification.

Performance matching may be performed only if `OFFX` operates. If a different transition point is selected, that will affect the parameters for the turboramjet when considering the required thrust and Isp. The entire analysis will change as the scramjet will develop a lower thrust, different value for drag and the size of the low-speed inlet will be different as will the required ramp angles. This change in transition point was not investigated in the present study. The transition point is determined by the upper operating limit of a turboramjet engine and the Mach 5 point is an optimistic initial assumption.

9.4 Integration and Optimisation

The inlet flowpath and positioning of the turboramjet is an important operational consideration and affects vehicle performance. An over / under concept was adopted, which places the turboramjet above the scramjet in a parallel configuration. The inlet then extends forward, until it meets the scramjet ramp. During low-speed operation, an inlet door diverts flow away from the scramjet to avoid incurring unnecessary drag. When not in use, the door simply retracts upwards, within the scramjet ramp. The low-speed inlet consists of a four-ramp configuration and is positioned on the roof of its flowpath. Before flow reaches the variable geometry inlet, it is first compressed by the fixed geometry forebody angle and ramp. It is believed that the low-speed cowling will meet the shocks generated by the first two angles to ensure minimum flow spillage. Simultaneous operation of the low-speed ramps will ensure the correct mass flow is delivered to the turbine engine, at the right conditions.

As the flow at the low-speed inlet is subject to prior compression, the total flow-turning

at its design point is minimised and hence produces a better pressure recovery. However, there is an expansion that will exist between the high-speed ramp and low-speed inlet that has not been accounted for. Its analysis depends on the precise orientation of the low-speed inlet with the aid of CAD, something that was not completed in this study due to time limitations.

A nozzle door completes the propulsion flowpath towards the rear of the turboramjet. It operates in a similar manner to the inlet door whereby the door opens to release the high-temperature and -pressure exhaust flow into the existing nozzle geometry formed by the aftbody expansion surface. When not required, the nozzle door once again closes to form a streamlined surface with the upper surface to eliminate any additional drag contribution. The nozzle-door will also minimise under and over expansion of the exhaust flow during its variable-geometry operation.

The entire undersurface of a hypersonic vehicle contributes to the propulsive thrust and lift. Therefore, hypersonic vehicle design epitomises a highly integrated, multi-variable procedure. In addition to these reasons and the existence of a large parameter set, numerical optimisation maximises the probability of system effectiveness. Optimisation becomes necessary to fully account for the non-linearities in the coupling of systems and the unconventional and sometimes counter-intuitive, design process that single parameter investigations would fail to notice.

The engine/airframe installation was numerically optimised to maximise $Isp \times L/D$. This merit function was deemed suitable for cruise vehicles as it relates to both aerodynamic and propulsive efficiency. Merit functions depend on mission requirements. High L/D is important for cruise range, but volume and packaging are other important factors as are static stability at cruise and off-design Mach numbers. These, however, may be represented as constraints in an overall optimised solution.

In this study, seven geometric wing curve variables, the engine span and the forebody shock angle were used to optimise vehicle configurations. The problem presents a severely-constrained design space and the simplex method proved successful in dealing with these violations without requiring function derivatives. The bounds to the constraints are within physically reasonable limits and these are based on the literature. Several variables are held constant such as the total vehicle length and the upper surface is assumed flat.

The wing-curve is central to the design of the waverider and has a direct effect on L/D estimation. Currently, a cubic polynomial is fit through the seven geometric points at the tail station. Referring again to Figure 7.42, the fit offers a trendline that represents the data well. If, however, a cubic spline method was used, this would ensure the endpoints are fixed when fitting the curve. The points would be further spaced allowing a greater curvature and this would permit a greater anhedral at the wing tips as is common for waveriders. It is expected that behavioural and side constraints would not be violated as often as the current analysis shows and lift and drag on the resulting configurations will change having a diverse affect on the results. This could be an area of further investigation.

A change in the characteristic length parameters, λ, as given in Table 4.3 would affect the rate of convergence in the simplex method. This has not been been considered in this study but it is likely that the optimiser would behave differently when attempting initial values. If for specific problems, convergence is not achieved, an area of future work could be the analysis of different input values for these parameters and perhaps even a dynamic change after a complete optimisation loop.

Optimisation followed a three step process: Isp determination, wing curve fitting, and L/D calculation. It was shown that a Mach 10 waverider was optimised to produce an $L/D = 4.26$ for a $60m$ length waverider, after 222 trials which took around 10 minutes on a 1.5 GHz processor with 512 MB RAM. This value and other performance values are in accordance with results presented in the literature for optimised configurations. A direct comparison is a difficult task as the number of parameters that were chosen in the present optimisation study vary significantly as does the mission objective etc. Also, the expected result would be different if the volume was added to the merit function in order to practically maximise range. Volume calculation procedures include tetrahedron-cell estimation methods.

The half span of the Mach 10 waverider is $y_7 = 22.82m$ and this produces a drag that is twice the value of the thrust generated. If a Thrust = Drag condition is imposed, it would be expected that this width would decrease to minimise the drag and in particular, the width of the high-speed ramp. This, however, was not investigated in this study. For future studies it would be useful to impose a Lift = Weight constraint to investigate its effect on the vehicle planform aerodynamics and shape. When the weight subroutine is

integrated in the design methodology, the exact lift could be calculated and the wing area adjusted accordingly using optimisation. Similarly, for a given drag, an equal thrust could be generated by adjusting engine performance parameters.

The number of optimisation parameters selected could be as long as the nomenclature presented at the start of this thesis. However, the designer must carefully select parameters that best reflect the mission objective. The initial study conducted here, serves to highlight the potential of the methodology. The methodology proves useful during tradeoff studies and investigating the sensitives associated with various parts of the vehicle design.

The inclusion of control surfaces is another important aspect of practical vehicle design. Contrary to conventional design practices, these must be considered together with propulsion and airframe couplings. The nozzle exerts a large pitching moment and control surface deflections will need to be designed accordingly to trim the vehicle and to minimise base drag. The nozzle orientation must be taken into consideration to prevent the exhaust plume from adversely affecting aerodynamic control surfaces.

9.5 Applications

Hypersonic concepts offer tremendous potential as future aerospace concepts. Their use in military operations are far reaching, however there are huge technical challenges before this can be realised. The common *vision* shared among leading aerospace companies is that there should be a more focused technology drive in order to avoid cancellation of projects due to budget concerns as goals are often over-ambitious.

The US in particular seek to conduct military operations that have rapid response and a high probability of success to deter aggression. For example, the Wright Patterson Air Force Base have documented the need for hypersonic technology in areas that include rapid-response military vehicles that span the entire aerospace capability be it tactical strike aircraft, hypersonic cruise missiles or orbital ascent vehicles for military space operations.

Emphasis is being placed on a Mach 7 airplane operational vehicle for long range strike/reconnaissance/SEAD of time critical targets and UAV's in the 2012 time frame with the technology extended to deal with routine RLV's by 2025.

A review of several appropriate organisations that include NASA, DARPA and Boeing

engaged in hypersonic research, have returned an apparent skills shortfall in key areas. This includes airbreathing propulsion and in particular scramjets whose numerical analysis can be improved by incorporating finite-rate chemistry and complex process of fuel-air mixing in a supersonic stream. The vast subject of airframe-propulsion integration requires further investigation and in particular the stability and control at hypersonic speeds. Also related is continual improvements in advanced materials for thermal protection systems that are lightweight, robust and cheap.

Given that most studies have concluded hydrogen to be a relevant fuel, there is a requirement for advanced structures to hold the cryogenic fuels that can withstand extreme environments. These structures then require fabrication and consequent testing.

Multi-variable optimisation has proven to be an invaluable method in vastly improving vehicle configurations at the conceptual design stage. These methods need to be improved to account for more detailed engineering models to gain confidence in the unconventional design practices. Optimisation studies can highlight sensitivities in physics-based models.

Design studies only prove useful if vehicles are flight tested so that engineering models can be validated and improved. The X-43A success proved that scramjet-airframe integrated vehicles can sustain hypersonic cruise speeds and provides exciting opportunities for future research. Perhaps, then one day in the near-future, the vision of global-range, hypersonic vehicles for both endo and trans-atmospheric missions will be cost-effective enough to become as routine as existing aircraft.

10

Conclusions

The main conclusions drawn from this work, are presented in the summary of points that follow. A list of publications that resulted from this research programme is provided and finally, recommendations for further work are made with reference to the overall aims and objectives.

10.1 Achievements

The work presented in this thesis has made contributions summarised in the following points.

- On-design analysis of a conically-derived waverider airframe for Mach 9/10 operation using hydrogen fuel.
- A turbine-based turboramjet has been used in conjunction with a dual-mode scramjet to provide thrust for the full Mach range of flight from takeoff to Mach 9/10.
- Integration of the scramjet and turboramjet and their multiple engine flowpaths with the waverider airframe in an over / under arrangement.
- The performance of the two engines has been matched such that a smooth transition can occur between the low and high-speed propulsion systems at a predefined transition speed for safe vehicle operation.
- Estimation of lift and drag on the vehicles surface using viscous analysis.

- The non-linear simplex method has been successfully used to optimise the generated hypersonic vehicle configuration using seven geometric parameters in conjunction with the engine span and forebody generating shock angle. Optimisation has been shown to capture the important synergy between the various components of the vehicle. That was successfully applied to a Mach 10 baseline waverider, subject to severe tight constraints.

- A conceptual design methodology and code that offers user flexibility with emphasis placed on rapid results through employing well-established quasi-one-dimensional scramjet combustor analysis and idealised cycle analysis for the turboramjet. `HICAD` operates in the familiar Windows® environment and consists of around 14,000 lines in code.

10.2 List of Publications Produced

1. Javaid, K.H. and Serghides, V.C. (2004). An Initial Design Methodology for Operational Hypersonic Military Aircraft. *Proceedings of 24th International Congress of the Aeronautical Sciences. ICAS 2004-1.1.2.* Yokohama, Japan.

2. Javaid, K.H. and Serghides, V.C. (2004). Airframe-Propulsion Integration Methodology for Waverider-Derived Hypersonic Cruise Aircraft Design Concepts. *Journal Of Spacecraft And Rockets,* vol. 42, no. 4

3. Javaid, K.H. and Serghides, V.C. (2004). Thrust-Matching Requirements for the Conceptual Design of Hypersonic Waverider Vehicles. *Journal Of Aircraft,* (Accepted).

10.3 Recommendations For Further Study

This thesis presents a methodology that is by no means yet, a complete design procedure. The anticipated full system was presented in Figure 3.2 and is intended for completion during follow-on research programmes. What is presented, however, is a firm foundation based on widely accepted methods and tools with several opportunities for future work. For practical operational vehicles, the low-speed flight characteristics need to be

adequately addressed. Furthermore, this study has only just *scratched the surface* of the vehicle in terms of investigating optimisation. This is a large subject area that requires a more detailed investigation including different objective functions and constraints analysis.

Recommendations for further investigation are outlined here.

Vehicle

- The main improvement in the configuration shape could arise from the use of an osculating-cones based waverider as an alternative to the conically-derived concept. The increased volumetric efficiency will be beneficial when dealing with initial sizing, fuel and systems packaging.

- A cubic spline method could be used as an alternative to the cubic polynomial applied to the seven geometric wing curve points. This is likely to change the shape of the lower surface and will affect the L/D calculation.

- In the present study, the upper surface is aligned parallel to the freestream. This could be modified to allow for an upper surface expansion and compression resulting in an increased volumetric capacity. On-design aerodynamics will be affected.

- Pitching moment, base drag and centre of pressure calculations should be estimated to ensure static stability is maintained during cruise and off-design conditions. A change in the upper-surface design will affect the pitching moment. During operation, the inlet cowl lips will tend to pitch the vehicle down when in scramjet-mode. The nozzle will have a significant effect on the resultant moments.

- The addition of vertical and horizontal stabilisers will affect both trim and stability. Their analysis will be important during low-speed vehicle configuration analysis.

Propulsion

- The scramjet design could be improved to deal with finite-rate chemistry effects. Different fuels could be incorporated, which could change packaging requirements. Also, the use of hydrocarbon fuels instead of hydrogen could significantly affect

planform shape. Inlet unstart in the scramjet has not been considered due to the 1D analysis.

- The performance of the RBCC engine could be compared to the turboramjet. The effect of changing the transition Mach number between engines could be analysed for its effect on the resulting performance and sizing process.

- Off-design operation needs to be fully addressed. This would embody scramjet variable-inlet geometry to minimise flow spillage and similarly for the nozzle cowl to prevent over- or under-expansion depending on conditions. Off-design performance estimation would require trajectory optimisation across the full flight envelope to estimate the fuel required for the non-cruise segment of the mission. Trajectory optimisation is complicated as a wide variety of Mach numbers and angle-of-attacks will be encountered leading to various types of shock-boundary interactions.

- The length by which the scramjet exterior cowl extends into the expansion flowfield will affect performance as will a change in chamfer angle. These could both be additional candidate parameters for optimisation as they are likely to increase drag but increase thrust also. A tradeoff is therefore necessary. Similar graphics output to `IMOC` could be incorporated within `HICAD`, as currently only an output data file is available. This will allow real time visualisation so that the user can modify the input conditions accordingly.

Methodology & Optimisation

- Overall, the development of `HICAD` should continue to provide a holistic design approach. New subroutines can be easily integrated within the existing framework as the code is written in a modular format.

- The methodology should be extended to analyse the full synergy between aerodynamics, initial sizing, weights, propulsion, stability, control and packaging. Analysis of the low-speed flight characteristics and aerodynamics for the same component studies will enable the design of practical, operational vehicles. A weights sizing based on empirical correlations was discussed in Chapter 3 and could be incorporated within the code.

- Improvements should not compromise the ease of use, flexibility and ability to produce rapid results, but should maintain a good degree of accuracy for the conceptual level of design.

- Optimisation in the current study focuses on the geometry of the wing-curve and two fundamental waverider variables. Additional variables would provide different and more accurate results leading to increased confidence. The current objective function, although adequate for this level of design, could be modified with more parameters. The successful vehicle design is highly dependent on optimisation to produce significantly better configurations and to capture the synergies amongst various contributing design disciplines. One particular area of improvement could lie in optimising for Thrust = Drag and Lift = Weight.

- The design process could be linked to a parametric CAD system that will allow geometric shape control. A lot of useful information could be gained by linking CAD with the geometry generation part of a design code coupled to Multidisciplinary Optimisation. The geometry and aerodynamics are interdependent; for example, the compression required at the combustor through the use of inlet ramps versus the drag they produce.

It is time not for a revolution,

but an evolution into hypersonic vehicle design.

A

Compressible Flow Relations

A wedge that produces a shock wave with a shock angle, β, has a wedge angle, θ, given by the following relation

$$tan(\theta) = \frac{M_{n1}^2 - 1}{tan(\beta)\left(\frac{\gamma+1}{2}M_1^2 - M_{n1}^2 + 1\right)} \tag{A.1}$$

where the the Mach number before and after the shock wave are given by M_{n1} and M_{n2} respectively. M_2 represents the Mach number parallel to the wedge.

$$M_{n1} = M_1 sin(\beta) \tag{A.2}$$

$$M_{n2}^2 = \frac{M_{n1}^2 + \frac{2}{\gamma-1}}{\frac{2\gamma M_{n1}^2}{\gamma-1} - 1} \tag{A.3}$$

$$M_2 = \frac{M_{n2}}{sin(\beta - \theta)} \tag{A.4}$$

The pressure, density and temperature ratios of the shock, respectively, are (calorically perfect gas)

$$\frac{p_2}{p_1} = 1 + \frac{2\gamma}{\gamma+1}(M_{n1}^2 - 1) \tag{A.5}$$

$$\frac{\rho_2}{\rho_1} = \frac{(\gamma+1)M_{n1}^2}{(\gamma-1)M_{n1}^2 + 2} \tag{A.6}$$

$$\frac{T_2}{T_1} = \frac{p_2}{p_1}\frac{\rho_2}{\rho_1} \tag{A.7}$$

Isentropic flow properties for the (stagnation) temperature, density and pressure, respectively for a calorically perfect gas are

$$T_{t0} = T_0 \left(1 + \frac{\gamma - 1}{2} M_0^2\right) \tag{A.8}$$

$$p_{t0} = p_0 \left(\frac{T_{t0}}{T_0}\right)^{\frac{\gamma}{\gamma-1}} \tag{A.9}$$

$$\rho_{t0} = \rho_0 \left(\frac{T_{t0}}{T_0}\right)^{\frac{1}{\gamma-1}} \tag{A.10}$$

A useful rearrangement of Equation A.1, is its closed form solution (Starkey (2000) for weak shock ($n = 0$) and strong shock (n=1) given by

$$\tan\beta = \frac{b + 9ac}{2(1 - 3ab)} - \frac{d(27a^2\sqrt{c} + 9ab - 2)}{6a(1 - 3ab)} tan\left[\frac{n\pi}{3} + \frac{1}{3} tan^{-1}\left(\frac{1}{d}\right)\right] \tag{A.11}$$

$$n = \begin{cases} 0 & \text{Weak Shock} \\ 1 & \text{Strong Shock} \end{cases}$$

$$a = \left[\frac{\gamma - 1}{2} + \frac{(\gamma + 1)c}{2}\right] tan\theta \tag{A.12}$$

$$b = \left[\frac{\gamma + 1}{2} + \frac{(\gamma + 3)c}{2}\right] tan\theta \tag{A.13}$$

$$c = tan^2 a sin(1/M) \tag{A.14}$$

$$d = \sqrt{\frac{4(1 - 3ab)^3}{(27a^2c + 9ab - 2)^2} - 1} \tag{A.15}$$

B

Waverider Calculations

B.1 Breguet Range Equation

To sustain a cruise condition is to fly at a steady, level altitude. During this regime, the weight, W of an aircraft must be balanced by the lift, L, *and* the drag, D, is matched by the propulsive thrust.

For a change in mass, dM, due to consumption of fuel over a period of time, dt, the following holds

$$-gI_{sp}\frac{dM}{dt} = \frac{W}{(L/D)} \tag{B.1}$$

Multiplying velocity, V, with time gives the range and integrating W from initial (i) to final (f) conditions yields the well known Breguet range equation

$$R = I_{sp}V\left(\frac{L}{D}\right)\ln\left(\frac{W_0}{W_f}\right) \tag{B.2}$$

B.2 Integration

B.2.1 Runge-Kutta

The Runge-Kutta technique is a method of numerically integrating an ordinary differential equation (ODE) without evaluating derivatives of a function $f(x, y)$.

$$y_{n+1} = y_n + \frac{1}{6}(k_1 + k_2 + k_3 + k_4) \tag{B.3}$$

where,

$$\begin{aligned} k_1 &= hf(x_n, y_n) \\ k_2 &= hf\left(x_n + \frac{h}{2}, y_n + \frac{k1}{2}\right) \\ k_3 &= hf\left(x_n + \frac{h}{2}, y_n + \frac{k2}{2}\right) \\ k_4 &= hf(x_n + h, y_n + k3) \end{aligned}$$

and h is the step size.

B.2.2 Simpson Method

The Simpson rule is used to integrate the streamfunction equation for the waverider calculation given by Equation 4.3. The method is briefly described below.

Consider the integral of a function $f(x)$ that is required between a lower limit a and upper limit b where a or b is equal to one of the range of values along an abscissa, x_i. The integration then for n steps with interval $[a, b]$ can be split into $2n$ pieces each with a width

$$h = \frac{b-a}{2n} \tag{B.4}$$

The x-coordinates range from $x_0, x_1, ..., x_{2n-1}, x_{2n}$. Let $y_i = f(x_i)$. The Simpson rule is then given by the following equation

$$\int_a^b f(x)\,dx = \frac{h}{3}[y_0 + 4y_1 + 2y_2 + ... + 4y_{2n-1} + y_{2n}] \tag{B.5}$$

B.3 Nozzle

The solution of a cubic polynomial applied to the design of an external nozzle was provided by Starkey (2000) and repeated here for convenience. Figure B.1 illustrates the initial (a) and end (b) point of the upper wall. The equations will be formulated accordingly.

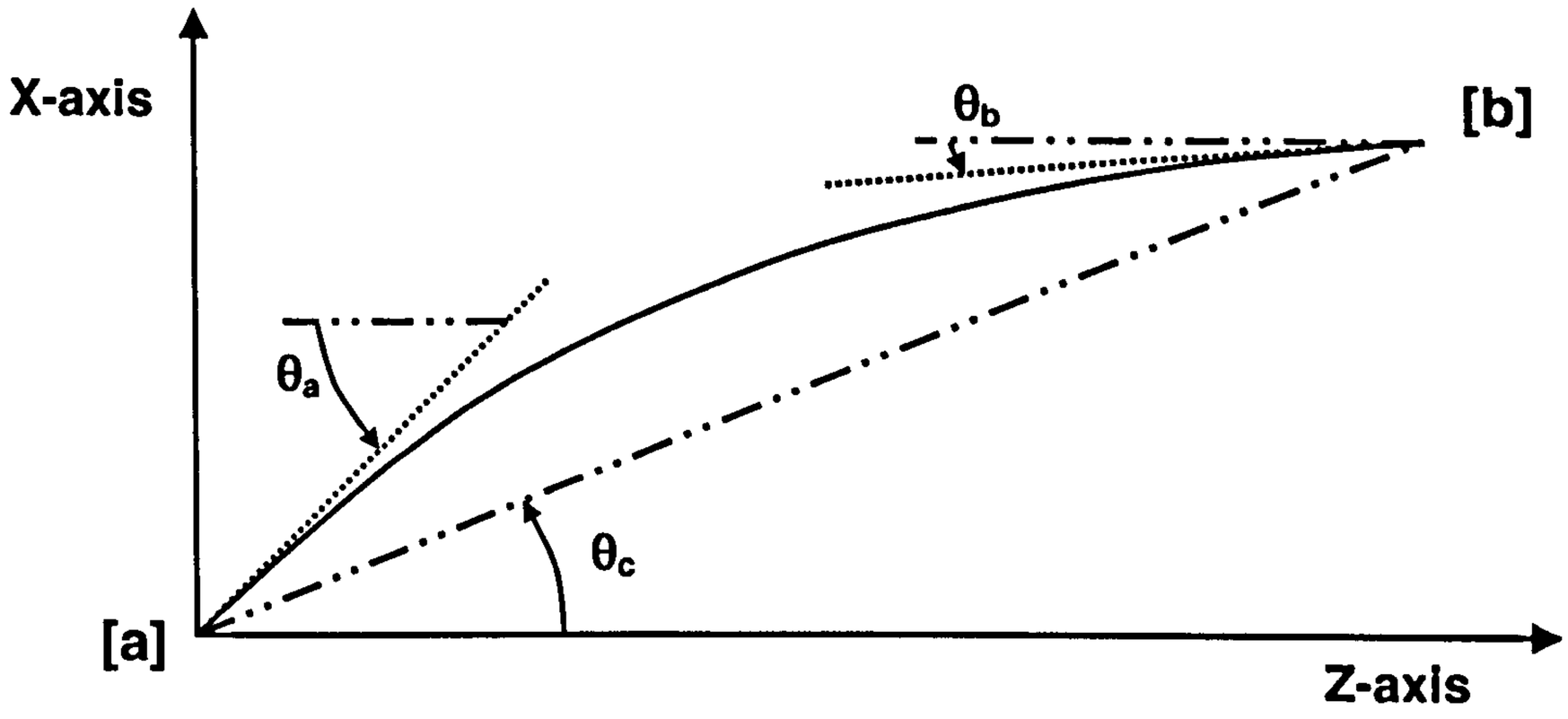


Figure B.1: Nozzle thrust surface defined by a cubic polynomial.

The general third order polynomial equation as written in the code is

$$x = ((A * z + B) * z + C) * z + D \tag{B.6}$$

where A, B, C, D are the coefficients of this equation. Their values are determined thought the following set of equations:

$$x_n = x_b - x_a \tag{B.7}$$

$$z_n = z_b - z_a \tag{B.8}$$

$$\theta_c = \arctan\left(\frac{x_n}{z_n}\right) \tag{B.9}$$

where the subscript n, denotes nozzle and θ_c is the chordal angle. Then the coefficients are determined as follows

$$A = \frac{1}{z_n^3}(z_n(tan(\theta_a+\theta_a)-2\lambda_3) \quad \text{(B.10)}$$

$$B = \frac{1}{z_n^3}(\lambda_1 tan(\theta_a)+\lambda_2 tan(\theta_b)+3(z_b+z_a)\lambda_3) \quad \text{(B.11)}$$

$$C = \frac{-1}{z_n^3}(\lambda_2 z_b tan(\theta_a)+\lambda_1 z_a tan(\theta_b)+6z_b z_a\lambda_3) \quad \text{(B.12)}$$

$$D = \frac{1}{z_n^3}(-z_b z_a z_n(z_b tan(\theta_a)+z_a tan(\theta_b)+ \quad \text{(B.13)}$$

$$z_b^2(z_b-3z_a)x_a+z_a^2(3z_b-z_a)(x_a+\lambda_3)) \quad \text{(B.14)}$$

where the following substitutions were made

$$\lambda_1 = -2z_b^2+z_b z_a+z_a^2 \quad \text{(B.15)}$$

$$\lambda_2 = -z_b^2+z_b z_a+2z_a^2 \quad \text{(B.16)}$$

$$\lambda_3 = z_n tan(\theta_c) \quad \text{(B.17)}$$

B.4 Simplex Method

The downhill simplex method `amoeba.cpp` original implementation from Press (2002) for a simplex of $n+1$ vertices where n is the dimension size. Return the vertices of a simplex minimizing the function `funk` to within pre-defined tolerance of a minimum function value.

```
#include <cmath>
#include "nr.h"

using namespace std;

namespace {
    inline void get_psum(Mat_I_DP &p, Vec_O_DP &psum)    {
int i,j;
DP sum;

int mpts=p.nrows();
int ndim=p.ncols();
for (j=0;j<ndim;j++) {
    for (sum=0.0,i=0;i<mpts;i++)
```

```
                sum += p[i][j];
            psum[j]=sum;
        }
    }
}

void NR::amoeba(Mat_IO_DP &p, Vec_IO_DP &y, const DP ftol,
    DP funk(Vec_I_DP &), int &nfunk)    {

const int NMAX=5000;
const DP TINY=1.0e-10;
int i,ihi,ilo,inhi,j;
DP rtol,ysave,ytry;

//Originals -1.0,0.5,2.0 KHJ 7 April 2004
double ALPHA = -1., BETA = 0.5, GAMMA = 2.;

int mpts=p.nrows();
int ndim=p.ncols();
Vec_DP psum(ndim);
nfunk=0;
get_psum(p,psum);
for (;;) {
    ilo=0;
    ihi = y[0]>y[1] ? (inhi=1,0) : (inhi=0,1);
    for (i=0;i<mpts;i++) {
        if (y[i] <= y[ilo]) ilo=i;
        if (y[i] > y[ihi]) {
            inhi=ihi;
            ihi=i;
        } else if (y[i] > y[inhi] && i != ihi) inhi=i;
    }
    rtol=2.0*fabs(y[ihi]-y[ilo])/(fabs(y[ihi])+fabs(y[ilo])+TINY);
    if (rtol < ftol) {
        SWAP(y[0],y[ilo]);
        for (i=0;i<ndim;i++) SWAP(p[0][i],p[ilo][i]);
        break;
    }
```

```
if (nfunk >= NMAX) nrerror("NMAX exceeded");
nfunk += 2;
ytry=amotry(p,y,psum,funk,ihi,ALPHA);        //alpha =-1.0
if (ytry <= y[ilo])
    ytry=amotry(p,y,psum,funk,ihi,GAMMA);    //gamma = 2.0
else if (ytry >= y[inhi]) {
    ysave=y[ihi];
ytry=amotry(p,y,psum,funk,ihi,BETA);     //beta  = 0.5
if (ytry >= ysave) {
    for (i=0;i<mpts;i++) {
        if (i != ilo) {
            for (j=0;j<ndim;j++)
                p[i][j]=psum[j]=0.5*(p[i][j]+p[ilo][j]);
            y[i]=funk(psum);
        }
    }
    nfunk += ndim;
    get_psum(p,psum);
}
        } else --nfunk;
    }
}
```

B.4.1 Rosenbrock's Parabolic Valley: A test problem

$$y = 100(x_2 - x_1^2)^2 + (1 - x_1)^2 \tag{B.18}$$

with starting position (-1,2,1) and minimum (1,1).

Bibliography

ALLEN, H. J. AND EGGERS, JR, A. J. 1958 A Study of the Motion and Aerodynamic Heating of Ballistic Missiles Entering the Earth's Atmosphere at High Supersonic Speeds. NACA Report 1381. NACA Ames Aeronautical Laboratory.

ANDERSON, G., MCCLINTON, C. AND WEIDNER, J. 2000 Scramjet Performance. In *Scramjet Propulsion* (ed. S. Murthy and E. Curran), *Progress in Astronautics and Aeronautics*, vol. 189, pp. 597–695. Reston, VA: AIAA, Inc.

ANDERSON, G. Y. AND GOODERUM, P. B. 1974 Exploratory Tests of Two Strut Fuel Injectors For Supersonic Combustion. NASA TN D-7581. NASA Langley.

ANDERSON, J. D. 1989 *Hypersonic and High Temperature Gas Dynamics*. New York: McGraw-Hill Publishing.

ANDERSON, JR., J. D. 1990 *Modern Compressible Flow: with Historical Perspective*, international edn., pp. 311–331. Singapore: McGraw-Hill, Inc.

ANDERSON, JR., J. D. AND LEWIS, M. J. 1993 Hypersonic Waveriders - Where Do We Stand? AIAA Paper 93–0399. Univ. of Maryland.

BEN-YAKAR, A. AND HANSON, R. K. 2001 Cavity Flame-Holders For Ignition and Flame Stabilization In Scramjets: An Overview. *Journal of Propulsion and Power* **17** (4), 869-877.

BERTIN, J. J. 1994 *Hypersonic Aerothermodynamics*. *AIAA Education Series* . Washington: AIAA.

BERTIN, J. J. AND CUMMINGS, R. M. 2003 Fifty Years Of Hypersonics: Where We've Been, Where We're Going. *Progress in Aerospace Sciences* **39** (6–7), 511–536.

BILLIG, F. 1991 *Propulsion Systems from Takeoff to High-Speed Flight*, *High-Speed Flight Propulsion Systems*, vol. 137, Progress In Aeronautics and Astronautics 1, pp. 21–100. Washington, DC: AIAA, editor-in-chief; A. Richard Seebass.

BILLIG, F. AND GRENLESKI, S. 1970 Heat Transfer In Supersonic Combustion Processes. In *Heat Transfer 1970, Fourth International Heat Transfer Conference, Paris-Versailles*, vol. III, pp. 1–11. Elsevier, Amsterdam.

BILLIG, F. S. 1990 Design And Development Of Single-Stage-To-Orbit Vehicles. *John Hopkins APL Technical Digest* **11** (3 and 4), 336–352.

BILLIG, F. S. 1993 Research On Supersonic Combustion. *Journal of Propulsion and Power* **9** (4), 499–514.

BLANKSON, I. 1994 Air-Breathing Hypersonic Cruise: Prospects For Mach 4-7 Waverider Aircraft. *Transactions of the ASME: Journal of Engineering for Gas Turbines and Power* **116** (1), 104–115.

BLOSSER, M. L., BLANKSON, I. M., SCHWOERKE, S., BRUNSON, D. AND HAGSETH, P. 1995 Wing Leading-Edge Design Concepts For Airbreathing Hypersonic Waveriders. *Journal of Aircraft* **32** (2), 307–312.

BOWCUTT, K., ANDERSON, J. AND CAPRIOTTI, D. 1987 Viscous Optimized Hypersonic Waveriders. AIAA Paper 87–0272.

BOWCUTT, K. G. 1992 Hypersonic Aircraft Optimization Including Aerodynamic, Propulsion, And Trim Effects. AIAA Paper 92–5055. Rockwell International Corp., Downey, CA.

BOWCUTT, K. G. 2001 Multidisciplinary Optimization Of Airbreathing Hypersonic Vehicles. *Journal of Propulsion and Power* **17** (6), 1184–1190.

BOWCUTT, K. G. 2003 A Perspective On The Future Of Aerospace Vehicle Design. AIAA Paper 2003–6957.

BRADFORD, J. E. AND OLDS, J. R. 1999 Sccream v.5 : A Web-Based Airbreathing Propulsion Analysis Tool. AIAA Paper 99–2104.

BRADLEY, M., BOWCUTT, K., MCCOMB, J., BARTOLOTTA, P. AND MCNELIS, N. 2002 Revolutionary Turbine Accelerator (RTA) Two-Stage-To-Orbit (TSTO) Vehicle Study. AIAA Paper 2002–3902.

CARREIRO, L. 1990 PDWAP - A Preliminary Design And Weights Analysis Program For Aerospace Vehicles. *Tech. Rep.* AD-A222 614. Wright Patterson AFB, OH.

CENTER, K., SOBIECZKY, H. AND DOUGHERTY, F. 1991 Interactive Design Of Waverider Geometries. AIAA Paper 91–1697. Univ. of Colorado.

CHAPUT, A. J. 1992 Preliminary Sizing Methodology For Hypersonic Vehicles. *Journal of Aircraft* **29** (2), 172–179.

COCKRELL, JR., C. E., HUEBNER, L. D. AND FINLEY, D. B. 1994 Aerodynamic Performance And Flow-Field Characteristics Of Two Waverider-Derived Hypersonic Cruise Configurations. AIAA Paper 95–0736.

COCKRELL, JR., C. E., HUEBNER, L. D. AND FINLEY, D. B. 1996 Aerodynamic Characteristics Of Two Waverider-Derived Hypersonic Cruise Configurations. NASA Technical Paper 3559. Langley Research Center, Hampton, VA.

COCKRELL, C. R., AUSLENDER, A. H. AND MCCLINTON, C. R. 2002 Technology Roadmap For Dual-Mode Scramjet Propulsion To Support Space-Access Vision Vehicle Development. AIAA Paper 2002–5188.

CORDA, C. AND ANDERSON, JR., J. D. 1988 Viscous Optimized Waveriders Designed From Axisymmetric Flow Fields. AIAA Paper 88–0369.

CROFT, J. 2004 Weapons Delivery Goes Hypersonic. *Aerospace America* pp. 38–42, May.

CZYSZ, P. AND LITTLE, M. 1993 Rocket Based Combined Cycle Engine (RBCC) - A Propulsion System For The 21st Century. AIAA Paper 93-5096. St. Louis University.

DOLVIN, D. J. 2002 System Concepts And Technology Development For Operationally Responsive Reusable Military Aerospace Vehicle. AIAA Paper 2002–5139.

ECKERT, E. 1956 Engineering Relations For Heat Transfer And Friction In High-Velocity Laminar And Turbulent Boundary-Layer Flow Over Surfaces With Constant Pressure And Temperature. *Transactions of the ASME* **78**, 1273–1283.

EGGERS, JR., A. J., ASHLEY, H. AND SPRINGER, G. S. 1990 Hypersonic Waverider Configurations From The 1950's To The 1990's. In *Proceedings of the 1st International Hypersonic Waverider Symposium*. Univ. of Maryland, College Park, MD.

ESPINOSA, A. M. AND BONDS, T. 1993 Hypersonic Airbreathing Propulsion: Mach 10 Cruiser Conceptual Design / Integration. AIAA Paper 93–4735.

FLOWER, J. W. 1963 Configurations For High Supersonic Speeds Derived From Simple Shock Waves And Expansions. *Journal of the Royal Aeronautical Society* **67**, 287.

FRY, R. S. 2004 A Century Of Ramjet Propulsion Technology Evolution. *Journal of Propulsion and Power* **20** (1), 27–58.

GILLUM, M. AND LEWIS, M. 1997 Experimental Results On A Mach 14 Waverider With Blunt Leading Edges. *Journal of Aircraft* **34** (3), 296–303.

GLASS, D. E., MERSKI, N. R. AND GLASS, C. E. 2002 Airframe Research And Technology For Hypersonic Airbreathing Vehicles. AIAA Paper 2002–5137. NASA Langley Research Center, Hampton, VA 23681.

GLATT, C. 1974 WAATS: A Computer Program For Weights Analysis Of Advanced Transportation Systems. NASA CR 2420.

GUSTAFSON, M. D. AND LIVINGSTON, J. W. 2002 An Approach Toward The Realization Of Airbreathing Hypersonic Systems. AIAA Paper 2002–5142. Wright-Patterson Air Force Base, Ohio.

HARLOFF, G. AND BERKOWITZ, B. 1988 HASA - Hypersonic Aerospace Sizing Analysis For The Preliminary Design Of Aerospace Vehicles. NASA CR 182226.

HEINZE, W. AND BARDENHAGEN, A. 1998 Waverider Aerodynamics And Preliminary Design For Two-Stage-To-Orbit Missions: Part 2. *Journal of Spacecraft and Rockets* **35** (4).

HEISER, W. H. AND PRATT, D. T. 1994 *Hypersonic Airbreathing Propulsion*, pp. 277–385. Washington, DC: AIAA.

HENRY, J. R. AND ANDERSON, G. Y. 1972 Design Considerations For The Airframe-Integrated Scramjet. NASA TM X 2895. NASA Langley.

HEWITT, F. AND JOHNSON, M. 1991 Propulsion System Performance And Integration For High Mach Air Breathing Flight. In *High-Speed Flight Propulsion Systems* (ed. S. Murthy and E. Curran), *Progress in Astronautics and Aeronautics*, vol. 137, pp. 101–142. Washington, DC: AIAA.

HORTON, I. 1998 *Beginning Visual C++ 6*, chap. 13–18. Indianapolis, IN: John Wiley & Sons Inc.

HUETER, U. AND MCCLINTON, C. R. 2002 NASAs Advanced Space Transportation Hypersonic Program. AIAA Paper 2002–5175.

HUNT, J. AND MCCLINTON, C. 1997 Scramjet Engine/Airframe Integration Methodology. AGARD Conference, Palaiseau, France, April 14-16 CP-479.

HUNT, J., PEGG, R. AND PETLEY, D. 1999 Airbreathing Hypersonic Vision-Operational-Vehicles Design Matrix. SAE 1999-01-5515. Presented 1999 World Aviation Congress and Exposition, San Francisco, CA.

HUNT, J. L. AND EISWIRTH, E. A. 1995 NASA's Dual-Fuel Airbreathing Hypersonic Vehicle Study. AIAA Paper 95–4591.

IKAWA, H. 1991 Rapid Methodology For Design And Performance Prediction Of Integrated Supersonic Combution Ramjet Engine. *Journal of Propulsion and Power* **7** (3), 437–444.

JACOBS, P. 2004 Interactive Method Of Characteristics, IMOC Version 0.1.3. Private Communication.

JOHNSON, J. 1996 Variable Cycle Engine Developments At General Electric 1955-1995. In *High-Speed Flight Propulsion Systems* (ed. S. Murthy and E. Curran), *Progress in Astronautics and Aeronautics*, vol. 165, pp. 105–158. Reston, VA: AIAA, Inc.

JONES, J., MOORE, K., PIKE, J. AND ROE, P. 1968 A Method For Designing Lifting Configurations For High Supersonic Speeds, Using Axisymmetric Flow Fields. *Ingenieur-Archive* **37**, 56–72.

KOSSIRA, H., BARDENHAGEN, A. AND HEINZE, W. 1993 Investigations On The Potential Of Hypersonic Waveriders With The Integrated Program PrADO-Hy. AIAA Paper 93–5098. Institute for Aircraft Design and Structural Mechanics (IFL).

KOTHARI, A., TARPLEY, C., MCLAUGHLIN, T. A., BABU, E. AND LIVINGSTON, J. W. 1996 Hypersonic Vehicle Design Using Inward Turning Flow Fields. AIAA Paper 96–2552.

KÜCHEMANN, D. 1978 *The Aerodynamic Design of Aircraft*, 1st edn. Oxford: Pergamon Press.

KUCZERA, H. 1993 The German Hypersonics Technology Programme Status 1993 And Perspectives. AIAA Paper 93–5159.

LEWIS, M. J. 2001 Significance Of Fuel Selection For Hypersonic Vehicle Range. *Journal of Propulsion and Power* **17** (6), 1214–1221.

LEWIS, M. J. 2003 The Promise Of Hypersonic Flight. *Physics World* p. 23, Dec.

LEWIS, M. J. AND KOTHARI, A. P. 1990 Hypersonic Waveriders For Planetary Maneuvering. In *Proceedings of the 1st International Hypersonic Waverider Symposium*. Univ. of Maryland, College Park, MD.

MAITA, M. 1993 Space Plane Concept Overview. AIAA Paper 93-5162. National Aerospace Laboratory, Japan.

MATTINGLY, J. D., HEISER, W. H. AND DALEY, D. H. 1987 *Aircraft Engine Design*, pp. 353–395. *Education Series* . New York: AIAA Education Series.

MCCLINTON, C., HUNT, J. AND RICKETTS, R. 1999 Airbreathing Hypersonic Technology Vision Vehicles And Development Dreams. AIAA Paper 99-4978. NASA.

MILLER, R. W., ARGROW, B. M. AND CENTER, K. B. 1998 Experimental Verification Of The Osculating Cones Method For Two Waverider Forebodies At Mach 4 And 6. AIAA Paper 98-0682.

MOLVIK, G., BOWLES, J. AND HUYNH, L. 1993 Analysis Of A Hypersonic Research Vehicle With A Hydrocarbon Scramjet Engine. AIAA Paper 93-0509. NASA Langley Research Center.

MOSES, P. L. 2003 X-43C Plans And Status. AIAA Paper 2003-7084. NASA Langley Research Center, Hampton, VA.

MOSES, P. L., BOUCHARD, K. A., VAUSE, R. F. AND PINCKNEY, S. Z. 1999 An Airbreathing Launch Vehicle Design With Turbine-Based Low-Speed Propulsion And Dual Mode Scramjet High-Speed Propulsion. AIAA Paper 99–4948.

NELDER, J. AND MEAD, R. 1965 A Simplex Method For Function Minimization. *Computer Journal* **7**, 308–313.

NONWEILER, T. 1959 Aerodynamic Problems Of Manned Space Vehicles. *Journal of the Royal Aerounautical Society* **63** (585), 521–528.

NONWEILER, T. 1963 Delta Wings Of Shapes Amenable To Exact Shock-Wave Theory. *Journal of the Royal Aeronautical Society* **67**, 39–40.

O'BRIEN, T. F. 2001 RBCC Engine-Airframe Integration On An Osculating Cone Waverider Vehicle. PhD thesis, Department of Aerospace Engineering, University of Maryland, College Park.

O'BRIEN, T. F. AND LEWIS, M. J. 2001*a* Quasi-One-Dimensional High-Speed Engine Mdel With Finite-Rate Chemistry. *Journal of Propulsion and Power* **17** (6), 1366–1374.

O'BRIEN, T. F. AND LEWIS, M. J. 2001*b* Rocket-Based Combined-Cycle Engine Integration On An Osculating Cone Waverider Vehicle. *Journal of Aircraft* **38** (6), 1117–1123.

O'NEILL, M. K. L. 1992 Optimized Scramjet Engine Integration On A Waverider Airframe. PhD thesis, Department of Aerospace Engineering, University of Maryland, College Park.

O'NEILL, M. K. L. AND LEWIS, M. 1993 Design Tradeoffs On Scramjet Engine Integrated Hypersonic Waverider Vehicles. *Journal of Aircraft* **30** (6), 943–952.

ORTWERTH, P. 2000 Scramjet Flowpath Integration. In *Scramjet Propulsion* (ed. E. Curran and S. Murthy), *Progress in Astronautics and Aeronautics*, vol. 189, pp. 1105–1290. Reston, VA: AIAA, Inc.

PEGG, R. J., HUNT, J. L. AND PETLEY, D. H. 1993 Design Of A Hypersonic Waverider-Derived Airplane. AIAA Paper 93–0401.

PRESS, W. H. 2002 *Numerical Recipes in C++ : The Art Of Scientific Computing*, 2nd edn. Cambridge University Press.

RASMUSSEN, M. 1980 Waverider Configurations Derived From Inclined Circular And Elliptic Cones. *Journal of Spacecraft and Rockets* **17** (6), 537–545.

ROGERS, R., CAPRIOTTI, D. AND GUY, R. 1998 Experimental Supersonic Combustion Research At NASA Langley. AIAA Paper 98–2506. NASA Langley Research Center.

ROGERS, R. AND SCHEXNAYDER, C. 1981 Chemical Kinetic Analysis Of Hydrogen-Air Ignition And Reaction Times. NASA TP 1856.

SCHINDEL, L. H. 1990 Design Model Of High-Performance Ramjet Or Scramjet-Powered Vehicles. *Journal of Spacecraft and Rockets* **27** (6), 613-617.

SEDDON, J. AND GOLDSMITH, E. 1985 *Intake Aerodynamics*. New York: AIAA Education Series.

SHAPIRO, A. H. 1953 *The Dynamics and Thermodynamics of Compressible Fluid Flow*, , vol. I, pp. 219–231. New York: The Ronald Press Company.

SHOUP, T. E. AND MISTREE, F. 1987 *Optimization Methods With Applications For Personal Computers*. Englewood Cliffs : Prentice-Hall.

SMALL, W. J., WEIDNER, J. P. AND JOHNSTON, P. 1976 Scramjet Nozzle Design And Analysis As Applied To A Highly Integrated Hypersonic Research Airplane. NASA TN D-8334. NASA Langley Research Center.

SOBIECZKY, H., DOUGHERTY, F. AND JONES, K. 1990 Hypersonic Waverider Design From Given Shock Waves. In *Proceedings of the 1st International Hypersonic Waverider Symposium*. Univ. of Maryland, College Park, MD.

STARKEY, R. P. 2000 Investigation Of Air-Breathing, Hypersonic Missile Configurations Within External Box Constraints. PhD thesis, Department of Aerospace Engineering, University of Maryland, College Park.

STARKEY, R. P. AND LEWIS, M. J. 2001 Critical Design Issues For Airbreathing Hypersonic Waverider Missiles. *Journal of Spacecraft and Rockets* **38** (4), 510–519.

TAKASHIMA, N. 1997 Optimization Of Waverider-Based Hypersonic Vehicle Designs. PhD thesis, Department of Aerospace Engineering, University of Maryland, College Park.

TAKASHIMA, N. AND LEWIS, M. 1994 Waverider Configurations Based On Non-Axisymmetric Flow Fields For Engine-Airframe Integration. AIAA Paper 94-0380.

TAKASHIMA, N. AND LEWIS, M. J. 1999 Optimization Of Waverider-Based Hypersonic Cruise Vehicles With Off-Design Considerations. *Journal of Aircraft* **36** (1), 235–245.

TANATSUGU, N. 1996 Development Study On Air Turboramjet. In *Developments in High-Speed-Vehicle Propulsion Systems* (ed. S. Murthy and E. Curran), *Progress in Astronautics and Aeronautics*, vol. 165, pp. 259–332. Reston, VA: AIAA, Inc.

TOWNEND, L. 1979 Research And Design For Lifting Reentry. *Prog. Aerospace Sci.* **18**, 1–80.

TOWNEND, L. 2001 Domain Of The Scramjet. *Journal of Propulsion and Power* **17** (6), 1205–1213.

VAN WIE, D. M. 2000 Scramjet Inlets. In *Scramjet Propulsion* (ed. S. Murthy and E. Curran), *Progress in Astronautics and Aeronautics*, vol. 189, pp. 447–511. Reston, VA: AIAA, Inc.

VANMOL, D. O. 1992 Heat Transfer Characteristics Of Hypersonic Waveriders With An Emphasis On The Leading Edge Effects. Master's thesis, Dept. of Aerospace Engineering, University of Maryland.

VENN, J. AND FLOWER, J. 1970 Shock Patterns For Simple Caret Wings. *Journal of the Royal Aeronautical Society* **74**, 339–348.

VOLAND, R., ROCK, K., HUEBNER, L., WITTE, D., FISCHER, K. AND MCCLINTON, C. 1998 Hyper-X Engine Design And Ground Test Program. AIAA Paper 98–1532. NASA Langley Research Center, Hampton, VA.

WALTRUP, P. AND BILLIG, F. 1973 Prediction Of Precompression Wall Pressure Distributions In Scramjet Engines. *Journal of Spacecraft and Rockets* **10** (9), 620-622.

WITTE, D. W., HUEBNER, L. D., TREXLER, C. A. AND CABELL, K. F. 2003 Propulsion Airframe Integration Test Techniques For Hypersonic Airbreathing Configurations At NASA Langley Research Center (invited). AIAA Paper 2003–4406. NASA Langley Research Center.

ZUCROW, M. J. AND HOFFMAN, J. D. 1977 *Gas Dynamics, Multidimensional Flow*, , vol. 2. New York: John Wiley and Sons.

BIBL. LONDIN. SCHV